The Design and Understanding of the Mechanism of Formation of Nanoporous Catalytic Materials

Kerry Simmance

University College London

A thesis presented in partial fulfilment of the

requirements for the degree of Doctor of Philosophy

2011

Declaration

I, Kerry Simmance confirm that the work presented in this thesis is my own. Where information has been derived from other sources, I confirm that this has been indicated in the thesis.

Signed _____

Kerry Simmance

2011

Abstract

The work described in this thesis is concerned with characterisation of metal-ion substituted aluminophosphates using synchrotron radiation techniques. The aim of this work is to expand the knowledge on the mechanistic aspects of formation and the framework substitution of nanoporous materials thereby enabling the design of the synthesis strategy.

The simultaneous measurement of X-ray diffraction (XRD) and X-ray absorption spectroscopy (XAS) was used to follow the formation of cobalt substituted AlPO-5 (AFI). The results obtained revealed that a cobalt-phosphorus network is formed prior to crystallization and with the aid of an *in situ* XRD study it was possible to propose a solid hydrogel transformation mechanism.

A study on the effect of the type of metal ion, organic template and metal concentration on the crystallisation of AFI materials revealed a distinct trend in the kinetics of formation with increasing metal concentration. This provided conclusive evidence that the trend seen in the kinetics is not related to the appearance of the chabazite phase, as previously suggested; the kinetic study also indicated that Zn(II) ions promote the formation of smaller rings in aluminophosphate materials.

While XAS provides information on the local structure, it is an average of all the environments including extra-framework cations, therefore XRD methods, which are sensitive to the long-range order, were employed to study the extent of metal substitution in large-pore aluminophosphates. An expansion of the lattice was

observed upon framework incorporation of metal ions; however results highlighted the need for the use of combined XRD and XAS techniques for the determination of the structure of multi-ion substituted materials. Furthermore, XAS and FTIR studies of cobalt substituted SAPO-34 materials highlighted the importance of the synthesis method on the incorporation of metal ions into the framework and their effect on the conversion of methanol to olefin.

Table of Contents

List of Tables

List of Figures

List of Equations

Acknowledgments

During the course of this research project and the subsequent writing up period, I have obtained assistance and guidance from many people and would like to express my gratitude to all those who have speeded me on my journey. Special thanks to Prof. Gopinathan Sankar (my supervisor), for his guidance, encouragement, knowledge and understanding throughout the last few years. I would also like to thank Dr. Robert Bell for his help and advice. It has been a pleasure working with both of them and I appreciate them taking me on for this project.

Thanks to all the staff at the SNBL, BM26 and BM29 beamlines of the ESRF synchrotron and to the staff at the I11 and B18 beamlines of Diamond Light Source. I would like to express my gratitude especially to Wouter Van Beek who introduced me to Topas and made my life a lot easier with teaching me batch analysis.

I am grateful to all the members of my group, Martin, Vladimir, John Kilmartin, Jon Keating, Andy, Nazarudin and Rozie for brightening up the lab and their support during the day to day running of my research project. Especially for their help during beamtime, keeping me both amused and awake during night shifts and for the entertaining conversations in the pub.

This thesis is dedicated to my parents, John and Janet, sisters Alison and Fiona, and my fiancé, Nicky. Without your love, patience, encouragement and support, my PhD would have been a lot harder and less enjoyable. Thanks for putting up with me through the stressful times and always believing in me.

Chapter 1. Introduction

1.1 Background to Nanoporous Materials

A wide range of crystalline open framework materials (pore diameter ≤ 2 nm) have been synthesized and characterized over the past 60 years. The first nanoporous material (commonly referred to as microporous materials, however in this thesis they are described as nanoporous as the dimensions of microporous materials are sub-nano) was synthesized by Barrer, Milton, Breck and co-workers in the late 1940s in the form of a synthetic aluminosilicate zeolite through mimicking of the geothermal formation of natural zeolites[1, 2]. This attracted increasing attention due to synthetic zeolites having many advantages over their natural analogues, such as high purity, uniform pore size and better ion-exchange abilities[3].

Zeolites form a diverse and exciting group of advanced inorganic materials, where their crystal structures contain regular arrays of channels and voids of similar dimensions to small molecules (ranging from 0.3 nm to over 1 nm) thereby allowing the diffusion of guest molecules into the interior of their structure. Their framework is built of $[SiO_4]^{4-}$ and $[AlO_4]^{5-}$ tetrahedra which corner share to form 3-dimensional nanoporous structures with varying ring size and shape, and dimensionality. Aluminosilicate zeolites have a negatively charged framework due to the charge deficiency from Al(III) in contrast to Si(IV) found in pure silica zeolites, therefore

charge compensating cations (e.g. protons) are required, which leads to the formation of a Brønsted acid site on a neighbouring oxygen atom, see Figure 1.1. The shape and size of the zeolite cavities, plus this Brønsted acidity, gives them the term "shape-selective catalysts". An example of this is the use of zeolite H-ZSM-5 as a catalyst in the methanol to gasoline (MTG) process, the resulting effect is no product longer than C_{11} (gasoline) is formed which corresponds to the channel length of the zeolite, consequently extra reprocessing of heavier fractions is not required[4].

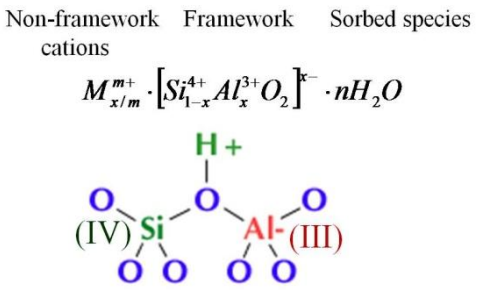

Figure 1.1. *Zeolite framework with alternating (if Si/Al =1) AlO_4 and SiO_4 tetrahedra, where charge deficiency from the Al(III) leads to the formation of a Brønsted acid site on a neighbouring oxygen, also shown is the general composition.*

In addition to their environmentally friendly character, zeolites have been found to be stable under vacuum up to high temperatures and therefore have potential industrial usage. This was first exploited in the early 1960s, in which synthetic zeolites X and Y were introduced, on an industrial scale, as heterogeneous acid catalysts in the fluidized catalytic cracking (FCC) of heavy petroleum distillates. The

use of these synthetic faujisites not only increased the rate of the process but significantly improved the yield of gasoline[5]. Consequently, companies within the petroleum industry began synthesizing zeolites with varying Si/Al ratio (Si/Al = 2-5), such as chabazite and clinoptilolite, and started using organic amines plus quaternary alkyl ammonium cations as templates since the zeolite structure appears to form around them[6, 7]. The steric requirements of the organic template limits the number of them accommodated within the structure, and imposes a restriction on the framework charge density. Therefore, the introduction of amines plus quaternary alkyl ammonium cations resulted in the synthesis of high-silica zeolites since only the aluminium sites are anionic. This brought about an increase in the type and structural diversity of aluminosilicate zeolites, which influenced the rapid development of zeolite use in other major applications such as ion-exchange, molecular sieving, gas purification and separation, and other 'shape-selective' catalytic processes.

1.2 Structural chemistry and properties

1.2.1 Aluminophosphates

In the last two decades the development of crystalline nanoporous materials has been extended to include a variety of other compositions such as phosphates and metal-organic frameworks (MOFs) due to their comparable, if not greater, surface areas and pore volumes with aluminosilicate zeolites. This milestone came in 1982 when the Union Carbide Corporation first reported the synthesis of a new family of molecular sieves based on the aluminophosphate framework, $AlPO_4$-*n* (where *n* denotes a particular structure type)[8]. The majority of these phosphate materials were found to have novel frameworks, such as AlPO-5, but some had framework topologies of known zeolites, such as AlPO-20 which is equivalent to the zeolite sodalite; where both AlPO-20 and sodalite have the same corner sharing network of tetrahedrally coordinated atoms. Aluminophosphates (hereafter designated AlPOs) and zeolites are assigned an IUPAC 3-letter code to represent their framework[9]. For example, AlPO-5 is given the code AFI to represent its structure, and both AlPO-20 and the zeolite sodalite have SOD framework code.

The structures of $AlPO_4$-*n* are based on strict alternation of corner sharing AlO_4 and PO_4 tetrahedra (with a strict framework composition of Al/P = 1) forming an electrically neutral open-framework, see Figure 1.2, which unlike aluminosilicate

zeolites, requires no extra-framework cations. Another characteristic which AlPOs differ from zeolites (which can be made using only inorganic reactants) is that AlPOs *must* be synthesized with an organic amine or quaternary ammonium ion, more frequently the former, which acts as a 'structure directing' agent (template). AlPOs are usually stable upon removal of the organic template and have been found to exhibit thermal stability up to 1000 ºC[10].

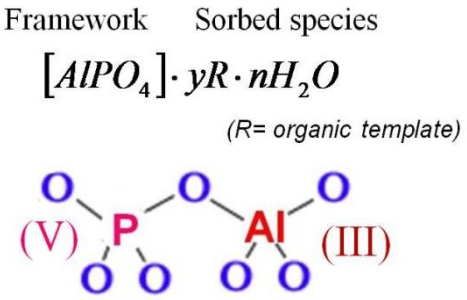

Figure 1.2. *Aluminophosphate framework with alternating AlO_4 and PO_4 tetrahedra forming a neutral framework, also shown is the general composition.*

1.2.2 Framework classification

The structures of AlPOs and other molecular sieve materials can be understood on the basis of their construction from fundamental building units. AlPOs and zeolites comprise of TO_4 tetrahedra (framework T atoms refers to Al, P or Si atoms) which are referred to as primary building units (PBUs) as they are the basic structural building units. Each T atom can be described as 4-connected vertices (as each T atom is connected to 4 oxygen atoms), and since each oxygen atom is connected to

two T atoms, the structure of AlPOs and zeolites can be described as a (4, 2)-connected net.

Their frameworks can be classified through defining a system of secondary building units (SBUs) which contain up to 16 T-atoms with an assumption that the entire framework is made up of only one type of SBU. These SBUs are always non-chiral, with the oxygen atoms omitted and represented by the presence of a single straight line between two T atoms (represented by a circle). The SBUs for various structure types of nanoporous materials containing tetrahedral PBUs are summarized in Figure 1.3[9]. For example, the AEI framework (e.g. AlPO-18 material) contains four types of SBUs; including 4, 6, 4-2, and 6-6 units, any of which can be used to describe its framework structure.

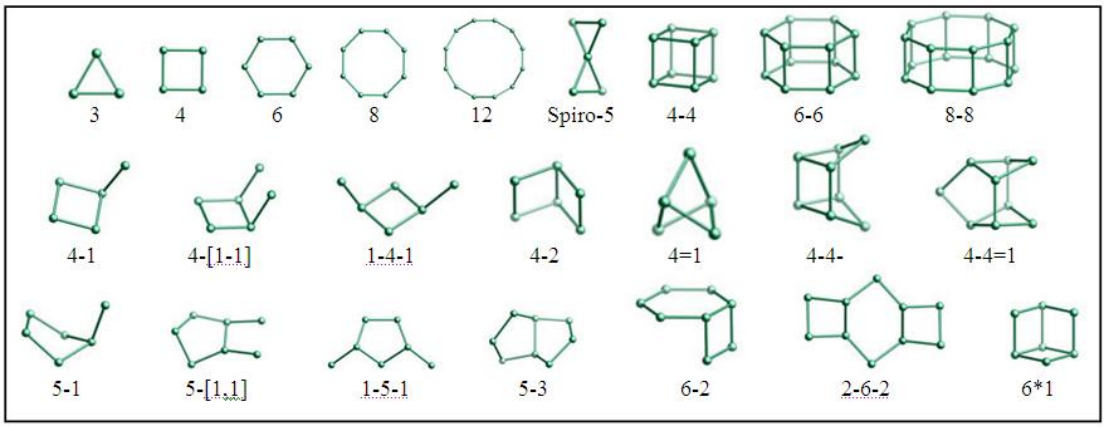

Figure 1.3. *Secondary building units (SBUs) found in nanoporous materials which contain TO_4 tetrahedra*[9].

Some molecular sieve materials contain cage-building units, which can be used to identify relationships between framework types. Cages are generally described in terms of the *n*-rings defining their faces and are different from SBUs since they are not required to be achiral, and cannot necessarily be used to build the entire framework. For example, a truncated octahedron (also known as a β-cage or sodalite cage) has a surface which is defined by six 4-rings and eight 6-rings, is designated a $[4^6 6^8]$ cage and is present in many zeolite frameworks including SOD, FAU, EMT, FAR, FRA, GIU, LTA, LTN, MAR, and TSC, see Figure 1.4. Other examples of common cages are D4R (designated 4^6) and D6R (designated $4^6 6^2$) which represent double 4-membered rings (4-4) and double 6-membered rings (6-6), respectively. A cage, possessing at least one face which has a ring size large enough for a guest species to enter is referred to as cavity.

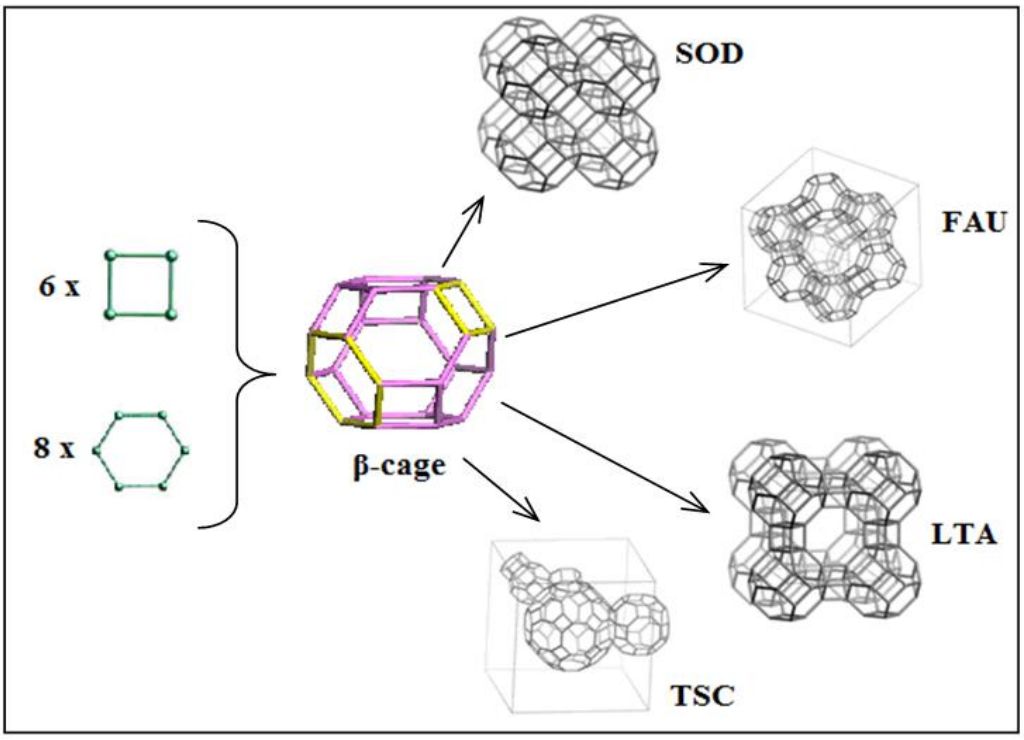

Figure 1.4. *The β-cage (sodalite cage) which is constructed from six 4-membered rings, and eight 6-membered rings. Examples of zeolite frameworks which contain this cage-building unit are also shown.*

Nanoporous materials can also contain chain-building units, in which there are five different types pictured in Figure 1.5. In general, the narsarsukite chain is found more often in AlPO structures, whereas the double narsarsukite chain is characteristic of high-silica zeolites[3]. Dimensionality is another characteristic which can be used to classify molecular sieve materials. For example, AlPO-18 (AEI) has pores which are 3-dimensional, compared to AlPO-12 (ATT) and AlPO-5 (AFI) which have pore dimensionalities of 2- and 1-dimensional, repectively.

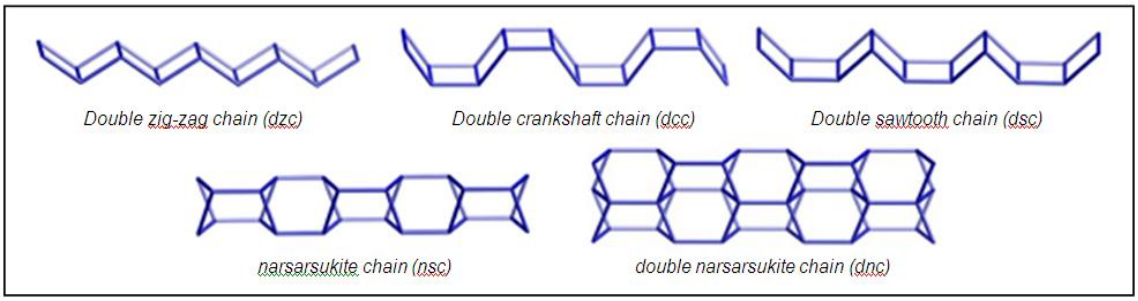

Figure 1.5. *Chain building units which occur in several molecular sieve materials.*

The AlPO-based family of nanoporous materials has over 200 members and in excess of 50 structure types ranging from structures with extra large pores (>12 T-atoms in a ring), such as AlPO-8 (AET), to structures with very small pores (6- T atoms in a ring), such as AlPO-20 (SOD), see Figure 1.6[11]. As with aluminosilicate zeolites, AlPOs obey Löwenstein's rule, in which Al-O-Al bonds are avoided due to Al-Al coulombic repulsion[12]. As a result of this, plus the instability of P-O-P bonds in these materials, along with the majority of AlPOs exhibiting (4,2)-connected networks, rings within the structure must be formed by an even number. This is in contrast with aluminosilicate zeolites, where stable Si-O-Si bonds form allowing odd numbered rings to form. However, this is not always the case with AlPOs; 3- and 5-memebered rings are found in AlPO-21 (AWO), however, the aluminium atoms in this material have coordination numbers greater than four due to aluminium coordinating with water groups and/or anionic species adopting five- or six- fold coordination[13].

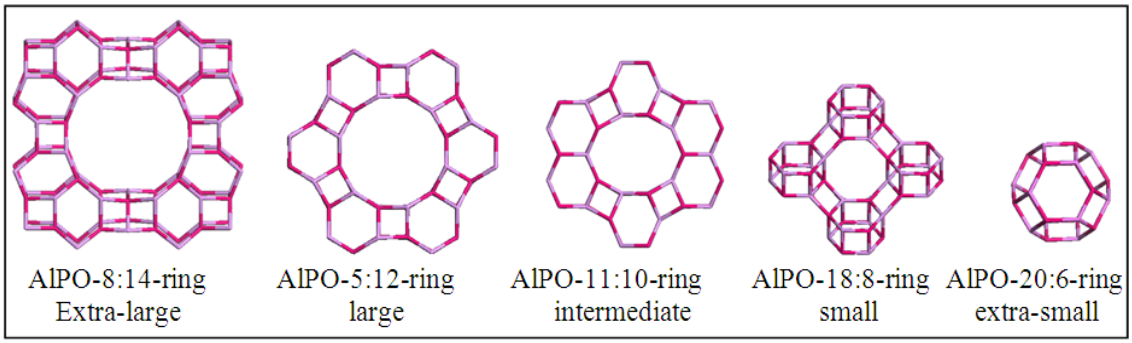

Figure 1.6. *Several $AlPO_4$-n structures with different ring sizes (pore openings).*

1.2.2.1 Typical aluminophosphate structures

The nanoporous materials concerned within this thesis are predominantly comprised of the large pore AlPO-5 (AFI) or the small pore AlPO-34 (CHA) frameworks. The AFI framework can be described as a 1-dimensional channel system consisting of a 12-ring pore opening with a diameter of 7.3 Å. The structure contains narsarsukite chains and can be built from the SBUs; 12, 6 or 4. Nanoporous materials with CHA structure are 3-dimensional frameworks with a pore opening of *ca.* 3.8 Å (8-ring). These small pore materials consist of 8, 6 and 4-membered rings, including the cha cage, and can be built from 6-6, 6, 4-2 or 4 SBUs.

A closely similar structure to the CHA framework is AEI (AlPO-18), this structure is also described as a 3-dimensional network with a similar pore opening (3.8 Å) built from the same SBUs. However, due to a difference in the stacking sequence of the SBUs, the AEI structure does not contain cha cages and is therefore classified as a

unique framework. Another small pore structure described in this thesis is the AEN framework (AlPO-53), this 2-dimensional framework also contains 8, 6 and 4-membered rings with asymmetric pore openings of 4.3 x 3.1 Å and 5.0 x 2.7 Å. Unlike the AEI and CHA structures, the AEN framework can only be built from the SBUs 6 or 4. All of these structures discussed are shown in Figure 1.7.

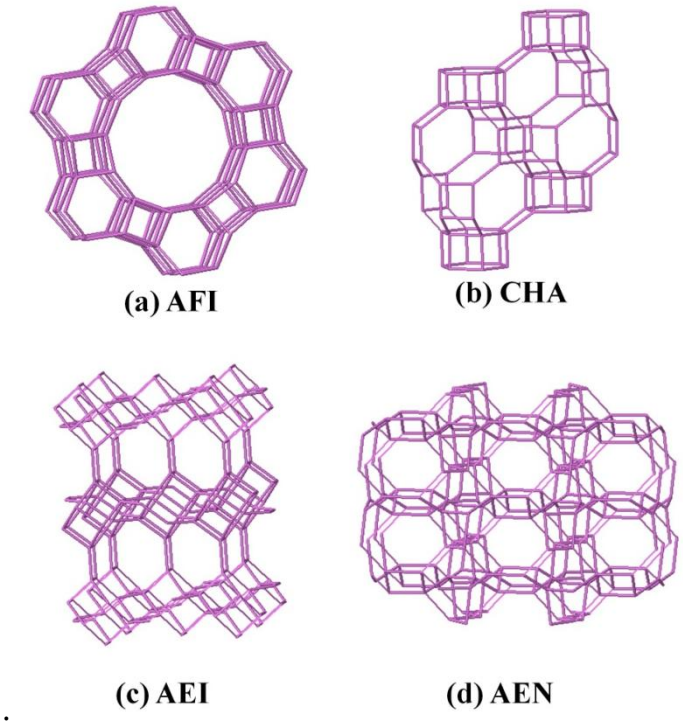

Figure 1.7. *Examples of aluminophosphate structures*[9].

1.2.3 Framework substitution: aluminophosphate derivatives

The incorporation of heteroatoms into AlPO materials can be achieved through incipient wetness impregnation, ion exchange or isomorphous substitution. Isomorphous substitution is of particular interest as the heteroatoms, such as transition metal ions, are substituted into framework sites through the direct addition of the metal source to the synthesis mixture.

AlPOs are isoelectronic with SiO_2, therefore, in theory, a neutral AlPO framework can be derived from a neutral pure silica zeolite by replacement of two Si(IV) cations with one Al(III) and one P(V) cation. This concept led the researchers at Union Carbide Corporation to synthesise a variety of AlPOs by isomorphism substitution of Al(III) and/or P(V) with silicon to form silicoaluminophosphates (SAPO)[14], or with divalent metal cations which are able to adopt tetrahedral coordination (e.g. Co(II), Zn(II), Fe(II), Mn(II) and Mg(II)) to form metalaluminophosphates (MeAlPO), or with a combination of both to form metalsilicoaluminophosphates (MAPSO)[15]. This bonding/substitution chemistry which AlPOs experience is not observed with their isostructural silica-based zeolites, and was therefore investigated by Corá et al. in a quantum-mechanical study[16]. Their results indicated that the Al-O interaction in AlPOs was essentially ionic compared to covalently bonded Si-O-Si bonds in the zeolites, therefore, when heteroatoms are substituted into the AlPO framework only minor perturbations to the electronic structure are found. As a result, a heteroatom

will more readily replace aluminium in the more flexible AlPOs compared to silicon in pure silica zeolites.

From observation of the bonding patterns in these materials, the Union Carbide researchers were also able to reveal that linkages such as P-O-Si, Me-O-Al and Me-O-Me were unlikely. As a result, these AlPO materials were found to have a framework composition of the *general* formula $(Si_xMe_yAl_{(1-y)}P_{(1-x)})O_4$ [where x is commonly between 0 and 0.2 and y between 0 and 0.25], in which a divalent metal cation substitutes into a hypothetical aluminium site and a silicon atom substitutes into a hypothetical phosphorus site.

In the early 1990s the incorporation of transition-metal ions and other elements into the AlPO framework was also reported[17] with monovalent (Li), divalent (Be), trivalent (Cr), tetravalent (Ti), and pentavalent (As) elements. The bonding concepts in these materials were studied by Martens et al.[18], who classified the different types of elements (e.g. monovalent) with a specific substitution mechanism. The monovalent, divalent and trivalent elements (El) were all found to substitute into a hypothetical aluminium site (substitution mechamism 1, SM1) resulting in an El-O-P bond; whereas the tetravalent and pentavalent elements were found to substitute into a hypothetical phosphorus site (SM2) resulting in an El-O-Al bond. They were also able to confirm that silicon is the only element which can substitute as pairs into adjacent aluminium and phosphorus sites with a "heterogeneous" substitution mechanism (SM3), forming what's known as silicon islands; if the substitution of Si(IV) into the Al(III) and P(V) sites is equivalent then the framework remains

neutral. It was also noted that these bonding concepts have remained valid for all stable, calcined structures describable as tetrahedral nets[10].

This incorporation of heteroatoms into the AlPO framework can render them with a negative charge, for example if a divalent metal ion such as Co(II) substitutes for Al(III) the framework is rendered anionic, hence a Brønsted acid site is created in which a proton charge balances, see Figure 1.8. These Brønsted acid sites are only formed after removal (through calcination) of the positively charged organic template which resides in the pores of the AlPO framework. These materials also exhibit Lewis acidity (anionic vacancies deriving from missing lattice oxygen atoms).

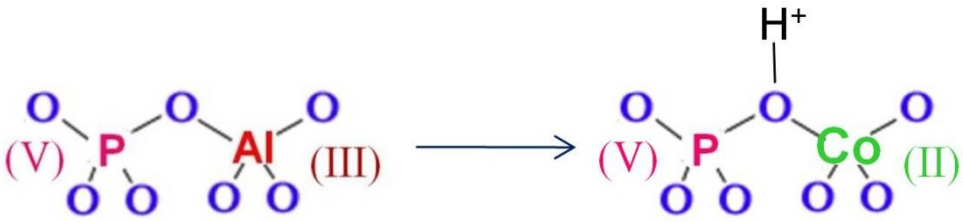

Figure 1.8. *AlPO and MeAlPO frameworks; the cobalt substituted MeAlPO framework has a Brønsted acid site due to charge compensation.*

The acidic nature of these materials, in combination with their shape selectivity and the possibility of redox centres from divalent metal cations such as Co(II) which can be reduced to Co(III), makes them ideal catalysts and leads to considerable interest in the substitution of heteroatoms into AlPO frameworks. The AlPO framework can be modified with a number of heteroatoms with varying concentrations generating materials with different acid strengths. In addition, the

redox chemistry of metal substituted AlPOs is found to differ depending on the framework topology; for example the ATS topology is much better in oxidizing cyclohexane to adipic acid compared to the AFI structure even though both have similar pore sizes and metal concentrations[19].

Metal substituted aluminophosphates have a wide range of applications in different acid catalysed reactions. This includes; SAPO-34 as a catalyst in the conversion of methanol to olefins[20], and the use of FeAlPO-5 as a catalyst in the selective oxidation of cyclohexane[19]. The introduction of metals ions into the framework of AlPOs is a significant advancement of their use in industrial processes; however the incorporation of heteroatoms lowers the thermal and hydrothermal stability of the crystal compared to the pure AlPO analogue, and it is common that leaching of the metal from the framework can occur upon thermal treatment of the sample.

The discovery of open-framework AlPOs has brought about a number of conceptual breakthroughs in the area of nanoporous materials. The compositional and structural diversity of these materials and their derivatives has also improved the current application areas of nanoporous materials in the fields of adsorption and separation, ion-exchange, formation of host-guest advanced materials (e.g. the fabrication of single-walled carbon nanotubes[21]) and catalysis, especially redox and acid catalysis (e.g. selective oxidation of methanol to olefins[22]).

1.3 Synthesis of nanoporous materials

The first confirmed laboratory synthesis of a naturally occurring nanoporous material was in 1948 by R.M. Barrer, where through examination of the composition of the naturally occurring zeolite was able to synthesize mordenite at 290ºC over 2 days using oxides as each reactant source ($Na_2O.Al_2O_3.8\text{-}12SiO_2.10\text{-}20H_2O$)[1]. In 1950, the Union Carbide Corperation researchers (Milton et al.[2]) postulated that a lower temperature would result in other metastable phases, and that the addition of a mineraliser (NaOH) instead of an oxide (Na_2O) would increase the solubility and form an alkali metal aluminosilicate gel. This mimicking of nature was successful and they were able to hydrothermally synthesize the first synthetic zeolite with a new structure in the form of zeolite A (LTA) at 100ºC, with autogenous pressure, over 4 hours.

Before 1961, the synthesis of molecular sieve materials, such as zeolites, only involved inorganic reactants which had a limiting effect on the structural and compositional diversity of nanoporous materials with the formation of very few new structures. The introduction of an organic base in the form of quaternary ammonium cations, and later amines, instead of alkali metal cations was found to be a key step in the synthesis of nanoporous materials, producing high-silica phase zeolites with new structures[6, 7]. The use of organic cations in nanoporous material synthesis increased rapidly, and in 1982 a significant advance emerged with the synthesis of a new porous family, aluminophosphates (AlPOs), which were synthesized under acidic or

neutral conditions in contrast to zeolites which are formed under strongly basic conditions[8].

Open-framework AlPOs and many other nanoporous materials are prepared and modified via numerous methods such as; hydrothermal synthesis, solvothermal synthesis, synthesis under microwave irradiation, hydrothermal synthesis in the presence of a fluoride source, dry gel conversion, ionothermal synthesis, and many other methods including secondary synthesis. So far, the best method to synthesize AlPOs, their derivatives and a large number of nanoporous materials is through the hydrothermal synthetic approach which is based on sol-gel chemistry under hydrothermal conditions.

1.3.1 Hydrothermal synthesis of aluminophosphates

In a typical hydrothermal AlPO synthesis, amorphous reactants containing aluminium (typically aluminium hydroxide hydrate, aluminium isopropoxide or pseudo-boehmite) and phosphorus (generally orthophosphoric acid) are mixed together with water plus a quaternary ammonium salt and/or an amine, in a weakly acidic or neutral medium (pH ~ 4 - 7). In the synthesis of AlPO derivatives, such as MeAlPO, MAPSO and SAPO materials, a solution of the metal salt (usually acetate or sulphate) and/or silica (silica sol or colloidal silica) are also introduced into the reactive mixture. The aqueous reaction mixture is then heated in a sealed autoclave at

temperatures between 100 and 250 ºC (generally AlPO and SAPO materials crystallize at higher temperatures compared to MeAlPO and MAPSO materials) under autogenous pressure for a specific amount of time, usually hours or days. This is illustrated schematically in Figure 1.9. Essentially, all amorphous material is replaced by an approximately equal mass of AlPO crystals which are recovered by filtration or centrifuge, washed thoroughly with water and dried. The crystals are then calcined at a temperature between 400 and 600 ºC to remove the organic cations occluded within the framework which results in empty cavities and channels which give nanoporous materials their interesting applications.

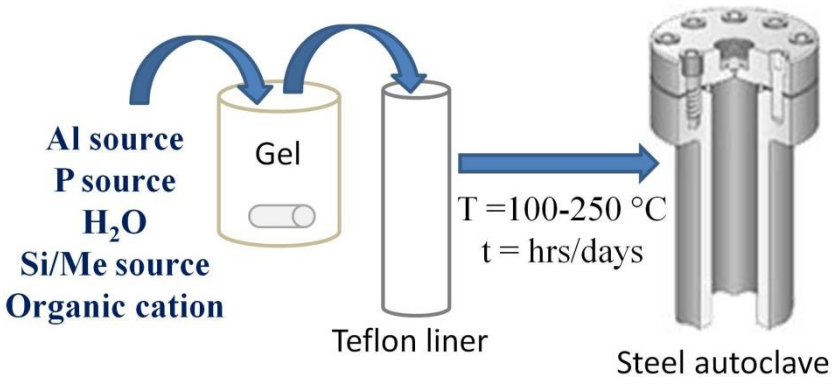

Figure 1.9. *Schematic illustration of the hydrothermal synthesis of AlPO materials; the starting materials are mixed together to form a gel which are then transferred to a steel autoclave containing a Teflon liner, and heated at a particular temperature (T) for a certain amount of time (t).*

The synthesis of AlPOs and other molecular sieve materials can be described as a "black art" due to the type of structure formed depending on the control of a large number of reaction variables, including; reactant gel composition and type, time, temperature, pressure (reaction cell fill volume), pH, type of cation used (organic and/or inorganic), history-dependent factors (ageing, stirring, nature of mixing and order of mixing), and so on. Most of these reaction variables are not independent of one another, which leads to great difficulty in evaluating the effect of varying any one of them, therefore a greater understanding of the reaction pathway and kinetics would be desirable as it could lead to a more rational approach in the synthesis of new molecular sieves.

1.3.2 Reactant gel composition

The chemical composition of a typical reactant gel in the hydrothermal synthesis of aluminophosphates is usually expressed in the following form; *1.0* Al_2O_3: *1±0.2* P_2O_5: *w* R: *x* H_2O (plus *y* Me: *z* SiO_2 for AlPO derivatives), where R is the organic cation (template), Me is the inorganic metal ion, and *w*, *x*, *y* and *z* represent the molar ratios[11]. Similar, for an aluminosilicate zeolite, the chemical composition is typically; *a* SiO_2: *(b+c)* Al_2O_3: *b* M_xO: *c* N_yO: *d* R: *e* H_2O, where R is the organic cation (template), M and N are the alkali metal ions, and a, b, c, d and e represent the molar ratios[23].

The type of molecular sieve that can be crystallized from a synthetic system depends on these reactant gel compositions, where it is evident that changing the molar ratios and/or types of reactants used will affect the nature of the final phase formed. However, the composition of the final product cannot simply be tailored by adjusting the molar ratios of the reactant gel composition, since the synthesis reactions consists of both solid and liquid components, adjusting one of these components changes the chemical composition of both. In general, changing the ratio and content of Al_2O_3, SiO_2 and P_2O_5 influences the product yield, framework composition and the type of structure formed. An example of this is in the synthesis of aluminosilicate zeolites; analcime (ANA) forms with a Si/Al ratio of 4-5, whereas mordenite (MOR) is produced with a Si/Al ratio greater than 8[24].

Both the water and hydroxide concentration are also important factors since they act as the gel transport medium, therefore increasing these concentrations can increase the nucleation and crystallization rates. In addition, the water and hydroxide concentrations have been found to have an effect on the degree of hydrolysis occurring in the system. In 1994, Oliver et al.[25] found that with triethylamine as the organic template and a low water concentration, an aluminophosphate material with a chain motif similar to the JDF structure formed, however, with higher water concentrations, AlPO-5 and AlPO-15 were favoured. These reactant species also influence the pH of the reactant gel which is central to the successful crystallisation of a molecular sieve given that aluminosilicate zeolites form under strongly basic conditions, whereas aluminophosphates form in weakly acidic or neutral conditions. An example of the importance of pH is in the synthesis of cobalt substituted AlPOs,

where at pH values of 5-6 CoAlPO-5 (AFI) forms with the organic template tetraethylammonium hydroxide, but at higher pH (approximately 7) CoAlPO-34 (CHA) impurities are found along with dense phases[26].

The amount and type of cations present in the reactant gel are also believed to be a dominant factor in governing which structure is obtained. In aluminosilicate zeolites, cations influence the Si/Al ratio since they balance the charge produced by the presence of aluminium and therefore have an effect on the structure formed. In the presence of alkali metal cations, aluminium rich zeolites are formed, whereas in the presence of larger organic cations, silicon rich zeolites are formed as less cations can be contained within the framework to charge balance. In aluminophosphates, inorganic ions influence the nucleation rate, since smaller ions are easier to condense around, and may also have an impact on the type of ring formed within the framework, e.g. inorganic cations with smaller ionic radius promote the formation of smaller rings such as a double 4-membered ring.

1.3.3 The effect of time and Ostwald's law of transformations

At ambient temperature, the period between the formation of a homogeneous gel and the start of crystallization of the molecular sieve material is named 'aging'. It is during this period that an aluminosilicate or aluminophosphate gel and a liquid phase are formed, therefore, the effect of time during this aging process has been

extensively studied. It was found that the composition and structure of the primary gel were affected by the aging time, which sequentially alters the nucleation and growth of such molecular sieve materials. Okubo and co-workers[27] were able to demonstrate this point through the synthesis of a faujisite-type zeolite at 90ºC using ^{29}Si-NMR: they were able to study the effect of ageing on the framework type formed and its effect on the crystallization time by keeping the gel system ratios and other reactant factors constant. It was found that with no aging (direct crystallization from the homogeneous gel) zeolites with SOD, ANA and CHA topologies formed, but with 1 day of aging pure phase faujisite (FAU) zeolite formed. Increasing the aging time, led to an increase in the amount of secondary aluminosilicate hydrogel being formed which resulted in the appearance of more nucleable aluminosilicate ions. Therefore, a decrease in the crystallization time was observed along with the formation of smaller particles and a narrower particle distribution. This demonstrates that the aging time of the homogeneous gel is a key role in the synthesis of molecular sieve materials.

Molecular sieve materials are metastable phases which are thermodynamically unstable compared to their dense oxide phases, such as silica (quartz) and alumina (α-Al_2O_3). Under kinetic control, metastable phases can form, however, the synthesis of molecular sieve materials obey Ostwald's Law of successive transformations. This law states that an initial metastable phase is successively converted into a thermodynamically more stable phase until the most stable phase is produced[28]. Therefore time is an important reaction variable, as too short or too long a crystallization time results in no molecular sieve product, an example of this is the

synthesis of aluminosilicate zeolite ZSM-4 (MAZ) using triethylamine (TEA) as the organic template; Faujasite (FAU) is the kinetically favoured product and at short reaction times it is the dominant product of the reaction, with a framework density of 12.7 T/1000 Å^3. At longer reaction times a transformation to the more thermodynamically stable MAZ phase occurs, with a framework density of 16.1 T/1000 Å^3, which eventually converts to the thermodynamically most stable dense oxide phase over a very long reaction time. This is illustrated in Figure 1.10. Similar transformations occur in AlPO materials, with large pore AlPO-5 (AFI) transforming over time to dense phases such as tridymite or berlinite[29].

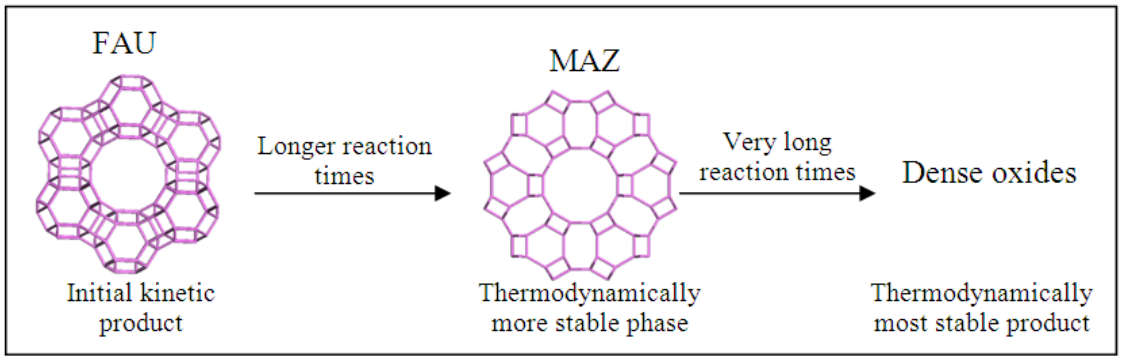

Figure 1.10. *Ostwald's law of successive transformations operating during the synthesis of ZSM-4 (MAZ). Faujasite (FAU) converts to ZSM-4 (MAZ) after a long reaction time, and eventually into the thermodynamically most stable dense oxide phase.*

1.3.4 Effect of temperature

The vast majority of molecular sieve materials are hydrothermally prepared at temperatures between 100 and 250 ºC under autogenous pressure. Under these conditions, water has an extremely effective solvating ability which allows for the dissolution and mixing of the solid reagents to form an inhomogeneous gel, followed by the formation of nucleation centres which subsequently grow to form the crystalline material. Therefore, the synthesis temperature, which affects the self generated pressure of water, directly influences the crystallization and structure of the molecular sieve material formed.

In general, studies have found that hydrothermal synthesis at high temperatures (consequently higher pressures) tends to form molecular sieve materials with a lower inter-crystalline void space, lower water content, and smaller ring secondary building units (SBU). Aluminosilicates such as Zeolite A (LTA) and Zeolite X (FAU), with large pore volumes of up to 50% and containing double 6-membered rings (D6R), form at temperatures at or below 100 ºC, whereas, small pore zeolites such as Sodalite (SOD) and Mordenite (MOR) with much lower pore volumes (20-30%) and with single 4- and 5- membered rings as the SBUs, synthesize at higher temperatures between 200 and 300 ºC. Once the temperature is increased above 350 ºC dense phases tend to form[3].

1.3.5 The role of the organic cation: structure-directing effect

There are over 100 organic species, typically amines and quaternary ammonium cations, which have successfully been used to facilitate the synthesis of open-framework AlPOs and high-silica zeolites through acting as 'templates'. They exert both a steric and an electronic influence on the framework, while acting as charge balancing cations and stabilizing the voids. Their role as a 'template' was first suggested due to the close correlation between the size and shape of the organic cation and the size and shape of the cavities formed within the framework[10]. One definition of this 'templating' effect was described by Lok et al.[30] as "the phenomenon occurring during either the gelation or the nucleation process whereby the organic species organizes oxide tetrahedra into a particular geometric topology around itself and thus provides the initial building block for a particular structure type". This 'templating' effect is evident in the synthesis of FAU materials using tetramethylammonium (TMA^+) cations, where the organic cations are found in the centre of the β-cages, from which it is too big to either enter or leave, suggesting that the framework must have formed around the cations. The organic cations are found to retain their chemical identity and it is believed that these organic cations stabilize the framework through non-bonded interactions; however, this template-framework interaction is not clearly understood[31].

Through experimental observations, it was apparent that there were discrepancies with this 'templating theory' since the correlation between the 'template' and the pore

shape was often weak. Furthermore, studies found that one 'template' could be used to form multiple structures, for example dipropylamine can be used to form 10 different AlPO structures including AlPO-11, AlPO-31, SAPO-34 and AlPO-41[32]. In addition, multiple 'templates' could be used to form one structure, an example of this is in the synthesis of AlPO-5 which can be formed from more than 25 different organic 'templates'[33]. Therefore, Davis et al.[34] suggested that the organic species plays the following roles in the formation of specific channels and cages: i) Space filling; ii) Structure directing; iii) True templating.

The space filling role of an organic cation is evident in the example of multiple templates-one structure (over 25 different organic species can form AlPO-5). The precise nature of the organic species is not of great importance indicating its role as a space-filler to simply exclude water molecules from the channels and cages to decrease unfavourable energetic interactions between the water molecules and the growing molecular sieve framework[11].

The structure-directing role of an organic cation implies that a specific structure can be directed only by a specific organic species and cannot be synthesized by the use of any other templates, for example, hexagonal faujisite (EMT) can only be synthesized with crown ether 18-crown-6 as the organic species[3]. This structure-directing effect observed in high-silica zeolites, in which there is a very high correlation between the size and shape of the organic species used and the size and shape of the framework pore produced, has been reported to be due to an optimized arrangement for maximizing the van der Waals contacts between the framework and organic species with no ionic interactions[35-37]. These van der Waals interactions may also be the

dominant factor in the structure determination of AlPOs since their frameworks are neutral, however, little work has been carried out to prove this[11].

A 'true template' is rare in molecular sieves and occurs only when a zeolite structure adopts the geometric and electronic configuration that is unique to the organic specie, and upon calcination, retains the shape of the organic molecule. An example of this is in the synthesis of ZSM-18 using tri quaternary amine as the organic species. Through energy minimization calculations, Davis et al.[34] were able to show that both the cage and organic cation posses the same 3-fold rotational symmetry in the lowest energy conformation, and that the organic "tri-quat" molecule cannot rotate in the cage. These results, plus subsequent studies[38], showed that the shape of the template played an important role in determining the framework due to strong guest-host interactions, and that true templating had taken place.

Overall, organic species are found to play a key role during the synthesis of molecular sieve materials through:

- encouraging the formation of nanoporous materials
- accessing more metastable states by stabilizing the voids of the molecular sieve materials
- modifying the Si/Al ratio and Si distribution in the gel and in the final product during the formation of zeolites and SAPO materials
- influencing the degree of metal-ion substitution of the framework in MeAlPOs (positive charge from template charge balances with negative charge from metal ion)

- increasing the nucleation and modifying the crystal growth rates

In general, organic cations are referred to as a ‘template’ or ‘structure directing agent’ as it is clear that the use of a specific organic species is necessary for the successful synthesis of a particular molecular sieve material. However, the precise role which the organic species plays during the hydrothermal synthesis of molecular sieve materials, such as aluminophosphates, and the template-framework interaction is not entirely understood, and still requires a more complete understanding to enable the synthesis of new topologies as well as the control of crystal size, crystal morphology, and the location of heteroatoms, if present.

1.3.6 The molecular processes which occur during the hydrothermal synthesis of molecular sieves

The synthesis of molecular sieve materials, such as zeolites and AlPOs, is found to proceed via three stages, pre-nucleation, followed by nucleation and then crystal growth. Pre-nucleation involves the initial dissolution of the solid starting reagents by the solvent water to form a randomly distributed array of reaction components (formation of a gel); this is followed by nucleation which involves ordering of these components on a microscopic scale (formation of nucleation sites). Finally crystal

growth at the nucleation sites occurs rapidly to form the final molecular sieve material[11].

The exact mechanism of the formation of molecular sieve materials is unclear due to the complexity of the reactions which occur throughout the heterogeneous synthesis mixture during hydrothermal crystallisation. At present, there are two main proposed mechanisms, the solution-mediated transport mechanism and the solid hydrogel transformation mechanism, with the key difference lying in whether the liquid component is involved during the crystallization of molecular sieve materials.

The solution-mediated transport mechanism, schematically illustrated in Figure 1.11, was first proposed by Kerr et al.[39] in the middle of the 1960s according to their crystallization studies on zeolite A, and later discussed in detail by Zhdanov[40] and colleagues. It involves the dissolution of the aluminosilicate/aluminophosphate gel in the solution phase to form active silicate/phosphate and aluminate ionic species. These dissolved ionic species are then transported to the nucleation sites via a solution-mediated diffusion where re-crystallization in the solution occurs to form the structure of the molecular sieve material and crystal growth takes place. There are many experimental observations of this mechanism, with the most convincing being reported by Ueda et al.[41] in which zeolites Y, S and P were synthesised from clear solutions where no solid phase hydrogel was present.

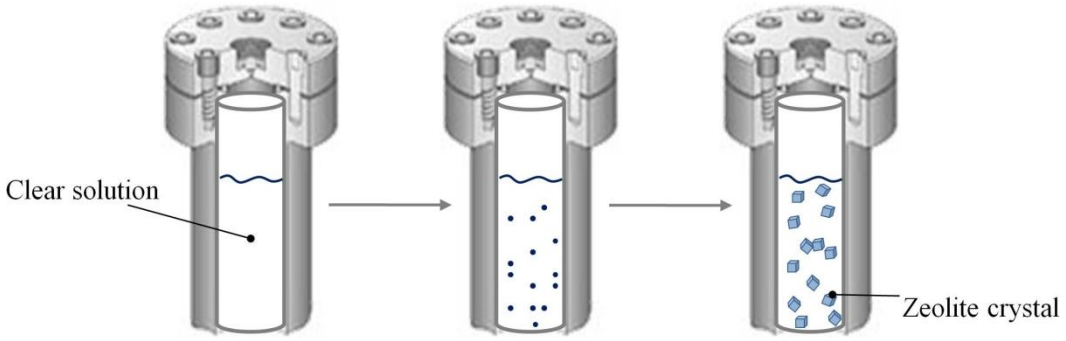

Figure 1.11. *Schematic illustration of the solution-mediated transport mechanism involving the diffusion of ionic aluminate, silicate/phosphate species from the liquid phase to the nucleation site for crystal growth*

The solid hydrogel transformation mechanism, schematically illustrated in Figure 1.12, was first proposed by Breck and Flanigen in 1968, and completely differs from the solution-mediated transport mechanism since it does not involve the dissolution of the solid gel or the liquid component[34]. In this mechanism it is believed that the structure of the molecular sieve material is obtained by re-organisation of the framework of solid phase aluminosilicate/aluminophosphate hydrogel formed from the condensation of silicate/phosphate and aluminate ions in the early stages of crystallization. An example of this mechanism was reported by Xu at al.[42] who synthesised ZSM-5 and ZSM-35 from non-aqueous reaction mixtures, in which an amorphous aluminosilicate gel was first dehydrated at 550 ºC and then treated with liquid triethylamine and ethylenediamine at 160 ºC in the absence of water. In this example it was clear that a solid phase transformation had occurred since no aluminate or silicate species in the liquid phase was observed.

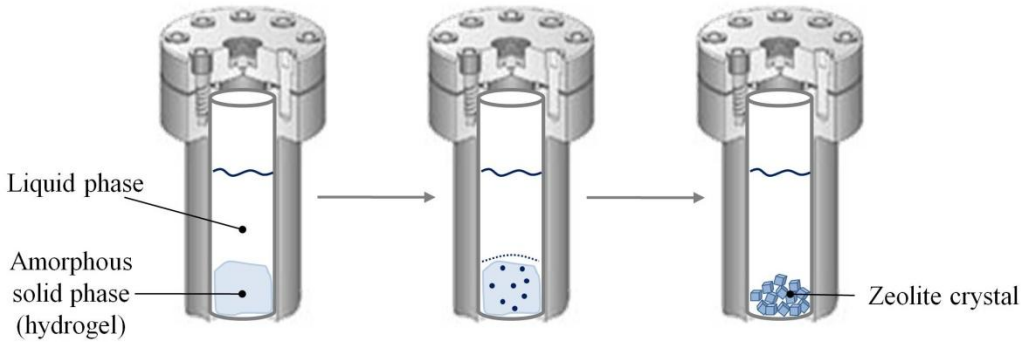

Figure 1.12. *Schematic illustration of the solid hydrogel transformation mechanism involving the reorganization of the solid hydrogel to form the molecular sieve structure.*

The views of these two mechanisms are opposite to each other with both having experimental evidence to support them. However, many studies have shown the synthesis of molecular sieve materials, such as AlPOs, to proceed via both mechanisms or could even lie somewhere between these two extremes. Many studies have focused on understanding the processes occurring during hydrothermal synthesis and have revealed details on crystal nucleation and growth for specific cases[11, 25, 43-45], but in general a more complete mechanistic understanding of molecular sieve formation is needed to lead to a more rational approach in their synthesis.

1.4 Objectives of the study

The overall aim of this project is to develop methodologies that will allow the determination of the mechanism of substitution of heteroatoms in aluminophosphate frameworks. Although several studies have been undertaken to determine the mechanism, still it is unclear whether the metal ions are incorporated prior to the formation of the crystalline solid or during the crystallisation processes. X-ray techniques, available at synchrotron radiation sources, provides means of a greater understanding of the structural features and properties associated with the substitution of divalent and tetravalent metal ions in aluminophosphate frameworks. Therefore, the primary techniques used in this work were X-ray diffraction (XRD) and X-ray absorption spectroscopy (XAS) which are ideal methods to determine the long- and short-range order of the atomic architecture. In addition, when used in conjunction with a specially designed *in situ* hydrothermal cell it is possible to observe *in situ* the crystallization of metal substituted aluminophosphate materials. Furthermore, the combination of these two techniques allowed the determination of the changes that takes place during calcination (removal of the template) of the as-synthesised AlPO materials with an *in situ* high temperature furnace.

The outline of the thesis is as follows. Chapter 2 describes the details of the experimental techniques along with relevant theory. The main emphasis of Chapters 3 and 4 are on the formation of metal substituted aluminophosphate materials, both the crystallization and substitution mechanism of formation and the kinetics of

crystallization, whereas Chapters 5 and 6 are structural studies which investigated the effect of heteroatoms on the long range order of the AlPO structures and the short range order around specific atoms.

In detail, Chapter 3 presents studies on the crystallisation mechanisms taking place during hydrothermal synthesis of open framework AlPOs. The objective of this study was to use, for the first time during a chemical reaction, the *simultaneous* combination of *in situ* XRD and XAS with an aim of gaining a greater understanding into the substitution mechanism of divalent metal ions into the large pore AlPO-5 framework since it could lead to a more rational approach towards the design and synthesis of new molecular sieve materials.

The primary aim of Chapter 4 was to study the effect of the type of divalent metal cations and the organic template on the kinetics of formation and the metastability of AlPO materials. In particular, *in situ* high-resolution XRD (HRXRD) methods were employed during the competitive phase formation of AFI and CHA structures to investigate whether the type (size) of divalent metal ions promotes one framework over another. A previous investigation on the kinetics of CoAlPO-5 formation found differences in the kinetic trend depending on the cobalt concentration; with a low cobalt concentration, the induction period decreases and the rate of crystallization increases, however with a cobalt concentration above 6 weight %, this trend is reversed[45]. This was attributed to the presence of the CHA phase which can form with cobalt concentrations above 4 wt % and in the presence of organic templates such as tetraethylammonium hydroxide (TEAOH) or triethylamine (TEA).

Therefore, the effect of divalent metal ion concentration on the kinetics of CoAlPO-5 formation but with methyldicyclohexylamine (MCHA) as the template was investigated. This organic species is known to have the highest specificity to form the AFI structure over a wide range of synthesis conditions[26] with no impurities from other AlPO phases.

The aim of the work presented in Chapter 5 was to develop indirect methods on verifying the extent of metal ion substitution in AlPO materials. For this purpose, a number of mono- and multi- ion substituted large pore AFI materials were investigated through HRXRD to determine the change in their unit cell parameters with increasing metal ion concentration. The incorporation of titanium(IV) into the framework of zeolitic and AlPO materials has been a challenge for many years, and has potential importance for a number of oxidation reactions, such as the epoxidation of alkenes and the oxidation of alkanes to their respective acids[19, 46, 47]. Therefore, AlPO-5 materials containing Ti(IV) were further characterized by XAS to determine whether the synthesis method or incorporation of more than one type of metal had a positive effect on the substitution of Ti(IV) into the AFI framework.

Finally, Chapter 6 presents an investigation on the effect of the addition of a redox metal cation, Co(II), on the acid catalytic properties of SAPO-34 to transform methanol to light olefins. The synthetic strategy for the isomorphous substitution of metal ions into the AlPO framework has been found to have a significant effect on their incorporation into the tetrahedral framework sites (observed for TAPO-5 in Chapter 5 and by Dubois et al. for the incorporation of Ni(II) into the NiSAPO-34 framework[20]). Therefore, this research focussed on understanding the effect of order

of addition of chemicals on the nature and extent of substitution of Co(II) and Si(IV) in CoSAPO-34. The nature and location of the transition metal ions, Co(II), in CoSAPO-34 prepared by two different methods were studied by XRD, Fourier-transform Infrared Spectroscopy (FTIR) and XAS. Results from these characterization studies give insights into the CoSAPO-34 acid catalytic properties which were compared to CoAlPO-34 and SAPO-34 for the conversion of methanol to light olefins.

1.5 References

[1] Barrer, R. M., *Journal of the Chemical Society*, (1948), 2158.

[2] Breck, D. W.; Eversole, W. G.; Milton, R. M., *Journal of the American Chemical Society*, (1956) **78**, 2338.

[3] Xu, P.; Pang, W.; Huo, Q.; Chem, J., *Chemistry of Zeolites and Related Porous Materials - Synthesis and Structure*, John Wiley and sons Ltd: Singapore, (2007).

[4] Meisel, S. L.; McCullough, J. P.; Lechthaler, C. H.; Weisz, P. B., *Chemtech*, (1976) **6**, 86.

[5] Weitkamp, J., *Solid State Ion.*, (2000) **131**, 175.

[6] Barrer, R. M.; Denny, P. J., *Journal of the Chemical Society*, (1961), 971.

[7] Kerr, G. T.; Kokotail.Gt, *Journal of the American Chemical Society*, (1961) **83**, 4675.

[8] Wilson, S. T.; Lok, B. M.; Messina, C. A.; Cannan, T. R.; Flanigen, E. M., *Journal of the American Chemical Society*, (1982) **104**, 1146.

[9] Baerlocher, C.; McCusker, L. B., Database of Zeolite Structures. http://www.iza-structure.org/databases/, In.

[10] Yu, J. H.; Xu, R. R., *Chem. Soc. Rev.*, (2006) **35**, 593.

[11] Francis, R. J.; O'Hare, D., *Journal of the Chemical Society-Dalton Transactions*, (1998), 3133.

[12] Lowenstein, W., *American Mineralogist*, (1954) **39**, 92.

[13] Cheetham, A. K.; Ferey, G.; Loiseau, T., *Angewandte Chemie-International Edition*, (1999) **38**, 3268.

[14] Lok, B. M.; Messina, C. A.; Patton, R. L.; Gajek, R. T.; Cannan, T. R.; Flanigen, E. M., *Journal of the American Chemical Society*, (1984) **106**, 6092.

[15] Flanigen, E. M.; Lok, B. M.; Patton, R. L.; Wilson, S. T., *Pure and Applied Chemistry*, (1986) **58**, 1351.

[16] Cora, F.; Catlow, C. R. A., *Journal of Physical Chemistry B*, (2001) **105**, 10278.

[17] Hartmann, M.; Kevan, L., *Chemical Reviews*, (1999) **99**, 635.

[18] Martens, J. A.; Jacobs, P. A., Crystalline microporous phosphates - a family of versatile catalysts and adsorbents, In *Advanced Zeolite Science and Applications*, Elsevier Science Publ B V: Amsterdam, (1994); Vol. 85, pp 653.

[19] Sankar, G.; Raja, R.; Thomas, J. M., *Catalysis Letters*, (1998) **55**, 15.

[20] Dubois, D. R.; Obrzut, D. L.; Liu, J.; Thundimadathil, J.; Adekkanattu, P. M.; Guin, J. A.; Punnoose, A.; Seehra, M. S., *Fuel Processing Technology*, (2003) **83**, 203.

[21] Wang, N.; Tang, Z. K.; Li, G. D.; Chen, J. S., *Nature*, (2000) **408**, 50.

[22] Liu, Z. M.; Liang, J., *Current Opinion in Solid State & Materials Science*, (1999) **4**, 80.

[23] Barrer, R. M., *Zeolites*, (1981) **1**, 130.

[24] Lewis, D. W., C4G2 New directions in materials chemistry lecture notes, In University College London: London, (2007).

[25] Oliver, S.; Kuperman, A.; Lough, A.; Ozin, G. A.; Garces, J. M.; Olken, M. M.; Rudolf, P., New insights into the mode of formation of AlPO4-n moleculare sieves, In *Zeolites and Related Microporous Materials: State of the Art 1994*, Weitkamp, J.; Karge, H. G.; Pfeifer, H.; Holderich, W. Eds.; Elsevier Science Publ B V: Amsterdam, (1994); Vol. 84, pp 219.

[26] Sanchez-Sanchez, M.; Sankar, G.; Simperler, A.; Bell, R. G.; Catlow, C. R. A.; Thomas, J. M., *Catalysis Letters*, (2003) **88**, 163.

[27] Ogura, M.; Kawazu, Y.; Takahashi, H.; Okubo, T., *Chemistry of Materials*, (2003) **15**, 2661.

[28] Dyer, A., *An introduction to zeolite molecular sieves*, Wiley and Sons Ltd: (1988).

[29] Budd, P. M.; Myatt, G. T.; Price, C.; Carr, S. W., *Zeolites*, (1994) **13**, 198.

[30] Lok, B. M.; Cannan, T. R.; Messina, C. A., *Zeolites*, (1983) **3**, 282.

[31] Gomez-Hortiguela, L.; PerezPariente, J.; Cora, F.; Catlow, C. R. A.; Blasco, T., *Journal of Physical Chemistry B*, (2005) **109**, 21539.

[32] Han, B.; Shin, C. H.; Cox, P. A.; Hong, S. B., *Journal of Physical Chemistry B*, (2006) **110**, 8188.

[33] Elanany, M.; Su, B. L.; Vercauteren, D. P., *Journal of Molecular Catalysis a-Chemical*, (2007) **270**, 295.

[34] Davies, M. E.; Lobo, R. F., *Chemistry of Materials*, (1992) **4**, 756.

[35] Burkett, S. L.; Davis, M. E., *Journal of Physical Chemistry*, (1994) **98**, 4647.

[36] Gies, H.; Marler, B., *Zeolites*, (1992) **12**, 42.

[37] Wiebcke, M., *Journal of the Chemical Society-Chemical Communications*, (1991), 1507.

[38] Stevens, A. P.; Gorman, A. H.; Freeman, C. M.; Cox, P. A., *Journal of the Chemical Society-Faraday Transactions*, (1996) **92**, 2065.

[39] Kerr, G. T., *Journal of Physical Chemistry*, (1966) **70**, 1047.

[40] Zhdanov, S. P., *Adv. Chem. Ser.*, (1971) **101**, 20.

[41] Ueda, S.; Kageyama, W.; Koizumi, M., In *6th International Zeolite Conference*, Olson, D.; Bidio, A. Eds.; Buttersworths, Guildford, (1984); Vol. 905.

[42] Xu, W.; Li, J.; Li, W.; Zhang, H.; Liang, B., *Zeolites*, (1989) **9**, 468.

[43] Aerts, A.; Kirschhock, C. E. A.; Martens, J. A., *Chem. Soc. Rev.*, (2010) **39**, 4626.

[44] Beale, A. M.; O'Brien, M. G.; Kasunic, M.; Golobic, A.; Sanchez-Sanchez, M.; Lobo, A. J. W.; Lewis, D. W.; Wragg, D. S.; Nikitenko, S.; Bras, W.; Weckhuysen, B. M., *Journal of Physical Chemistry C*, (2011) **115**, 6331.

[45] Davies, A. T.; Sankar, G.; Catlow, C. R. A.; Clark, S. M., *Journal of Physical Chemistry B*, (1997) **101**, 10115.

[46] Sheldon, R. A.; Wallau, M.; Arends, I.; Schuchardt, U., *Accounts of Chemical Research*, (1998) **31**, 485.

[47] Thomas, J. M.; Raja, R.; Sankar, G.; Bell, R. G., *Nature*, (1999) **398**, 227.

Chapter 2. Characterisation techniques and analysis

2.1 Chapter Overview

This chapter discusses the characterisation techniques employed to study the molecular sieve catalysts described within this work. A brief description of the theory, practice and data analysis procedures of the advanced techniques used, in particular, X-ray diffraction (XRD) and X-ray absorption spectroscopy are given.

2.2 Introduction

Characterisation of nanoporous materials is essential in understanding their physical properties, their structure–application relationships, why certain structures favour specific reactions, and for a greater knowledge into the design of new materials. There are a variety of techniques that can be used to characterise the structure and properties of solid state materials, including; X-ray and neutron techniques, infrared spectroscopy, computer modelling etc.

X-ray techniques, in particular X-ray diffraction, have been one of the basic and most useful tools for characterization of nanoporous materials for the reasons that they are non-destructive, can be used on many types of materials and in non-ambient conditions (e.g. high pressure and temperature), more importantly they can be performed in the laboratory providing details of the atomic arrangement (structure). X-rays are electromagnetic waves which have a wavelength, λ, between 0.1 and 100 Å or an energy ranging from 124 eV to 124 keV. They are produced when high energy (accelerated) electrons, released from a heated filament under vacuum, are impacted into a target (e.g. a metal anode), producing two different X-ray radiations, continuous and characteristic radiation.

In a laboratory-based X-ray machine, typically continuous X-ray radiation (known as white radiation) is produced from the sudden deceleration of these fast moving electrons which causes the target to release energy in the form of X-rays with a continuous ‘Bremsstrahlung’ spectrum.

If, however, a bombarding electron has enough energy to knock an electron from an innermost shell of an atom (e.g. from the 1s orbital/K shell), X-ray photon emission known as characteristic radiation occurs (in this example K-shell emission) when electrons from higher energy levels (e.g. from L, M etc. shells) fill the vacancy. This radiation depends on the target metal anode and as it is atom specific, the various shells have fixed energies which produces X-rays with a fixed wavelength or energy. It is this characteristic radiation which is used for laboratory X-ray techniques, most commonly copper Kα emissions. Where for example, an electron from the inner K shell is ejected, resulting in K shell emission in which electrons from either the $L_{2,3}$ (Kα emission with $\lambda = 1.54$ Å) or $M_{2,3}$ (Kβ emission with $\lambda = 1.39$ Å) shells drop to the vacant K shell with the emission of an X-ray photon characterized by the difference in energy levels[1]. This is illustrated in Figure 2.1.

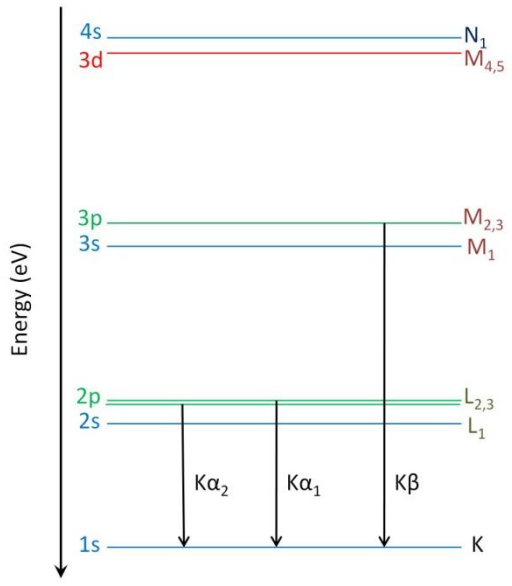

Figure 2.1. *Electronic energy levels and radiation transitions for a copper anode.*

Laboratory X-ray sources are easy to set-up and can be classified into two types: sealed-tube water-cooled anode and rotating anode. Both may be used to generate monochromatic X-ray radiation (single wavelength commonly used for X-ray diffraction), differing only in the intensity of the radiation produced. Use of a water-cooled anode produces X-rays with a brilliance (the flux/brightness of photons per unit source area) in the range of 1×10^8 (units = photons.s^{-1}.0.1%bandwidth^{-1}.mrad^{-1}.mm^{-2}), whereas with the use of a rotating anode, X-rays with a brilliance in the range of 12×10^8 are produced. It is clear, that experimental data would be more accurate and precise employing the more powerful X-rays from a rotating anode, however, they demand high maintenance and have short continuous use times, therefore X-rays produced from a sealed-tube water-cooled anode (copper) have been employed in the laboratory based X-ray studies in this thesis.

Advances in recent decades has seen the development in the use of synchrotron radiation, which produces X-rays with a much higher brilliance, in the range of 1×10^{16}, compared to a laboratory water-cooled anode or rotating anode. Therefore synchrotron radiation has many advantages over conventional X-ray radiation produced in a laboratory.

2.2.1 Synchrotron Radiation

Synchrotron radiation (SR) is white continuous radiation produced when a beam of electron bunches, produced from a linear accelerator (LINAC), are accelerated to relativistic velocities and travel at near the speed of light (almost 3 x 10^8 ms^{-1}). These electron bunches are fired into a booster ring and then injected into the main synchrotron storage ring and held under ultrahigh vacuum (10^{-10}mbar) to prevent them from losing energy as they circulate the closed storage ring a vast number of times. The electrons have a high energy in the GeV range, and are held constant at this energy in the storage ring by a constant magnetic field from powerful bending magnets which force them to circulate in orbit. The components of the synchrotron storage ring are schematically shown in Figure 2.2.

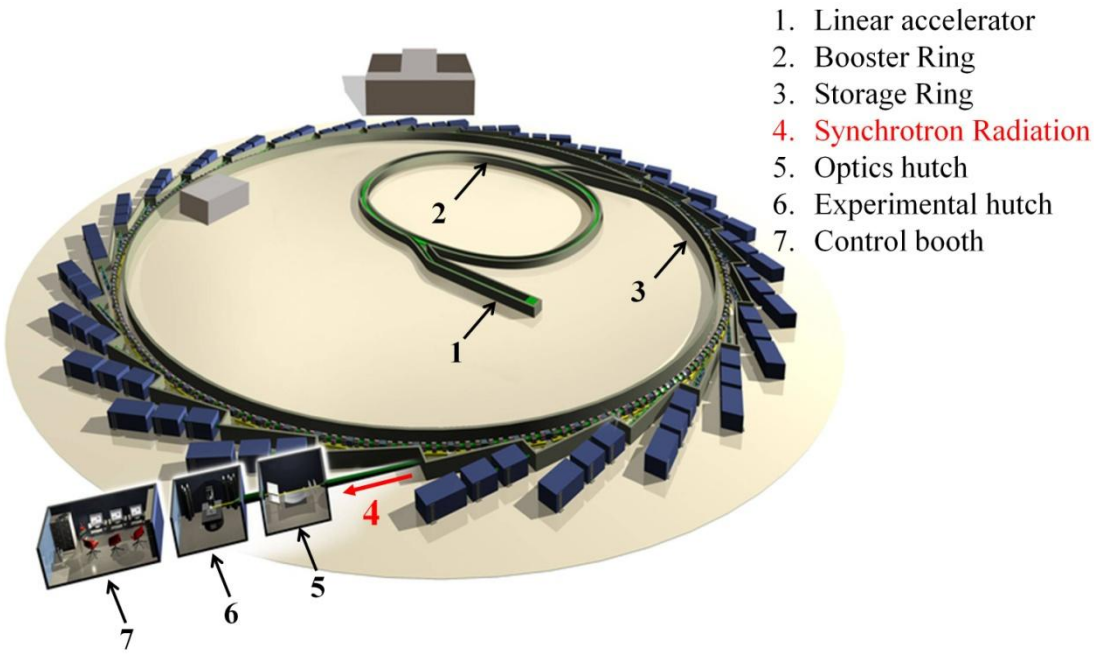

Figure 2.2. *The components of a Synchrotron*[2].

When a charged particle is accelerated it emits electromagnetic radiation, thus, when electrons interact with the bending magnets, white continuous (variety of energies/wavelengths) electromagnetic radiation is produced. This synchrotron radiation is produced in the form of a radiation fan of X-rays, which is highly collimated with a typical energy range from the radiofrequency to the hard X-ray region of the electromagnetic spectrum, which is given off tangentially at the point of the bending magnet.

The first generation of SR research was performed in a high current accelerator laboratory for high-energy or nuclear physics. In the 1980s, SR facilities were purposely built, known as the second generation, with great improvements made by the 1990s which saw the third generation facilities built that provided greater beam brilliance, compared to bending magnets, with higher X-ray intensities using magnetic insertion devices such as a wiggler or undulator.

Insertion devices present a different emission spectrum, thus increasing the flexibility of the synchrotron facility in accommodating experiments with different spectral requirements. These insertion devices are magnet systems which accept and return electrons in the same direction; therefore they do not affect the operation of the dipole magnet, and are inserted in the straight sections between the bending magnets[3]. A simple wiggler magnet consists of three magnets, with the two outer magnets opposed to the central magnet; these force electrons through a trajectory with a small radius of tight curvature, and results in a greater radial acceleration producing higher energy photons, and therefore harder X-rays with greater penetration. A wiggler produces a spectrum similar to that of a bending magnet

radiation but with a much greater brightness, e.g. a greater number of X-ray photons of a desired wavelength hitting the sample. An undulator, which is similar to a series of wigglers, consists of approximately 20 - 30 alternating low field magnetic poles which produce a series of oscillations of the electrons around their otherwise straight trajectories. Each oscillation provides a source of radiation and at some point downstream, these radiation emissions interfere either constructively or destructively, to produce a radiation spectrum which is very bright but concentrated in a narrow band around the fundamental wavelength of the insertion device. The overall spectrum has very intense peaks at specific photon energies, therefore insertion devices, such as undulators, allow enhancement at certain frequencies/wavelengths which can accommodate and enrich certain experiments. The differences in the radiation produced by the various insertion devices are compared to that from a bending magnet in Figure 2.3[1].

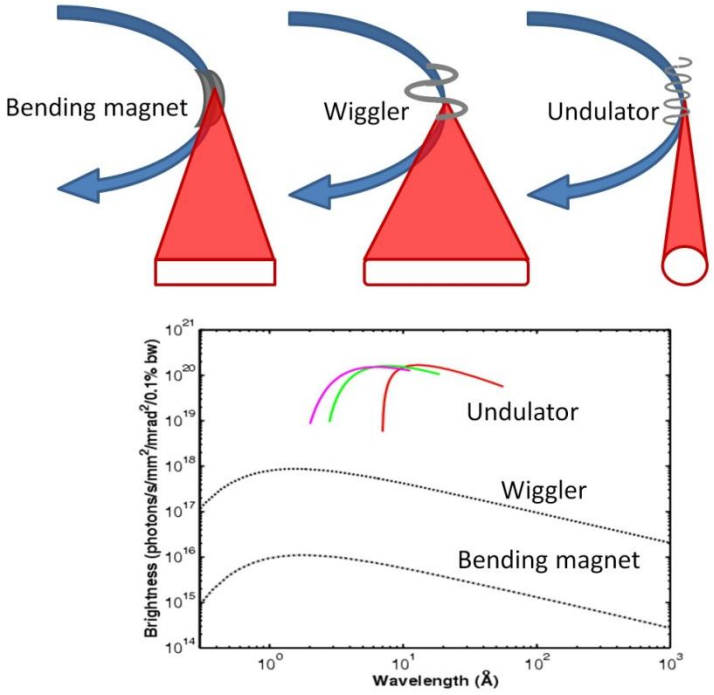

Figure 2.3. *Schematic illustrations, comparing the radiation emitted with the use of a bending magnet with a wiggler and an undulator. Also shown is a graph comparing brightness and wavelength of the radiation produced from the different insertion devices*[1].

Overall, synchrotron radiation has many advantages over conventional laboratory X-ray sources, these include:

1. High Intensity (x 10^6); allowing for high-speed data collection, the ability to follow chemical processes *in situ* (even fast dynamical processes), and allows investigations of samples which are dilute or have a small volume.

2. Very broad continuous spectral range which is also tunable; white radiation allows for techniques such as energy dispersive diffraction (EDD) to be used which cannot be used with laboratory radiation sources, production of hard X-rays allows for techniques such as infrared spectroscopy, and the ability to choose and fine tune the wavelength allows for the implementation of element specific techniques such as Extended X-ray Absorption Fine Structure (EXAFS).

3. Narrow angular collimation (neither converges nor diverges); allows for more efficient and angularly precise experiments with a greater resolution and reduced peak overlap, plus less X-ray beam damage to the sample.

4. High degree of polarization; laboratory X-ray sources produce X-rays which have random polarization, synchrotron radiation is 100% plane polarized (horizontally) which allows for the diffraction geometries to be arranged and improves the sensitivity of the fluorescence signal, therefore, reducing the background and resulting in no loss in intensity.

5. Regularly pulsed time structure; electrons travel the storage ring in bunches, e.g. the Daresbury Synchrotron Radiation Source (SRS) had 160 equally spaced bunches of electrons travelling in its storage ring, each a few centimetres long with a separation of 2 nanoseconds, each bunch of electrons

produces a ‘flash’ of radiation, therefore, an accurate time structure can be obtained.

6. Computability of properties; specific properties of the X-rays can be changed with relative ease through computers to accommodate the experiment.

These many advantages which synchrotron radiation has over conventional laboratory X-ray radiation make them a very powerful characteristic tool, especially in the development of *in situ* methods. In this work, *in-situ* experiments were carried out using synchrotron radiation from third generation sources; both the European Synchrotron Radiation Facility (ESRF) in Grenoble, France and Diamond Light Source in Oxfordshire, UK.

2.3 X-ray diffraction

As described in Chapter 1, the nanoporous materials studied in this thesis are crystalline solids and are thus very suitable for characterisation by X-ray diffraction (XRD). Powder XRD is amongst the most widely used analytical technique in solid-state chemistry due to the fact that the data provided by this method can give insight into the crystallinity of the material, phase purity and identification, crystallite size,

and the crystal structure (size of the unit cell, the spatial arrangement of the atoms inside the unit cell and the symmetry).

2.3.1 Basic XRD Theory

X-rays are scattered in all directions by liquids, gases and amorphous solids resulting in relatively little useful information. However, as shown by Laue and co-workers in 1912, X-ray scattering from crystalline (regularly repeating lattice) materials is not featureless and instead results in sharp spots seen on a photographic film, a diffraction pattern. When the wavelength of X-rays is similar in size to the distance between atoms, it is possible for diffraction to occur. While this diffraction is caused by the electrons of the atoms in the crystal, for ease of description it is often considered to be caused by the lattice planes (ordered atoms form planes).

In 1913, William L. Bragg noticed the similarity of diffraction with reflection and was the first to envisage crystals in terms of having imaginary planes of atoms which behave as reflecting planes, for which the angle of incidence and the angle of reflection are equal. A set of such planes consists of parallel evenly spaced planes which are extended to exactly fill the entire crystal; each plane being an equal distance, *d*, from its neighbouring plane. Depending on the atomic arrangement, constructive interference of two scattered X-rays (resulting in a strong/in-phase 'reflected' beam) occurs when the path difference between two diffracted rays, from

successive planes, differ by an integral number of wavelengths. This selective condition is described by Bragg's Law, shown in Equation 2.1, where *n* is an integer, λ is the wavelength of the X-rays, *d* is the atomic d_{hkl}-spacing, and θ is the angle of incidence to the crystal planes.

Equation 2.1. *Bragg's Law*

$$n\lambda = 2d \sin\theta$$

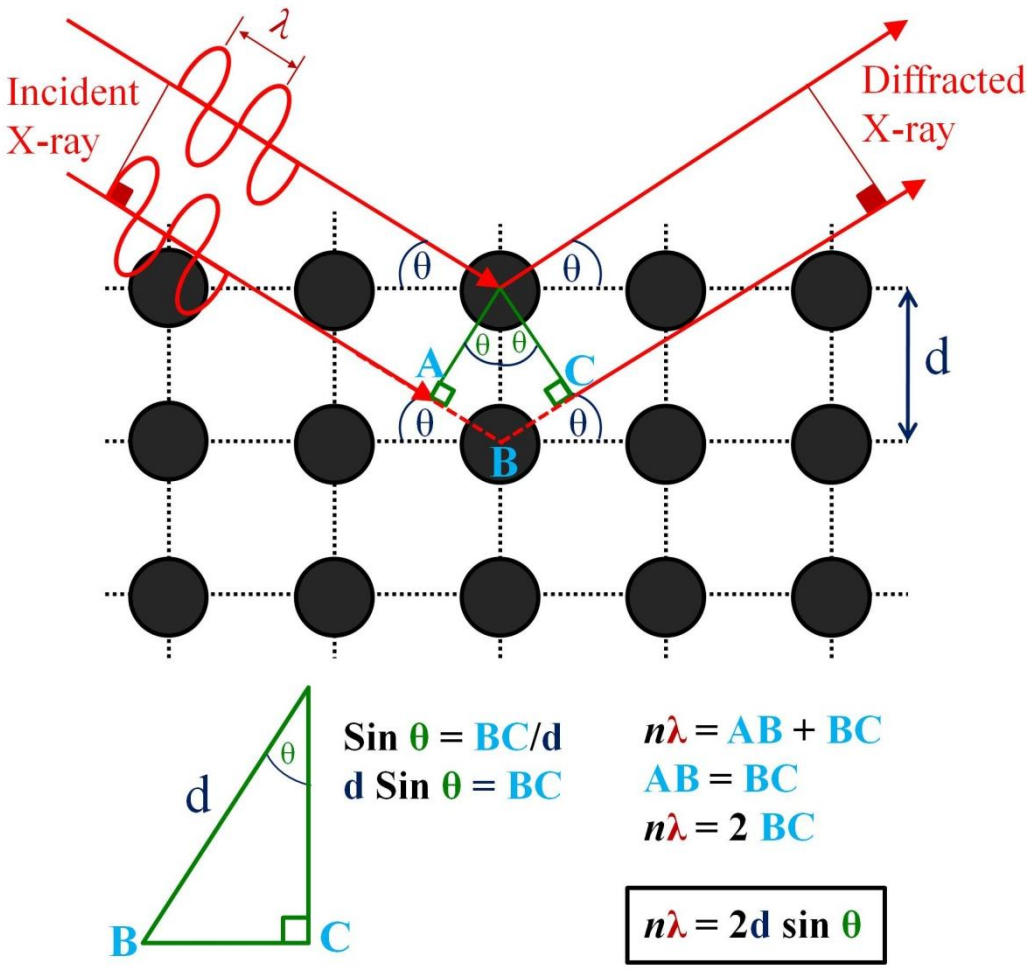

Figure 2.4. *Diffraction of X-rays by an ordered crystal and the derivation of Bragg's Law.*

Figure 2.4 illustrates how Bragg's Law is derived from the diffraction of X-rays by crystalline materials; the incident X-rays are always in phase and parallel until they interact with the electrons of the atoms, in which the second X-ray has to travel a further distance before it is reflected. This further distance is equivalent to the sum of AB and BC, and for maximum constructive interference to occur; this path difference

must be an integral (n) multiple of the wavelength (λ). Trigonometry can then be used to relate the wavelength to the d-spacing and angle of incidence (θ).

Bragg's law basically states that for a given wavelength and set of planes, one can plan for diffraction to occur by, for example, continuously changing the orientation of the crystal, e.g. θ, until Bragg's Law is satisfied and constructive interference occurs. At other angles of incidence, reflections will be weak or non-existent because the diffracted X-rays interfere destructively. In powder diffraction, it is not the re-orientation of a single crystallite which takes place to allow for diffraction to occur, instead diffraction occurs due to a powder consisting of many crystallites each at different orientations, therefore, every possible orientation of any given set of planes should be present in the powder, and statistically a number of planes should satisfy Bragg's law and produce diffraction[4, 5]. A diffraction pattern is therefore obtained by measuring the intensity of the diffracted X-rays as a function of the angle of incidence.

2.3.2 Crystal planes and pattern indexing

The peaks in a diffraction pattern are identified according to the crystal planes with which they are associated. Crystallographers use an identification system referred to as Miller indices with hkl numbers, which define a unique set of planes with different orientations relative to the co-ordination system of the unit cell (repeat unit of a

crystal). A hkl plane can be visualised as a plane which intersects the *x*,*y*,*z*-axes (with unit spacings *a*,*b*,*c*) of the unit cell at distances *a/h*, *b/k* and *c/l* respectively[6]. An example of crystal planes with different miller indices in a cubic unit cell is illustrated in Figure 2.5. The naming of the planes depends on how many times the unit cell is intersected by any set of planes. For example; for the (110) set of planes, the a and b axes are intersected once by the planes, the planes are parallel to the c unit cell edge and do not intersect it.

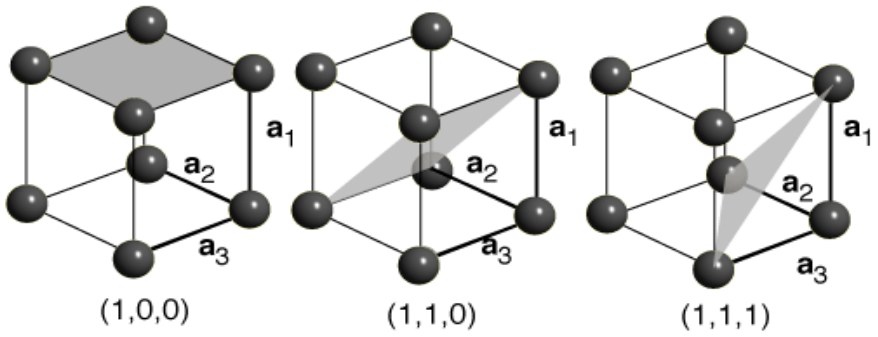

Figure 2.5. *Crystal planes with different Miller indices (h,k,l) for a cubic crystal system. Taken directly from reference*[7].

The hkl planes are related to the reciprocal lattice according to the vector equation $\mathbf{d}^* = h\mathbf{a}^* + k\mathbf{b}^* + l\mathbf{c}^*$ which is directly related to the d-spacing of the material according to $1/d_{hkl} = d^*$. The magnitude (d^{*2}) of this reciprocal lattice vector equation is also related to the d-spacing, and with the application of symmetry constraints, directly associates the lattice cell parameters with the calculated d-spacing of the peaks in a diffraction pattern[8]. For example, the d-spacing for any set

of planes in a cubic crystal is given by Equation 2.2, where all parallel Miller indices for a specific crystal structure are separated by the same d-spacing.

Equation 2.2. *The relationship between the d-spacing and lattice parameters for a cubic crystal system.*

$$\frac{1}{d_{hkl}^2} = (h^2 + k^2 + l^2)/a^2$$

The equivalent formulas for all crystal systems (i.e hexagonal, orthorhombic etc) can also be calculated and related to the observed d-spacing. This allows the Bragg angle of each set of hkl planes in a given crystal to be calculated for a given wavelength. Thus, a given set of observed reflections, recorded at a known wavelength, can be indexed and used to calculate the space group (once systematic absences are identified) and cell parameters of a crystalline material.

2.3.3 Applications of powder XRD in solid-state chemistry

Powder X-ray diffraction has been widely used in the area of solid-state chemistry due to the various, qualitative and quantitative, information which can be obtained and since many materials are only available as powders. The peak positions,

intensities, and the width/breadth and shape of the diffraction peaks can all be used to obtain information on the crystal geometry, structure and physical states of the sample.

Powder XRD is mainly used for phase identification, in which the positions of the reflections in the XRD pattern are matched (indexed) to a data set from a database of already known structures, e.g. the International Centre for Diffraction Data (ICDD) PDF database[9]. Once a powder sample has been successfully indexed, the unit cell can be determined (approximately based on its match) and its lattice parameters refined. This information can be highly beneficial in deducing information regarding the substitution of metal ions into the framework of nanoporous materials[10]. In addition, powder XRD can be used to obtain information on the phase purity of the sample; if there are additional reflections observed in the samples diffraction pattern, then it can be concluded that the sample is not phase pure.

Furthermore, the integrated intensity and the shape and width of the diffraction peaks are used to obtain information on the crystallinity of the sample and information regarding the crystallite perfections, such as size and strain. The relative intensity of the reflections can give an indication of the crystallinity of the sample, however, this may not be accurate due to effects from preferred orientation, for example with the use of a flat plate for data collection, the sample has to be flat packed into the holder which may result in the alignment of the crystals in a particular way (instead of randomly) and can affect the relative intensities of the reflections. Therefore, the crystallinity of powder samples is better measured based on the peak shape; generally the sharper the shape and more intense the peaks the more crystalline

the sample. The line broadening of the peaks is also related to the crystallite size; in 1918, Scherrer noted that the line breadth varies inversely as the size of crystallites in the sample, this lead to the Scherrer equation, Equation 2.3, where λ is the wavelength, K is the shape factor, θ is the incidence Bragg angle, β is the full-width at half maximum (FWHM) of the instrument corrected line profile of the reflections, and ε is a measure of the crystallite size. It should be noted that throughout this work a measure of the crystallite size was calculated based on the FWHM of the observed reflections employing a Gaussian fit with the program Topas-academic[11].

Equation 2.3. *Scherrer Equation*

$$\beta = \frac{K\lambda}{\varepsilon \cos\theta}$$

In the last three decades, powder XRD has become increasingly used for the refinement and solution of crystal structures with the use of synchrotron radiation. Unfortunately, XRD was not used to its fullest extent in this thesis, e.g. structure solution was not carried out or Rietveld refinement as the majority of the aluminophosphate materials sampled in this work were not calcined prior to their analysis, and unless the location of the template is known, Rietveld analysis proves difficult. Instead, high-resolution X-ray diffraction (HRXRD) with the use of synchrotron radiation was employed to attain diffraction patterns which were well defined with a high resolution, reducing any inaccuracies in the analysis from peak

overlap. This data provided sufficient information on the unit cell parameters and crystallite sizes of the structures through Pawley procedures employing a fundamental parameter approach in Topas-academic.

2.3.4 Data collection

Diffraction is an event which occurs when Bragg's Law (Equation 2.1) is satisfied, therefore diffraction relies on three principle parameters, the wavelength (λ), the angle of incidence (θ) and the lattice plane spacing (d_{hkl}), where d_{hkl} is constant and derived from the material. To obtain a diffraction pattern from a crystalline material using synchrotron radiation (white continuous X-rays), two experimental methods can be used, energy or angular dispersive diffraction. Whereas, for laboratory X-ray sources only angular dispersive diffraction is available due to the use of a single wavelength.

In energy dispersive X-ray diffraction (EDXRD), the angle of incidence is kept constant and the energy (E is related to λ) of the diffracted X-rays varied through use of synchrotron white radiation. A schematic illustration of the experimental set-up employed for a typical EDXRD data collection is shown in Figure 2.6. White continuous X-rays are radiated at the sample through a pin hole, with a diameter in the range 10 μm to 1 mm, to produce a fine X-ray beam. The energy distribution of the diffracted X-rays, which satisfy Bragg's Law at a fixed angle (or several fixed

angles) are determined using an energy dispersive detector, e.g. a solid state detector which is essentially a semiconductor detector which produces free charge carriers when an X-ray is absorbed, resulting in a pulse whose amplitude is proportional to the energy lost by the X-ray[12]. A collimator is used before the diffracted X-rays are detected, which contains slits/foils, to achieve diffraction from only a selected volume element within the sample or to ensure that diffraction detected comes only from the sample and not the supporting medium[13].

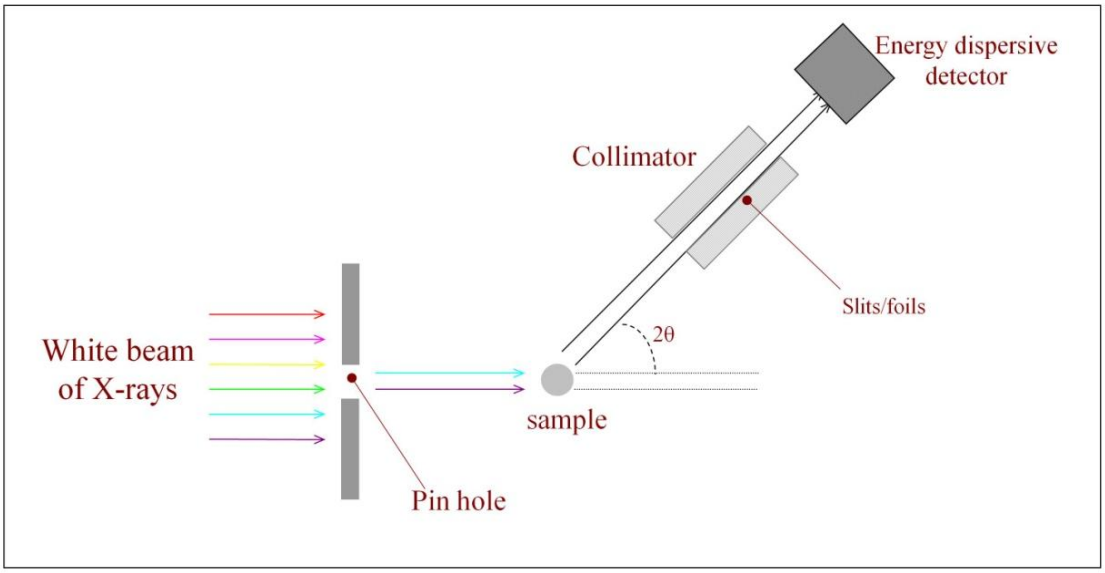

Figure 2.6. *Schematic illustration of the experimental setup used for EDXRD, all optics are fixed and the energy/wavelength of the X-ray beam varies (white radiation) to satisfy Bragg's Law.*

In angular dispersive X-ray diffraction (ADXRD), monochromatic radiation is used (e.g. constant wavelength) with the detector scanning a variety of angles in small

increments. A schematic illustration of a typical experimental set-up employed for ADXRD is shown in Figure 2.7. A white beam of X-rays is radiated onto a monochromator, e.g. silicon crystal, to select X-rays with a very narrow and precise wavelength. These parallel monochromatic X-rays are radiated at the sample, generally held in a capillary tube or flat plat, which is usually spun to reduce preferred orientation effects, and therefore improve the reliability of the intensities. The diffracted X-rays are then detected as a function of scattering angle using a point detector (step scanning in small increments) in which the step size is governed by the mechanical conditions of the diffractometer plus the time available to collect the diffraction pattern.

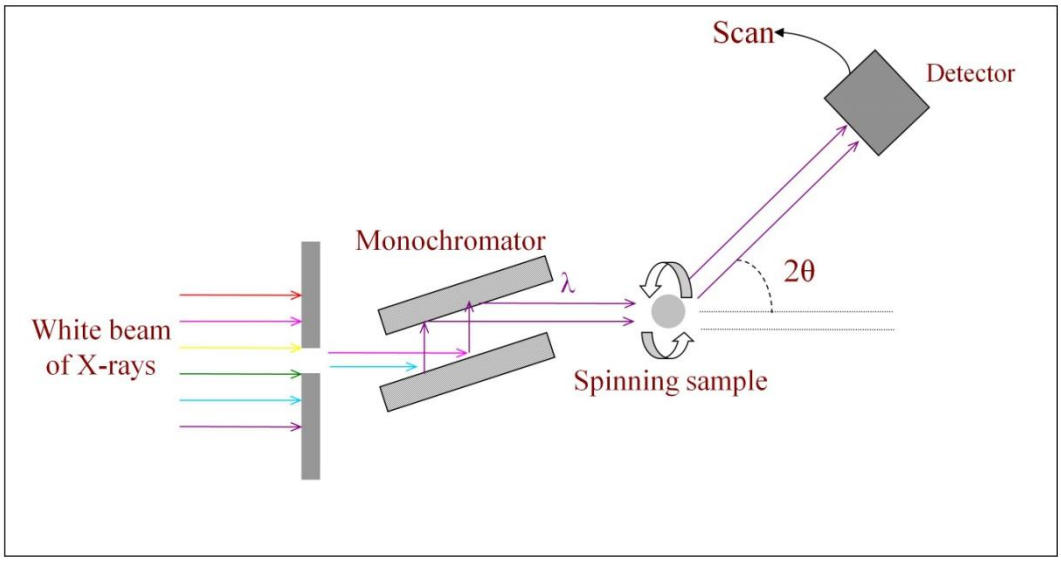

Figure 2.7. *Schematic illustration of the experimental setup used for ADXRD, in which the detector scans a range of angles with the wavelength kept constant through use of a monochromator.*

2.3.4.1 *In situ* data collection

Both angular-dispersive and energy-dispersive powder diffraction methods have been employed for time-resolved studies of chemical reactions, e.g. the hydrothermal synthesis of nanoporous materials[14-16]. EDXRD has been the principal method used for two main reasons. The first reason is that it makes use of the energetic white X-ray beam (high flux) which can penetrate thick bulky materials; it is therefore possible to use a reaction cell which is very similar to a laboratory autoclave and permits reproduction of the exact conditions required for a reaction to proceed and to be investigated *in situ*[17]. The second reason is that EDXRD uses fixed optics; this allows for the use of small X-ray windows (pin-hole) which simplifies the sample environmental cells (e.g. high temperature/pressure experiments), plus, due to there being no mechanical movement, an entire diffraction pattern can be obtained simultaneously resulting in very fast data collection times making this method suitable for time-resolved experiments.

EDXRD also has disadvantages, for example, with use of a single solid-state detector the careful selection of an optimal detector angle has to be carried out so that the most intense reflections are covered, this may be inappropriate for monitoring any other product formation or for identifying the instability of the phase formed. However, this has been greatly improved in recent years through use of multiple detector methods, e.g. a three-element detector system which consists of three energy-dispersive detectors fixed at different angles, in which the 2θ ranges partially

overlap and results in a very extended range of d-spacing of approximately 0.5 - 20 Å[18]. Another disadvantage is that there is less software available for EDXRD compared to angular-dispersive diffraction, plus the diffraction pattern can be contaminated with absorption edges due to fluorescence, however this can also be an advantage since fluorescence peaks can give information about the composition of the sample. The significant disadvantage of EDXRD over angular-dispersive diffraction is the low resolution of the diffraction peaks which is due to the limited energy resolution of the detectors; this result in broader peaks which may overlap, therefore structural refinement of the diffraction patterns is more difficult. For this reason, EDXRD is only a good method in time-resolved investigations which look at the kinetics and activation energy of the reaction, and is not suitable for *in situ* experiments which require structural characterisation and unit cell refinement.

ADXRD also has some disadvantages, its main drawback owing to the much lower flux of radiation since monochromatic X-rays are required. This makes the construction of large volume reaction cells for *in situ* experiments difficult seeing as X-rays with a low flux do not have the ability to penetrate thick bulky materials. This scaling down of the reaction cell compared to laboratory experiments may change important reaction parameters and because only small volumes can be used, inconsistent results may be obtained due to the difficulty in reproducing the starting ratio. For *in situ* experiments, the time-resolution of data collection is an important factor, with the developments in instrumentation (e.g. position sensitive detectors), the time-resolution obtained in angular-dispersive diffraction experiments is no longer a problem and is comparable to EDXRD experiments.

Overall, since angular-dispersive diffraction produces a diffraction pattern with good angular (d-spacing) resolution allowing for structural characterisation, it is the diffraction method which has been employed throughout this thesis, and from this point is just denoted XRD.

2.4 X-ray absorption Spectroscopy

X-ray absorption spectroscopy (XAS) is also a powerful tool which has been widely applied to provide detailed structural information on nanoporous materials; in particular, XAS gives local information on the probed element such as the coordination number, bond distances of the coordinated atoms and the oxidation state. This method is not confined to systems exhibiting long-range order, therefore, this technique, in contrast to XRD, can provide information on the atom type of interest prior to crystallization or in an amorphous state, in addition XAS data can be collected in a short time. Therefore XAS is an invaluable tool for gaining information of active species in catalysts, such as metal substituted aluminophosphate materials, and can be employed *in situ* to monitor the formation of these species from their amorphous state.

2.4.1 Basic Theory of XAS

When a beam of X-rays impinge on a material, they interact with the electrons and are either scattered (diffracted) or absorbed. The atoms absorb part of the incoming photons and results in a decrease in the intensity of the transmitted X-ray beam. At a specific energy, depending on the atom type, a sharp rise in the absorption is observed, called the absorption edge; this is a result of the excitation of an electron from a core level to a fully or partially unoccupied level (Fermi level). The energy of this absorption is determined by the binding energy of a core level, therefore the amount of absorption that occurs at a given energy is characteristic for each compound.

XAS is primarily concerned with the absorption coefficient, μ(E), which gives the probability that X-rays will be absorbed according to Beer's Law, Equation 2.4, where I_t is the intensity of the transmitted X-ray, I_0 is the intensity of the incident X-ray, *x* is the sample thickness, and μ(E) is the absorption coefficient, as illustrated in Figure 2.8.

Equation 2.4. *Beer's law*

$$I_t = I_0 e^{-\mu(E)x}$$

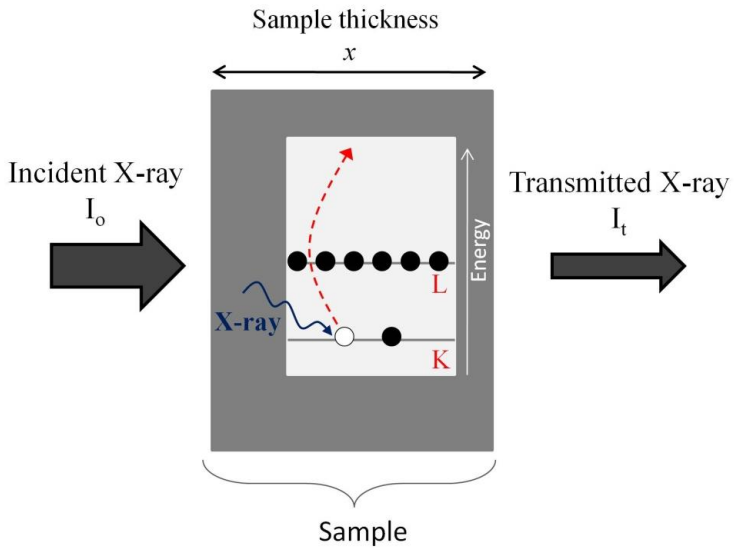

Figure 2.8. *Diagram illustrating X-ray absorption of a sample and, inset, showing the excitation of an electron.*

A plot of the absorption coefficient against energy reveals three features of interest; an overall decrease in absorption with an increase in energy, the presence of sharp absorption edges at specific energies, and just above the edges are a series of oscillations, see Figure 2.9. The absorption edge is labelled depending on the core electron which is excited, for example absorption of an X-ray which results in the excitation of a 1s core-level electron is labelled the K-edge. The absorption edge energies vary with atomic number and are well tabulated; therefore most elements can be probed by XAS techniques. The region at the absorption edge and immediately below and above it is known as the X-ray absorption near edge structure (XANES) region which is sensitive to the oxidation state and coordination environment of the probed element. The oscillatory structure observed contains detailed structural information, such as interatomic distances and details on the

species of the neighbours of the absorbing atom, and is known as the extended X-ray absorption fine structure (EXAFS) region. The regions observed in an XAS spectrum are shown in Figure 2.10, in which the energy of the incident X-ray beam at the edge (E_0) is greater than the pre-edge region and less than the XANES and EXAFS regions.

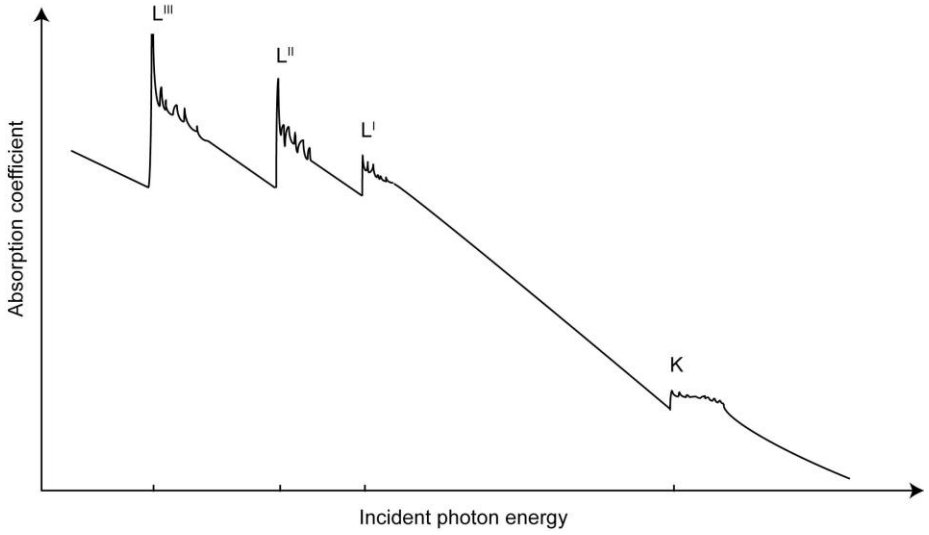

Figure 2.9. *Diagram of the absorption coefficient as a function of X-ray energy, labelled are the K and L edges, directly taken from a review by Rehr et al*[19].

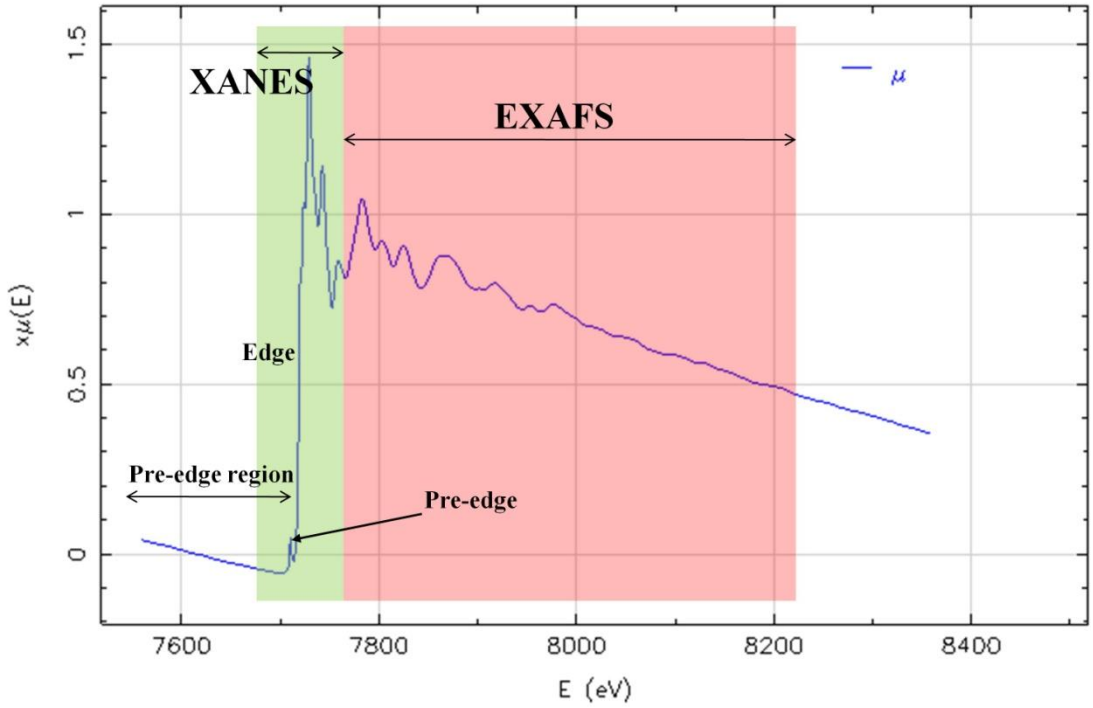

Figure 2.10. *Diagram illustrating the different regions of an X-ray absorption spectroscopy spectrum.*

2.4.2 XANES

The X-ray absorption near edge structure (XANES) region covers the region which is *ca.* 50 keV below the edge (E_0) and *ca.* 100 keV above the edge. The XANES region is governed by the electric dipole selection rule which states that for an 'allowed' transition to occur there must be a change in parity, e.g. $\Delta l \pm 1$, therefore transitions such as s → s or s → d are forbidden[4]. Therefore, absorption at the K-edge represents allowed transitions of s → p, similarly for the L_1 edge (s → p) and $L_{2,3}$ edges (p → d), and so on. The absorption edge of a specific element represents

the same allowed transition and is strongly sensitive to its oxidation state, for example elements with a higher oxidation state require more energy to knock the same electron out of the core shell[20], therefore XANES can be used to look at changes in the oxidation state of redox metals in the framework of aluminophosphate materials[21].

In addition, the XANES region can provide information on the coordination environment of the probing element, for example changes form an octahedral to a tetrahedral coordination environment is indicated by the appearance of a pre-edge feature. The pre-edge feature is the result of quadrupole (forbidden) transitions, such as the 1s → 3d transition observed in 3d transition metals, and is observed due to structural distortions around the central atom, non centrosymmetric geometry (e.g. tetrahedral coordination), or p-d orbital mixing in covalently bonded systems[22]. For example, in a CoO_4 tetrahedral coordination environment, the Co-O bonds are short resulting in the d-states of the metal becoming more p in character from orbital mixing with the oxygen atoms.

The main absorption edge is also sensitive to the coordination environment plus multiple scattering effects and can therefore be used as a 'fingerprint' for a number of compounds, however due to the many complex interactions that take place, quantitative interpretation of XANES data is a highly complex task.

2.4.3 EXAFS

The extended X-ray absorption fine structure (EXAFS) region consists of oscillations from 50 to 1000 eV above the absorption edge. These oscillations are a result of the scattering of the excited photoelectron by the neighbouring atoms of the excited probed atom. For quantitative analysis, the excited photoelectron can be imagined as a spherical wave; the backscattering of this wave by neighbouring atoms leads to interference between the outgoing photoelectron wave and the incoming scattered wave. It is this effect which gives rise to oscillatory variation from constructive or destructive interference; this is illustrated in Figure 2.11.

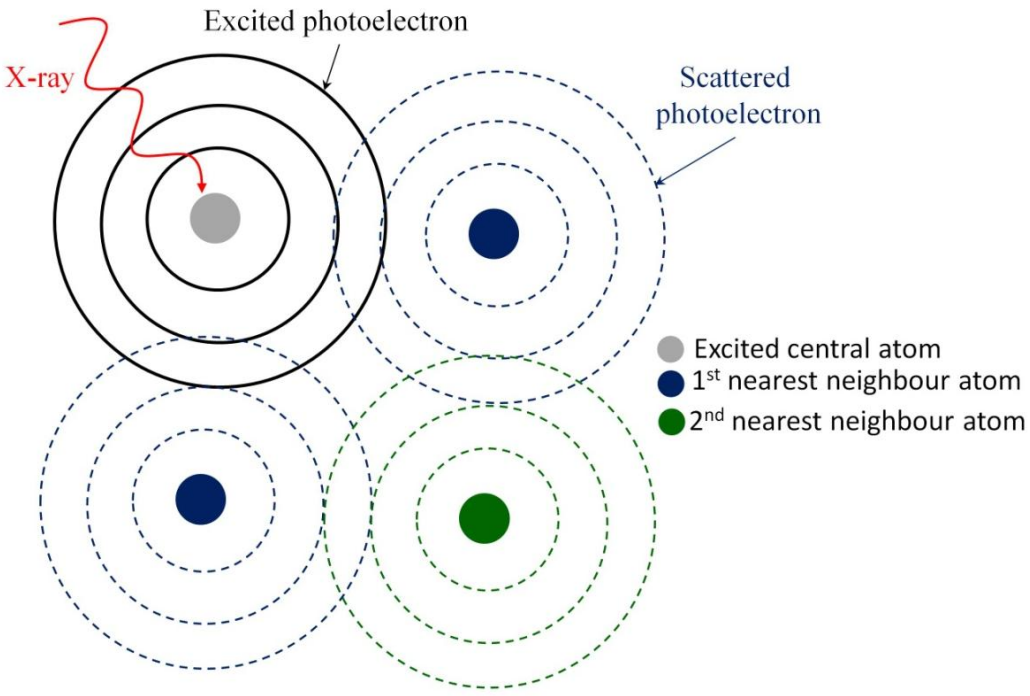

Figure 2.11. *Diagram illustrating the outgoing excited photoelectron wave and the back scattered photoelectron wave from the 1st and 2nd nearest neighbours.*

The final EXAFS spectrum is a sum of the outgoing and backscattered incoming waves, $\mu(E)$, which can be represented by Equation 2.5, where $\mu_0(E)$ is the smooth atomic background (representative if there only a single atom and no backscattering) and $\chi(E)$ is the EXAFS fine-structure function.

Equation 2.5. *Absorption coefficient / sum of the outgoing and incoming waves.*

$$\mu(E) = \mu_0(E)[1 + \chi(E)]$$

The EXAFS fine-structure function is best understood in terms of a wave vector, therefore the X-ray energy is converted to *k*, the wavenumber of a photoelectron. The oscillatory frequencies which correspond to the different near-neighbour coordination shells can therefore be described in terms of $\chi(k)$ and is calculated according to the EXAFS equation (Equation 2.6). Where N_j is the number of neighbouring atoms (coordination number), R_j is the inter-atomic distance, σ^2 is the mean square displacement arising from disorder in the neighbour distances and both $f_j(k)$ and $\delta j(k)$ are scattering properties of the atoms neighbouring the excited central atom, in particular $f_j(k)$ is the back scattering amplitude and $\delta j(k)$ is the phase-shift[23]. In particular, the scattering factors depend on the atomic number of the neighbouring atoms and can therefore distinguish what types of neighbours are present if the atomic number is not closely similar.

Equation 2.6. *EXAFS equation*

$$\chi(k) = \sum_j \frac{N_j}{kR_j^2} e^{\left(-2k^2\sigma_j^2\right)} f_j(k) \sin\left(2R_j k + \delta_j(k)\right)$$

2.4.4 Absorption decay (fluorescence)

Following an absorption event, the atom is said to be in an excited state, and a vacancy is left in one of the core shells (a core hole). Subsequently, decay of the absorption event occurs via one of two possible main mechanisms; X-ray fluorescence or Auger emission. X-ray fluorescence occurs when a higher energy electron, in the core-level, fills the deeper core hole resulting in the emission of an X-ray with a well-defined energy which is characteristic of the atom. Auger emission occurs when a higher energy electron drops to fill the core hole and emits an electron. Either of these decay processes can also be used to measure the absorption coefficient, however the use of fluorescence is more common as it is more likely to occur in the hard X-ray regime (>2 keV)[23].

2.4.5 Data collection

Before XAS data is collected, the energy range to which data will be collected over needs to be calculated, this is based on which edge is suitable for the X-ray source to produce, e.g. the K-edge of tungsten is extremely difficult to produce (λ = 0.1783 Å), therefore a higher edge is required. In addition, the amount of sample required to achieve an optimum spectrum should be determined, for example too much sample results in a loss of features but too little sample produces less well defined features. The amount of sample depends on the chemical content and is calculated based on the absorption coefficient of the probing element.

Throughout this thesis, XAS spectra were collected in transmission or fluorescence mode, in which the energy dependence of the absorption coefficient were measured based on Equation 2.7 or Equation 2.8, respectively, where I_t is the intensity of the transmitted X-ray and I_f is the monitored intensity of the fluorescence line.

Equation 2.7. *Calculation of the absorption coefficient for transmission mode.*

$$\mu(E) = \log\left(I_0/I_t\right)$$

Equation 2.8. *Calculation of the absorption coefficient for transmission mode.*

$$\mu(E) \propto I_f/I_0$$

Transmission data are collected using airtight chambers containing a carefully measured mixture of noble gases separating two highly (oppositely) charged parallel plates, known as ion chambers. X-rays enter the chambers, through X-ray transparent windows, and ionize the gases resulting in an ionization current which is measured. Ion chambers are placed before (incident X-ray beam) and after the sample in the path of the X-ray beam to record the difference in the ionization currents which is related to a change in the X-ray intensity.

XAS data are collected in fluorescence mode through the use of highly sensitive detector arrays that record the X-rays which are emitted from the sample when a high energy electron fills the core hole. Fluorescence data are particularly useful when samples are dilute with the element of interest, for example a thick pellet may be required for sufficient collection of XAS spectra in transmission mode which may result in the prohibition of the X-ray beam through the sample to the second ion chamber.

2.4.6 Data Analysis

The first step of XAS data analysis is to convert the recorded data to energy vs absorption coefficient, this is followed by removal of the background and normalization of the data (to allow for comparison with other datasets); in this thesis this was achieved employing the program Athena[24]. In particular, the background is

removed by fitting a smooth line to the pre-edge slope (Figure 2.12(a)); this removes any mass absorption contributions and instrumental background. The data is normalised with respect to the 'edge jump' resulting in data where the absorption coefficient has been normalised from 0 to 1, Figure 2.12(c).

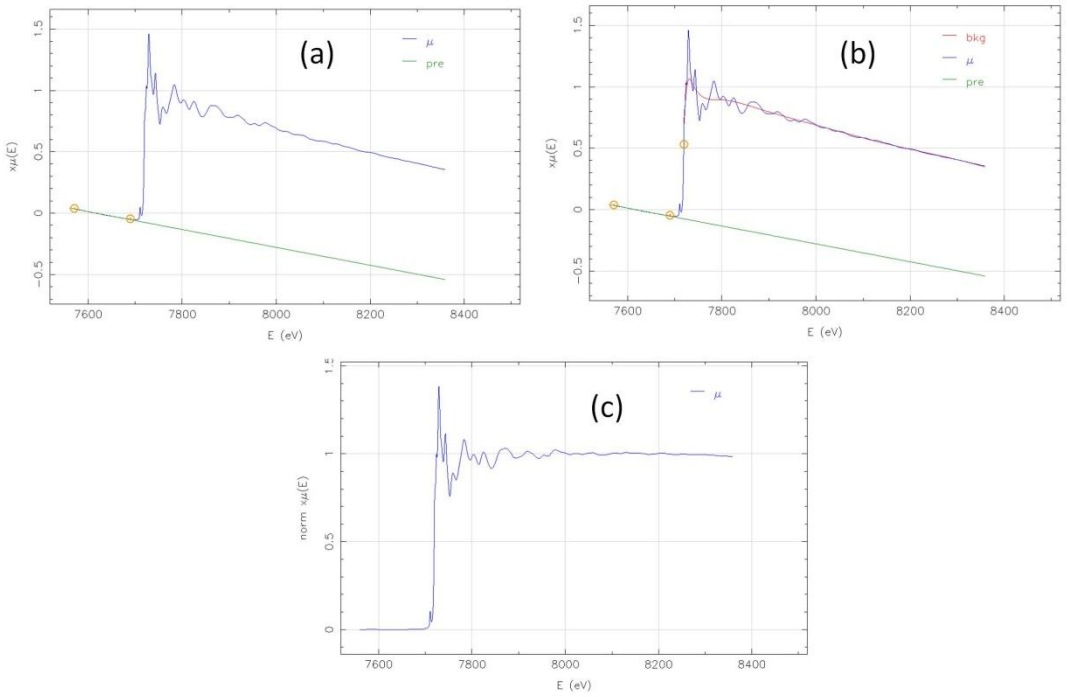

Figure 2.12. *Data analysis procedures; (a) pre-edge background, (b) post-edge background, and (c) the normalised data.*

EXAFS data, χ(k) are obtained by fitting the post-edge region with a polynomial function (represents the absorption by a single atom), Figure 2.12(b), and subtracting it from the recorded data. To compensate for the attenuation of the EXAFS

amplitude at higher k values and to prevent large oscillations at low k values from dominating the spectrum, the EXAFS data χ(k) is multiplied by a power, most commonly 3, Figure 2.13(a and b). For further analysis EXAFS data χ(k) can be converted to R-space by Fourier transform which reveals contributions from individual shells, see Figure 2.13(c), including the number and distance of atoms from the absorbing atom.

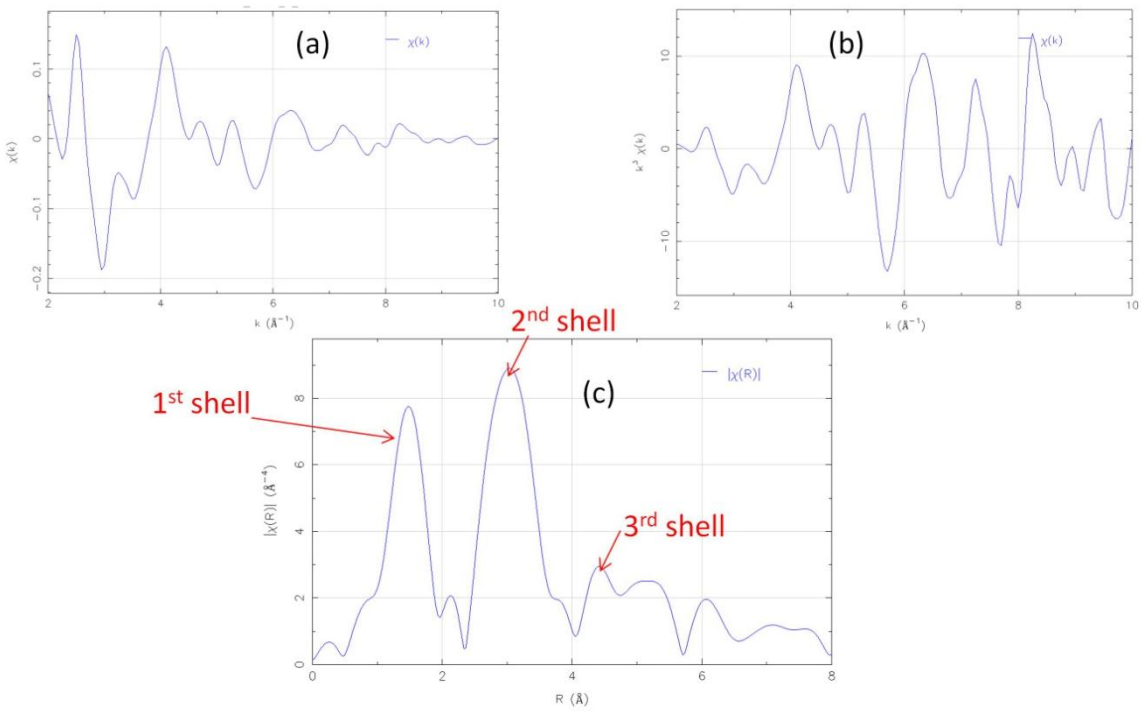

Figure 2.13. *EXAFS data, (a) χ(k), (b) k^3χ(k) and the Fourier transform related to the position of the surrounding shells.*

To extract useful information such as what elements are bound to the central probe atom and the bond distances, structural models must be built and refined to fit the recorded EXAFS data. In this work, the FEFF program employed in Artemis[24] was employed to theoretically calculate the scattering amplitude and phase shifts of the probing atom, in particular cobalt surrounded by oxygen atoms. The first shell was fitted refining the N, R and σ^2 parameters of the EXAFS equation, in either *k*- or *R*-space, examples of fittings are given in Figure 2.14(a) and (b).

It should be noted that higher shells can be fitted to EXAFS data; however this analysis is much more complex with effects from multiple scattering, in which the photoelectron scatters from two or more atoms before returning to the absorbing atom. More sophisticated fitting models are required for the analysis of these data. However, it's sufficient to extract structure and oxidation states of active sites in catalysts from the first shell coordination and bond distances, where analysis of higher shell coordination is not essential in this work.

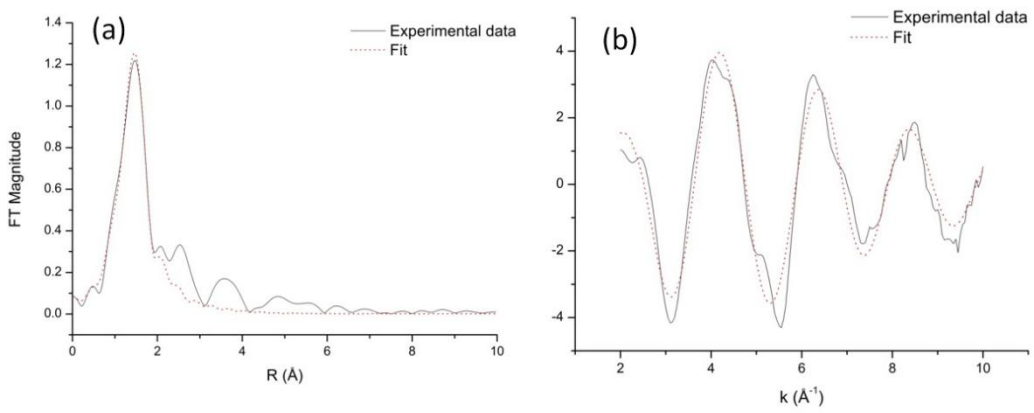

Figure 2.14. *Fitting of EXAFS data in (a) R-space or (b) k-space.*

2.5 Other techniques

As described, the majority of the work undertaken in this thesis was carried out employing X-ray techniques, in particular HRXRD and XAS. The data collected with these advanced methods were carried out at either the Diamond Light Source in Oxfordshire (England) or the European Synchrotron Radiation Facility (ESRF) in Grenoble (France). The specific optics of the beamlines used and the experimental set-up are described in the respective chapters.

Standard laboratory XRD data wre collected with a Bruker D4 flat plate diffractometer equipped with a copper X-ray tube. Other complementary laboratory based *ex situ* techniques, including thermogravimetric analysis (TGA) and solid-state nuclear magnetic resonance (NMR), and *in situ* Fourier transform infrared

spectroscopy (FTIR) were also employed throughput the work described in this thesis. These methods are also described in the respective chapters.

2.6 References

[1] Cockcroft, J. K.; Barnes, P.; Csoka, T., Advanced certificate in Powder Diffraction on the Web, In School of crystallography, Birkbeck College, University of London: (1997-2006).

[2] 3D model of the machine. www.diamond.ac.uk, In *Diamond Light Source*, (2010).

[3] Ide-Ektessabi, A., *Applications of Synchrotron Radiation. Micro Beams in cell micro biology and medicine*, Springer: Berlin, (2007).

[4] Atkins, P. W., *Physical Chemistry*, Press, O. U. Ed. (1990).

[5] Will, G., *Powder Diffraction: The Rietveld method and the two-stage method*, Springer: (2006).

[6] West, A. R., *Solid State Chemistry and its Applications*, Wiley: (1984).

[7] Hofmann, P., Solid State Physics, In *http://www.phys.ac.dk*, (2007).

[8] Hammond, C., *The Basics of Crystallography and Diffraction*, Oxford Science Publications: (1997).

[9] JCPDS, International Centre for Diffraction Data PDF-2, In (1997-2010).

[10] Hartmann, M.; Kevan, L., *Res. Chem. Intermed.*, (2002) **28**, 625.

[11] Software, C., TOPAS-Academic Version 4.1, In Coelho, A. Ed. Brisbane, Australia, (2007).

[12] Nasai, N.; Kakudo, M., *X-ray Diffraction by Macromolecules*, Springer: (2005).

[13] Norby, P., *Current Opinion in Colloid & Interface Science*, (2006) **11**, 118.

[14] Walton, R. I.; Millange, F.; O'Hare, D.; Davies, A. T.; Sankar, G.; Catlow, C. R. A., *Journal of Physical Chemistry B*, (2001) **105**, 83.

[15] Walton, R. I.; Norquist, A.; Smith, R. I.; O'Hare, D., *Faraday Discussions*, (2003) **122**, 331.

[16] Walton, R. I.; O'Hare, D., *Chemical Communications*, (2000), 2283.

[17] Moron, M. C., *Journal of Materials Chemistry*, (2000) **10**, 2617.

[18] Muncaster, G.; Davies, A. T.; Sankar, G.; Catlow, C. R. A.; Thomas, J. M.; Colston, S. L.; Barnes, P.; Walton, R. I.; O'Hare, D., *Physical Chemistry Chemical Physics*, (2000) **2**, 3523.

[19] Rehr, J. J.; Albers, R. C., *Reviews of Modern Physics*, (2000) **72**, 621.

[20] Ankudinov, A. L.; Ravel, B.; Rehr, J. J.; Conradson, S. D., *Phys. Rev. B*, (1998) **58**, 7565.

[21] Sankar, G.; Fiddy, S.; Beale, A. M.; Harvey, I.; Hayama, S.; Bushnell-Wye, G., *X-Ray Absorption Fine Structure-Xafs13*, (2007) **882**, 585.

[22] Gleeson, D.; Sankar, G.; Catlow, C. R. A.; Thomas, J. M.; Spano, G.; Bordiga, S.; Zecchina, A.; Lamberti, C., *Physical Chemistry Chemical Physics*, (2000) **2**, 4812.

[23] Newville, M., Fundamentals of XAFS, In Consortium for Advanced Radiation Sources, University of Chicago: Chicago, (2004).

[24] Ravel, B.; Newville, M., *Journal of Synchrotron Radiation*, (2005) **12**, 537.

Chapter 3. A study on the substitution and crystallization mechanism of divalent metal ions in large pore AFI-type materials

3.1 Chapter Overview

This chapter discusses the results obtained from an investigation into the crystallization, and substitution mechanism of cobalt ions into the CoAlPO-5 framework. An *in situ* simultaneous X-ray diffraction/X-ray absorption spectroscopy (XRD/XAS) study revealed Co(II) ions transforming from octahedral coordination in the gel to a tetrahedral environment in the framework via a two stage conversion, in which a stable intermediate Co(II) pseudo-octahedral species exists. To ascertain additional detailed information, such as the effect of divalent metal cations on the structure and the change in unit cell parameters over crystallization time, *in situ* high-resolution X-ray diffraction (HRXRD) techniques were employed. The combined results from the two *in situ* studies revealed a solid hydrogel transformation mechanism for the formation of CoAlPO-5 catalysts.

3.2 Introduction

Aluminophosphates and other zeotype materials are of importance due to their wide applications in catalysis, ion exchange, adsorption, chemical seperation, and host-guest chemistry[1-6]. Although, a large variety of zeotype structures have been successfully synthesised via trial and error of synthesis parameters and through experimental findings, understanding the crystallisation mechanisms taking place during hydrothermal synthesis of open framework AlPOs, including the metal incorporation mechanism, is of considerable interest, since it could lead to a more rational approach towards the design and synthesis of new molecular sieve materials with specific crystalline structure, morphology and particle size for specific applications, such as catalysis.

A variety of *ex situ* techniques have been employed to obtain a better understanding of this complex problem, these include X-ray diffraction (XRD)[7, 8], nuclear magnetic resonace (NMR)[9] and electron microscopy[10]. Although these *ex situ* methods provide useful information, they cannot give a complete picture of the processes occurring under reaction conditions.

A large number of *in situ* studies have been devoted to understanding the transformation of gel to nanoporous materials using a variety of techniques.[11-15] Depending on the specific *in situ* technique used, a variety of information can be obtained including identification of intermediate phases and the nature of molecular species. The majority of *in situ* studies have employed X-ray

diffraction (XRD) as the principal technique since it provides information on the long-range ordered structures that are formed during the crystallisation processes.[1, 11, 16, 17] However, if there are small amounts of dopant ions, which are essential for catalytic applications, XRD may not provide adequate information on the local structural changes that take place during the formation of nanoporous materials. Knowledge of changes in the local environment of the dopant ion during the formation of materials from the initial gel is extremely important in gaining an understanding of the crystallisation mechanisms. X-ray absorption spectroscopy (XAS), which is sensitive to local structure, is thus also a very valuable tool in studying these processes.[18-22] While this atom specific technique provides the local structural information, it is an average of all the environments, in particular, both the framework and extra-framework cations, see Figure 3.1. In addition, if both the sites have a similar coordination environment, it will not be able to distinguish between them. XRD is therefore a complementary technique to XAS, as information on the long range order of the system maybe useful in resolving whether the dopant ions are in the framework.

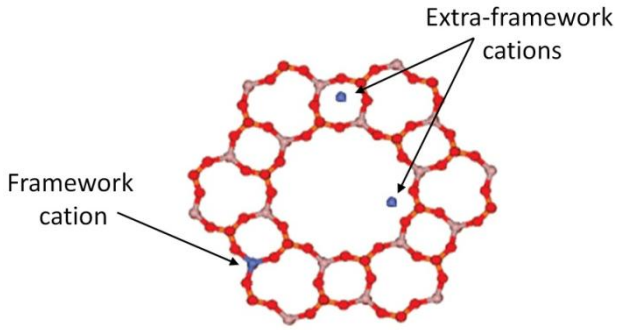

Figure 3.1. *Diagram showing the difference between framework and extra-framework cations.*

A combination of these two methods (XRD/XAS), in addition to other spectroscopy techniques, has been successfully employed in several previous studies[13, 16, 18, 20, 23-26]; however, to our knowledge no studies have combined these two powerful techniques *simultaneously*. The advantage with simultaneous measurements is that the changes in the long and short range order are monitored together, which is particularly useful in a continuously reacting system.

So far, different synthesis mechanisms relating to specific zeotype systems have been proposed with the majority of conclusions falling into two extremes; the solution-mediated transport mechanism involving the dissolution of the gel in solution phase to form active ionic species which diffuse to the nucleation sites and re-crystallize to form the molecular sieve[27-29], and the solid hydrogel transformation mechanism relating to the re-organization of the solid phase from an amorphous state to one with long-range order[27, 30]. Many studies have shown the synthesis of molecular sieve materials, such as AlPOs, to proceed via both mechanisms or could even lie somewhere between these two extremes, but in general a more complete mechanistic understanding of molecular sieve formation is needed to lead to a more rational approach in their synthesis.

3.2.1 Large pore AFI framework

Among the various hetero-atom substituted AlPO's, AlPO-5 (AFI), AlPO-18 (AEI), AlPO-36 (ATS), AlPO-34 (CHA) and AlPO-11 (AEL) have attracted considerable interest due to their ability to induce shape selective catalytic reactions. Within this range of systems, AlPO-5 (illustrated in Figure 3.2) is one of the most extensively studied, as it has a large pore one-dimensional channel system and more importantly it is the only system which can be prepared in a relatively short time, with the inclusion of a range of metal ions (hetero-atoms such as Zn, Co, Mg, Cr, Fe or Mn) [31-33] and using a large number of structure directing agents, typically quarternary ammonium salts and amines. For example, AlPO-5 can be synthesized using triethylamine (TEA) [34], tripropylamine (TPA) [35], ethyldicyclohexylamine (ECHA)[36] or tetraethylammonium hydroxide (TEAOH). However, most of these organic templates only form the AFI topology under very specific conditions. Methyldicyclohexylamine (MCHA), on the other hand, has been shown to form only phase pure AFI over a wide range of synthesis conditions, e.g. pH and temperature [37]. The AFI framework also shows a high thermal stability during catalysis and it does not collapse upon calcination, when removing the organic template, showing complete integrity [38, 39]. Therefore, it is of general interest to understand the detailed processes involved in the synthesis of this system, in particular the substitution mechanism of the divalent metal ions as these impart catalytic activity.

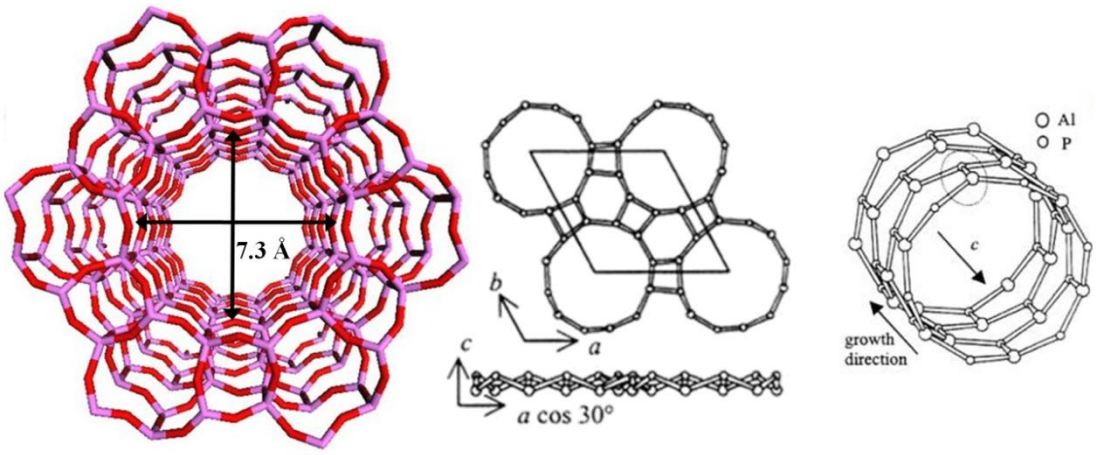

Figure 3.2. *Showing the 1- dimensional channel system of AlPO-5, with a pore opening of 7.3 Å. The structure consists of 4-, 6- and 12- membered rings, in which crystal growth occurs in the c direction*[40].

3.2.2 Aims and objectives

The aim of this work was to develop methods to determine the substitution mechanism and the mechanism of formation of large pore AlPO-5 systems. For this purpose, *in situ* simultaneous XRD/XAS methods were employed to investigate the substitution of cobalt(II) ions into the AFI framework. This system was studied as it is well-known that cobalt substitutes for framework sites and results in a transformaton from an octahedral coordination to a tetrahedral environment[21, 22, 41]. Investigations with XAS on the incorporation of other divalent metal ions, such as Zn(II) and Fe(II), do not provide such beneficial information. For example, Zn(II) ions adopt a tetrahedral coordination in the

precursor gel, therefore no change is seen in XAS during its substitution into the AlPO framework.

N-methyldicyclohexylamine (MCHA) was employed as the organic template, which is unique as it produces only the AlPO-5 structure, over a wide range of pH, temperature and with a variety of metal ions, without any competing phases[37]. This is an important issue, as when other organic templates are used, for example tetraethylammonium hydroxide or triethylamine, there is the possibility that CHA (AlPO-34) or other materials are formed as a competing phase during the synthesis of AlPO-5 material.

Recent developments, particularly in the area of angular-dispersive high resolution synchrotron powder XRD (HRXRD) made it possible to collect high-quality diffraction data in a very short time scale. This technique was employed during the synthesis of CoAlPO-5 to determine the precise structural parameters, in particular the variation in the lattice parameters. Results were compared to other AFI-type materials, such as ZnAlPO-5 and AlPO-5, to ascertain additional information on the crystallization mechanism of CoAlPO-5. Nuclear magnetic resonance and thermogravimetric analysis data of the as-synthesised AFI materials was subsequently collected, not only, to ascertain the aluminium and phosphorus coordination environments but to also quantify and determine the nature of the desorbing species.

3.3 Experimental

3.3.1 Synthetic procedure

Using hydrothermal methods, CoAlPO-5 was synthesized from a procedure based on work carried out by Sankar et al[42] employing *N*-methyldicyclohexylamine (MCHA) as the organic template.

The AFI type material was synthesized from a synthesis gel with composition **1.5 P: 0.95 Al: 0.05 Co: 25 H_2O: 0.8 MCHA**, by dissolving aluminium hydroxide hydrate (Aldrich) in an aqueous solution of phosphoric acid (85 wt % Aldrich), followed by addition of an aqueous solution of cobalt(II) acetate tetrahydrate (Aldrich). After rigorous stirring for *ca.* 10 minutes the gel attains homogeneity and the organic template, MCHA (97 wt% Aldrich), was added to form the final gel which was stirred for *ca.* 1h. Where necessary, the dilution of the precursor, in particular the organic template, in their commercially available form was taken into consideration when calculating the amount of distilled water required.

The pH of the final gel was measured to be 7.5. The gel was then transferred to either a specially designed synthesis cell (described in section 3.3.2.1) for *in situ* characterization or to a Teflon lined steel autoclave for *ex situ* characterization, with an approximate 60% fill volume. The gel was heated at temperatures between 160-

170 ºC for an appropriate amount of time. For *ex situ* characterization, the samples were washed with distilled water, filtered and dried at 100°C for 2 hours.

Additional samples of AlPO-5 and ZnAlPO-5 (zinc(II) acetate dihydrate Aldrich) were prepared using the same method with the general gel composition **1.5 P: (1-*x*) Al: *x* Me: 25 H_2O: 0.8 MCHA,** where Me is the divalent metal.

3.3.2 *In situ* Characterization

In situ characterization has an advantage over *ex situ* as, not only does it eradicate systematic errors, but intermediate phases can be characterized which may be destroyed upon filtration and drying. Therefore, *in situ* methods were employed during the formation of AFI-materials, in particular CoAlPO-5, in order to understand the mechanisms of hydrothermal reactions under direct synthesis conditions. Whilst X-ray absorption spectroscopy (XAS) measurements were undertaken to ascertain the coordination of cobalt(II) within the system, *simultaneous* X-ray diffraction (XRD) was carried out to study its crystallinity and phase purity. High resolution XRD data was collected to examine the structural changes occurring throughout the crystallization.

3.3.2.1 *In situ* synthesis Cell

A specially designed hydrothermal synthesis cell, as shown in Figure 3.3 and designed by Prof G. Sankar, was used throughout the *in situ* experiments. The *in situ* synthesis cell, equipped with a Teflon ring spacer (8 mm thick) in the centre of the brass cell, is sealed on one side with a circular mica window (0.5 mm thick, 25 mm diameter) followed by a PTFE (Teflon) ring (1.5 mm thick, 25mm diameter), an aluminium ring and finally a brass ring. The components of the cell are shown in Figure 3.4. The precursor gel is loaded on the opposite side with maximum fill of *ca*. 60% of its total volume (approx. 1 ml) to avoid possible overpressure developing against the windows during the reaction. The gel is then sealed in the cell using another circular mica window (on top of the sample), followed once again by a PTFE (Teflon) ring, aluminium ring and tightly sealed with a brass ring. The *in situ* synthesis cell, containing the precursor gel, is then mounted onto a heating block, a thermocouple is inserted into the cell and the temperature of the synthesis system monitored and programmed with a temperature controller.

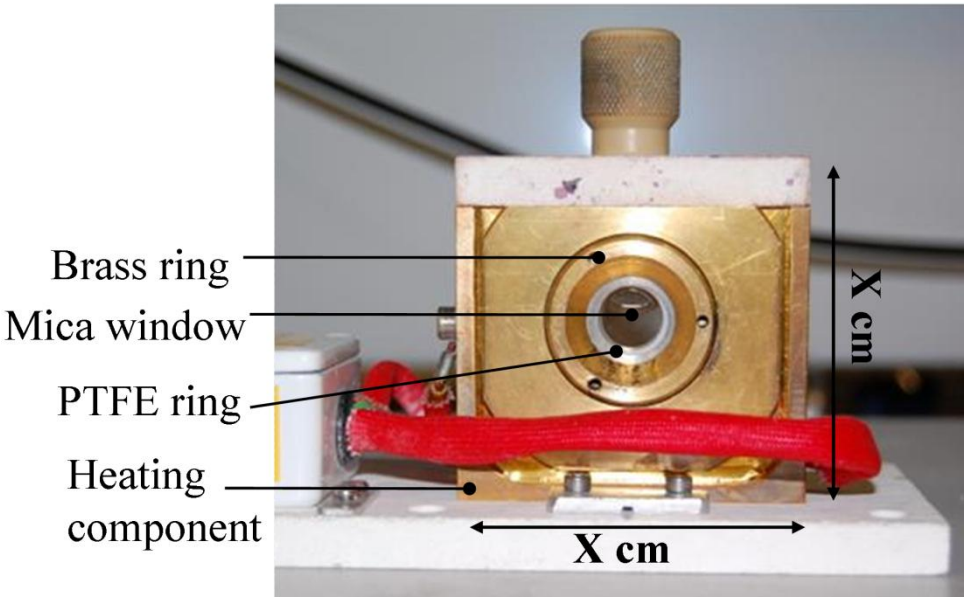

Figure 3.3. *Showing the synthesis cell used throughout the in situ hydrothermal synthesis studies, where X is 6 cm.*

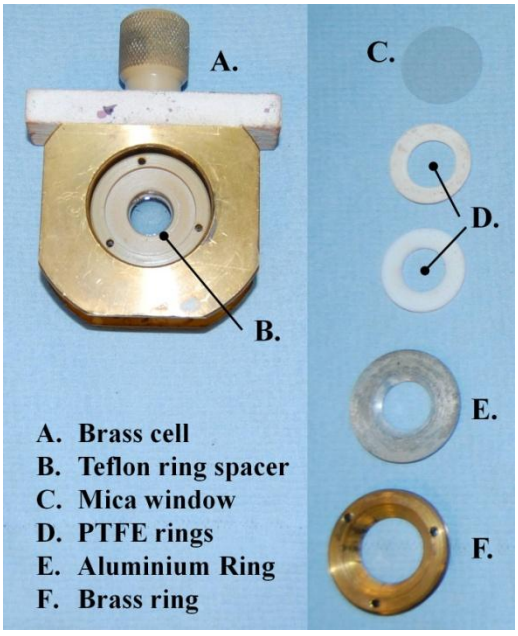

Figure 3.4. *Photograph showing the components of the specially designed in situ synthesis cell.*

3.3.2.2 *Simultaneous* X-ray diffraction and X-ray absorption spectroscopy

Simultaneous *in situ* XAS with XRD data were recorded on the BM29 beamline of the European Synchrotron Radiation Facility (ESRF) in France, during the hydrothermal synthesis of CoAlPO-5. A schematic illustration of the set-up used is shown in Figure 3.5. The gel, as described in section 3.3.1, was transferred to an *in situ* synthesis cell and heated to 160°C with a ramp rate of 5°C per minute, and dwelled for an appropriate length of time.

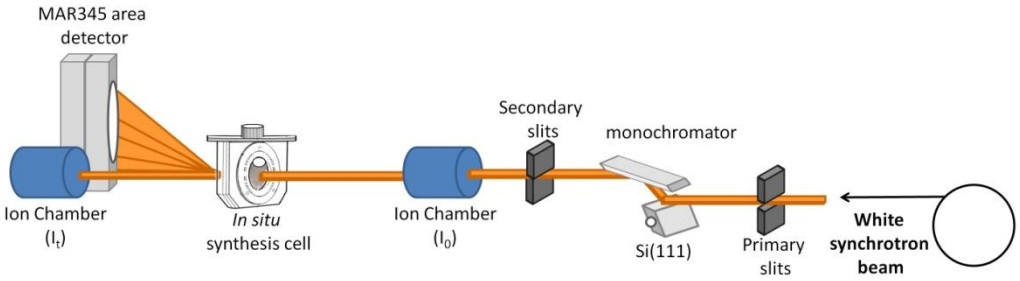

Figure 3.5. *Schematic illustration of the set-up used at the BM29 beamline of the ESRF.*

XAS measurements were recorded at the Co K edge in transmission mode, with an energy range between 7.69 and 7.77 keV, which was sufficient enough for X-ray Absorption Near-Edge Structure (XANES) analysis. An acquisition time of 1s per scan point resulted in a scan time of 3 minutes.

Generally, angle-dispersive XRD measurements are recorded using a constant wavelength. In this work, XRD data was collected simultaneously with XAS which resulted in a varying wavelength between 1.612 and 1.596 Å (Energy = 7.69 – 7.77 keV). This change in the wavelength was found to be relatively small as it resulted in only a small broadening of the peaks which was sufficient for phase identification. Figure 3.6, simulated XRD patterns (taken from a single-crystal study[43]) of the AFI structure at the two extreme wavelengths, demonstrates this as there is no peak overlap. However, major concern arises from a variable wavelength when XRD data is collected above the absorption edge as fluorescence radiation from dopant ions in the reacting system can produce a large background and mask the data. Due to the large 17 bit dynamic range of a MAR345 image plate detector available at BM29 it was possible to record good quality XRD data without much effect due to the fluorescence.

XRD patterns were collected utilizing the MAR345 area plate detector which records data between 0° and 60° 2-theta, however, due to the geometry of the synthesis cell only data recorded above 15° 2-theta was usable. An acquisition time of 3 minutes per scan followed by a read-erase time of 3 minutes resulted in data being recorded every 6 minutes.

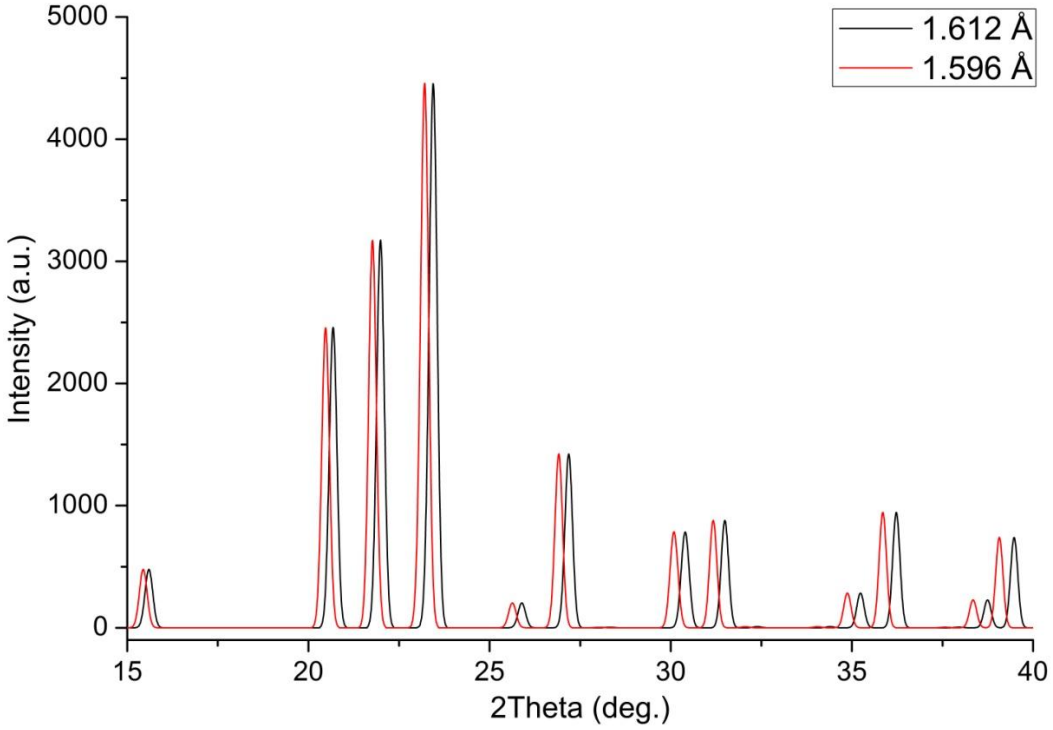

Figure 3.6. *Simulated XRD patterns of the AFI framework at wavelengths of 1.612 and 1.596 Å*[43].

3.3.2.3 High resolution X-ray diffraction (HRXRD)

High resolution *in situ* X-ray diffraction (HRXRD) studies were performed on the BM01b Swiss-Norwegian beamline of the European Synchrotron Radiation Facility (ESRF) in Grenoble, France, which operates at 6 GeV with a current of 200 mA. The experimental set-up employed is schematically illustrated in Figure 3.7[44].

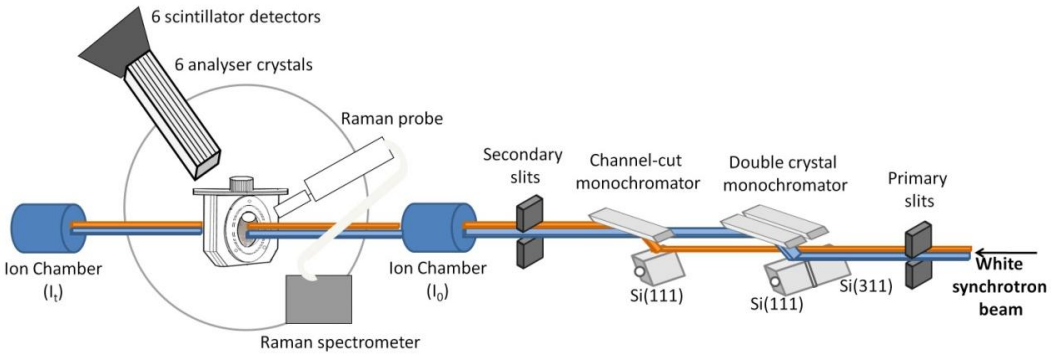

Figure 3.7. *Schematic illustration of the set-up available at the BM01b beamline of the ESRF.*

The beamline uses a robust 2-circle powder diffractometer equipped with six analyzer crystals and scintillator detectors which results in the simultaneous collection of six complete patterns with a very small off-set in 2-theta. HRXRD patterns were collected at 170 ºC and at a fixed wavelength of 0.5 Å with a 2-theta range of 2-10º. The duration of each data collection was tuned with the reaction speed to optimize the counting statistics without losing the time evolution of the HRXRD pattern, in which the optimized duration was found to be 2 minutes per scan. In addition to this, to improve the time resolution data was collected in both directions of 2-theta, for example one pattern was collected from 2 to 10 degrees and the following pattern collected from 10 to 2 degrees.

As depicted in Figure 3.7 with the presence of ion chambers, the beamline is also set-up so that X-ray absorption spectroscopy (XAS) studies can be carried out in combination with HRXRD and raman spectroscopy. This study did not employ the XAS technique during the synthesis of the AFI-type materials since the beamline is

not equipped to carry out quick XAS data collection. The longer data collection time required to collect XAS data would have resulted in the lost of vital data during the quick hydrothermal synthesis and therefore would not give supplementary information during the *in situ* experiment. Raman spectroscopy data was collected throughout the formation of the AFI materials, however, the data was very noisy possibly due to the movement of the gel and/or because the raman probe had to be a set distant from the hot cell. Therefore reliable analysis and interpretation of this data could not be attained.

3.3.2.4 Data Analysis

Background-subtraction and normalization of the XANES data was performed using the XAS analysis software Athena[45]. XRD phase identification of each crystalline phase was achieved by indexing the reflections, using either the DIFFRAC^{plus} EVA (utilising the ICDD database PDF-2[46]) program or by comparison with standard XRD data sets available[47]. For the HRXRD data, a Pawley reflection fitting was performed utilizing the fundamental parameter approach (FPA) available with TOPAS-academic[48]. This provided information on the unit cell parameters and crystallite size. Starting unit cell parameters of the AFI phase taken from Klap et al.'s single crystal XRD study, a(=b) = 13.718 Å, c = 8.4526 Å, $\alpha=\beta = 90°$ and $\gamma = 120°$ with hexagonal space group P6cc (184), were utilized[43].

All plots were prepared using the data analysis and graphing Origin Pro 8 software[49].

3.3.3 *Ex situ* Characterization

The as-prepared AFI materials were further characterized by solid-state nuclear magnetic resonance (NMR) and thermogravimetric analysis (TGA). ^{27}Al and ^{31}P MAS NMR was carried out to give information about the coordination of aluminium and phosphorus in the aluminophosphate framework. TGA coupled with a mass spectrometer was employed to identify and quantify the desorbing species.

3.3.3.1 Nuclear Magnetic resonance (NMR)

Solid state nuclear magnetic resonance (NMR) studies on powder samples of AlPO-5 and ZnAlPO-5 were carried out at the NMR research service available at Durham University. Direct ^{27}Al and ^{31}P spectra (quantitative) were collected using a Varian VNMRS spectrometer operating at frequencies of 104 and 162 MHz, respectively, equipped with a 4 mm probe. A spin rate of 14 kHz and 10 kHz for ^{27}Al and ^{31}P spectra was utilized with an acquisition time of 10 and 20 ms, respectively. In addition, ^{1}H-^{31}P cross-polarization spectra for each sample were acquired to study

(qualitatively) the ^{31}P environments closest to ^{1}H. Spectral referencing was carried out with respect to 1M solutions of $AlCl_3$ and 85 wt% H_3PO_4.

3.3.3.2 Thermogravimetric analysis coupled with a mass spectrometer

Thermogravimetric analysis (TGA) was carried out using a Netzsch STA machine which was calibrated using an empty aluminium sample holder. Approximately 12 mg of the as-synthesized AFI sample was loaded into the machine in the sample holder and heated from room temperature to 550°C at a rate of 5ºC per minute. A flowing helium atmosphere was employed and a mass spectrum collected with a mass-to-charge (*m/z*) ratio range of 10 to 60 and a time acquisition of 5 per minute.

3.4 Results and Discussion

Results are presented firstly for the *simultaneous* XRD/XAS data discussing the formation of a crystalline AFI-phase and the changes in white line intensity during the formation of cobalt substituted aluminophosphate type-5. Next the results from the analysis of HRXRD data collected during the crystallization of CoAlPO-5 are presented and compared to those from its un-substituted analogue with the aim of deriving more detailed information on the structure in respect to the mechanism of substitution and formation.

3.4.1 Simultaneous *in situ* X-ray diffraction and X-ray absorption study during the formation of CoAlPO-5

A three-dimensional stack plot of the XRD data collected during the synthesis of cobalt (5%) substituted AlPO-5 at 160°C is given in Figure 3.8. The starting synthesis gel was pink in colour, which is indicative of cobalt(II) ions in an octahedral coordination. First signs of crystallization in the XRD data appeared after approximately one hour (66 minutes), and resulted in final crystals which were blue, suggesting cobalt(II) ions in a tetrahedral environment. All reflections, collected with a 2θ range of 15º – 40º, could be indexed to the large pore AFI structure revealing the formation of phase pure CoAlPO-5. Employing a changing wavelength (1.612 to

1.596 Å) during the collection of the XRD data produces a broadening in the observed reflections, therefore it was not possible to obtain detailed structural information such as unit cell parameters.

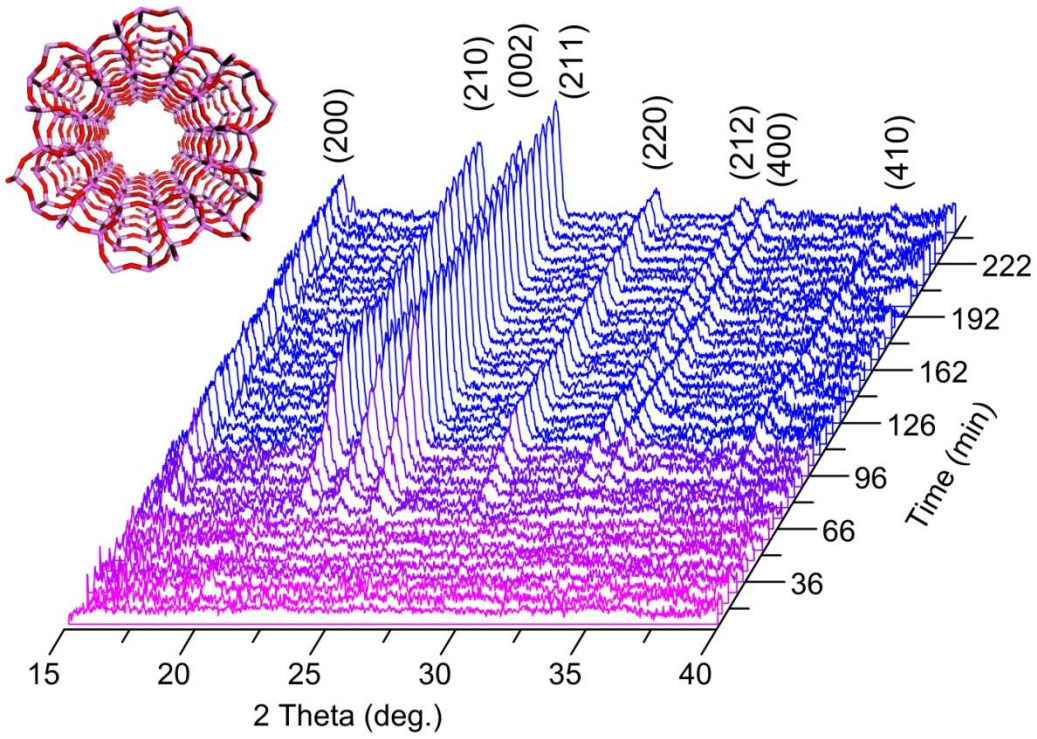

Figure 3.8. *3D stacked plot of the XRD (λ = 1.612 - 1.596 Å) data collected during the formation of CoAlPO-5 at 160°C. All reflections can be indexed to the AFI structure shown. Data are coloured appropriately based on observations of the gel colour which is associated with the cobalt(II) coordination environment.*

The background-subtracted and normalized stacked X-ray absorption data, as well as the variation in the normalized pre-edge intensity, recorded during the formation of CoAlPO-5 as a function of time are presented in Figure 3.9.

It is clear from the XANES data that the white line intensity, corresponding to an electric dipole-allowed 1s-4p transition, decreases over synthesis time. A rapid decrease is first observed (region I) at the onset of heating and corresponds to a temperature change from 51°C to 160°C, this is followed by a short period in which the white line intensity is relatively stable (region II). Subsequently, there is a gradual decrease in its intensity over a 48 minute time interval (region III) before eventually remaining constant (region IV). It is well-known that the white line intensity (marked 1s→4p) is not only affected by electronic factors, but also by the coordination environment of the metal resulting from the presence of multiple scattering effects; for example, octahedral coordination has linear O-Co-O bonds (larger multiple-scattering effects) giving rise to large white line intensity compared to tetrahedral coordinated Co[18, 20, 21]. Thus, the decrease in the white line feature observed is indicative of a change in the cobalt(II) coordination from an octahedral to tetrahedral environment. It should be noted that there was no change in the position of the white line feature, indicative of the oxidation state of cobalt(II) remaining the same throughout the formation of the AlPO product.

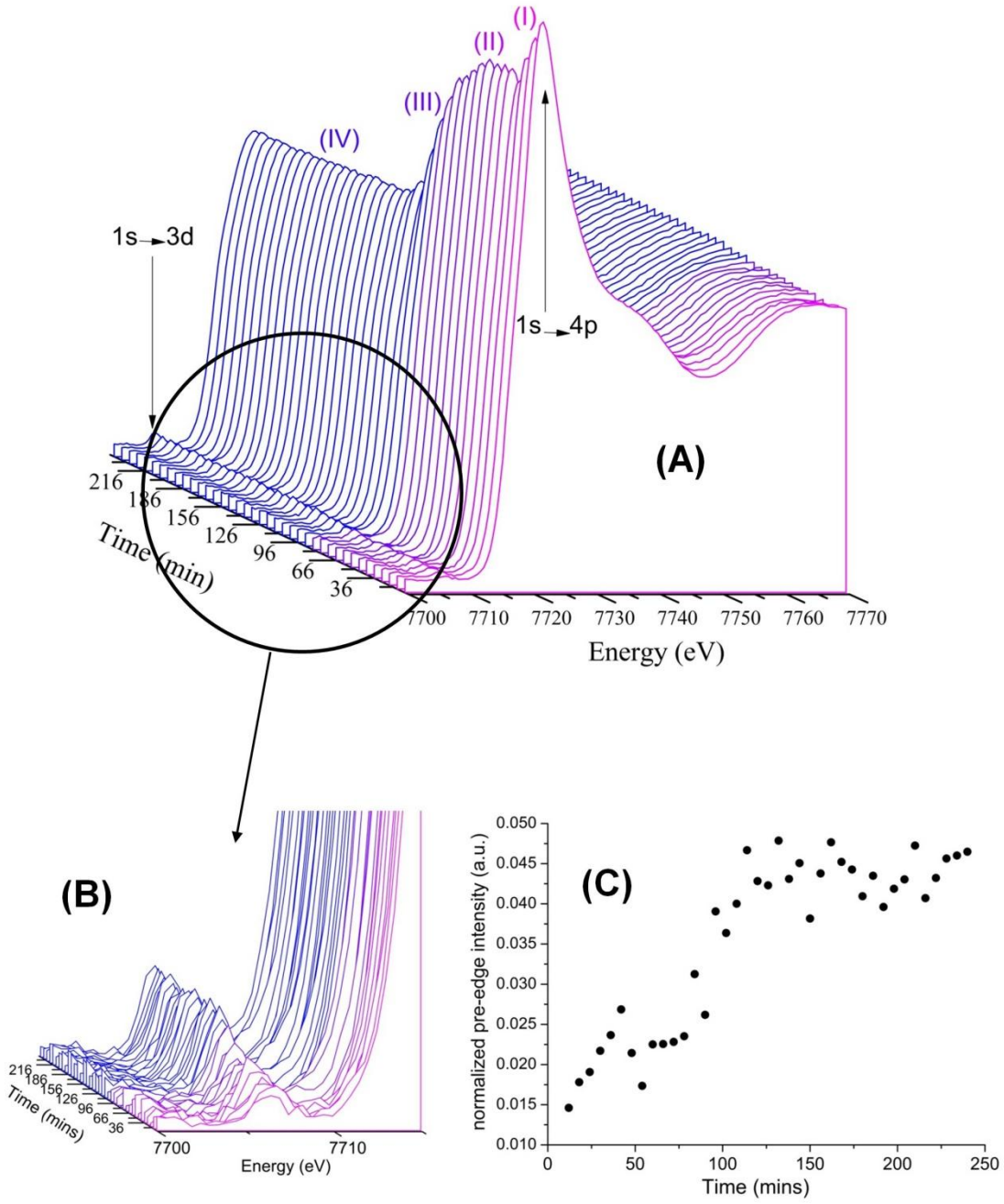

Figure 3.9. *Stacked plot of the normalized Co K-edge XANES data (A) recorded during the crystallization of CoAlPO-5. The pre-edge peak (1s-3d transition) and the white line absorption peak (1s-4p transition) are indicated, along with regions from I-IV. (B) and (C) shows the variation in the normalized pre-edge feature as a function of synthesis time. Data are coloured appropriately based on observations of the gel colour which is associated with the cobalt(II) coordination environment.*

The pre-edge feature, a dipole-forbidden 1s → 3d transition, which is affected by pure electric quadrupole coupling and a change in geometric contribution, can also be examined to follow a change in the coordination environment of the probing atom. A change from a symmetric cobalt(II) octahedral to a non-symmetric tetrahedral environment results in an overlap of the oxygen 2p orbital with the cobalt(II) 3 d orbital, these metal 3d orbital's become more p in character due to the shortening of the bond distances and gives rise to a pre-edge feature in the XANES data[18, 20, 21]. A plot of the normalized pre-edge (7.708keV for cobalt) intensity as a function of time is presented in Figure 3.9(C), and confirms a transition from octahedral to tetrahedral. It should be noted that the small pre-edge feature observed at the onset of the reaction may be due to some distortions around the octahedral Co(II) environment.

The XANES (normalized intensity of the white line feature) and XRD (area under the (210) Bragg reflection) data collected *simultaneously* as a function of synthesis time are shown in Figure 3.10.

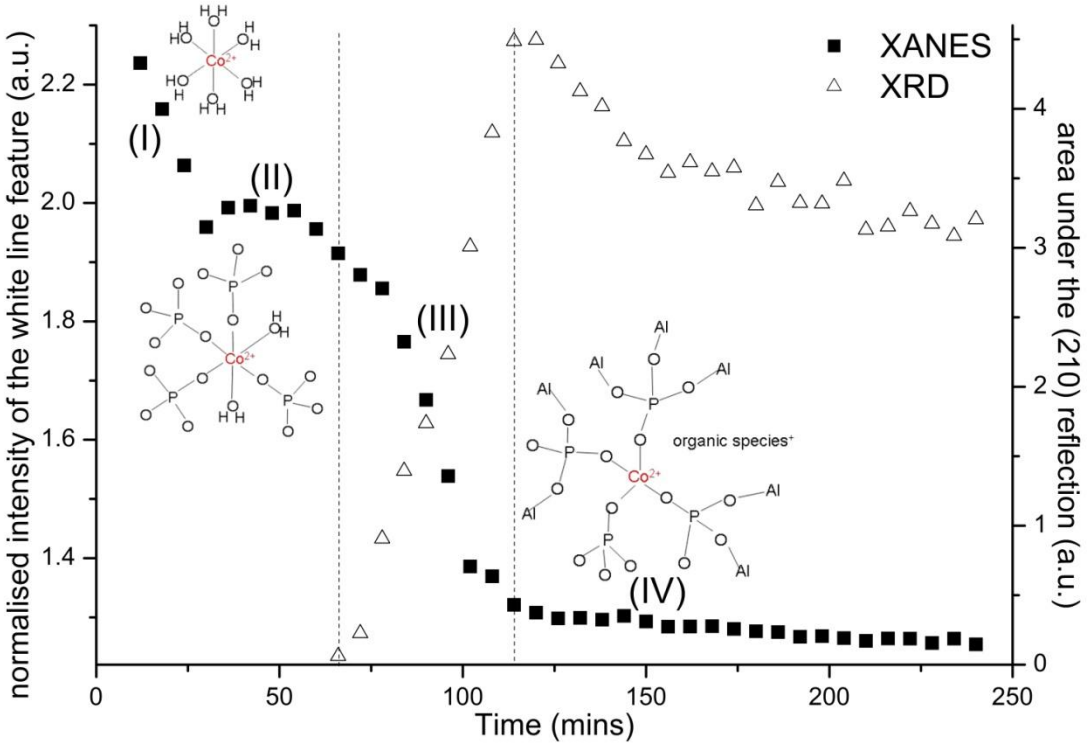

Figure 3.10. *Normalized intensity of the white-line, represented by solid squares (marked 1s→4p in Figure 3.9) and the area under the (210) reflection, symbolized with hollow triangles (indicated in Figure 3.8), are plotted against the synthesis time. The beginning and end of crystallization are marked with a dashed line, respectively, in addition, models of possible molecular species that are formed at different time are shown.*

The results indicate a two stage conversion from octahedral Co(II) ions to tetrahedral coordination. The first stage, a decrease in the intensity of the white line peak (region I), suggests a transformation from regular octahedral coordination, in which the Co(II) ions are surrounded by water molecules, to a less symmetrical, pseudo-octahedral coordination $[CoO_4(H_2O)_2]^{2+}$ or $[CoO_5(H_2O)]^{2+}$ in which some of the coordinating oxygen atoms bridge between two cations (P(V)-O-Co(II)).

Previously such a change in intensity was thought to arise from the presence of a mixture of octahedral and tetrahedral coordination[18, 20]. However, if a direct octahedral-tetrahedral transformation takes place, the intensity would decrease continuously over the reaction time, rather than staying constant for a short period (region II). UV-Vis spectroscopy studies also observed a cobalt(II) pseudo-octahedral species[50].

The second stage, a gradual decrease in the white line intensity (region III), occurs after 66 minutes of the hydrothermal reaction, and indicates the conversion of Co(II) ions in a pseudo-octahedral environment to one with tetrahedral coordination (region IV) in which all the coordinating oxygen atoms bridge between cobalt(II) and phosphorus(V). The changes in the pre-edge intensity also support this two-stage transformation.

These results provide exciting new information about the crystallization mechanism of CoAlPO-5 since this second stage (a transformation from pseudo-octahedral Co(II) to tetrahedral coordination) occurs at the same time that Bragg reflections are observed in the XRD data.

This is in contrast to a previous sequential *in situ* XAS/wide-angle X-ray scattering (WAXS) study by Grandjean et al.[20], who reported that during the crystallization of CoAlPO-5, synthesized with triethylamine as the organic template, cobalt(II) gradually transforms from octahedral to tetrahedral coordination *before* the appearance of Bragg reflections, followed by rapid conversion of any remaining octahedral Co(II) at the onset of crystallization. The main contradictions reside in the

assignment of the intermediate phase to a pseudo-octahedral cobalt(II) species, as is reported here, or as a mixture of octahedral and tetrahedral, which Grandjean et al. have reported. *In situ* UV-Vis studies together with XRD revealed the presence of intermediate pseudo-octahedral Co(II) species in the initial synthesis stages (as mentioned previously), however this study could not distinguish if Co(II) ions converted to tetrahedral coordination just prior to or during crystallization[50].

It is important to note that both the studies referred to above used triethylamine as the organic template, which is well-known to produce a CHA phase as a competing material, under certain conditions[16]. Although the CHA phase was not observed during the crystallization process (within the limits of XRD detection), the use of this template may have a different effect on the Co(II) ions. For example, an *ex situ* XRD/Diffuse Reflectance Spectroscopy (DRS) study[51] on the formation of MeAlPOs observed a pseudo-octahedral Co(II) species during the formation of CoAlPO-5 (AFI), however, this species was not present during the formation of CoAlPO-34 (CHA). This study is unique, since MCHA was used as the organic template in the synthesis, which produces only the AFI structure (over a wide range of pH, temperature and with a variety of metal ions) without any competing phases.

From this *simultaneous* XRD/XANES investigation during the formation of CoAlPO-5, it is possible to suggest a cobalt(II) transformation mechanism; in which octahedral $[Co(H_2O)_6]^{2+}$ species present in the initial gel, transform to pseudo-octahedral $[CoO_4(H_2O)_2]^{2+}$ with some of the oxygen possibily bridging two cations prior to crystallization. These relatively stable intermediate species gradually lose the bonding water molecules concomitant to the formation of the ordered phase

containing tetrahedral framework Co(II) ions. The possible molecular species that may be present at the various stages of the crystallization process are also shown in Figure 3.10. These findings may suggest a possible solid-hydrogel transformation mechanism (re-organization of the solid phase from an amorphous state to one with long-range order) as it is evident that the Co(II) ions are part of solid-phase units in the form of a pseudo-octahedral species.

3.4.2 *In situ* high-resolution X-ray diffraction study of the crystallization of MeAlPO-5

X-ray absorption spectroscopy (XAS) is a good, atom specific, technique for monitoring the coordination environment of dopant ions during the formation of aluminophosphate materials. XAS examines the local structural changes that occur throughout the synthesis process and produces information on cobalt(II) ions in both the amorphous and crystalline phases. As a result, the data collected is an 'average' of the local structure of the cobalt(II) ions observed in both phases. Although the cobalt(II) ions demonstrate the necessary coordination environment (tetrahedral) for their substitution into an aluminophosphate framework, difficulty arises in determining whether all the dopant ions, and to what extent they are substituted into the framework.

X-ray diffraction (XRD), a long-range order technique, produces information on only the crystalline phase, hence, only data relating to the framework. For this reason, the crystallization of CoAlPO-5 (plus ZnAlPO-5), was monitored with high-resolution XRD (HRXRD) and compared to its un-substituted analogue with an aim of deriving more detailed information on the structure with respect to the mechanism of substitution and formation. It should be noted that although the CoAlPO-5 synthesis gel was kept the same as that used in the *in situ* simultaneous XAS/XRD investigation, a temperature of 170°C (*cf.* 160°C) was employed in the HRXRD due to time constraints.

Three-dimensional stacked plots of the HRXRD data of AlPO-5, CoAlPO-5 (5%) and ZnAlPO-5 (5%), as a function of crystallization time are shown in Figure 3.11. All reflections could be indexed to the AFI structure, indicating phase purity irrespective of metal content.

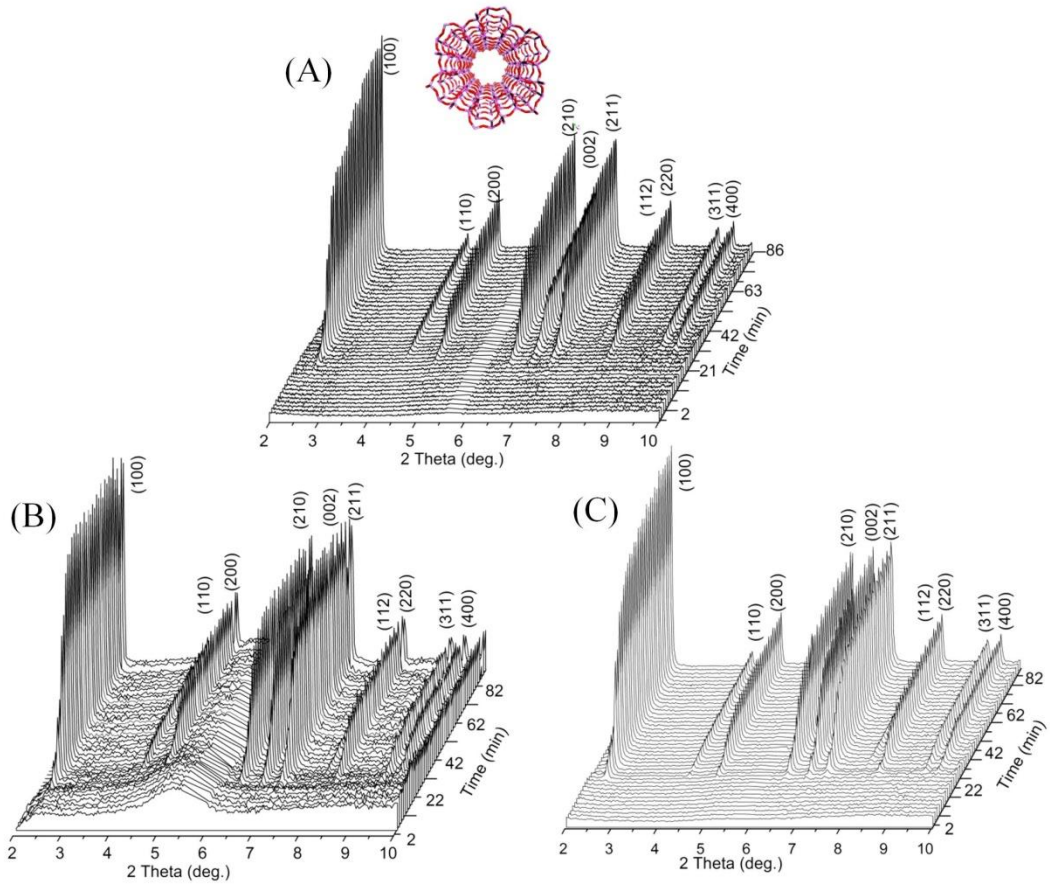

Figure 3.11. *3-D stacked plots of HRXRD data collected during the synthesis of (A) AlPO-5, (B) CoAlPO-5 and (C) ZnAlPO-5. All reflections can be indexed to the AFI structure shown inset. It should be noted that the small amorphous hump observed throughout the synthesis of CoAlPO-5 (B) is due to a higher water amount in the synthesis cell. These XRD datasets were collected at the SNBL beamline of the ESRF employing a wavelength of 0.5 Å.*

The HRXRD data were analyzed in detail employing a fundamental parameter approach (FPA) (FPA uses a convolution-based method to build up X-ray line profiles) to extract not only the crystallite size (Figure 3.12) but also the unit cell parameters of each crystalline AFI phase; the a(=b) and c parameters and the unit cell

volume as a function of crystallization time (Figure 3.13). It should be noted that the a(=b) and c directions are indicated in the structural model of AFI depicted in Figure 3.2. The results yield interesting additional information on the structural aspects during the crystal growth process.

Information on the crystallite size can be obtained from analysis of the full width at half maximum (FWHM) of the observed diffraction reflections (section 2.3.3). Figure 3.12 shows the variation in the crystallite size (Lorentzian component) during the crystallization of AlPO-5, CoAlPO-5 and ZnAlPO-5 as a function of time. Results show that in all three AFI materials, the crystallite size was large at the onset of crystallization, ranging between 80 to 120 nm, and grew by approximately 30 percent during the hydrothermal crystallization.

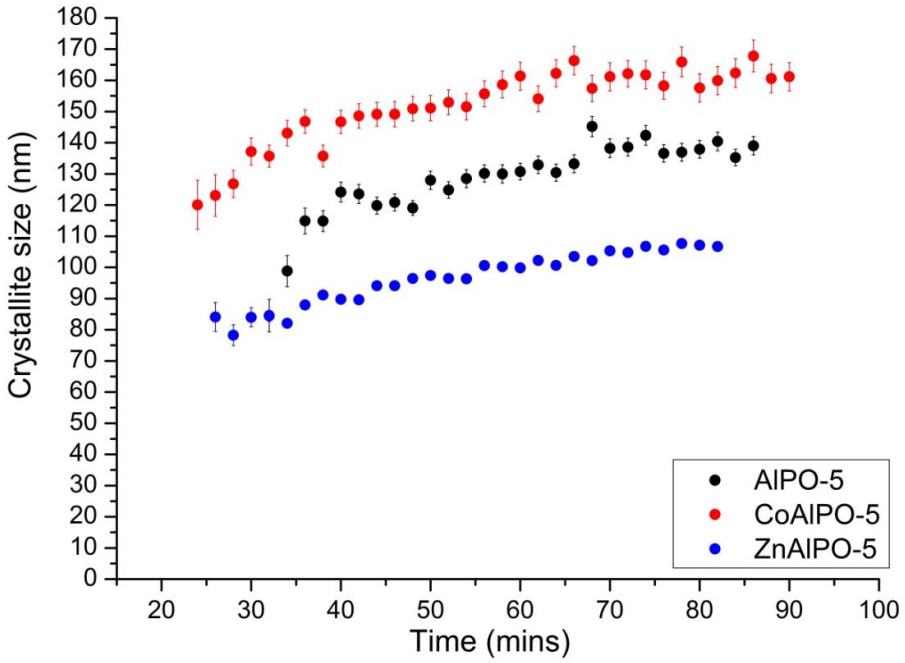

Figure 3.12. *The variation in the crystallite size of the AFI particles is plotted against crystallization time.*

The a(=b) parameter, of all AFI materials, remained relatively constant during the crystallization process and was found to be largest for metal substituted AlPO-5; 13.781 Å (CoAlPO-5) and 13.780 Å (ZnAlPO-5), compared to un-substituted AlPO-5, 13.735 Å. This is indicative of the metal cations substituting for aluminium in the framework. Tetrahedrally coordinated Co(II) and Zn(II) cations have larger ionic radii, 0.58 Å and 0.6 Å respectively, compared to Al(III) which has an ionic radius of 0.39Å[52]; therefore an expansion in the a(=b) direction is observed when a metal ion is substituted into the framework.

On examination of the c parameter at the end of crystallization, surprisingly, it was found to be largest for un-substituted AlPO-5 (8.433 Å) compared to CoAlPO-5

(8.420 Å) and ZnAlPO-5 (8.413 Å). This difference is relatively small (*ca.* 0.01 – 0.02 Å) compared to the difference found in the a(=b) parameter (*ca.* 0.05 Å) however it is unexplainable. The variation in the c parameter over crystallization time was analyzed with an effort in trying to explain the difference found in the c parameter when a metal ion is incorporated into the AFI structure.

The c parameter was found to increase over crystallization time, more predominantly for un-substituted AlPO-5 which increased by 0.019 Å, compared to CoAlPO-5 and ZnAlPO-5, in which only an increase of 0.005 and 0.009 Å was observed in the c parameter, respectively.

The AFI framework is known to be have mild hydrophilicity, in which water molecules either bind to framework Al(III) or are physisorbed and reorientate isotropically within the channels[53, 54]. Recently, through computational methods it has been shown that water molecules reside in the 6-membered ring channels or, with the organic template, in the 12-membered ring channels pointing in the same direction as crystal growth, the c direction[55]. Therefore, this increase in the c parameter, over crystallization time, could be due to be the uptake of water molecules which may coordinate to Al(III) ions accessible in the channel direction, increasing the Al-O bond distance from 1.74 Å for tetrahedral Al(III) up to 1.9 Å for an octahedral environment; the more hydrophilic pure AlPO-5 material would therefore show a larger increase in the c parameter compared to MeAlPO-5. It should be noted that template orientation within the structure could also play a role in this change in c parameter and cell volume.

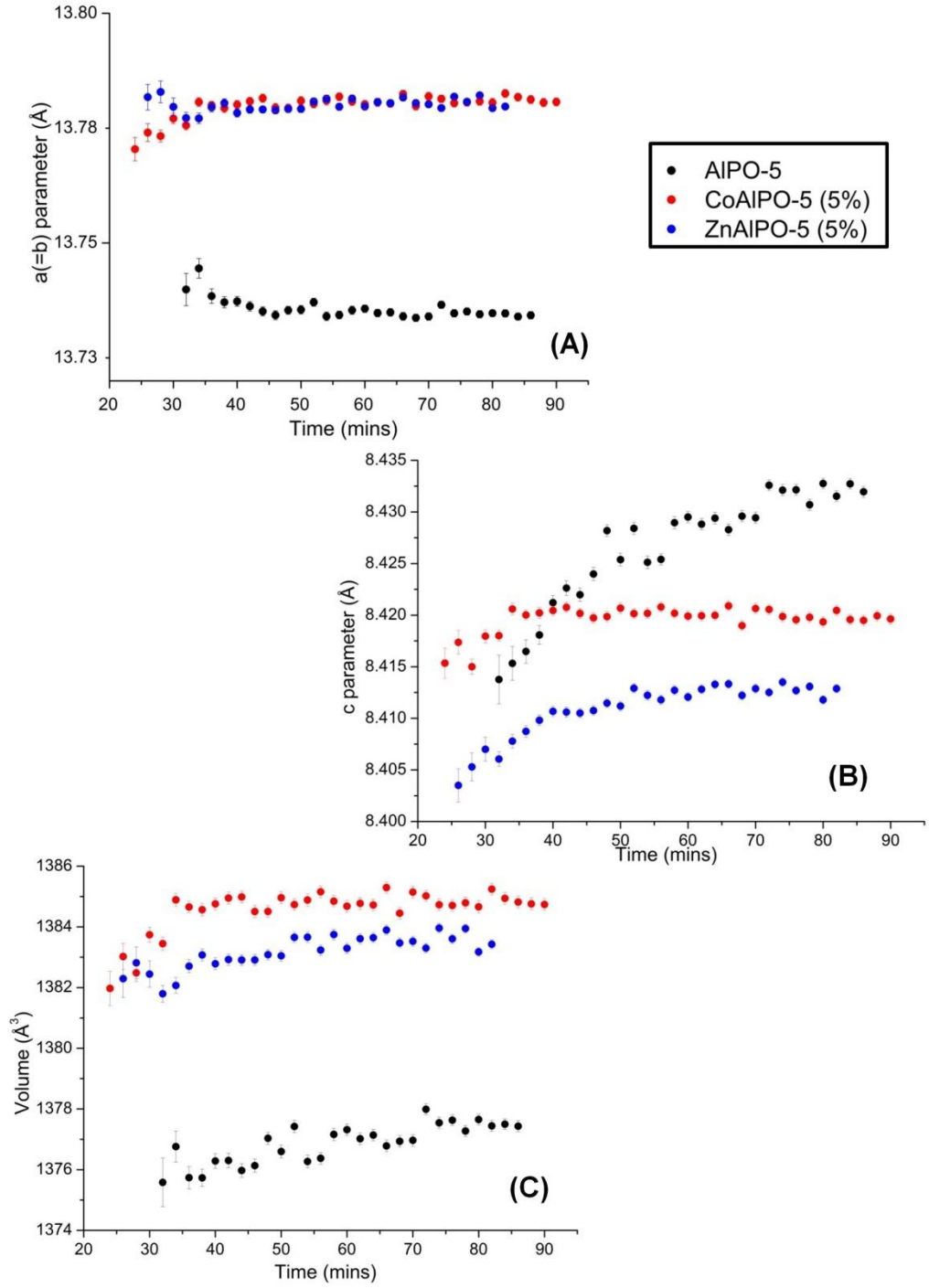

Figure 3.13. *Variation in the a(=b) parameter (A), c parameter (B) and cell volume (C), obtained from HRXRD data as a function of time during the crystallization of CoAlPO-5 (red), ZnAlPO-5 (blue) and AlPO-5 (black). The analysis was performed only on data above ca. 20 minutes, below which the reflections were absent or too few.*

The uptake of water molecules would also explain the differences seen on comparison of the c parameter, at the end of crystallization, in which AlPO-5 was found to have a larger c parameter compared to MeAlPO-5. XRD patterns collected of the dry as-synthesized forms of these AFI-type materials revealed a c parameter decrease with the following trend: MeAlPO-5 > AlPO-5, which is similar to that observed in the a(=b) parameter.

3.4.3 NMR measurements

To further assist the above interpretation of water molecules binding to framework Al(III), ^{27}Al and ^{31}P , plus $\{^{1}H\text{-}^{31}P\}$ cross polarization, NMR spectra were collected for the dried AlPO-5 and ZnAlPO-5 (5%) materials (NMR spectra of CoAlPO-5 was not collected as Co(II) is paramagnetic).

The ^{27}Al NMR spectra are shown in Figure 3.14(A), all give a major signal (with similar intensity) at around 38 ppm which is typical for a tetrahedrally coordinated aluminium Al-O-P environment. This signal is shifted by 1 ppm to 37.5 ppm for the ZnAlPO-5 sample, which suggests the isomorphous substitution of Zn(II) ions for Al(III) in the framework[52, 56]. A smaller signal is also observed in both materials at *ca.* -11 ppm which has been attributed to an octahedral Al environment, in which Al(III) coordinates to four PO_4 tetrahedra and two water molecules[57-59]. This signal was found to be slightly higher in intensity for the un-substituted AFI material,

suggesting that more framework Al(III) ions are coordinated to water molecules in AlPO-5 and may imply the presence of more defects. Indication of the pure AlPO-5 material containing more bound water molecules compared to the metal substituted form becomes even more apparent as an additional signal at *ca.* 16 ppm is observed in the un-substituted AFI material. In the literature this peak has typically been associated to unreacted pseudoboehmite[60], which was not employed in this synthesis, however, it has also been associated with pentacoordinated Al(III) atoms, in which a single water molecule is bound to the framework Al[61, 62].

Figure 3.14(B) displays the ^{31}P direct NMR spectra of the AFI materials, all spectra consist of a main peak at -30 ppm which is characteristic of a tetrahedral P(4Al) environment[62]. Complex multiplets of overlapping peaks ranging from -24 to -5 ppm are also visible in both spectra with a difference in the ZnAlPO-5 materials which has a pronounced feature at -22 ppm. This signal can be attributed to P(3Al, 1Zn)[63], however, as this peak gets significantly enhanced in the $\{^{1}H\text{-}^{31}P\}$ cross polarization spectra (Figure 3.14(C)) it may also have considerable contributions from POH groups and/or the organic species. As the multiplets, between -24 and -5 ppm, get more enhanced in the $\{^{1}H\text{-}^{31}P\}$ cross polarization spectra of ZnAlPO-5; it is also clear that either the organic species interacts more strongly with the AFI framework or there are more POH defects (or a combination of both) in the ZnAlPO-5 material compared to un-substituted AlPO-5.

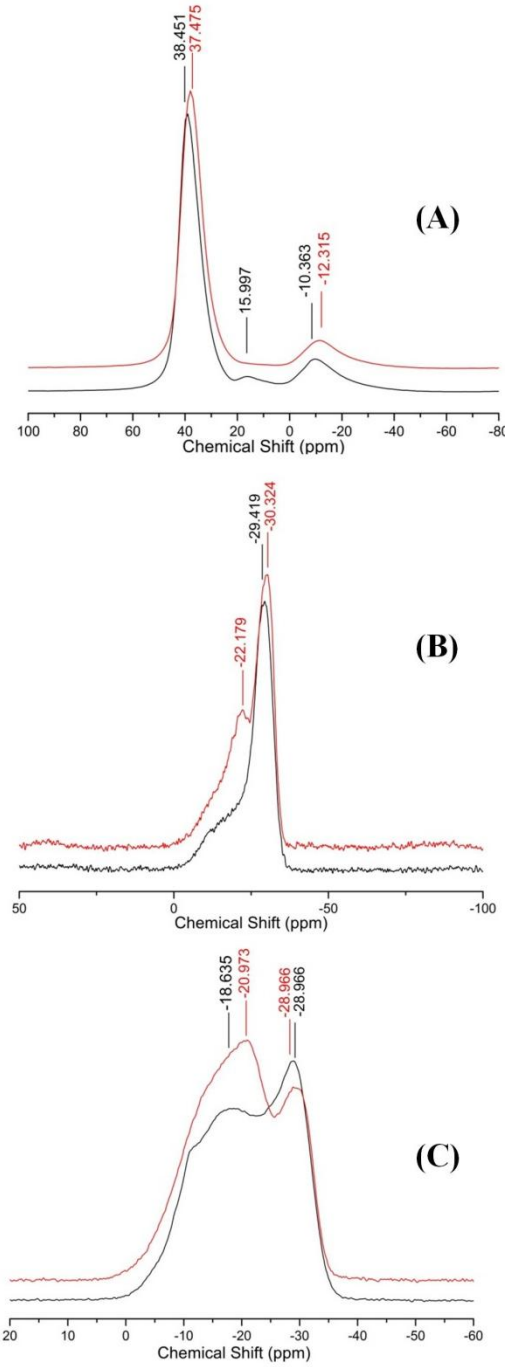

Figure 3.14. *Showing ^{27}Al MAS-NMR (A), ^{31}P direct (B) and {^{1}H-^{31}P} cross polarization (C) NMR spectra collected for AlPO-5 (black) and ZnAlPO-5 (red).*

3.4.4 TGA measurements

Thermogravimetric analysis (TGA) equipped with a mass spectrometer was ascertained to determine the nature of various loosely bound species and to further quantify the amount of chemically attached water within the AFI materials.

Figure 3.15 shows the TGA data recorded (in helium) for the AlPO-5 and CoAlPO-5 (5%) as synthesised materials. Two different weight losses were observed in both materials; an exotherm at temperatures below 200 °C and a second in the region 250 < T < 460 °C. This multi-step lost has been observed many times before for aluminophosphate materials [55, 64].

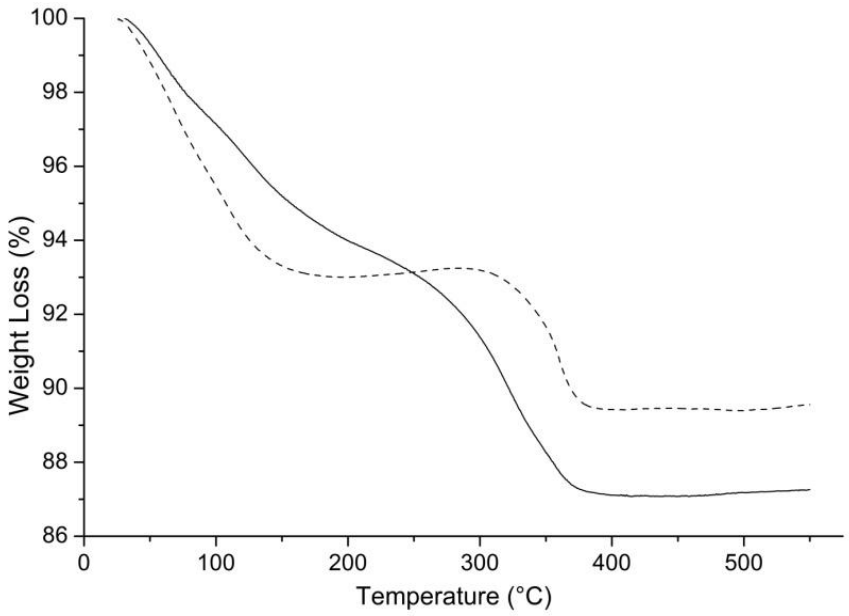

Figure 3.15. *TGA results of the as-synthesized AlPO-5 (solid line) and CoAlPO-5 (dashed line) materials in helium.*

The evolving gases were chemically analysed through mass spectrometry. The first loss in the TGA data was found to coincide with the detection of H_2O molecules; the loss of surface and framework water, whereas the second is associated with the decomposition and desorption of the occluded organic template molecule. The normalized TGA mass spectra of AlPO-5 and CoAlPO-5 are shown in Figure 3.16 (normalized to the sample mass).

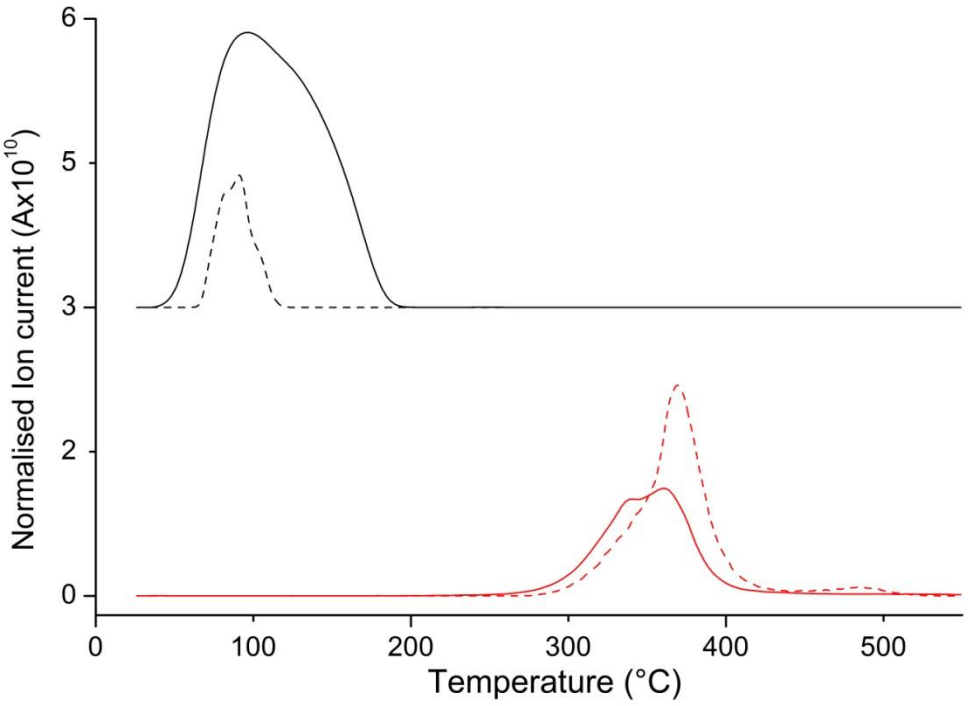

Figure 3.16. *Normalized TGA mass spectra of AlPO-5 (solid lines) and CoAlPO-5 (dashed lines) in helium. Desorption of water (monitored my m/z 18) is displayed in black and desorption of the organic template (monitored by m/z 41) is displayed in red.*

On comparison of the un-substituted material with CoAlPO-5, it is clear that there is a higher amount of water loss from the AlPO-5 structure (approximately 6 times), confirming that there is a larger uptake of water molecules in the more hydrophilic AlPO-5 material. These water molecules desorb from the pure AlPO-5 material over a wider range of temperature. Similarly the organic template is found to decompose and desorb over a wider range of temperature, 265 – 420 °C, in AlPO-5 compared to CoAlPO-5. It should be noted that both AFI materials had an equivalent amount of template desorbing from their structure.

3.5 Summary and Conclusions

The formation of cobalt substituted AlPO-5 catalyst was monitored, for the first time, through *simultaneous* XRD/XAS. Results showed cobalt transforming from octahedral to framework tetrahedral via a pseudo-octahedral intermediate. More importantly, the second stage occurred simultaneously with the appearance of Bragg peaks in the diffraction data.

Structure analysis of HRXRD data collected during the crystallization of CoAlPO-5 was performed and the results compared to ZnAlPO-5 and pure AlPO-5. A study of the change in the a(=b) parameters over time revealed that Co(II) ions substitute into the AFI framework. The c parameter was found to differ to the a(=b) parameter in that it increased over crystallization time for all AFI materials. This was explained through additional NMR and TGA studies. These investigations showed that the uptake of water molecules to Al(III) ions in the channel system, leads to an expansion of the unit cell in the c direction.

Overall, by combining the information obtained from these different techniques it is possible to derive a mechanism and a crystallization model for the formation of CoAlPO-5. The HRXRD result coupled with the simultaneous XRD/XAS investigation indicates that CoAlPO-5 material is formed via a solid hydrogel transformation mechanism. In this mechanism it is believed that the structure of the molecular sieve material is obtained by reorganization of the framework of solid

phase aluminophosphate hydrogel formed from the condensation of phosphate and aluminate ions in the early stages of crystallization[65].

The crystallographic a(=b) parameter is large even at the onset of phase formation (compared to un-substituted AlPO-5) and remained constant throughout the reaction, indicating that the cobalt(II) ions are part of the solid-phase network prior to crystallization and it is unlikely the Co(II) ions are incorporated into the structure from solution phase. This is also supported by evaluation of the crystallite size over time, which revealed the formation of large particles at the onset of crystallization.

A schematic illustration of the mechanism of formation and substitution of cobalt(II) into the AFI structure is given in Figure 3.17. It is generally accepted that the synthesis gel consists of AlO_4 and PO_4 tetrahedrons which form a 1D chain unit[22, 66-68], along with a $[Co(H_2O)_6]^{2+}$ species. The octahedral Co(II) transforms to a $[CoO_4(H_2O)_2]^{2+}$ or $[CoO_5(H_2O)]^{2+}$ species, in which some of the coordinating oxygen atoms bridge between two cations (P(V)-O-Co(II)). At the onset of crystallization, Co(II) ions start to lose the bound water molecules to form a tetrahedral environment and, simultaneously, water molecules bind to Al(III) ions accessible in the channels. The majority of these water molecules bound to the Al(III) ions are then lost upon dehydration of the solid. A solid hydrogel transformation mechanism and similar phenomena have previously been observed in zeolite and aluminophosphate synthesis[30].

In relation to other divalent metal substituted AFI materials, such as ZnAlPO-5, the unit cell parameters were found to have the same trend over crystallization time,

indicating a similar mechanism of formation. Although, XAS does not provide additional supporting information on the zinc ion incorporation, Zn(II) ions adopt a tetrahedral coordination environment in the synthesis gel. This study has shown that HRXRD can be a very powerful tool in elucidating information on the crystallization mechanism.

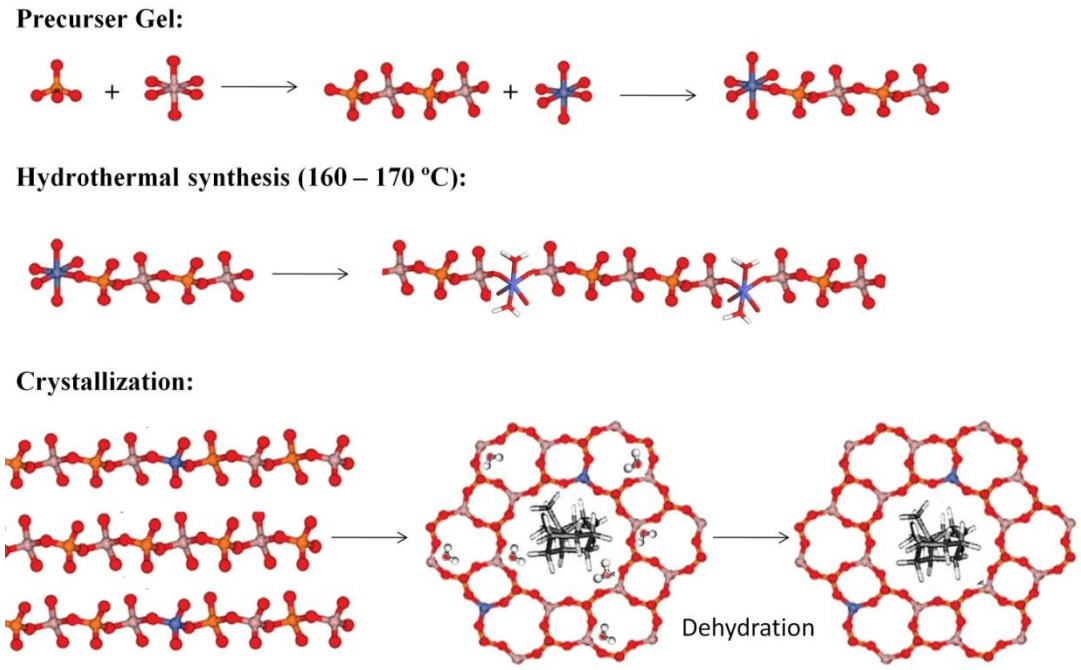

Figure 3.17. *A schematic illustration of the formation of CoAlPO-5; Co(II) = blue, P(V) = orange, Al(III) = light pink, O = red, H = white. The organic template is shown in grey scale. Adapted from reference*[22].

3.6 References

[1] Walton, R. I.; O'Hare, D., *Chemical Communications*, (2000), 2283.

[2] Cundy, C. S.; Cox, P. A., *Microporous and Mesoporous Materials*, (2005) **82**, 1.

[3] Cundy, C. S.; Cox, P. A., *Chemical Reviews*, (2003) **103**, 663.

[4] Byrappa, K.; Yoshimura, M., *Handbook of Hydrothermal Technology*, McGuire, G. E.; Rossnagel, S. M. Eds.; William Andrew Publishing: Norwich, (2001).

[5] *Chemistry of Zeolites and Related Porous Materials - Synthesis and Structure*, Xu, R.; Pang, W.; Yu, J.; Huo, Q.; Chen, J. Eds.; John Wiley & Sons: Singapore, (2007).

[6] Yan, W.; Song, X.; Xu, R., *Microporous and Mesoporous Materials*, (2009), 50.

[7] Lechert, H., *Zeolites*, (1996) **17**, 473.

[8] Weyda, H.; Lechert, H., *Zeolites*, (1990) **10**, 251.

[9] Shi, J. M.; Anderson, M. W.; Carr, S. W., *Chemistry of Materials*, (1996) **8**, 369.

[10] Shigemoto, N.; Sugiyama, S.; Hayashi, H.; Miyaura, K., *Journal of Materials Science Letters*, (1994) **13**, 660.

[11] Norby, P., *Current Opinion in Colloid & Interface Science*, (2006) **11**, 118.

[12] Walton, R. I.; Smith, R. I.; O'Hare, D., *Microporous and Mesoporous Materials*, (2001) **48**, 79.

[13] Kongmark, C.; Martis, V.; Rubbens, A.; Pirovano, C.; Lofberg, A.; Sankar, G.; Bordes-Richard, E.; Vannier, R.-N.; Van Beek, W., *Chem Commun (Camb)*, (2009), 4850.

[14] O'Brien, M. G.; Beale, A. M.; Catlow, C. R. A.; Weckhuysen, B. M., *Journal of the American Chemical Society*, (2006) **128**, 11744.

[15] Barnes, P., *Journal of Physics and Chemistry of Solids*, (1991) **52**, 1299.

[16] Rey, F.; Sankar, G.; Thomas, J. M.; Barrett, P. A.; Lewis, D. W.; Catlow, C. R. A.; Clark, S. M.; Greaves, G. N., *Chemistry of Materials*, (1995) **7**, 1435.

[17] Hooper, D.; Barnes, P.; Cockcroft, J. K.; Jupe, A. C.; Jacques, S. D. M.; Bailey, S. P.; Lupo, F.; Vickers, M.; Hanfland, M., *Physical Chemistry Chemical Physics*, (2003) **5**, 4946.

[18] Sankar, G.; Thomas, J. M.; Rey, F.; Greaves, G. N., *Journal of the Chemical Society-Chemical Communications*, (1995), 2549.

[19] Sankar, G.; Bras, W., *Catalysis Today*, (2009) **145**, 195.

[20] Grandjean, D.; Beale, A. M.; Petukhov, A. V.; Weckhuysen, B. M., *Journal of the American Chemical Society*, (2005) **127**, 14454.

[21] Dong, M.; Wang, G. F.; Qin, Z. F.; Wang, J. G.; Liu, T.; Yuan, S. P.; Jiao, H. J., *Journal of Physical Chemistry A*, (2007) **111**, 1515.

[22] Beale, A. M.; van der Eerden, A. M. J.; Grandjean, D.; Petukhov, A. V.; Smith, A. D.; Weckhuysen, B. M., *Chemical Communications*, (2006), 4410.

[23] Sankar, G.; Thomas, J. M.; Catlow, C. R. A., *Topics in Catalysis*, (2000) **10**, 255.

[24] Couves, J. W.; Thomas, J. M.; Waller, D.; Jones, R. H.; Dent, A. J.; Derbyshire, G. E.; Greaves, G. N., *Nature*, (1991) **354**, 465.

[25] Clausen, B. S.; Topsoe, H.; Frahm, R., Application of combined X-ray diffraction and absorption techniques for in situ catalyst characterization, In *Advances in Catalysis, Vol 42*, (1998); Vol. 42, pp 315.

[26] Clausen, B. S.; Grabaek, L.; Steffensen, G.; Hansen, P. L.; Topsoe, H., *Catalysis Letters*, (1993) **20**, 23.

[27] Davies, M. E.; Lobo, R. F., *Chemistry of Materials*, (1992) **4**, 756.

[28] Ueda, S.; Kageyama, W.; Koizumi, M., In *6th International Zeolite Conference*, Olson, D.; Bidio, A. Eds.; Buttersworths, Guildford, (1984); Vol. 905.

[29] Zhdanov, S. P., *Adv. Chem. Ser.*, (1971) **101**, 20.

[30] Xu, W.; Li, J.; Li, W.; Zhang, H.; Liang, B., *Zeolites*, (1989) **9**, 468.

[31] Arends, I.; Sheldon, R. A.; Wallau, M.; Schuchardt, U., *Angewandt Chemie-International Edition in English*, (1997) **36**, 1144.

[32] Hartmann, M.; Kevan, L., *Chemical Reviews*, (1999) **99**, 635.

[33] Wilson, S. T.; Flanigen, E. M., *Acs Symposium Series*, (1989) **398**, 329.

[34] Liu, Y.; Withers, R. L.; Noren, L., *Solid State Sciences*, (2003) **5**, 427.

[35] Weiss, O.; Ihlein, G.; Schuth, F., *Microporous and Mesoporous Materials*, (2000) **35-6**, 617.

[36] Bennett, J. M.; Cohen, J. P.; Flanigen, E. M.; Pluth, J. J.; Smith, J. V., *Acs Symposium Series*, (1983) **218**, 109.

[37] Sanchez-Sanchez, M.; Sankar, G.; Simperler, A.; Bell, R. G.; Catlow, C. R. A.; Thomas, J. M., *Catalysis Letters*, (2003) **88**, 163.

[38] Barrett, P. A.; Sankar, G.; Catlow, C. R. A.; Thomas, J. M., *Journal of Physical Chemistry*, (1996) **100**, 8977.

[39] Sankar, G.; Raja, R.; Thomas, J. M., *Catalysis Letters*, (1998) **55**, 15.

[40] Baerlocher, C.; McCusker, L. B., Database of Zeolite Structures. http://www.iza-structure.org/databases/, In.

[41] Norby, P.; Hanson, J. C., *Catalysis Today*, (1998) **39**, 301.

[42] Davies, A. T.; Sankar, G.; Catlow, C. R. A.; Clark, S. M., *Journal of Physical Chemistry B*, (1997) **101**, 10115.

[43] Klap, G. J.; van Koningsveld, H.; Graafsma, H.; Schreurs, A. M. M., *Microporous and Mesoporous Materials*, (2000) **38**, 403.

[44] BM01 beamline, In *ESRF*, Grenoble, France, (2009).

[45] Ravel, B.; Newville, M., *Journal of Synchrotron Radiation*, (2005) **12**, 537.

[46] JCPDS, International Centre for Diffraction Data PDF-2, In (1997-2010).

[47] Treacy, M. M. J.; Higgins, J. B., *Collection of Simulated XRD Powder Diffraction Patterns for Zeolites*, Elsevier: Amsterdam, (2007).

[48] Software, C., TOPAS-Academic Version 4.1, In Coelho, A. Ed. Brisbane, Australia, (2007).

[49] OriginLab, OriginPro 8 SRO, In Northampton, USA, (1991-2007).

[50] Weckhuysen, B. M.; Baetens, D.; Schoonheydt, R. A., *Angewandte Chemie-International Edition*, (2000) **39**, 3419.

[51] Weckhuysen, B. M.; Rao, R. R.; Martens, J. A.; Schoonheydt, R. A., *European Journal of Inorganic Chemistry*, (1999), 565.

[52] Akolekar, D. B., *Applied Catalysis a-General*, (1998) **171**, 261.

[53] Goldfarb, D.; Li, H. X.; Davis, M. E., *Journal of the American Chemical Society*, (1992) **114**, 3690.

[54] Pillai, R. S.; Jasra, R. V., *Langmuir*, (2010) **26**, 1755.

[55] Gomez-Hortiguela, L.; Perez-Pariente, J.; Cora, F., *Chemistry-a European Journal*, (2009) **15**, 1478.

[56] Fan, W. B.; Fan, B. B.; Song, M. G.; Chen, T. H.; Li, R. F.; Dou, T.; Tatsumi, T.; Weckhuysen, B. M., *Microporous and Mesoporous Materials*, (2006) **94**, 348.

[57] Blackwell, C. S.; Patton, R. L., *Journal of Physical Chemistry*, (1984) **88**, 6135.

[58] Deng, F.; Yue, Y.; Xiao, T. C.; Du, Y. U.; Ye, C. H.; An, L. D.; Wang, H. L., *Journal of Physical Chemistry*, (1995) **99**, 6029.

[59] Muller, D.; Grunze, I.; Hallas, E.; Ladwig, G., *Zeitschrift Fur Anorganische Und Allgemeine Chemie*, (1983) **500**, 80.

[60] Gomez-Hortiguela, L.; Blasco, T.; Perez-Pariente, J., *Microporous and Mesoporous Materials*, (2007) **100**, 55.

[61] Akolekar, D. B.; Howe, R. F., *Journal of the Chemical Society-Faraday Transactions*, (1997) **93**, 3263.

[62] Zibrowius, B.; Loffler, E.; Hunger, M., *Zeolites*, (1992) **12**, 167.

[63] Rakoczy, R. A.; Ernst, S.; Hartmann, M.; Traa, Y.; Weitkamp, J., *Catalysis Today*, (1999) **49**, 261.

[64] Zenonos, C.; Sankar, G.; Cora, F.; Lewis, D. W.; Pankhurst, Q. A.; Catlow, C. R. A.; Thomas, J. M., *Physical Chemistry Chemical Physics*, (2002) **4**, 5421.

[65] Xu, P.; Pang, W.; Huo, Q.; Chem, J., *Chemistry of Zeolites and Related Porous Materials - Synthesis and Structure,* John Wiley and sons Ltd.: Singapore, (2007).

[66] Yu, J. H.; Xu, R. R., *Accounts of Chemical Research*, (2003) **36**, 481.

[67] Adair, B. A.; Neeraj, S.; Cheetham, A. K., *Chemistry of Materials*, (2003) **15**, 1518.

[68] Ayi, A. A.; Neeraj, S.; Choudhury, A.; Natarajan, S.; Rao, C. N. R., *Journal of Physics and Chemistry of Solids*, (2001) **62**, 1481.

Chapter 4. A study on the kinetics of formation and the metastability of large pore aluminophosphates

4.1 Chapter Overview

This chapter discusses the results obtained from a kinetic study on the formation and metastability of AlPO-5 catalysts. An *in situ* synchrotron high-resolution X-ray diffraction (HRXRD) investigation on the kinetic effect of inorganic metal ions on the competitive phase formation of AFI type materials revealed preferred nucleation of the CHA phase over the AFI phase when Zn(II) ions are present with tetraethylammonium hydroxide (TEAOH) as the organic template. This suggests that Zn(II) ions promote denser rings and 'pockets' in AlPO materials as these are absent from the AFI structure. In addition, the effect of cobalt(II) concentration on the kinetic formation of pure phase CoAlPO-5 was studied and revealed that as the metal ion concentration increases above 6 wt %, the induction period increases and the crystallization rate decreases. Finally, through an *ex situ* Lab XRD study on the decomposition of AFI materials in their reaction medium, a new approach was proposed to correlate the ability to form the most metastable AlPO-5 structure with framework-template interactions, which can also be applied in general to the synthesis of other template microporous materials.

4.2 Introduction

The hydrothermal synthesis of aluminophosphates (AlPOs) and other molecular sieve materials can be described as a "black art" due to the type of structure formed depending on the control of a large number of reaction variables, including; reactant gel composition and type, time, temperature, pressure (reaction cell fill volume), pH, type of cation used (organic and/or inorganic), history-dependent factors (ageing, stirring, nature of mixing and order of mixing), and so on. Most of these reaction variables are not independent of one another, which leads to great difficulty in evaluating the effect of varying any one of them. Therefore a greater understanding of the reaction pathway and kinetics would be desirable as it could lead to a more rational approach in the synthesis of new molecular sieves.

The kinetic control of the formation of AlPOs and other zeotype materials is of vital importance in the synthesis of these materials as it is well known that these microporous materials are metastable in the reaction medium and are not true thermodynamic products. In addition, their formation may follow Ostwald's Law of Successive Transformations which states that an unstable system may transform into another transient, state whose formation from the original is accompanied by the smallest loss of free energy, before forming the most thermodynamically favorable product[1, 2]. For example, the synthesis of zeolite ZSM-4 (MAZ) with TEA as the organic template, results in the formation of the kinetically favoured Faujisite (FAU) material at short times, which transforms into the MAZ phase and finally the

thermodynamically most stable dense oxide phase over a very long reaction time. At present, the observation of one kinetically favoured structure transforming to another kinetic product has not been seen in the synthesis of AlPOs, and in general, it is known that AlPO materials transform to the dense thermodynamically favourable tridymite or berlinite phase[3]. The hydrothermal synthesis of AlPOs has therefore been centred on optimizing the reaction conditions for the isolation of the desired microporous material. It should be noted that although the metastable phase precedes the more stable successors, if the metastable phase is isolated from the reaction medium it can remain unchanged indefinitely thereafter.

In a typical lab autoclave approximately 3 grams of AlPO material can be formed in a 30 ml Teflon liner, with a 60% fill. For the use of AlPO catalysts at an industrially scale this synthesis procedure requires scale-up, therefore, knowledge of the kinetics of formation of AlPOs is highly desirable so that the synthetic route to the required product is reliable and reproducible to the same specification[1]. To achieve this goal, both practical (such as yield, purity, reproducibility, particle size, colour and catalytic performance) and fundamental (for instance solubility, nucleation rate and growth rate) parameters need to be considered which often influence the choice of starting reagents, such as organic template or type of divalent metal ion. In addition, the reagent choice (in particular the organic template) may affect the cost and ease of processing and could offer an optimum route to a particular structure. Therefore the effect of reagent choice on both the practical and fundamental parameters would be beneficial in the improvement of AlPO synthesis.

4.2.1 Aims and objectives

In situ synchrotron radiation has been found to be essential in accurately and reliably studying the kinetics of AlPO formation and in evaluating the nucleation and growth rates[4]. Diffraction, in particular, is an efficient way of studying the crystallization kinetics as it only provides information on the crystalline phase[5]. Therefore, this study investigated the effect of divalent metal ions and organic cations on the kinetics of formation of AlPOs by *in situ* high-resolution X-ray diffraction (HRXRD). However, it should be noted that the nucleation stage of AlPO synthesis cannot be directly probed by this technique, this is due to the material possessing no long-range order.

This work reports on the large-pore AFI structure (described in 3.2.1) as a large number of heteroatoms can be easily incorporated into the framework and it can be synthesized from over 25 organic templates. In particular, the kinetics of MeAlPO-5 formation with tetraethylammonium hydroxide (TEAOH) or *N*-methyldicyclohexylamine (MCHA) was investigated to ascertain the competitive phase formation between AFI and CHA structures and phase purity formation of the AFI structure, respectively.

A previous investigation on the kinetics of CoAlPO-5 formation found differences in the kinetic trend depending on the cobalt concentration; with a low cobalt concentration, the induction period decreases and the rate of crystallisation increases, however with a cobalt concentration above 6 weight %, this trend is reversed[6]. This

was attributed to the presence of the CHA phase which can form with cobalt concentrations above 4 wt % and in the presence of organic templates such as TEAOH or triethylamine (TEA). Therefore, the aim of this study was to investigate the effect of divalent metal ion concentration on the kinetics of CoAlPO-5 formation but with MCHA as the template as this organic species is known to have the highest specificity to form the AFI structure over a wide range of synthesis conditions[7] with no impurities from other AlPO phases.

In addition to the kinetics of formation, the metastability of AFI materials was investigated based on the incorporation of a divalent metal ion and the type of organic template utilized. *Ex situ* measurements are at a disadvantage to *in situ* as they may involve systematic errors and the loss or gain of intermediate phases upon the wash, filter and drying stages. However, due to the long reaction times required to follow the decomposition of the AFI materials in the reaction medium and the lack of synchrotron beam time, *ex situ* lab XRD was employed to study the AFI metastability up to a synthesis time of 1 week.

4.3 Experimental

4.3.1 Synthetic procedure

There are a variety of procedures which have been developed for the synthesis of high quality AFI-type materials [8-18]. The synthesis procedure (described below) employed was based on work carried out by Sankar et al.[6] on the optimum conditions to produce pure phase highly crystalline AlPO-5 crystals, with some modifications applied such as the type of organic template utilized.

A range of synthesis gels with the general composition, **1.5 P: (1-*x*) Al: *x* Me: 25 H_2O: 0.8 *R***, were prepared, where Me is a divalent metal ion source and *R* is an organic amine or quaternary ammonium cation (template). The divalent metal ion concentration ranged from $x = 0$ (un-substituted AlPO-5) to $x = 0.15$ (15 wt %) depending on the investigation, with either cobalt(II) or zinc(II) as the metal ion. AFI materials can be synthesized with over 25 different organic templates. In this study; either *N*-methyldicyclohexylamine (MCHA), triethylamine (TEA) or tetraethylammonium hydroxide (TEAOH) was employed as the structure directing agents. In particular, MCHA is known to have the highest specificity to direct the synthesis of the AFI structure[7] and TEAOH has been found to have the strongest ability to form the AlPO-5 framework due to strong nonbonding framework-template interactions[19].

In all synthesis procedures, the starting materials were aluminium hydroxide hydrate, $Al(OH)_3 \cdot xH_2O$, (Aldrich); 85 wt % in water phosphoric acid solution, H_3PO_4 (Aldrich); distilled water; cobalt(II) acetate tetrahydrate, $(CH_3COO)_2Co \cdot 4H_2O$ (Aldrich); zinc(II) acetate dihydrate, $Zn(CH_3COO)_2 \cdot 2H_2O$ (Aldrich); 97 wt% MCHA, $(C_6H_{11})_2NCH_3$, (Aldrich); 35 wt % in water of TEAOH solution, $(C_2H_5)_4N(OH)$, (Aldrich) and >99 wt % TEA, $(C_2H_5)_3N$ (Sigma-Aldrich). Where necessary, the dilution of the precursor, in particular the organic template, in their commercially available form was taken into consideration when calculating the amount of distilled water required.

The precursor gel was prepared by firstly dissolving the metal acetate in a minimum amount of distilled water. The remaining water was then added (in the case of pure AlPO-5, all 25 moles of water were added) to phosphoric acid, along with the aluminium hydroxide hydrate, and stirred vigorously by hand in a PTFE beaker until homogeneous (approximately 15 minutes). The dissolved metal acetate solution was added followed by the organic template and stirring continued for a further 30 minutes. Finally, the pH of the gel was measured using universal pH paper. Unless stated, the pH was kept at 7 which allowed for the competitive phase formation between AFI and CHA structures when TEAOH was employed as the organic template. For the metastability study of the effect of organic template on the decomposition of the AFI framework, pH 5 was used since at this pH only phase pure AlPO-5 forms at 3 hours synthesis time for all three templates.

The resulting precursor gels were then added to either a specially designed *in-situ* synthesis cell (described in section 3.3.2.1) for *in situ* characterization or a standard

Teflon-lined steel Lab autoclave for *ex situ* characterization, with an approximate 60% fill volume. The gels were heated at set temperatures between 160-175 ºC for an appropriate amount of time. For *ex situ* characterization, the samples were washed filtered and dried at 80°C overnight.

4.3.2 *In situ* High resolution X-ray diffraction

4.3.2.1 SNBL beamline

High resolution *in situ* X-ray diffraction (HRXRD) studies were performed on the BM01b Swiss-Norwegian beamline (SNBL) of the European Synchrotron Radiation Facility (ESRF) in Grenoble, France. Details of the beamline and diffractometer are given in section 3.3.2.3. HRXRD patterns were collected at 170 ºC and at a fixed wavelength of 0.5 Å. The duration of each data collection was tuned with the reaction speed in which the optimized collection period was found to be 2 minutes to cover a 2-theta range of 2-10º (2.89 to 11.89 d-spacing). High-resolution powder diffraction data were collected in both directions of movement from low to high 2θ and vice versa.

4.3.2.2 I11 beamline

HRXRD data was also collected at the I11 beamline of the Diamond Light Source in Oxford, England[20]. The schematic set-up of the beamline is shown in Figure 4.1 which makes use of a collimator, Si(111) monochromator (mono), Harmonic rejection mirrors (HR mirrors) and a number of slits. The I11 beamline is equipped with 5 MAC detectors (which scan positive angles) and a position sensitive detector (PSD). The experiments described in this chapter were time-resolved, therefore the PSD detector was employed as data can be collected in a shorter time scale compared to the MAC detector. Although the PSD detector has a 90° aperture, due to the geometry of the cell, only data in the region of 2.5° to 40° 2θ was possible, which was adequate for the purpose of this study. Data was collected at $\lambda = 0.82743$ Å with a time acquisition of 15 seconds resulting in 4 scans per minute, with two aluminium filters to avoid saturation of the detector.

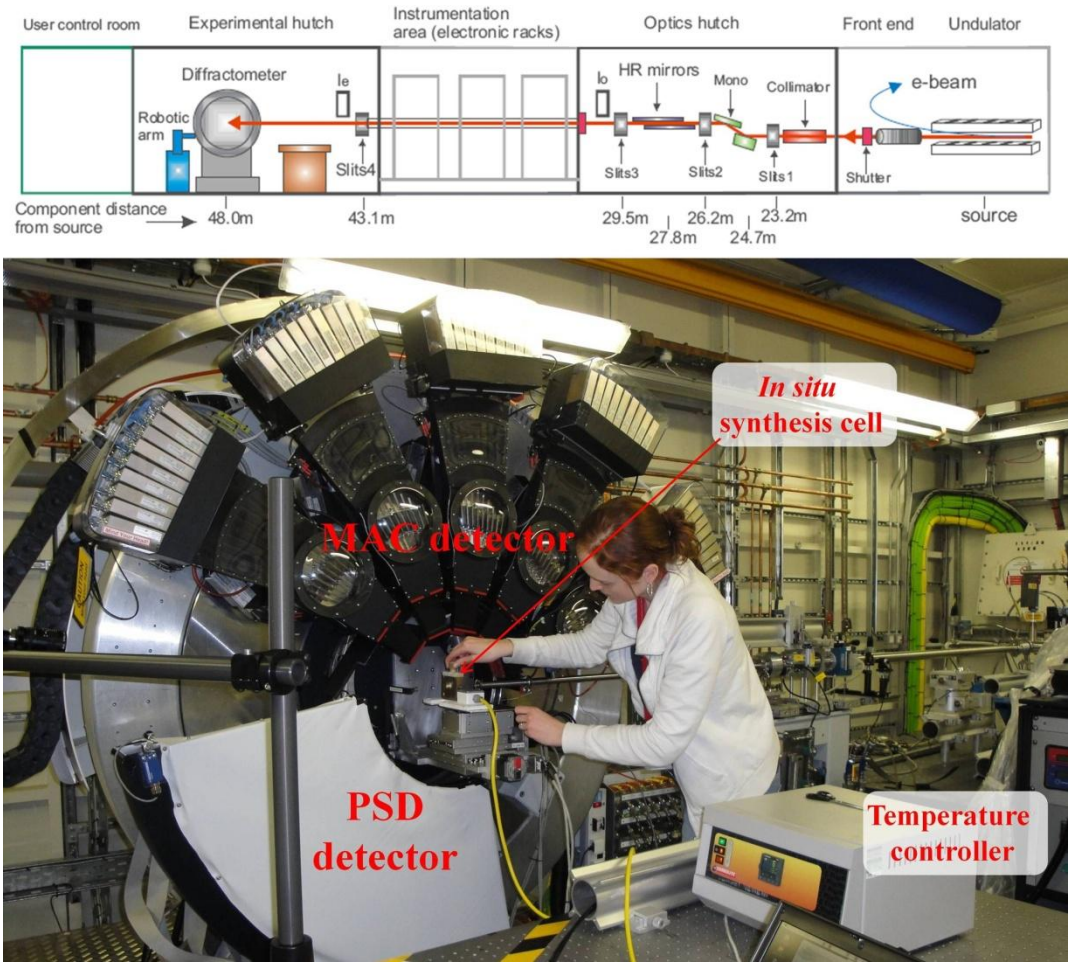

Figure 4.1. *A schematic illustration of the high resolution I11 beamline*[20] *and a photograph showing the set-up used with the in situ synthesis cell. A capillary set-up is also available to use.*

4.3.3 *Ex situ* Laboratory X-ray diffraction

Ex situ X-ray diffraction analysis was performed on a number of as-synthesised AFI-type materials to identify phases and study their metastability and crystallinity. Measurements were performed using a Bruker D4 employing Cu-Kα radiation (λ =

1.5418 Å). In a typical experiment, the dried samples were pressed onto flat plates and placed in positions. These samples were loaded automatically with a robot and the materials were subsequently analysed over a range of 2 – 65 degrees 2θ with a step of 0.05° and an acquisition time of 2 seconds per scan point.

4.3.4 Data analysis

Phase identification of each crystalline phase observed in the XRD patterns was achieved through indexing the reflections using either the DIFFRAC^{plus} EVA program or by comparison with standard XRD data sets available[21]. Data analysis was performed with TOPAS-academic[22]; a Pawley fit was performed using either, the fundamental parameter approach (FPA) for the *in situ* HRXRD data, or a Thompson-Cox-Hastings (TCHZ) pseudo Voigt function for the *ex situ* XRD data. This provided information on the evolution of diffraction peak intensity (area) and unit cell parameters. Starting unit cell parameters of the AFI phase, hexagonal a(=b) = 13.718 Å, c = 8.4526 Å, α=β = 90° and γ = 120° with space group P6cc (184), were taken from a single-crystal study on AlPO-5 by Kalp et al.[23].

Similarly, the other phases were analyzed based on information from previous studies; hexagonal CHA (a = b = 13.675 Å, c = 14.767 Å, R-3m)[24], AEI phase (a = 13.5116 Å, b = 12.6235 Å, c = 18.4394 Å, α = γ = 90°, β = 95.55°, C12/C1)[25], AEN

structure (a = 10.292 Å, b = 13.636 Å, c = 17.344 Å, α = β = γ = 90°, $P2_12_12_1$)[26] and Tridymite (a = 25.878 Å, b = 5.001 Å, c = 18.526 Å, β = 117.60°, A1A1)[27].

The evolution of diffraction peak intensity (area) as a function of time can be used to derive valuable information on the kinetics and mechanism involved in the crystallization process. The corresponding crystallite area measured (or the area under the most intense reflection) for each phase was converted to the extent of the reaction, α, scaled from 0 to 1, using the relationship $\alpha(t)=I_{hkl}(t)/I_{hkl}(\max)$, where $I_{hkl}(t)$ is the area of a given peak at a given time, t, and $I_{hkl}(\max)$ is the maximum area of this peak[28], this resulted in crystallization curves as a function of time.

Information of the kinetics of formation was derived from the Avrami-Erofe'ev expression which is widely used to study crystal growth in solid-state chemistry[29]:

$$\alpha = 1 - \exp[(-(k(t - t_0))^n]$$

where α is the extent of reaction, t is a given time, t_0 is the induction time, k is the rate constant and n is the Avrami exponent. In addition to the kinetics of formation, k, mechanistic information can be deduced from the Avrami exponent, and both of these parameters can be obtained from Sharp-Hancock plots[30], a plot of ln{-ln(1-α)} vs ln(t-t_0). These resulting linear plots, which have been found to be most applicable in the range $0.15 < \alpha < 0.8$[31], have a gradient n and intercept $n \ln k$.

4.4 Results and Discussion

An investigation on the effect of varying both inorganic and organic cations on the kinetics of AFI formation through an *in situ* HRXRD study, are first discussed. Subsequently, results from a kinetic study on the effect of cobalt concentration on the formation of phase pure AlPO-5 are presented and discussed. Finally, the hydrothermal decomposition of these metastable aluminophosphate materials, in relation to the incorporation of a dopant ion and the organic template utilized, are reported.

4.4.1 Effect of varying cations on the formation of AlPO-5 catalysts.

Crystallization of six different precursor gels was monitored by *in situ* HRXRD so that the effect of varying both the organic template and the divalent metal cations on the structure and the kinetics of formation could be studied. The experiments were conducted at the Swiss-Norwegian beamline (SNBL) of the ESRF at 170°C. Three-dimensional stacked plots of the HRXRD data of AlPO-5, CoAlPO-5 and ZnAlPO-5, as a function of synthesis time are shown in Figure 4.2 and Figure 4.3, formed from either the amine *N*-methyldicyclohexylamine (MCHA) or the quarternary ammonium cation tetraethylammonium hydroxide (TEAOH) as the organic template, respectively.

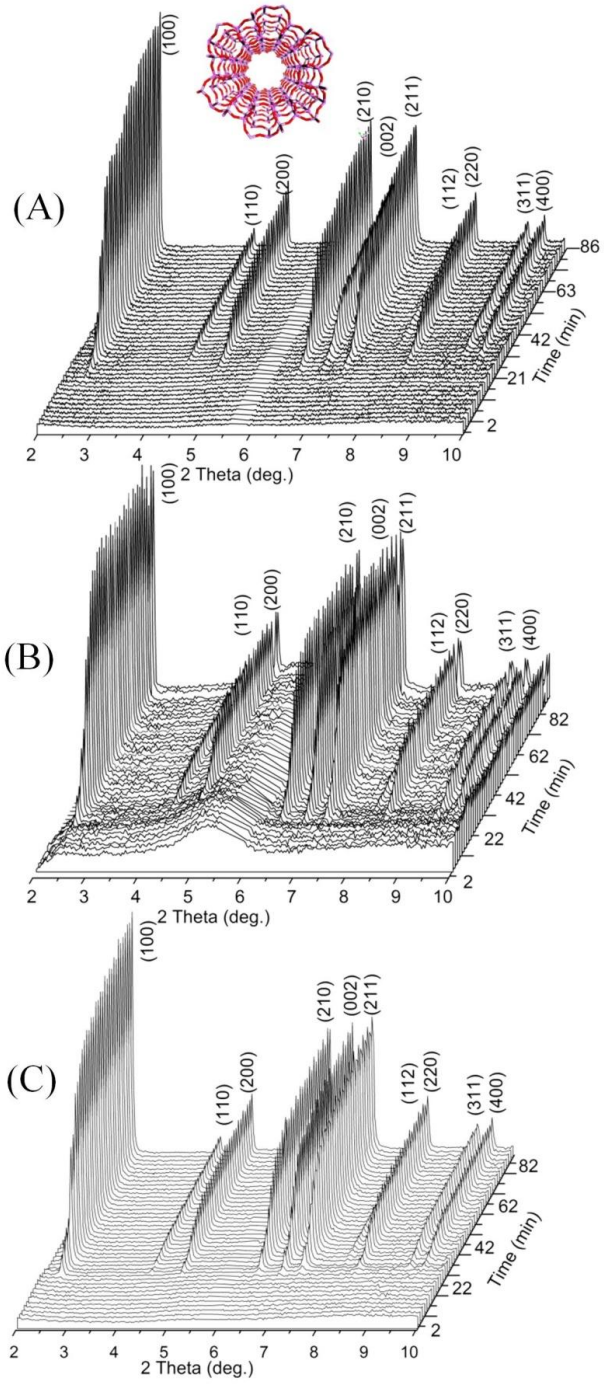

Figure 4.2. *3-D stacked plots of HRXRD data collected during the synthesis of (A) AlPO-5, (B) CoAlPO-5 and (C) ZnAlPO-5, utilizing MCHA as the template. All reflections can be indexed to the AFI structure, as shown inset. It should be noted that the small amorphous hump observed throughout the synthesis of CoAlPO-5 (B) is due to a higher water amount in the synthesis cell.*

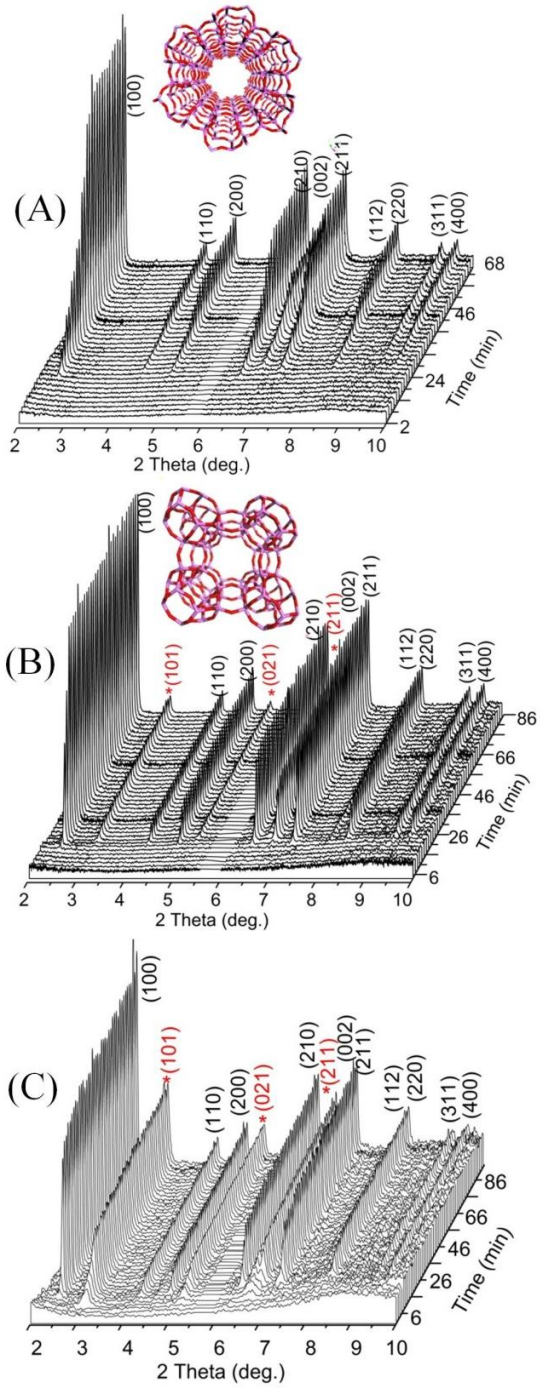

Figure 4.3. *3-D stacked plots of HRXRD data collected during the synthesis of (A) AlPO-5, (B) CoAlPO-5 and (C) ZnAlPO-5, utilizing TEAOH as the template. Reflections indexed to the AFI structure, shown inset in (A), are coloured black, and those indexed to the CHA impurity phase, illustrated in inset of (B), are marked with an asterix(*) and coloured red.*

All reflections were indexed to a crystalline phase based on comparison with standard XRD patterns from the database of zeolite structures[32].

It is clear from the stacked plots illustrated in Figure 4.2, in the presence of MCHA all reflections could be indexed to the AFI structure indicating only phase pure AlPO-5 materials form irrespective of the metal content. This result supports other investigations which have also shown that only phase pure AFI structure forms when MCHA is used as the template, over a large range of synthesis conditions such as temperature, pH and metal content, and is noted to have the highest specificity to direct the AFI structure implying the true structure-directing aspect of MCHA[7]. Similarly, when TEAOH was used as the organic template in the presence of no heteroatom, Figure 4.3(A), and under the experimental conditions used in this work, only phase pure AlPO-5 forms.

Differences arise between the use of TEAOH and MCHA as the organic template when a divalent metal cation is introduced into the precursor gel; the organic template plays a significant role in determining whether phase pure AFI structure forms. This is demonstrated in Figure 4.3(B) and (C); stacked HRXRD patterns recorded *in situ* during the crystallization of CoAlPO-5 and ZnAlPO-5 with TEAOH as the organic template, respectively. The majority of the reflections can be indexed to the AFI structure, however, an impurity phase is also observed. These additional reflections are indexed to the CHA structure and marked with an asterix (*). The CHA structure is described in section 1.2.2.1. Previous studies[6, 7, 19, 33-39] have recorded this competitive phase formation between AlPO-5 and AlPO-34 type materials under various synthesis conditions, and which has been found to only occur with metal

concentrations above 4 wt % corresponding to larger amounts of organic template which is required to charge balance the system and may favour the formation of the CHA phase[36, 40, 41]. In particular, a study by Weckhuysen and colleagues[42], which followed not only the structural changes but also the template conformation during crystallization of ZnAlPO-34 and AlPO-5, discovered that TEAOH adopts a different conformation when zinc ions are in the synthesis gel which generates the formation of the CHA structure. In addition, the effect of inorganic metal cations on the conformation of the organic species was found to be general for other divalent cations illustrating no differences between zinc and cobalt ions on the lattice topology.

It should be noted that the above study by Weckhuysen et al. investigated the formation of pure phase AlPO-5 and MeAlPO-34 materials. The HRXRD study, on the other hand, examined the competitive phase formation of *both* the AFI and CHA structures together. Through this method, differences in the formation of these materials depending on the incorporation of either zinc(II) or cobalt(II) ions, were deduced. Comparison of the integrated area under a number of single AFI and CHA reflections from an *in situ* experiment revealed crystallization curves which were generally superimposable over the duration of the experiment, indicating that both the AFI and CHA growth is isotropic on all crystallographic planes. Therefore all peak areas should be representative of the growth mechanism occurring; for further analysis the intensity of the (100) and (101) reflections from the AFI and CHA phases, respectively, was converted to the extent of reaction and plotted against crystallization time. These crystallization curves of both AFI and CHA phases with

TEAOH as the organic template and either Co(II) or Zn(II) ions are shown in Figure 4.4.

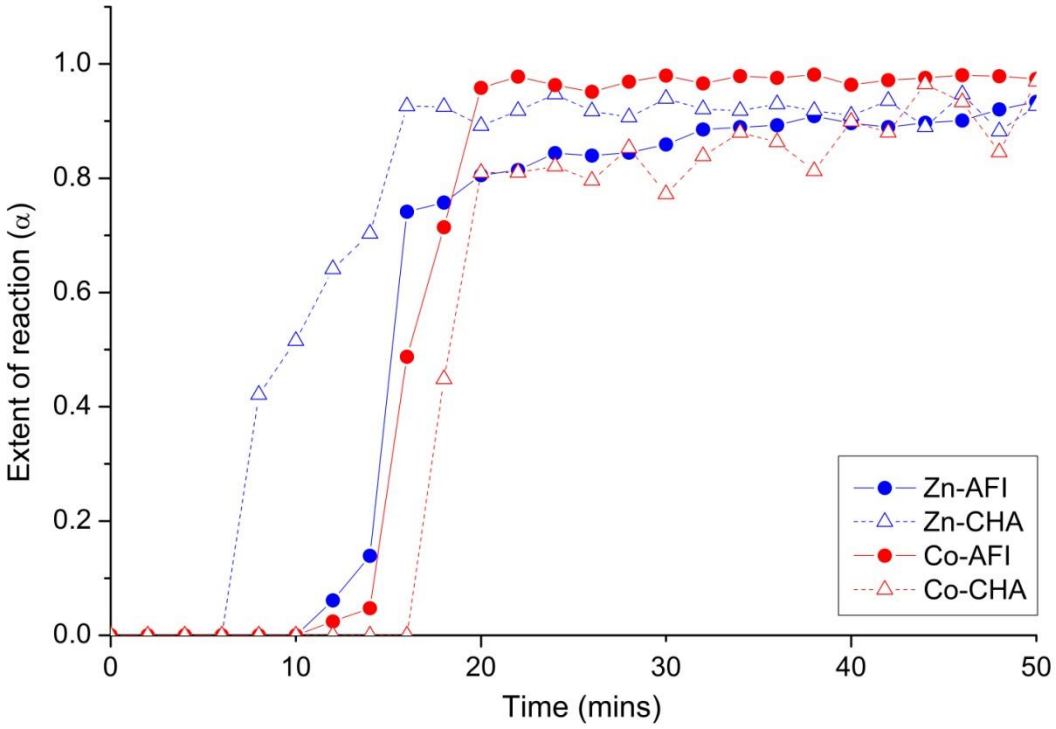

Figure 4.4. *Crystallization curves of the formation of both AFI (solid symbols) and CHA (hollow symbols) phases with TEAOH as the organic template and either zinc (blue) or cobalt (red) cations.*

In the presence of Co(II) ions, reflections from the AFI phase appear first followed (*ca.* 4 minutes) by the addition of CHA structure reflections. However, when Zn(II) ions are present in the precursor gel along with TEAOH, the opposite is observed, in which reflections from the CHA phase are seen to appear first in the diffraction

patterns with the appearance of AFI phase reflections a very short time later (*ca.* 6 minutes). To date, no previous studies have been able to obtain data showing which phase, AFI or CHA, forms first when they co-crystallize. The preferred nucleation of one phase over another, depending on the incorporation of the type of divalent metal ion, may provide additional information on the mechanism of formation and can be of importance when determining which metal cation to incorporate in the attempt to form new molecular sieves.

From these observations it can be speculated that Zn(II) ions promote the formation of denser rings or 'pockets' such as double 6-membered (6-6) and 4-2 rings since these are present in the CHA structure, which forms first, but are nonexistent in the AFI structure. Conversely, as the AFI phase forms prior to the CHA structure when Co(II) ions are incorporated into the precursor gel, Co(II) ions appear to promote the formation of more open structures such as AlPO-5 with larger 12-membered rings. Previous XAS studies[28, 37, 39] on the divalent metal ion local changes during the synthesis of Zn(II)- and Co(II)- substituted aluminophosphates reveal that Zn(II) ions are in a tetrahedral environment in the precursor gel prior to crystallisation, whereas Co(II) ions are in an octahedral environment. Tetrahedral Zn(II) ions, ionic radius of 0.6 Å, are smaller compared to octahedral Co(II) ions, 0.65 – 0.745 Å, which may allow for these divalent metal ions to form denser or smaller rings in aluminophosphate materials.

Furthermore, the kinetics of formation of all six AFI-type materials (AlPO-5, CoAlPO-5 and ZnAlPO-5 with either MCHA or TEAOH) was examined. The extent of reaction (α) for each crystalline phase was calculated based on the overall

crystalline AFI area (sum of the area of the Bragg peaks). The resulting crystallization curves for the AFI materials are shown in Figure 4.5 and are typical for a crystallization process consisting of an initial period of induction/nucleation followed by rapid crystallization of the material and gradual growth of the crystallites until a constant value is reached, implying completion of crystal growth.

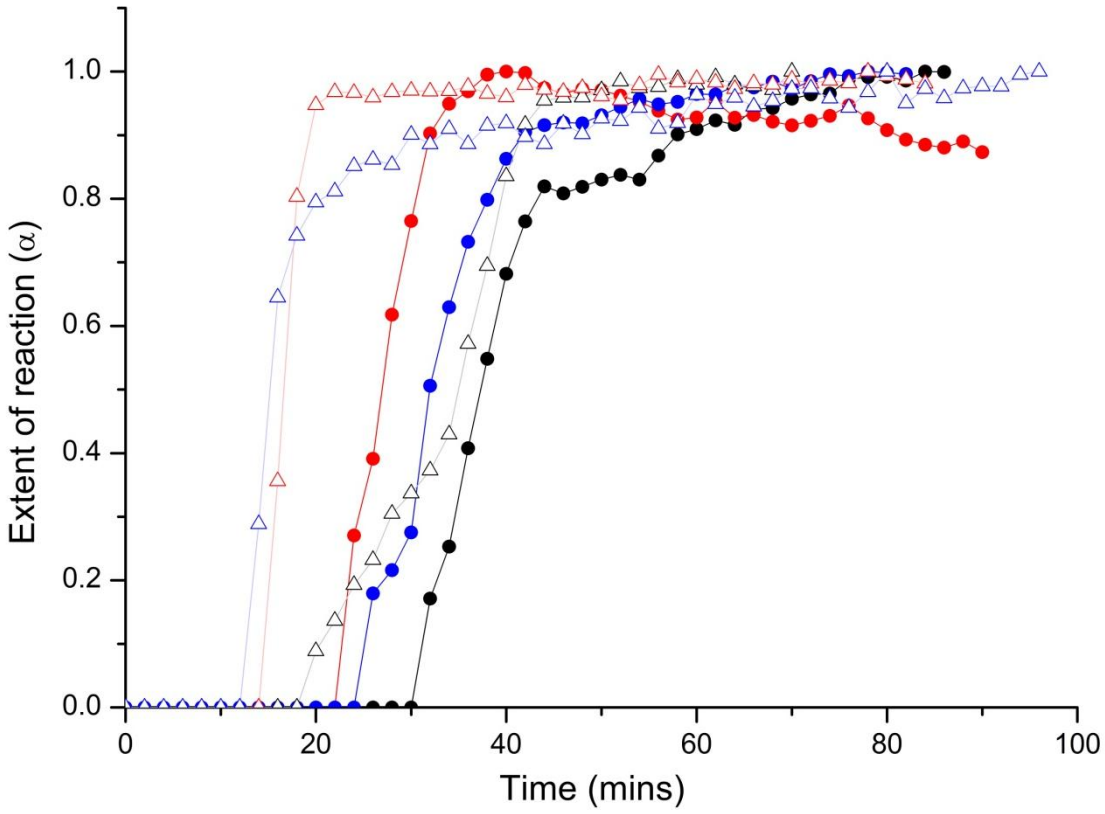

Figure 4.5. *Crystallization curves of AlPO-5 (black symbols), CoAlPO-5 (red symbols) and ZnAlPO-5 (blue symbols), synthesized with MCHA (solid circles) or TEAOH (hollow triangles) as the organic template.*

From the crystallization curves, it is clear that in the presence of a divalent metal cation, Co(II) or Zn(II), the induction period is shortest compared to un-substituted AlPO-5 irrespective of the organic template utilized, implying that metal ions (5 wt %) promote the formation of AFI type materials. Similar observations of divalent metal ions (importantly with a weight % < 6) promoting the formation of the AFI structure have been made by others [6]. However, there are controversies in the literature, for example, an investigation[28] on the kinetics of AFI growth contradicts these observation, finding that cobalt (5 wt %) significantly retards nuclei growth and crystallization. Apart from various experimental factors, differences may have been due to the use of triethylamine (TEA) as the organic template, which like TEAOH can produce more than one phase, unless a specific pH is used for a given metal ion containing system. This study had the advantage of not only utilizing TEAOH as the organic template, which has been found to have the highest templating power to form AlPO-5[19], but also MCHA which has the highest specificity to direct the AFI structure over a wide range of pH and temperature[7].

On comparison of the effect of these templates on the crystallization of AlPO-5, a shorter induction period is observed when TEAOH is employed compared to MCHA. This can be attributed to the fact that TEAOH has the best templating ability for the formation of AFI materials with the strongest nonbonding template-framework interaction energy[19].

All AFI materials follow a typical sigmoidal crystallization curve with the exception of AlPO-5, formed with TEAOH, which seems to resemble a double-sigmoidal curve. Although the competing CHA phase was not observed during the

crystallization of AlPO-5 with TEAOH, resulting factors such as template conformation may have an effect on its crystallization process. To further explain these observations, kinetic information was derived from the crystallization curves.

The crystallization curves can be used to obtain information on the crystal growth and mechanism which is derived using the Avrami-Erofe'ev equation[43] described in section 4.3.4. Sharp-Hancock plots of $\ln(-\ln(1-\alpha))$ vs $\ln(t-t_0)$, where t_0 is the induction time, are given in Figure 4.6 for each AFI material, with the exception of the metal substituted AFI materials formed with TEAOH. The rate constant for the formation of these MeAlPO-5 materials was not estimated for two reasons. The first reason is due to the fact that the CHA phase was observed; not only might the crystallization process be affected by this impurity phase but its presence may also effect the substitution of the divalent metal ions into the AFI structure (it is known that pure AlPO-34 can only form in the presence of HF[44]) which may give a false representation of the effect of Co(II) and Zn(II) ions on the crystallization of AlPO-5 with TEAOH. Secondly, the relevance of the Avrami-Erofe'ev equation in modelling solid-state reactions is only applicable in the range $0.15 < \alpha < 0.8$[45, 46]; when TEAOH is utilized as the organic template and in the presence of divalent metal cations the crystallization is very fast resulting in only one or two points which fall in the applicable range which is not sufficient enough to get a clear representation of the mechanism or rate of crystallization.

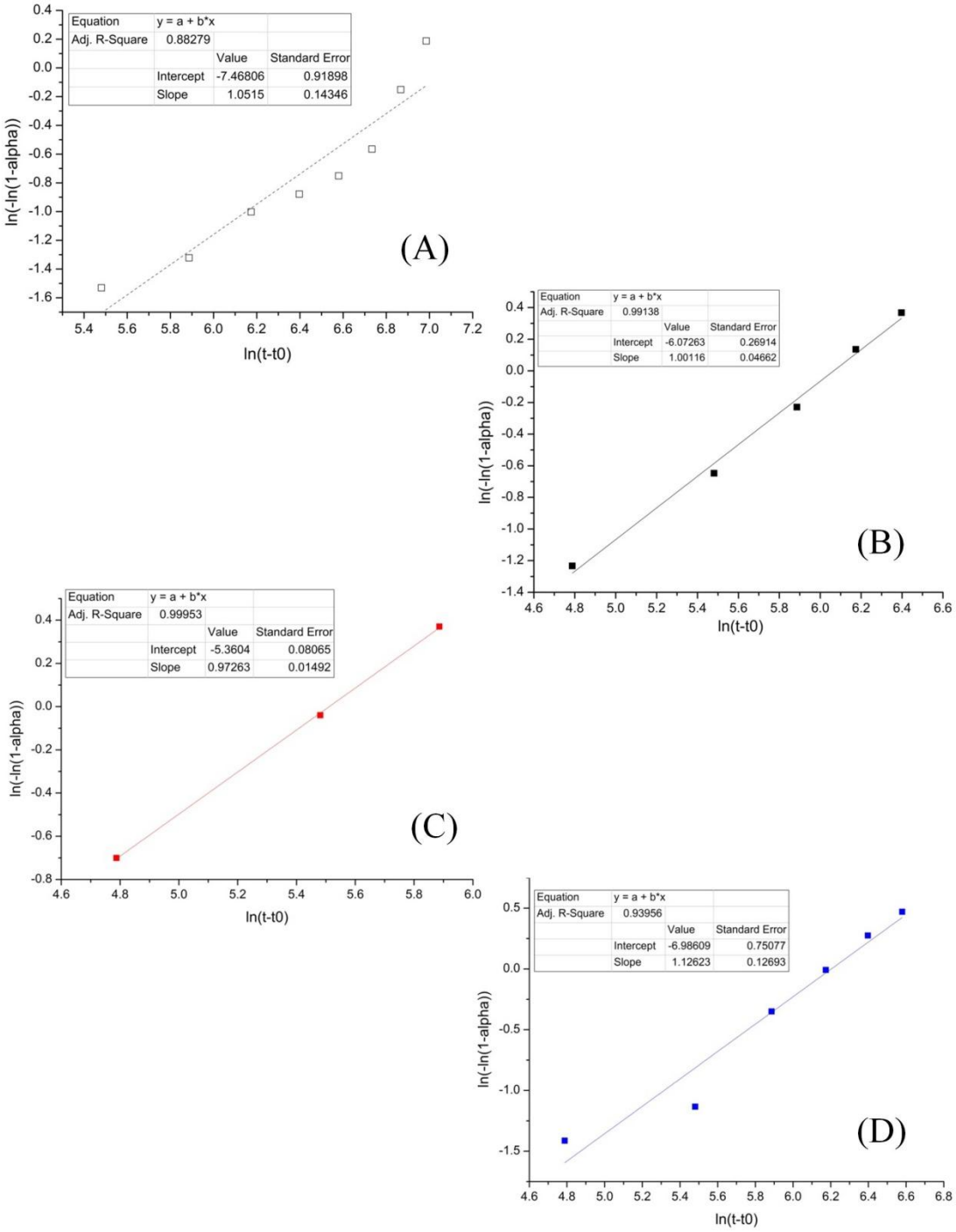

Figure 4.6. *Linear Sharp-Hancock plots for the crystallization of AlPO-5 with TEAOH (A), and AlPO-5 (B), CoAlPO-5 (C) and ZnAlPO-5 (D) with MCHA as the organic template.*

	Induction time (mins)	Rate constant k x 10^{-3} (sec^{-1})	Avrami Constant n
AlPO-5 (MCHA)	32	2.32	1.00
ZnAlPO-5 (MCHA)	26	2.02	1.13
CoAlPO-5 (MCHA)	24	4.04	0.97
AlPO-5 (TEAOH)	20	0.82	1.05

Table 4-1. *Showing the induction time and the parameters, k and n, obtained from a Sharp-Hancock plot for AlPO-5 (TEAOH), and AlPO-5, CoAlPO-5 and ZnAlPO-5 synthesized with MCHA.*

The Sharp-Hancock plots were used to obtain the rate constant, k (the y intercept = n ln k) and the Avrami constant, n (the gradient), which can contain information on the dimensionality and process of crystallization. The resulting parameters along with the induction time are given in Table 4-1.

It should be noted that the calculated rate and Avrami constant for the crystallization of AlPO-5 with MCHA (k = 2.32 x 10^{-3} s^{-1}, n = 1.00) was found to be similar to previous studies on the formation of AlPO-5 with TEA (k = 2.00 x 10^{-3} s^{-1}, n = 1.02) as the organic template, implying that the reaction taking place between the reactants and products is the rate determining step (phase-boundary controlled) [28]. However, when TEAOH is employed as the organic template, although a similar Avrami constant is obtained (n = 1.05), a lower rate constant is calculated (k = 0.82 x

10^{-3} s^{-1}), implying that the use of TEAOH retards crystallization of AlPO-5. Although this can be true, there may also be inaccuracies in the evaluation of the rate of the crystallization of AlPO-5 (TEAOH) as it resembles a double sigmoidal curve in which the rate or dimensionality of crystallization changes during the formation of AlPO-5.

The effect of divalent metal cations on the rate of AFI crystallization and the Avrami constant was compared for the utilization of MCHA as the organic template since only pure phase AlPO-5 materials formed. The introduction of a dopant ion, Co(II) or Zn(II) ions, into the synthesis gel was found to have a similar effect on the induction period, 24 and 26 minutes, respectively. However, large differences in the rate constant were observed depending on the divalent metal ion present. For example, the crystallization of ZnAlPO-5 was found to have a rate constant, 2.02 x 10^{-3} s^{-1}, similar to the corresponding AlPO-5 material, whereas the formation of CoAlPO-5 occurred with a rate constant of 4.04 x 10^{-3} cm^{-1}. In other words, the *k* rate constant shows a crystallization rate 2 times faster in CoAlPO-5 compared to ZnAlPO-5 and pure AlPO-5, indicating that Co(II) ions significantly increases the rate of crystal growth.

The Avrami constant, which can indicate the mechanism and rate of nucleation, was found to be similar in all materials, indicating that all AFI materials crystallize with the same mechanism irrespective of the dopant ion or organic template. From scanning electron microscopy (SEM) analysis, the crystals of the AFI samples were found to have a rod/needle like shape that agglomerated into spheres, therefore an approximate *n* value of one indicates a 1-dimensional diffusion controlled growth

with zero nucleation. For the crystallization of ZnAlPO-5, *n* was found to be slightly larger at 1.13, which is indicative of ZnAlPO-5 crystallizing with the same 1D mechanism but with a slightly slower nucleation rate. This may also explain why the rate constant of ZnAlPO-5 is similar to pure AlPO-5 but its induction time is comparable to CoAlPO-5. It should also be noted that *n* is sensitive to data analysis, therefore large errors may be present.

4.4.2 Effect of cobalt concentration on the kinetics of formation of aluminophosphate type-5.

In the synthesis of divalent metal substituted aluminophosphate catalysts, the choice of template and dopant ions (in particular the concentration of Me(II) ions) are of vital importance in directing synthesis toward particular structures. For example, when TEAOH or TEA are employed as the organic templates for the synthesis of AlPO-5 and with cobalt concentrations greater than 4 wt %, impurities from the CHA phase are observed[36, 40, 41]. The concentration of divalent metal ions in the synthesis gel has been shown to not only affect the type of structure formed but also the kinetics of formation; similar to the study above, Davies et al.[6] found the addition of Co(II) ions to the synthesis gel reduced the induction period and increased the rate of AFI crystallization. However, this trend was found to reverse with cobalt concentrations above 6 wt. % which was attributed to the presence of the impurity

CHA phase resulting in a reduction in the cobalt and template concentrations in the AFI structure.

MCHA is known to only produce phase pure AlPO-5, over a wide range of pH and temperature, and, significantly, irrespective of the metal concentration. For this reason, the effect of divalent metal concentration on the kinetics of AlPO-5 formation with MCHA as the organic template was investigated to elucidate whether the competitive phase formation between CHA and AFI phases plays a role in the kinetics of crystallization of the AFI structure.

HRXRD data was collected at the I11 beamline of Diamond Light Source during the crystallization of CoAlPO-5, with MCHA as the template, and cobalt concentrations of 0, 4, 7, 10 and 15 wt %. A temperature of 160 °C was utilized which is lower compared to the previous study (section 4.4.1 employed a temperature of 170°C) so that the reaction would crystallize at a slower rate with an aim of revealing more detail. Figure 4.7(A) shows the 3D stacked HRXRD plot collected during the formation of AlPO-5 (zero cobalt concentration) in which all reflections could be indexed to the AFI structure. This AFI phase purity was found to be typical for all materials, irrespective of the cobalt content and is illustrated in Figure 4.7(B); final XRD plots collected during the formation of CoAlPO-5 with Co(II) concentrations of 4, 7, 10, and 15 wt %.

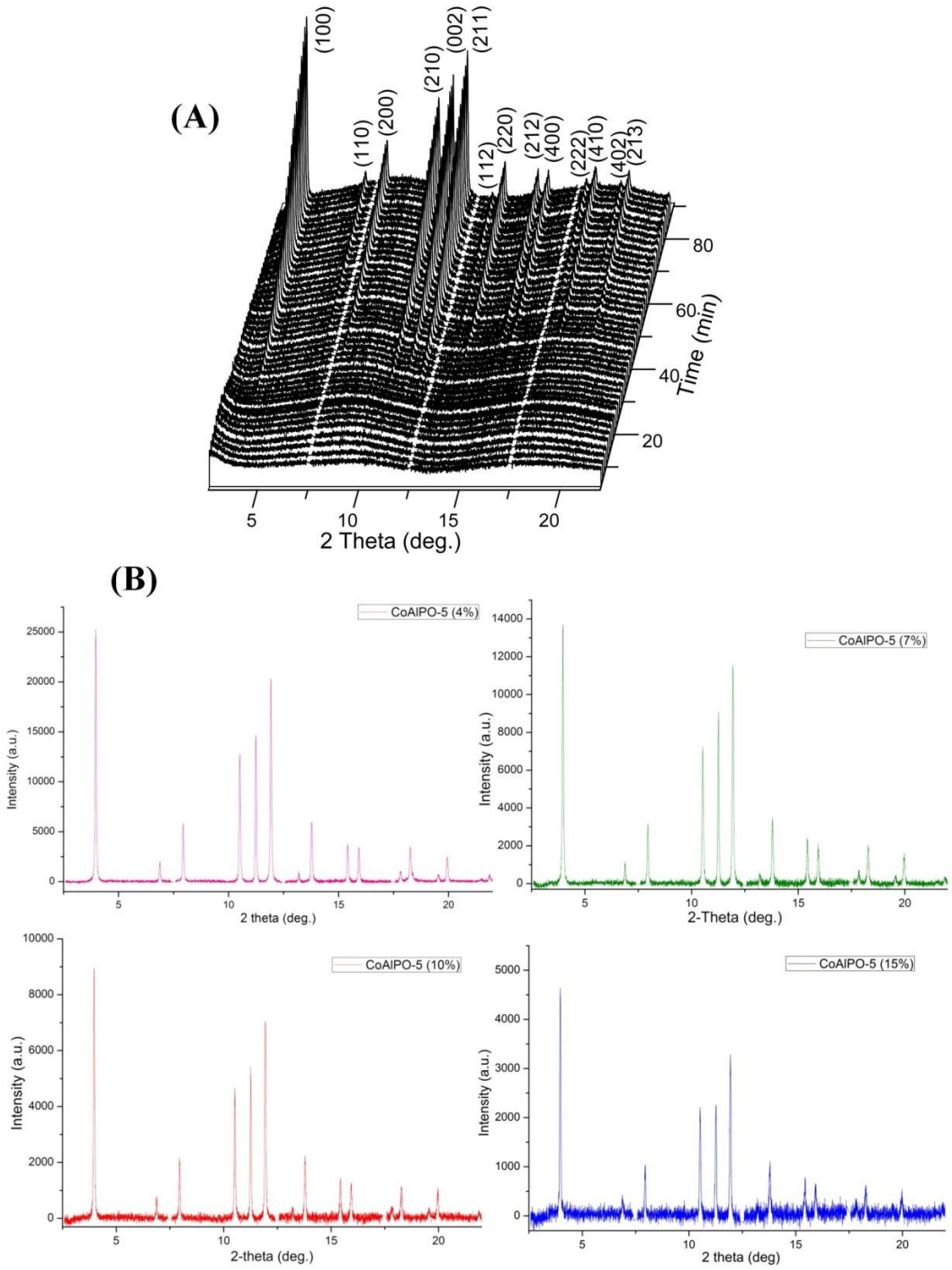

Figure 4.7. *3D stack plot of the crystallization of AlPO-5 (A), and the final HRXRD patterns (B) of the CoAlPO-5 materials with Co(II) concentrations of 4 (pink), 7 (green), 10 (red) and 15 (blue) wt %. All reflections can be indexed to the AFI structure.*

To evaluate the effect of cobalt concentration on the formation of these AFI materials, the extent of reaction (based on the total area of the Bragg peaks) vs synthesis time was plotted, Figure 4.8. The crystallization curves show an initial period of induction followed by crystal growth and in the synthesis of CoAlPO-5 (4%) a final stage of crystal growth completion. Although the synthesis of the other AFI materials was stopped before completion, kinetic data can still be determined as it is the induction time and actual crystal growth which have the most relevance. However, it should be noted, from the extent of reaction (Figure 4.8) that all AFI materials were near completion with the exception of CoAlPO-5 (15%).

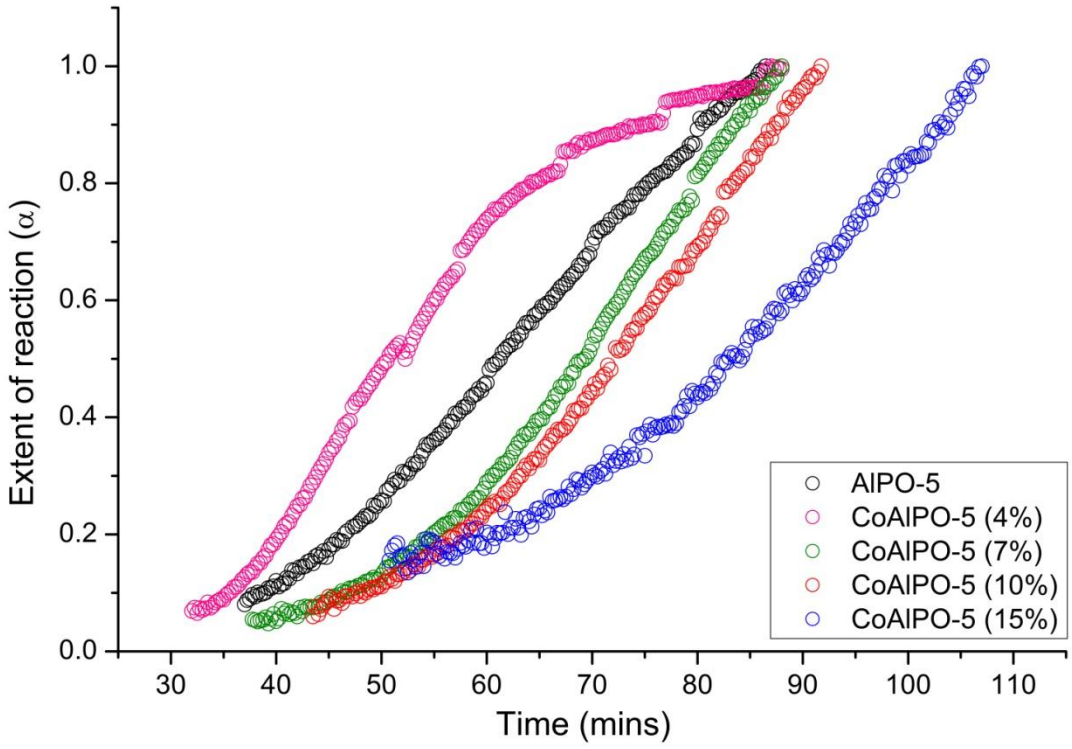

Figure 4.8. *Crystallization curves of the formation of CoAlPO-5 synthesized with MCHA and cobalt concentrations of 0 (black), 4 (pink), 7 (green), 10 (red) and 15 (blue) wt %.*

With a lower cobalt concentration of 4 wt %, the induction period to crystallization is shorter (32 minutes) compared to the formation of pure AlPO-5 (37 minutes). This is similar to the previous study on the mechanism of formation (Chapter 3) with a cobalt concentration of 5 wt %. As the amount of divalent metal ions increases to 7, 10 and 15 wt %, the reverse trend is observed, in which the induction time to crystallization increases (38, 43 and 51 minutes, respectively) compared to that of the un-substituted AFI material. As stated above, this reverse in the kinetic trend has been observed previously, however, the increase in the induction period of AFI crystallization with Co(II) concentration above 6 wt % was attributed to the presence of the CHA phase[6]. The results clearly show a similar trend in the crystallization induction period without the presence of any impurities, such as CHA structure. Therefore, this hindrance of AFI crystallization is solely attributed to an increase in cobalt concentration (above 6 wt %).

To further evaluate this kinetic trend, the rate constant, k (the y intercept = n ln k) and Avrami constant, n (the gradient) were calculated from Sharp-Hancock plots, Figure 4.9. A linear fit was found to be sufficient for the crystallization of all AFI materials, with larger errors present for CoAlPO-5 (15%) as crystal growth was not close to completion. The resulting kinetic parameters for the formation of all AFI-type structures are tabulated in Table 4-2.

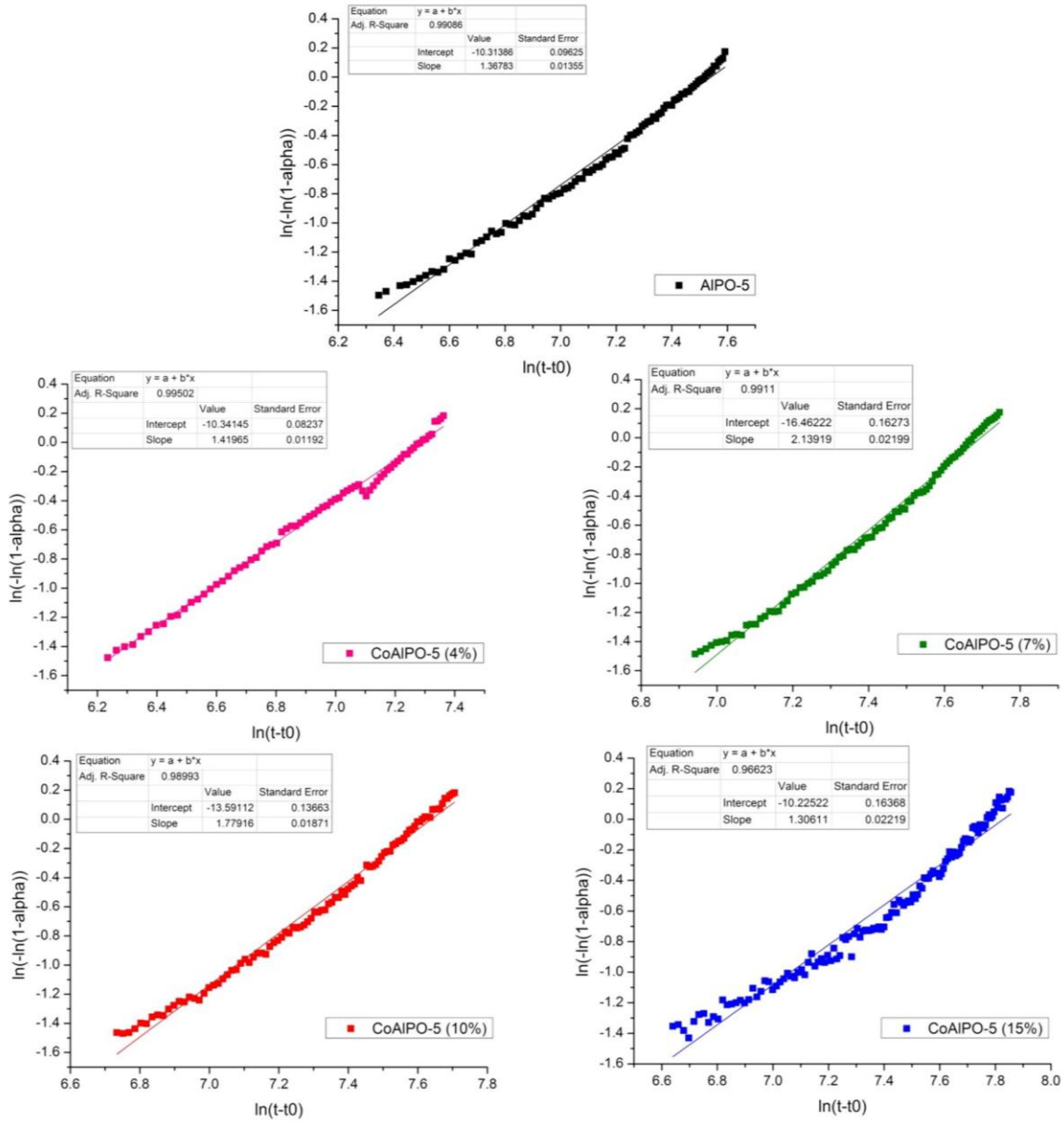

Figure 4.9. *Sharp-Hancock plots of the crystallization of AFI materials with a cobalt concentration of 0 (black), 4 (pink), 7 (green), 10 (red) and 15 (blue).*

	Induction time (mins)	Rate constant k x 10^{-3} (sec^{-1})	Avrami Constant n
AlPO-5	37	0.53	1.37
CoAlPO-5 (4%)	32	0.69	1.42
CoAlPO-5 (7%)	38	0.45	2.14
CoAlPO-5 (10%)	43.5	0.48	1.78
CoAlPO-5 (15%)	51	0.40	1.31

Table 4-2. *Showing the induction time and the parameters, k and n, obtained from Sharp-Hancock plots for CoAlPO-5 with cobalt concentration 0, 4, 7, 10 and 15 wt %.*

The rate constant for the crystallization of CoAlPO-5 (4%) was found to be the fastest, 0.69 x 10^{-3} s^{-1}, coinciding with the shortest induction period, followed by pure AlPO-5, 0.53 x 10^{-3} s^{-1}. All three CoAlPO-5 materials with a Co(II) concentration above 6 wt % were found to have a similar slower rate constant, *ca.* 0.45 x 10^{-3} s^{-1}, which coincided with the longest induction period. It should be noted that the rate constant and Avrami constant for the formation of pure AlPO-5 are different from those obtained previously in section 4.4.1 due to various synthesis and experimental factors such as temperature.

The Avrami constant, which may provide information on the mechanism and rate of nucleation, was found to be similar, *ca.* n = 1.5, for all AFI-type materials with the exception of CoAlPO-5 (7%). An n value of *ca.* 1.5 may indicate a 1D growth

mechanism with the formation of nucleation sites being more significant in determining the rate of crystallization compared to the diffusion of the nuclei species to the crystallization sites or the rate of growth on the crystallite surface[28]. A larger n value of over 2 that was observed for CoAlPO-5 (7%) may be due to an extremely slow nucleation rate or it may be large due to the agglomeration of the 1-D rod/needle like crystals into 3-D spheres as observed in SEM.

From the crystallization curves and kinetic parameters obtained, the study revealed that the induction period was shorter and the rate constant faster for the crystallization of CoAlPO-5 (4%) compared to un-substituted AlPO-5. This can be explained in terms of a stronger interaction of the positively charged template with the negative framework units when a divalent metal ion is present, therefore promoting the formation of the AFI materials. However, as the cobalt concentration increases above 6 wt. %, the induction period increases and the rate constant decreases, indicating that large cobalt concentrations retard AFI formation. This kinetic trend may be due to complexities in distributing cobalt into the framework with higher cobalt concentrations since only a specific amount of cobalt ions can substitute into the framework to charge balance the template occluded within the pores. In addition, as divalent metal ions only substitute for Al(III) ions in the framework, difficulties may arise in the chemical ordering of Co-O-P-O-Al- units with larger Co(II) loadings.

4.4.3 The metastability of AlPO-5 catalysts.

The kinetic control of the formation of aluminophosphates is of vital importance in the synthesis of these materials for catalytic applications. It is well known that these microporous materials are metastable in the reaction medium and are not true thermodynamic products; for example, the kinetically favoured AlPO structure transforms over time to the thermodynamically stable phase such as berlinite or tridymite[1]. For the application of AlPO materials as shape selective catalysts in industry, scale-up of the synthesis with prolonged time occurs and may have an effect on the optimization of the product. Therefore, not only is the control of the kinetic product important but also the metastability and transformations of the AlPO framework should be taken into account in determining/optimising the synthesis procedure. In addition, the metastability of aluminophosphates during the hydrothermal reaction may provide detailed information on the framework-template interactions since the dense tridymite phase does not encapsulate the organic species.

An *ex situ* study on the decomposition of large pore AlPO-5 materials in their reaction medium was performed in the laboratory and the effect of divalent metal ions and organic templates on their metastability investigated. In addition, the effect of pH on the stability of AlPO-5 with MCHA in the reaction medium was examined. The hydrothermal reaction was stopped after 3, 7, 10, 18.5 and 60 hours, and in some cases after 1 week. It should be noted that the resulting solids were washed filtered and dried before they were characterized by lab XRD.

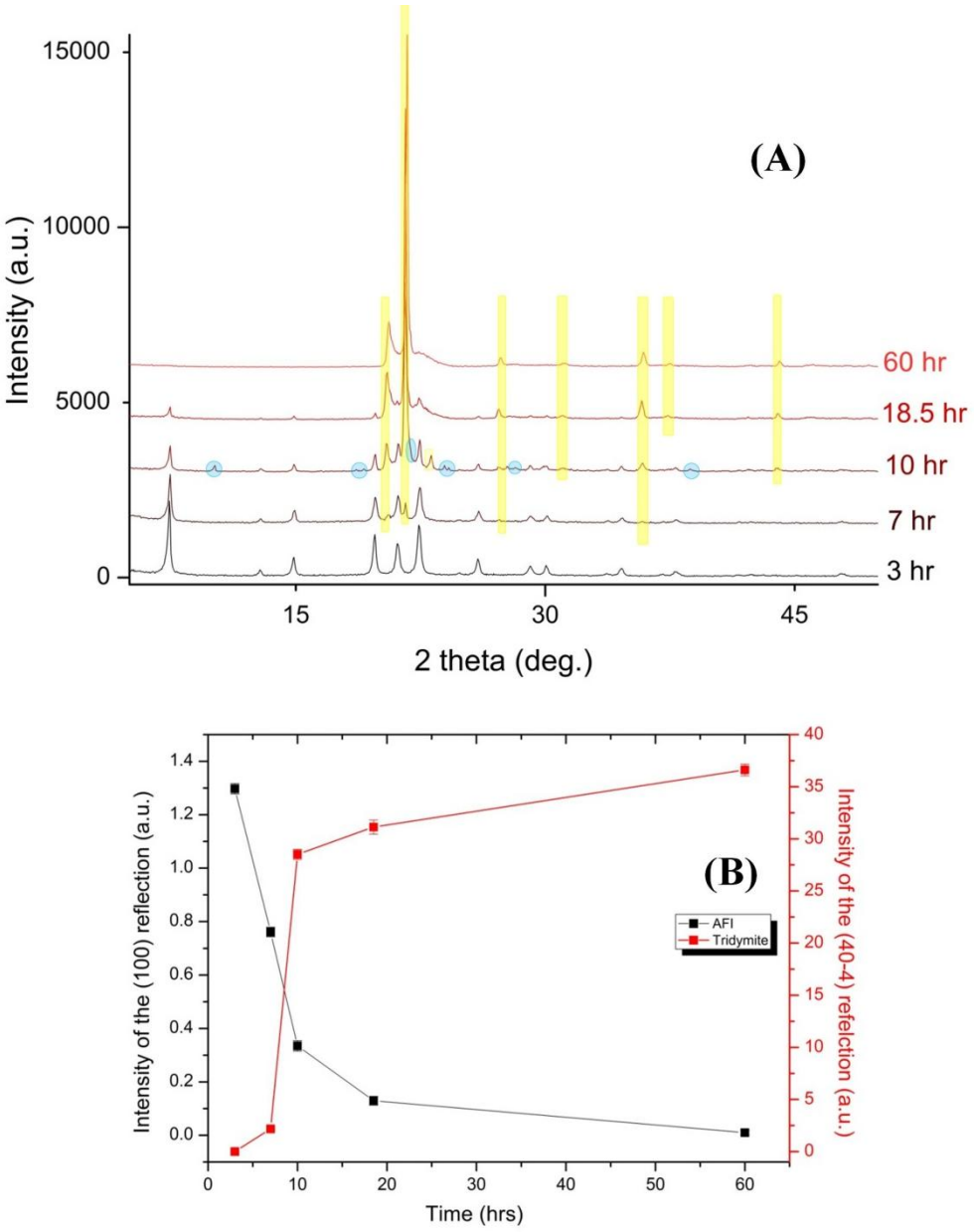

Figure 4.10. *XRD patterns (A) of **AlPO-5** synthesized at **pH 5** employing **MCHA** as the template at different times, the dense tridymite phase is highlighted in yellow and the AlPO-53 phase in blue. The decomposition of the AFI phase (black) and the evolution of the tridymite phase (red) as a function of crystallization time are shown in (B).*

Resulting *ex situ* XRD patterns collected at the different times for the synthesis of AlPO-5 with MCHA and a pH of 5 are displayed in Figure 4.10(A). At short times (3 hrs), as expected based on optimum conditions, phase pure AlPO-5 forms. As time increases small impurities from other phases are observed in the diffraction patterns along with the AFI structure, these were indexed to the dense tridymite phase[27] (highlighted in yellow) and the small pore cage structure of AlPO-53 (AEN)[26] (highlighted in blue). It should be noted that the AlPO-53 phase may be an impurity from the 'wash filter and dry' stages of the synthesis procedure as it is only observed after 10 hrs. In addition, *ex situ* studies may produce inaccuracies and differences in the synthesis gels which could result in impurities, therefore repetition of all *ex situ* studies would be required to fully confirm the presence of any impurities. Nevertheless, the presence of this impurity AlPO-53 phase appears reasonable as it is known to form from the organic template methylamine (CH_3NH_2), which could indicate the breakdown of methyldicyclohexylamine (MCHA). At the longest time (60 hrs), all reflections are indexed to the tridymite structure with no signs of the AlPO-5 phase. A plot of the intensity of the most intense AFI reflection, $2\theta = 7.32°$ corresponding to the (100) crystallographic plane, and the most intense tridymite peak, $2\theta = 21.7°$ relating to the (40-4) plane, versus synthesis time is shown in Figure 4.10(B) and clearly shows the decomposition of the AlPO-5 structure coinciding with the crystallization of the dense tridymite phase. This is indicative of the kinetic AFI product transforming to the more thermodynamically stable tridymite.

4.4.3.1 Effect of divalent metal ions

The effect of divalent metal ions (10 wt %) on the AFI metastability was also investigated, the resulting *ex situ* XRD plots of the formation of ZnAlPO-5 at pH 5 employing MCHA as the organic template are illustrated in Figure 4.11. All reflections could be indexed to the AFI structure irrespective of the synthesis time, confirming phase purity throughout.

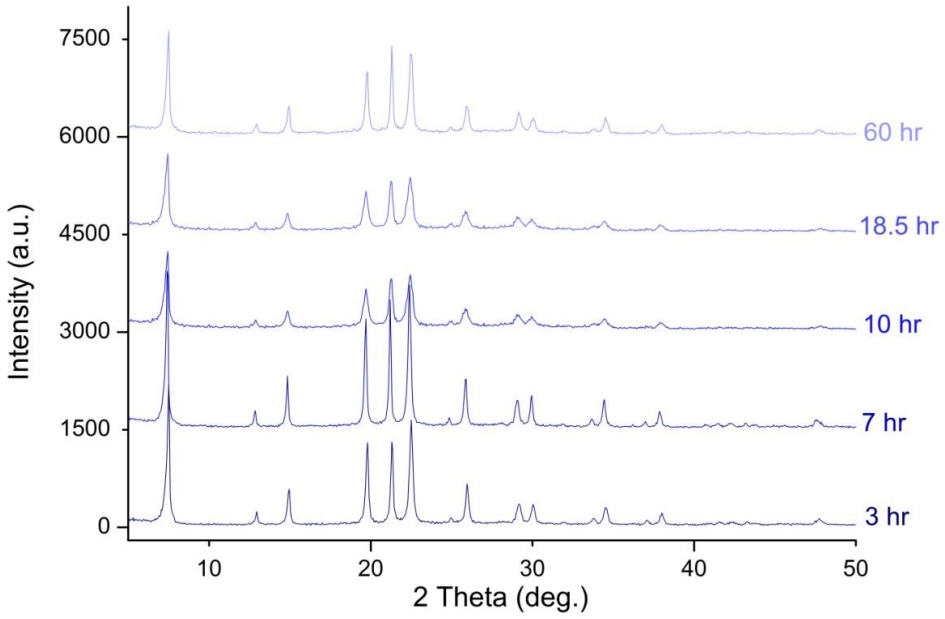

Figure 4.11. *XRD patterns at various times of* ***ZnAlPO-5*** *synthesized at* ***pH 5*** *employing* ***MCHA*** *as the organic template.*

To evaluate any decomposition of the ZnAlPO-5 structure, the intensity of the (100) reflection was compared to that of the AFI phase present for the analogous un-substituted AlPO-5 and plotted against time, Figure 4.12. The optimum crystallized ZnAlPO-5 structure is found at 7 hrs as the intensity of the (100) reflection is highest at this time indicating that crystal growth is not complete after 3 hrs, once again confirming divalent ions (10 wt %) retard AFI crystal growth. At longer times, the AlPO-5 phase decomposes gradually, however, in the presence of Zn(II) ions the intensity of the (100) reflection plateaus after 10 hrs and does not decompose any further. These results imply that the ZnAlPO-5 phase is more stable than the un-substituted AlPO-5 form (in terms of metastability) which may be indicative of a stronger non-bonding framework-template interaction in the presence of divalent metal ions. The transformation of the large pore AlPO-5 framework to the dense tridymite phase implies the expulsion of the organic template from the framework, and as this transformation was only observed with pure AlPO-5, this suggests a weaker interaction of MCHA with the neutral framework compared to the negatively charge ZnAlPO-5 structure.

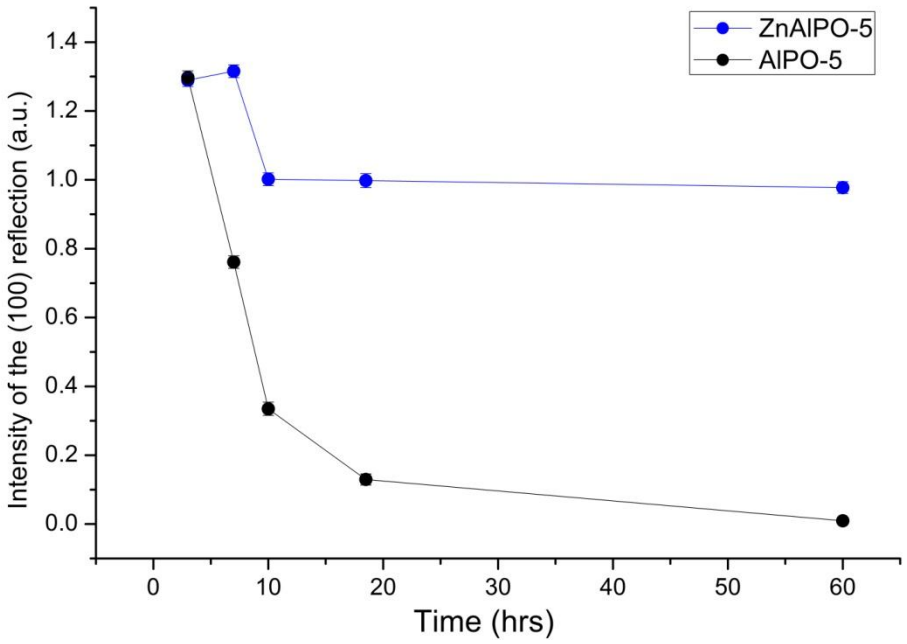

Figure 4.12. *Intensity of the most intense (100) reflection of the AFI phase present in AlPO-5 (black) or ZnAlPO-5 (blue) at pH 5 employing MCHA as the template.*

4.4.3.2 Effect of organic template on the stability of AFI

The large pore AlPO-5 structure can be formed with over 25 templates, and it is believed that these organic species stabilise certain phases during the synthesis via framework-template interactions[47]. Previously (section 4.4.1), the kinetics of AFI formation was found to be different depending on the organic template utilised, TEAOH promoted the AlPO-5 formation compared to MCHA. The decomposition of AlPO-5 involves the transformation of the porous framework, with the template located within the pores, to a dense phase in which the organic species is absent. Therefore, the type of organic template employed in the synthesis of AFI materials

may play a role in the metastability of this large-pore structure. Subsequently, the effect of the amines MCHA, TEA, and the quarternary ammonium cation TEAOH, on the decomposition of AlPO-5 in the reaction medium was investigated.

The XRD patterns collected at various times for the synthesis of AlPO-5 at pH 5, employing TEAOH or TEA as the organic template are shown in Figure 4.13. The results for the utilization of MCHA were shown and discussed previously (Figure 4.10). Although all templates produce pure phase AlPO-5 after 3 hours, as the synthesis time increases it is clear that the type of template not only affects the rate of decomposition but also what impurity phases are present.

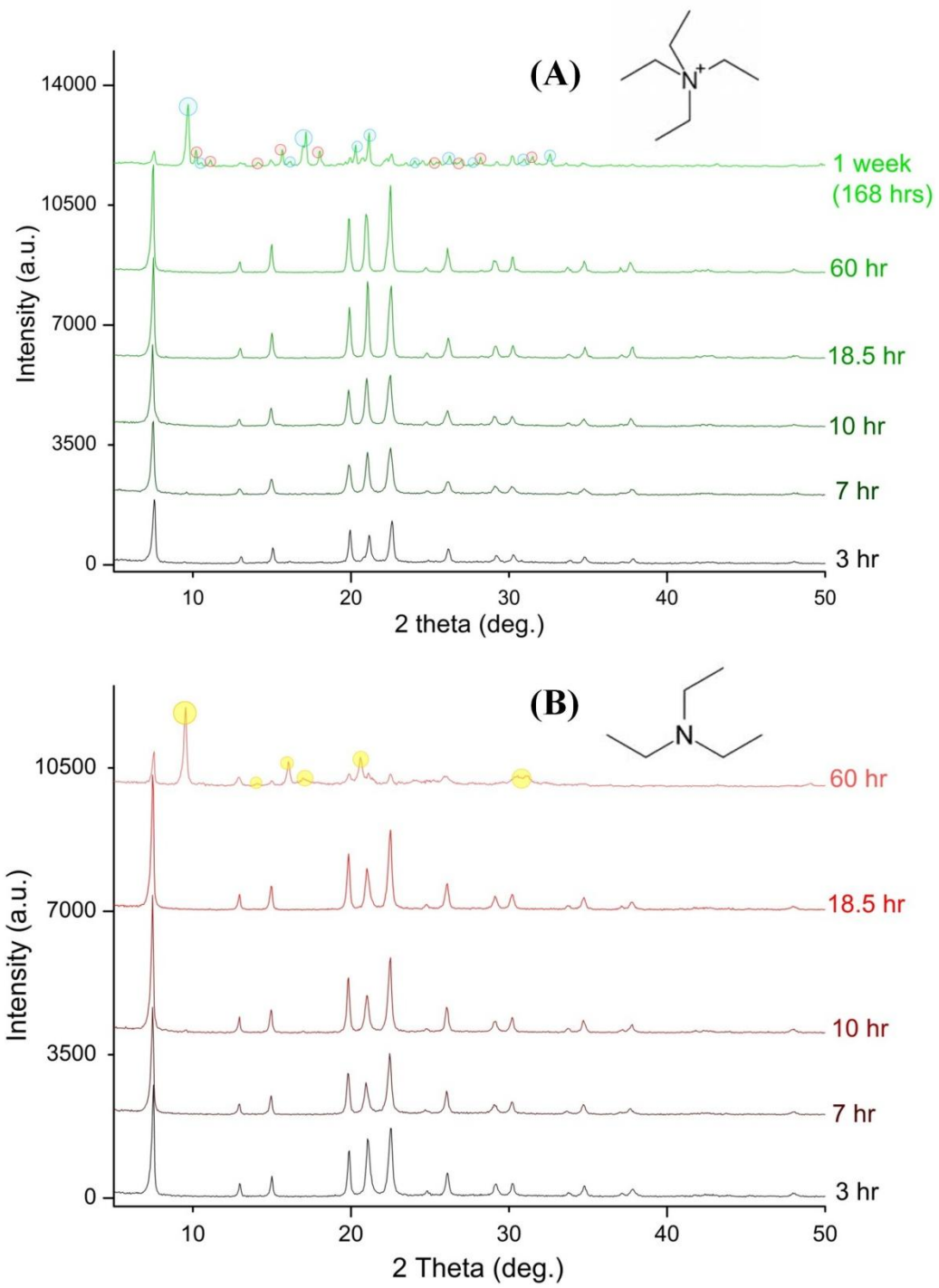

Figure 4.13. *XRD patterns of* ***AlPO-5*** *synthesized at* ***pH 5*** *employing either* ***TEAOH*** *(A) or* ***TEA*** *(B) as the organic template. Impurities from AlPO-18, AlPO-53, and AlPO-34 are highlighted in blue, red and yellow, respectively.*

As discussed previously, in the presence of MCHA (Figure 4.10), the first signs of tridymite appear after 7 hours as an impurity in the diffraction pattern and completely transforms from AlPO-5 to tridymite after 60 hours.

When TEAOH, Figure 4.13(A), is employed as the organic template and at times up to 60 hours, no impurities from tridymite, or any other phase are observed in the XRD data. It is only after 1 week that the AlPO-5 (TEAOH) structure is seen to decompose and large impurities from the small-pore AlPO-18 (AEI) structure, which is known to form with TEAOH and a pH greater than 6[35, 48], and the AlPO-53 (AEN) structure (also seen during AFI decomposition with MCHA) are observed. Surprisingly, there are still no reflections present form the dense tridymite phase, therefore this could indicate a transformation from the AFI structure to the AEI or AEN phases, with the most probable being to the more dense AEI structure. To clarify whether this is a sign of aluminophosphates following Ostwald's Law of Successive Transformations and not impurities from the 'wash filter dry' stage of the synthesis or from human errors, *in situ* XRD data collection would be required.

In the presence of TEA, Figure 4.13(B), decomposition of the AlPO-5 phase is only observed at times greater than 18.5 hours. Once again, the dense tridymite phase is not observed, instead reflections from the small pore AlPO-34 (CHA) structure appear. This is somewhat surprising since, although the CHA structure can form in the presence of TEA (pH >6), a dopant ion, such as cobalt or silicon, or hydrogen fluoride (HF) must be present [44, 49, 50]. As with the use of TEAOH, this may show AlPOs following Ostwald's Law of Successive Transformations but to support this

evidence, an *in situ* study during the decomposition of AlPO-5 with these two templates would be necessary.

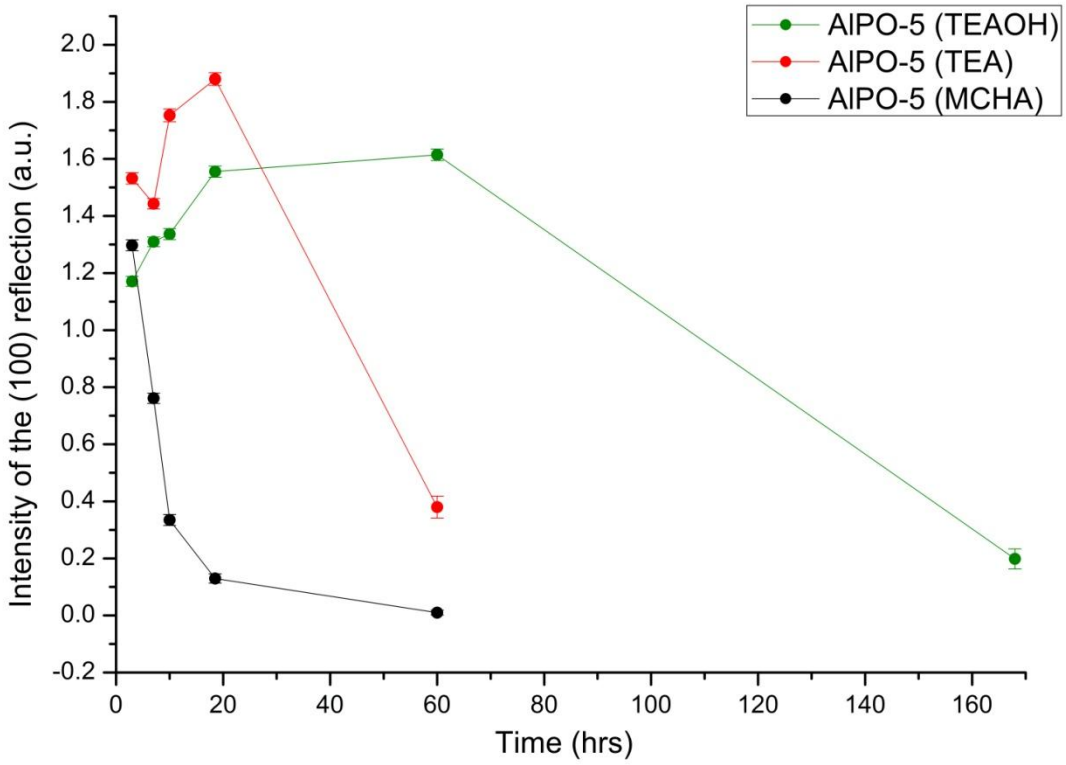

Figure 4.14. *The intensity of the most intense reflection associated with the (100) crystallographic plane of the AFI phase is plotted against synthesis time, for the use of MCHA (black), TEAOH (green) and TEA (red) as the organic template.*

The effect of the type of organic template used on the decomposition of the AFI structure was further examined; the intensity of the most intense (100) reflection as a function of time for each crystalline AFI phase for MCHA, TEAOH and TEA is represented in Figure 4.14. It is clear that the rate of decomposition of the AFI

structure in the reaction medium is the fastest when MCHA is employed as the template, followed by TEA and finally TEAOH. This is indicative of the protonated TEAOH template possessing stronger framework-template interactions compared to the amines MCHA and TEA. This agrees with a previous XRD combined with Density Functional Theory (DFT) study on the hydrothermal genesis of AlPO-5 with four different templates (MCHA, TEA, tripropylamine (TPA) and TEAOH)[19]. This investigation found, for both neutral and protonated forms of the organic templates, that TEAOH had the highest templating ability to form the AFI structure due to stronger framework-template interactions. In addition to this, the trend in the framework-template interactions was found to be TEAOH > TEA > MCHA > TPA, which agrees with this study for the metastability of AlPO-5; TEAOH is more stable than TEA which is more stable than MCHA.

From these results, a new approach of correlating the framework-template interactions and the ability to form the most metastable AlPO-5 structure can be proposed. This approach can also be applied in general to the synthesis of other template microporous materials.

4.4.3.3 Effect of pH

The pH of the synthesis gel is known to not only affect the type of structure formed but also the kinetics of aluminophosphate formation[4, 49, 51]. Therefore, the effect of pH on the metastability of the AFI framework in the reaction medium may provide additional information on the structural stability. The stability of the AlPO-5 framework in the reaction medium was investigated with MCHA as the organic template at pH 5 (Figure 4.10A), and at higher pH of 6.5 and 8 (Figure 4.15).

The XRD patterns collected at synthesis times of 3 hrs, confirm that MCHA produces pure phase AFI materials irrespective of the pH. At a longer synthesis time of 7 hrs, and in the presence of an amine, MCHA or TEA, reflections from the dense tridymite phase are also observed which grow in intensity as the synthesis time increases. This is not the case when a quarternary ammonium cation, TEAOH, is employed, large impurities from other phases do not appear in the diffraction pattern until 60 hours; in particular, reflections from the dense tridymite phase do not appear until after 1 week.

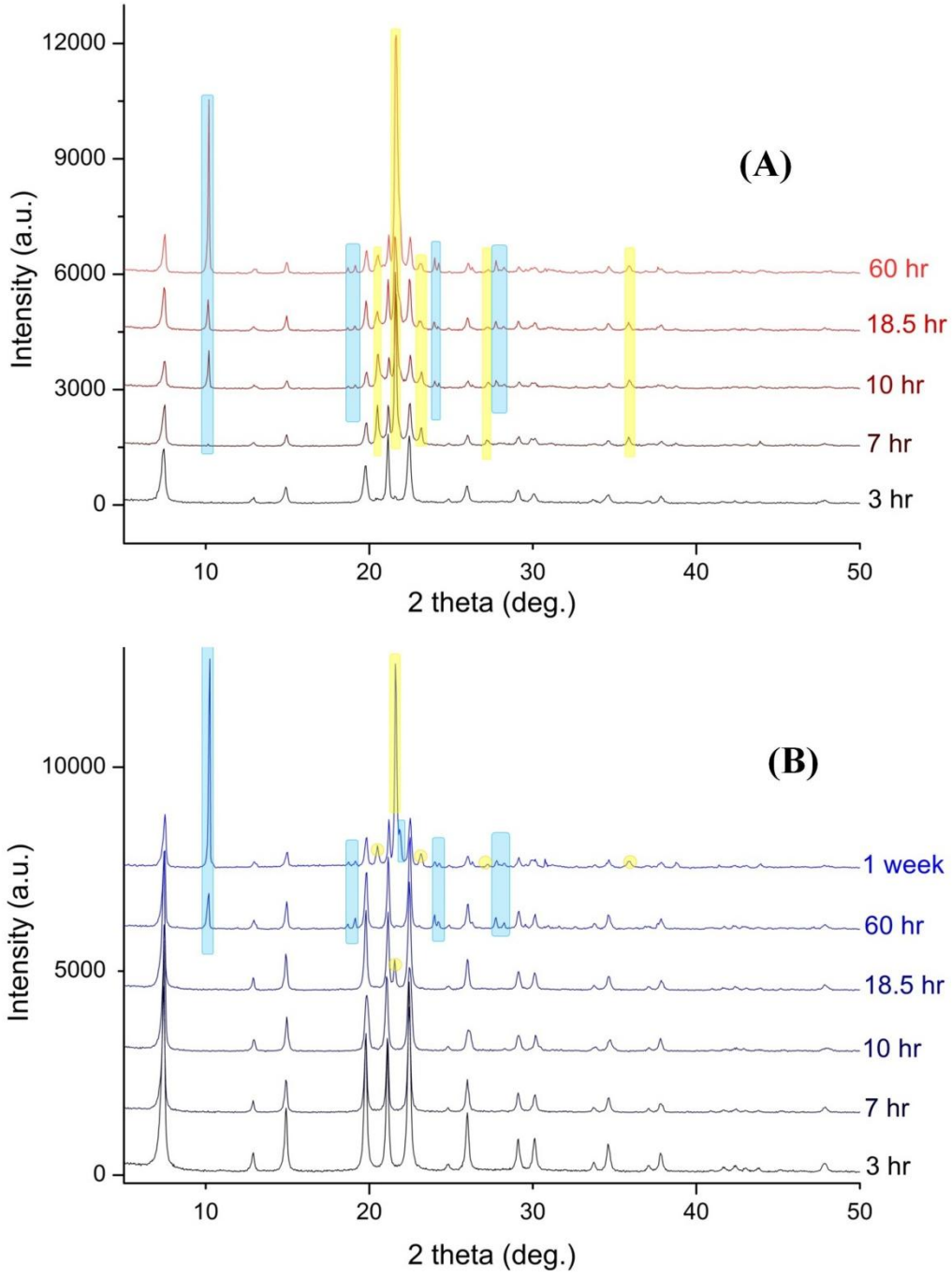

Figure 4.15. *Shown are the XRD patterns of* ***AlPO-5*** *synthesised at different times, with* ***MCHA*** *as the organic template, and at* ***pH 6.5*** *(A) or* ***pH 8*** *(B). ALL reflections at 3 hrs could be indexed to the AFI structure. Impurities from the AEN phase are highlighted in blue and the dense tridymite phase highlighted in yellow. The XRD patterns for AlPO-5 synthesized at pH 5 are shown in Figure 4.10(A).*

It is clear from the diffraction patterns collected at different synthesis times for AlPO-5 with MCHA and at various pH, that only impurities from the dense tridymite phase or the AEN structure are observed. The metastability of both the large pore AFI and small pore AEN structure appear to be pH dependent. Table 4-3 shows the phases formed at each synthesis time of pure AlPO-5 with MCHA at the various pHs. As the pH increases, the AFI phase becomes more stable in the reaction medium as the presence of the dense tridymite phase at pH 8 is not observed until after 1 week. The stability of the small pore AEN phase also appears to be pH dependent, increasing the pH increases its metastability as it is observed over a wider time range at higher pH.

Time / pH	3 hr	7 hr	10 hr	18.5 hr	60 hr	1 week
5	AFI	AFI TRI	AFI AEN TRI	AFI TRI	TRI	
6.5	AFI	AFI TRI	AFI AEN TRI	AFI AEN TRI	AFI AEN TRI	
8	AFI	AFI	AFI	AFI	AFI AEN	AFI AEN TRI

Table 4-3. *Illustrating the phases formed during the synthesis of AlPO-5 with MCHA as the organic template; AlPO-5 (AFI), AlPO-53 (AEN) and tridymite (TRI).*

The pH dependence of these phases and their metastabilities highlights the important role which OH^- anions play in the nucleation of aluminophosphates.

4.4.4 Summary and Conclusions

The kinetics of AlPO-5 formation was monitored by *in situ* HRXRD and the effect of divalent metal ions and organic template studied. Results showed that the quaternary ammonium cation, TEAOH, promotes the rapid formation of AFI crystals compared to the amine MCHA and may be a result of the larger positive charge on the TEAOH template. However, when a metal ion is incorporated into the synthesis gel along with TEAOH, impurities from the CHA phase are observed. This study found that zinc ions promote CHA formation before the AFI phase which suggests that these Zn(II) ions encourage denser rings and 'pockets' to form compared to Co(II) ions. This may be critical in the synthesis of new molecular sieves. In addition it was shown that when phase pure AlPO-5 materials form, divalent metal ions (5 wt %) reduce the induction period, and in the case of Co(II) ions doubles the rate constant.

The investigation on the effect of cobalt concentration on the kinetics of AFI formation confirmed with a weight % greater than 6, the kinetic trend is reversed; the induction period increases and the rate constant decreases. This study was unique, in that MCHA was used as the organic template with no impurities present in the XRD data. As a result, the reversal in the kinetics of formation could be solely attributed

to the increase in the metal ion concentration, and importantly not due to the presence of the CHA phase[6].

Finally, the findings showed that the metastability of these AlPO catalysts was directly related to the extent of framework-template interactions. In the presence of a divalent metal ion (zinc) and after 60 hours synthesis time, the XRD pattern still shows the formation of pure phase AFI. However, without a dopant ion the AlPO-5 material had transformed to the dense tridymite phase. This is indicative of weaker framework-template interactions of the neutral AlPO-5 framework (compared to the negatively charge ZnAlPO-5 framework) with MCHA as the dense tridymite phase does not encapsulate the organic species.

A study on the effect of organic templates on the metastability of AlPO-5 concluded that the quarternary ammonium cation, TEAOH, stabilised the AFI framework better than the amines TEA or MCHA. This agrees with a previous XRD/DFT investigation on the hydrothermal genesis of AlPO-5 which found that TEAOH had the best templating ability to form the AFI structure compared to TEA, MCHA and TPA due to greater template-framework interactions[19]. From these results, a new approach of correlating the framework-template interactions and the ability to form the most metastable AlPO-5 structure was proposed. This approach can also be applied in general to the synthesis of other template microporous materials. This study gives a better understanding of the role of the organic template in the synthesis of AlPOs, and may be useful in industrial scale up and optimization of AlPO-5 catalysts.

4.4.5 References

[1] Cundy, C. S.; Cox, P. A., *Microporous and Mesoporous Materials*, (2005) **82**, 1.

[2] Ostwald, W., *Physical Chemistry* (1897) **22**, 289.

[3] Budd, P. M.; Myatt, G. T.; Price, C.; Carr, S. W., *Zeolites*, (1994) **13**, 198.

[4] Francis, R. J.; O'Hare, D., *Journal of the Chemical Society-Dalton Transactions*, (1998), 3133.

[5] Norby, P., *Current Opinion in Colloid & Interface Science*, (2006) **11**, 118.

[6] Davies, A. T.; Sankar, G.; Catlow, C. R. A.; Clark, S. M., *Journal of Physical Chemistry B*, (1997) **101**, 10115.

[7] Sanchez-Sanchez, M.; Sankar, G.; Simperler, A.; Bell, R. G.; Catlow, C. R. A.; Thomas, J. M., *Catalysis Letters*, (2003) **88**, 163.

[8] Bennett, J. M.; Cohen, J. P.; Flanigen, E. M.; Pluth, J. J.; Smith, J. V., *Acs Symposium Series*, (1983) **218**, 109.

[9] Chiang, A. S. T.; Lee, C. K.; Chang, Z. H., *Zeolites*, (1991) **11**, 380.

[10] Concepcion, P.; Nieto, J. M. L.; Mifsud, A.; PerezPariente, J., *Applied Catalysis a-General*, (1997) **151**, 373.

[11] Finger, G.; Richtermendau, J.; Bulow, M.; Kornatowski, J., *Zeolites*, (1991) **11**, 443.

[12] Girnus, I.; Jancke, K.; Vetter, R.; Richtermendau, J.; Caro, J., *Zeolites*, (1995) **15**, 33.

[13] Qiu, S. L.; Pang, W. Q.; Kessler, H.; Guth, J. L., *Zeolites*, (1989) **9**, 440.

[14] Robson, H.; Lillerud, K. P., *Verified Syntheses of Zeolitic Materials*, Robson, H. Ed. Elsevier: Amsterdam, (2001).

[15] Tuel, A., *Zeolites*, (1995) **15**, 228.

[16] Wilson, S. T.; Flanigen, E. M., *Acs Symposium Series*, (1989) **398**, 329.

[17] Wilson, S. T.; Lok, B. M.; Messina, C. A.; Cannan, T. R.; Flanigen, E. M., *Journal of the American Chemical Society*, (1982) **104**, 1146.

[18] Young, D.; Davis, M. E., *Zeolites*, (1991) **11**, 277.

[19] Elanany, M.; Su, B. L.; Vercauteren, D. P., *Journal of Molecular Catalysis a-Chemical*, (2007) **270**, 295.

[20] Thompson, S. P.; Parker, J. E.; Potter, J.; Hill, T. P.; Birt, A.; Cobb, T. M.; Yuan, F.; Tang, C. C., *Review of Scientific Instruments*, (2009) **80**,

[21] Treacy, M. M. J.; Higgins, J. B., *Collection of Simulated XRD Powder Diffraction Patterns for Zeolites*, Elsevier: Amsterdam, (2007).

[22] Software, C., TOPAS-Academic Version 4.1, In Coelho, A. Ed. Brisbane, Australia, (2007).

[23] Klap, G. J.; van Koningsveld, H.; Graafsma, H.; Schreurs, A. M. M., *Microporous and Mesoporous Materials*, (2000) **38**, 403.

[24] González, G.; Piña, C.; Jacas, A.; Hernández, M.; Leyva, A., *Microporous and Mesoporous Materials*, (1998) **25**, 103.

[25] Simmen, A.; McCusker, L. B.; Baerlocher, C.; Meier, W. M., *Zeolites*, (1991) **11**, 654.

[26] Kirchner, R. M.; Grosse-Kunstleve, R. W.; Pluth, J. J.; Wilson, S. T.; Broach, R. W.; Smith, J. V., *Microporous and Mesoporous Materials*, (2000) **39**, 319.

[27] Hirose, T.; Kihara, K.; Okuno, M.; Fujinami, S.; Shinoda, K., *Journal of Mineralogical and Petrological Sciences*, (2005) **100**, 55.

[28] Grandjean, D.; Beale, A. M.; Petukhov, A. V.; Weckhuysen, B. M., *Journal of the American Chemical Society*, (2005) **127**, 14454.

[29] Norquist, A. J.; O'Hare, D., *Journal of the American Chemical Society*, (2004) **126**, 6673.

[30] Hancock, J. D.; Sharp, J. H., *Journal of the American Ceramic Society* (1972) **55**, 74.

[31] Hulbert, S. F., *Journal of the British Ceramic Society*, (1969) **6**, 11.

[32] Baerlocher, C.; McCusker, L. B.; Olson, D. H., *"Atlas of Zeolite Framework Types", 6th edition*, Elsevier: Amsterdam, (2007).

[33] Deng, F.; Yue, Y.; Xiao, T. C.; Du, Y. U.; Ye, C. H.; An, L. D.; Wang, H. L., *Journal of Physical Chemistry*, (1995) **99**, 6029.

[34] Hartmann, M.; Kevan, L., *Chemical Reviews*, (1999) **99**, 635.

[35] Muncaster, G.; Davies, A. T.; Sankar, G.; Catlow, C. R. A.; Thomas, J. M.; Colston, S. L.; Barnes, P.; Walton, R. I.; O'Hare, D., *Physical Chemistry Chemical Physics*, (2000) **2**, 3523.

[36] Rey, F.; Sankar, G.; Thomas, J. M.; Barrett, P. A.; Lewis, D. W.; Catlow, C. R. A.; Clark, S. M.; Greaves, G. N., *Chemistry of Materials*, (1995) **7**, 1435.

[37] Sankar, G.; Okubo, T.; Fan, W.; Meneau, F., *Faraday Discussions*, (2007) **136**, 157.

[38] Sankar, G.; Thomas, J. M.; Rey, F.; Greaves, G. N., *Journal of the Chemical Society-Chemical Communications*, (1995), 2549.

[39] van Santen, R. A., *Nature*, (2006) **444**, 46.

[40] Lewis, D. W.; Catlow, C. R. A.; Thomas, J. M., *Chemistry of Materials*, (1996) **8**, 1112.

[41] Norby, P.; Christensen, A. N.; Hanson, J. C., *Stud. Surf. Sci.Catal.*, Weitkamp, J.; Karge, H. G.; Pfeifer, H.; Holderich, W. Eds.; Elsevier: Amsterdam, (1994); Vol. 84.

[42] O'Brien, M. G.; Beale, A. M.; Catlow, C. R. A.; Weckhuysen, B. M., *Journal of the American Chemical Society*, (2006) **128**, 11744.

[43] Raghavan, V.; Cohen, M., *Solid State Phase Transformations. Treatise on Solid State Chemistry*, Hannay, N. B. Ed. Plenum Press: New York, (1975); Vol. 5, Chapter 2.

[44] Marchese, L.; Frache, A.; Gianotti, E.; Martra, G.; Causà, M.; Coluccia, S., *Microporous and Mesoporous Materials*, (1999) **30**, 145.

[45] Beale, A. M.; Sankar, G., *Chemistry of Materials*, (2003) **15**, 146.

[46] Fogg, A. M.; Price, S. J.; Francis, R. J.; O'Brien, S.; O'Hare, D., *Journal of Materials Chemistry*, (2000) **10**, 2355.

[47] Gomez-Hortiguela, L.; PerezPariente, J.; Cora, F.; Catlow, C. R. A.; Blasco, T., *Journal of Physical Chemistry B*, (2005) **109**, 21539.

[48] Wendelbo, R.; Akporiaye, D.; Andersen, A.; Dahl, I. M.; Mostad, H. B., *Applied Catalysis a-General*, (1996) **142**, L197.

[49] Jhung, S. H.; Hwang, Y. K.; Chang, J. S.; Park, S. E., *Microporous and Mesoporous Materials*, (2004) **67**, 151.

[50] Concepcion, P.; Nieto, J. M. L.; Mifsud, A.; PerezPariente, J., *Zeolites*, (1996) **16**, 56.

[51] Newalkar, B. L.; Kamath, B. V.; Jasra, R. V.; Bhat, S. G. T., *Zeolites*, (1997) **18**, 286.

Chapter 5. A structural study on the extent of heteroatom incorporation in mono- and multi-ion substituted aluminophosphate catalysts.

5.1 Chapter Overview

This chapter discusses the results obtained from an investigation into the extent of heteroatom incorporation into the framework of a number of mono- and multi-substituted AFI materials. An *ex situ* high-resolution X-ray diffraction (HRXRD) study revealed an expansion of the a(=b) parameter in the AFI structure with increasing metal ion concentration and with an increase of the ionic radii for a number of different divalent and tetravalent metal ions. Relative information on the amount of heteroatom substitution was obtained and is discussed for both mono- and multi- metal ion substituted AlPO-5 materials. To ascertain additional detailed information on the extent of substitution in multi-ion AFI materials containing titanium, *in situ* XAS at the Ti K edge during calcination in air was carried out. The XAS results, in accordance with the expansion of the unit cell, suggested that the introduction of a divalent metal ion to the TAPO-5 synthesis gel does not have a significant effect on the Ti(IV) incorporation in the AFI framework. In contrast, the incorporation of a tetravalent metal ion with Ti(IV) in the AFI synthesis mixture decreases the amount framework titanium.

5.2 Introduction

Zeolitic and aluminophosphate (AlPO) materials are of interest due to their applications in industrially important catalytic processes, in which their acidic and catalytic properties can be controlled through the substitution of heteroatoms into their frameworks. The concentration and types of metal ions that may be substituted in silicate based zeolitic systems are limited to the trivalent (Fe, Al Ga, B) or tetravalent (Ti, V) metal ions. Conversely, aluminophosphate based systems can host a wider range of metal ion types with higher concentrations (*ca.* 10 wt. % compared to *ca.* 1 wt. % of redox metal ions in siliceous zeolites) in a variety of structures. For example, Al(III) can be substituted by divalent or trivalent metal ions (Fe(III), Co(II) etc), and the P(V) sites can be replaced by tetravalent or pentavalent heteroatoms (Si(IV), V(V) etc). The incorporation (in this work via isomorphous substitution) of heteroatoms into the AlPO framework renders the framework negative and leads to the formation of Brønsted and/or redox acid sites, resulting in the materials possessing catalytic activity. In addition, the introduction of heteroatom ions into the framework of AlPOs has led to the discovery of more than 20 novel structures. For these reasons, their incorporation has been the subject of extensive research.

More recently, multi-metal ion substituted nanoporous zeolitic solids have attracted considerable attention due to the creation of multi-functional catalytic solids. For example, substituting a combination of both redox metal ions, such as Co(II) or

Ti(IV), and metal ions that generate a Brønsted acid site, such as Zn(II) or Si(IV), into a AlPO framework will introduce both acid and redox functionality upon removal (calcination in air) of the charge compensating organic template.

Only a few publications have investigated the simultaneous incorporation of more than one heteroatom into the AlPO framework [1-5]. The majority of these studies have focussed on the large pore 1-dimensional channel system AlPO-5 (the structure of which is discussed in Chapter 3 (3.2.1)) as a large number of heteroatoms can be easily incorporated into its framework [3, 6, 7]. Recently, a higher activity for the selective oxidation of cyclohexane[2] and the oxidation of ethane[8] has been observed in the presence of multi-ion metal (combinations of Co(II), Cr(III) and V(IV)) incorporated AFI materials compared to the single metal substituted analogues. Blasco et al.[9] found MgVAPO-5 to have a higher selectivity towards ethylene in the oxidative dehydrogenation of ethane compared to VAPO-5 due to the presence of Brønsted acid sites. Similarly, Kapoor et al.[4] concluded that VTAPO-5 was more active for the partial oxidation of methanol compared to TAPO-5, with the formation of more complex products compared to VAPO-5. These studies suggest that substituting the AlPO framework with more than one type of metal ion may have many advantages. These include the creation of new potential catalysts, the formation of different reaction intermediates (due to the difference in acid strength and the number of reactive sites) and may even reveal the preference of one metal over another[2].

5.2.1 Indirect and direct methods for verifying isomorphous substitution

Heteroatoms, such as transition metal ions, can either exist in the framework sites of the AlPO structure or as oxides and extra-framework cations on the surface. There are many different techniques which are commonly employed to confirm the incorporation of metal ions into the framework of AlPOs. These include both indirect methods – for example, chemical analysis, expansion of the unit cell, formation of Brønsted acid sites and weight loss during calcination and direct methods such as spectroscopic techniques including UV-Vis spectroscopy (DRS), electron spin resonance (ESR) and X-ray absorption spectroscopy (XAS)[10, 11]. Each technique offers many advantages and disadvantages suggesting that a combination of two or more complementary techniques may be an effective approach to elucidate whether a heteroatom has been incorporated into the framework of AlPO-5.

Expansion of the unit cell assumes that the symmetry of the material remains unchanged upon the incorporation of a metal ion into the framework. The majority of high-spin tetrahedrally coordinated metal ions have larger ionic radii compared to that of Al(III) and P(V), therefore an expansion in the unit cell is expected depending on the extent of incorporation. A technique used to determine the unit cell parameters of crystalline materials is X-ray diffraction (XRD). The AFI framework has hexagonal symmetry, therefore the unit cell parameters are related to the measured *d* spacing of the observed peaks in the diffraction pattern via Equation 5-1. Where *a* and *c* are the unit cell parameters of the hexagonal structure, *hkl* are the miller indices, *d* is the

inter-planar spacing between the crystal planes, θ is the diffraction angle and λ is the X-ray wavelength.

Equation 5-1. *Relationship of the unit cell parameters with the measured d spacing and Bragg's Law for a structure with hexagonal symmetry.*

$$\frac{1}{d^2} = \frac{4(h^2 + hk + k^2)}{3a^2} + \frac{l^2}{c^2} = \frac{4sin^2\theta}{\lambda^2}$$

An expansion of the AFI unit cell upon heteroatom incorporation has been reported in the literature, both experimentally and theoretically, for a number of different types of metals, including Co(II), Zn(II), Sn(II), Ca(II), Mg(II), Sr(II), Ba(II), Fe(III) and V(V)[12-17]. In particular, the a(=b) parameter increases (including the volume) with the substitution of a larger metal ion for Al(III) or P(V), however there are mixed opinions in the literature on whether the c parameter increases or decreases. Overall, it is clear that more experimental and theoretical studies are required to attain a general trend on the expansion of the unit cell of mono- and multi- metal substituted AlPOs.

One possible disadvantage with this method (expansion of the unit cell) for verifying the extent of metal ion incorporation is that there may not be a sufficient change in the unit cell dimensions, within experimental error, when small amounts of heteroatoms are incorporated into the AlPO framework. Furthermore, it may be difficult to distinguish between heteroatoms for multi-metal ion substituted materials.

XAS, on the other hand, is a direct method for determining the extent of metal ion incorporation in AlPO frameworks. This technique is sensitive to the local structure of a specific atom and provides information on the average coordination environment and oxidation state. This information can then be used to determine whether the heteroatom is incorporated into the AlPO framework in the tetrahedral sites. Therefore, it is apparent that the combination of both XRD and XAS can provide sufficient information to determine the extent of metal ion substitution in mono- and multi- metal ion substituted AFI materials.

5.2.2 Aims and objectives

The objective of this work was to use indirect methods to verify the extent of metal ion substitution in AlPO materials. For this purpose, a number of mono- and multi-ion substituted large pore AFI materials were investigated through XRD to determine the change in their unit cell parameters with increasing metal ion concentration.

The incorporation of titanium(IV) into the framework of zeolitic and AlPO materials has been a challenge for many years, and has potential importance for a number of oxidation reactions, such as the epoxidation of alkenes and the oxidation of alkanes to their respective acids[18-20]. Therefore, AlPO-5 materials containing Ti(IV) were further characterized by XAS to determine whether the synthesis method or incorporation of more than one type of metal had a positive effect on the substitution of Ti(IV) into the AFI framework. XAS is particularly sensitive to

distortions around the framework ions which may occur in the presence of adsorbed species such as water molecules, therefore, for reliable results this technique was carried out during calcination of the AFI materials which removes the organic template and any water molecules.

5.3 Experimental

5.3.1 Synthesis of mono- and multi-metal substituted AFI materials

In a typical synthesis experiment, AFI molecular sieves were prepared by the hydrothermal reaction of a gel mixture with the following general composition: **(1-*x*) Al: *x* Me(II): (1-*y*) P: *y* Me(IV): 25 H_2O: 0.8 MCHA**, where Me(II) is a divalent metal ion, Me(IV) is a tetravalent metal ion and MCHA is the organic template *N*-methyldicyclohexylamine. The precursors for each component were phosphoric acid (H_3PO_4 in H_2O, 85 wt %), aluminium hydroxide hydrate ($Al(OH)_3$) and MCHA (97 wt%). The metal ions were sourced from the following precursors: cobalt(II) acetate tetrahydrate ($(CH_3COO)_2Co{\cdot}4H_2O$), zinc(II) acetate dihydrate ($Zn(CH_3COO)_2{\cdot}2H_2O$), iron(II) acetate ($Fe(CO_2CH_3)_2$), LUDOX AS-40 colloidal silica (SiO_2, 40 wt % in H_2O) and titanium(IV) butoxide ($Ti(OCH_2CH_2CH_2CH_3)_4$). In addition, the titanium(IV) butoxide was dissolved in a small amount of Propan-2-ol ($(CH_3)_2CHOH$) to avoid hydrolysis of the titanium centre. It should be noted that all precursors were purchased from Aldrich.

A number of different mono- and multi- metal substituted AFI materials were synthesised; the molar weights of the divalent and tetravalent metal ions for each AFI sample are listed in Table 5-1.

AFI sample name	Co(II)	Zn(II)	Fe(II)	Si(IV)	Ti(IV)	
					Ti(IV) butoxide	Propan-2-ol
AlPO-5	-	-	-	-	-	-
CoAlPO-5 (4%)	0.04	-	-	-	-	-
CoAlPO-5 (7%)	0.07	-	-	-	-	-
CoAlPO-5 (10%)	0.10	-	-	-	-	-
ZnAlPO-5 (1%)	-	0.01	-	-	-	-
ZnAlPO-5 (4%)	-	0.04	-	-	-	-
SAPO-5 (4%)	-	-	-	0.04	-	-
TAPO-5 (4%)	-	-	-	-	0.04	0.65
TAPO-5 (7%)	-	-	-	-	0.07	0.80
TAPO-5 (10%)	-	-	-	-	0.10	0.95
CoZnAlPO-5 (4:1%)	0.04	0.01	-	-	-	-
CoZnAlPO-5 (4:4%)	0.04	0.04	-	-	-	-
CoSAPO-5 (4:1%)	0.04	-	-	0.01	-	-
CoSAPO-5 (4:4%)	0.04	-	-	0.04	-	-
CoTAPO-5 (4:1%)	0.04	-	-	-	0.01	0.50
CoTAPO-5 (4:4%)	0.04	-	-	-	0.04	0.65
FeTAPO-5 (4:4%)	-	-	0.04	-	0.04	0.65
TAPSO-5 (4:4%)	-	-	-	0.04	0.04	0.65

Table 5-1. *The associated molar weights of the divalent (x) and tetravalent (y) metal ions in the synthesis of a number of mono- and multi- ion substituted AFI materials with general composition; (1-x) Al: x Me(II): (1-y) P: y Me(IV): 25 H_2O: 0.8 MCHA. For the multi- metal substituted AFI materials, the metal added first to the synthesis gel is highlighted in red and the metal which followed is highlighted in blue.*

The mono- and multi- metal ion substituted AFI materials were prepared in accordance with the following procedure. First, the divalent metal acetate was dissolved in a minimum amount of distilled water. The remaining water was then added to phosphoric acid. Aluminium hydroxide hydrate was slowly added to the phosphoric acid solution and stirred until the solution was homogeneous. Next, either the divalent metal ion solution was added or the equivalent metal precursor (SiO_2 or titanium butoxide dissolved in propan-2-ol) and the solution stirred for *ca.* 15 minutes. For the multi-metal substituted AFI materials, another metal source was then added to the gel and stirred for a further 15 minutes. The gel was stirred with a magnetic stirrer for an hour, followed by the drop wise addition of the organic template, MCHA. Once again the gel was stirred for another hour and the pH measured. The pH was adjusted through the addition of phosphoric acid to achieve a pH of 7.

TAPO-5 (4%) was also synthesised via a different procedure, 'method 2', in this method the titanium precursor (dissolved in propan-2-ol) was added to the synthesis gel after the organic template instead of prior.

The gel was transferred to a Teflon lined steel autoclave with an approximate 60% fill volume and heated at temperature 170 ºC for 3 hours. The resulting solids were washed with distilled water, filtered and dried at 100°C overnight.

5.3.2 Characterisation

5.3.2.1 X-ray Diffraction

Ex situ high-resolution X-ray Diffraction (HRXRD) data was collected at the I11 beamline of the Diamond Light Source in Oxford, England[21]. The set-up of this beamline is described elsewhere (Chapter 4: 4.3.2.2). The samples were loaded into 0.5mm capillaries and data collected at λ = 0.82743 Å employing the position-sensitive detector (PSD) available, with an acquisition time of 1 minute per scan (total of 2 scans per sample).

Accurate unit cell parameters of the AFI structures were calculated with a Pawley reflection fit performed with the fundamental parameter approach (FPA) available with TOPAS-academic[22]. Starting unit cell parameters of the AFI phase taken from Klap et al.'s single crystal XRD study, a(=b) = 13.718 Å, c = 8.4526 Å, α=β = 90° and γ = 120° with hexagonal space group P6cc (184), were utilized[23]. All plots were prepared using the data analysis and graphing Origin Pro 8 software[24].

5.3.2.2 X-ray absorption spectroscopy

In situ X-ray Absorption Spectroscopy (XAS) measurements were carried out to determine the substitution, oxidation state and coordination environment of titanium in a number of mono- and multi- metal substituted AFI materials during calcination in air. XAS measurements were collected at the B18 (core EXAFS) beamline[25] of Diamond Light Source, which operates at 3 GeV with a typical current of 300 mA. The optics hutch was constructed of a collimating mirror, a water-cooled double crystal (Si(111) and Si(311)) monochromator and a focusing mirror. The experiment hutch was equipped with ion chambers for measuring incident, I_0, and transmitted, I_t, beam intensities and a fluorescence detector, FF, for collecting information on dilute samples (a portable Vortex 9 element Ge detector). A schematic illustration of the setup available is shown in Figure 5.1.

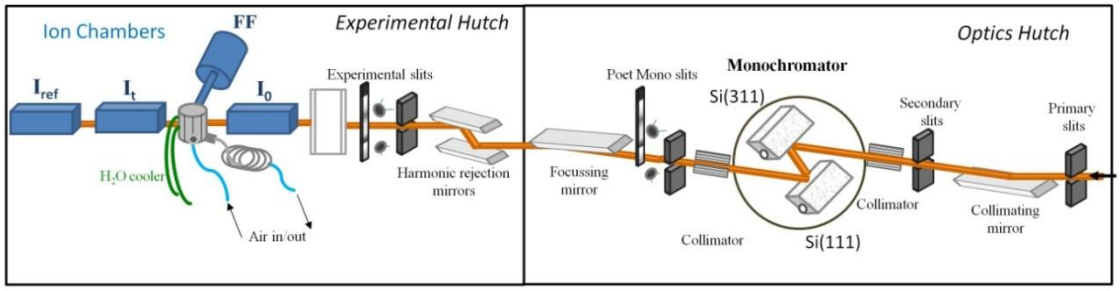

Figure 5.1. *A schematic illustration of the set-up used at the B18 beamline of Diamond Light Source, showing the optics and experimental hutches. It should be noted that the fluorescence screens have not been shown for clarity.*

In a typical experiment, ca. 80 mg of sample was pressed into a 13 mm disc and placed into a custom built *in situ* high temperature furnace (see Figure 5.2) for heat treatment to 550 °C (5 °C/minute), which was dwelled for 40 minutes, in an atmosphere of oxygen (air). X-ray Absorption Near Edge Structure (XANES) data were recorded during the calcination at the Ti K edge (4966 eV) in fluorescence mode with a total acquisition time per scan of *ca.* 40 minutes. All XANES data was processed utilising the program Athena to background remove and normalise the data[26].

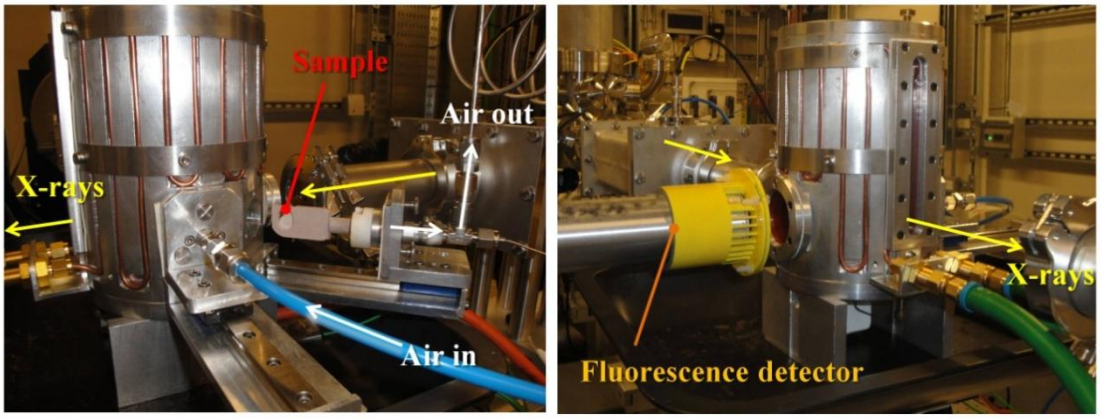

Figure 5.2. *Photographs of the in situ high temperature furnace employed for the XAS experiments during the calcination of a number of aluminophosphate materials.*

5.4 Results and Discussion

5.4.1 HRXRD study of mono- and multi- heteroatom substituted AlPO-5 materials

High resolution X-ray diffraction (HRXRD) data was collected for a variety of mono- (Co, Zn, Si, Ti) and multi- (CoZn, CoSi, CoTi) ion substituted AFI- type materials which had a mixture of heteroatom weight percentages (wt. %). These were then compared to their un-substituted analogue, AlPO-5.

Figure 5.3 shows the HRXRD patterns acquired for the as-synthesised mono- (4 wt. %) and multi- (4 wt. % + 4 wt. %) metal substituted AFI- type materials. The results indicate that, irrespective of the type of dopant ion and with MCHA as the organic template, all AlPO-5 type materials were crystalline and phase pure on comparison with reported literature[27]. This illustrates the high specificity that MCHA is known to have to direct the formation of the AFI structure[28].

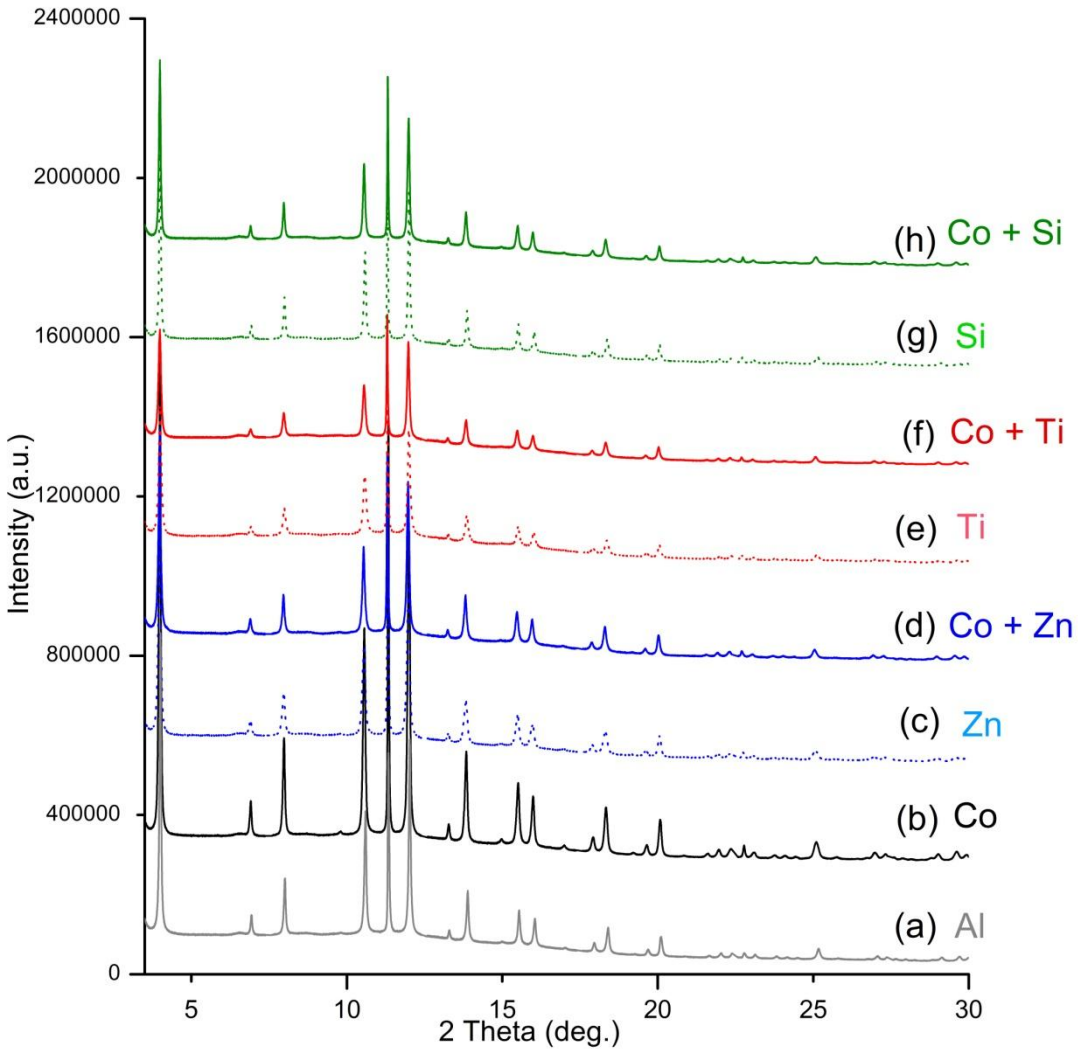

Figure 5.3. *HRXRD patterns of the as synthesised (a) AlPO-5 material and the mono- (4 wt. %) and multi- (4 wt. % + 4 wt. %) ion substituted analogues; (b) CoAlPO-5, (c) ZnAlPO-5, (d) CoZnAPO-5, (e) TAPO-5, (f) CoTAPO-5, (g) SAPO-5 and (h) CoSAPO-5. All reflections could be indexed to the AFI structure.*

5.4.1.1 Crystallinity

All mono- and multi- metal substituted AlPO-5 materials were subjected to the same synthesis procedure, with a temperature of 170 °C and a time of 3 hours, irrespective of the type and weight percent of the metal ion. Therefore, the crystallinity of the AFI products may provide information on whether the type of metal ion and the incorporation of two metal ions, promotes the formation of the AlPO-5 structure.

The crystallinity of the mono- (4 wt. %) ion substituted AlPO-5 materials were compared to each other and the resulting crystallinity trend was as follows: CoAlPO-5 > AlPO-5 > ZnAlPO-5 = SAPO-5 > TAPO-5.

This corresponds with the previous study on following the formation of CoAlPO-5 materials with *in situ* XRD (Chapter 4), which revealed that below 6 wt. % cobalt ions promoted the formation of AlPO-5. The substitution of Al(III) with a different divalent metal ion, Zn(II), affects the kinetics of formation in such a way as to slow down the crystallinity and may be a direct consequence from Zn(II) ions having a slightly larger ionic radii (0.6 Å, an increase of 54 % from Al(III)) compared to Co(II) (0.58 Å, an increase of 49 % from Al(III)).

Similarly, the substitution of phosphorus with a larger tetravalent ion, such as silicon (0.26 Å, an increase of 53 % from P(V)) or titanium (0.42 Å, an increase of 147 % from P(V)), decreases the kinetics of formation resulting in diffraction patterns with lower crystallinity. Therefore, this trend observed in the crystallinity of the

mono- substituted AFI materials suggests that an increase greater than 50 % in the ionic radii of the substituting ion retards crystal growth.

On comparison of the crystallinity of the mono- (4 wt. %, Co, Zn, Si, Ti) with the multi- (4 wt. % + 4 wt. %, CoZn, CoSi, CoTi) ion substituted AFI materials, as shown in Figure 5.4, no difference is observed in the crystallinity of the diffraction patterns when 4 wt. % of cobalt ions are introduced into the synthesis gel. For example, the crystallinity of ZnAlPO-5 (4%) was comparable to CoZnAlPO-5 (4:4%), similarly the crystallinity of TAPO-5 (4%) was comparable to CoTAPO-5 (4:4%) and so on. This suggests that the introduction of 4 wt. % Co(II), which substitutes for Al(III) and has been found to promote the formation of AFI materials, does not have a significant effect on the crystallisation of the large pore AlPO-5 framework when another metal is present in the framework. Therefore, the crystallisation is limited to the heteroatom which has the slowest crystallisation rate or longest induction period.

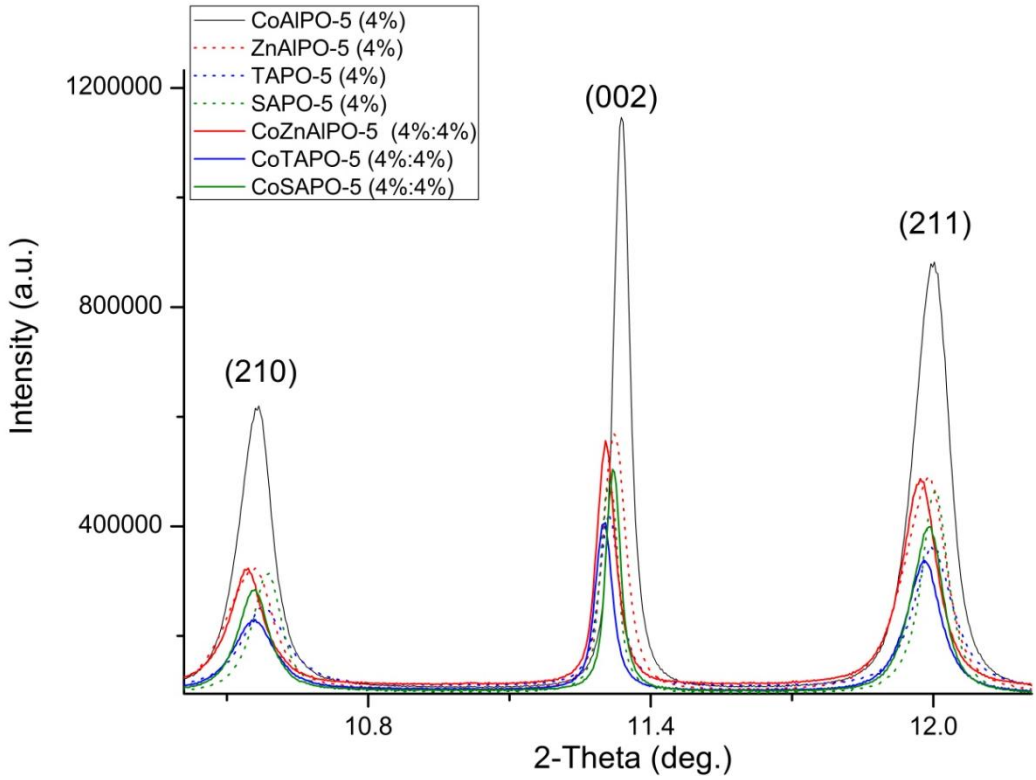

Figure 5.4. *Illustrating the change in the crystallinity of the mono- and multi- metal ion substituted AFI materials. Shown are the (210), (002) and (211) reflections.*

In addition, the increase in weight percent of the heteroatoms substituting into the AFI framework, from 4 wt. % (mono metal) to 8 wt. % (multi metal, 4 wt.% + 4wt. %) does not retard the crystallisation process. This is surprising since it has been shown previously that increasing the percentage (>6 wt. %) of a single heteroatom substituting into the AlPO-5 framework, significantly retards the AFI crystallisation. This was also apparent on analysis of the HRXRD patterns collected for CoAlPO-5 (Co(II) substitutes for Al(III)) and TAPO-5 (Ti(IV) substitutes for Al(III)) with metal percents of 4, 7 and 10, in which the crystallinity of the diffraction pattern was found to decrease on increasing the metal percent (see Figure 5.5). Therefore, it appears

that the heteroatoms in the multi-ion substituted AFI materials are independent of one another.

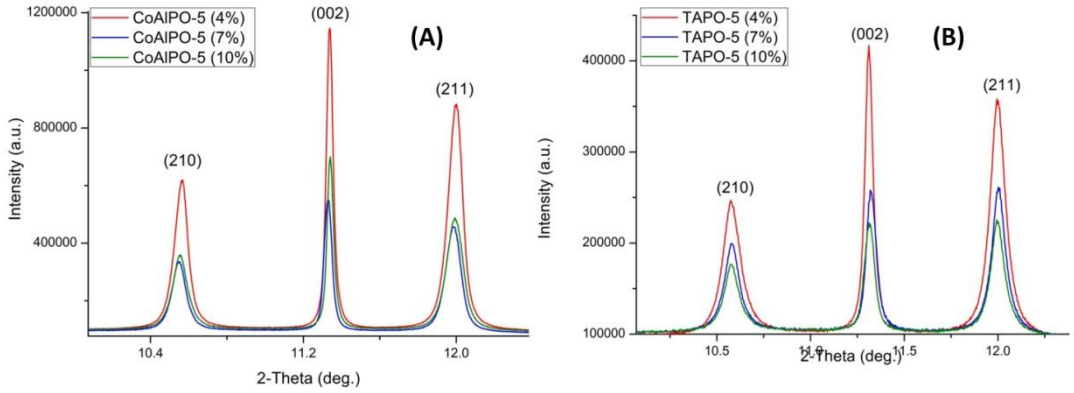

Figure 5.5. *Illustrating the difference in crystallinity of the mono- metal substituted AFI materials as the metal percent increases. Showing the trend similarities for (A) cobalt substituting for Al(III) and (B) titanium substituting for P(V).*

5.4.1.2 Structural unit cell parameters

A previous investigation on understanding the substitution mechanism of divalent metal ions in AFI-type materials (Chapter 3) revealed an expansion of the unit cell in the a(=b) direction when a metal ion is incorporated into the framework. In addition, the *in situ* HRXRD study showed that the a(=b) parameter was large at the onset of crystallisation and remained constant throughout crystallisation (Chapter 3: 3.4.2). Although the crystallinity increases during the crystallisation of AlPO-5 materials (Chapter 4), the a(=b) unit cell parameter remains constant from the onset, therefore

the variation in the unit cell parameters of each mono- and multi- metal substituted AFI material were analysed to examine the extent of framework substitution.

The HRXRD data for all the mono- and multi- metal ion substituted AlPO-5 materials were analyzed in detail employing a fundamental parameter approach (FPA) for a Pawley fit to extract the unit cell parameters of each crystalline AFI phase. The a(=b) and c unit cell parameters, including cell volume, were calculated for each AFI phase to evaluate the effect of the type of metal ion and the weight percent of each heteroatom on the extent of framework substitution.

To evaluate the extent of framework substitution, the a(=b) unit cell parameter of each material was plotted against an estimated relative average ionic radii. The relative average ionic radius ($R_{average}$) was calculated using Equation 5-2; *Wt* is the weight percent of the ion taken from the gel composition and *R* is the ionic radii in angstroms of the tetrahedral ion[29]. The framework oxygen atoms were not included as these are theoretically equivalent for each AFI material. In addition, the assumption that divalent metal ions substitute for Al(III) and tetravalent metal ions substitute for P(V) was made; $Me^{2+}_{x}Me^{4+}_{y}Al_{(1-x)}P_{(1-y)}O_4$.[11]

Equation 5-2. *Relative Average Ionic Radius*

$$R_{average} = \frac{1}{2}\{(Wt_{Al} \times R_{Al}) + (Wt_P \times R_P) + (Wt_{Me} \times R_{Me})\}$$

For example, the relative average ionic radius for CoTAPO-5 (4 wt.% : 1wt.%), was calculated as follows:

$$R_{average}\left(\boldsymbol{CoTAPO-5(4:1)}\right) =$$

$$= \frac{1}{2}\{(Wt_{Al} \times R_{Al}) + (Wt_P \times R_P) + (Wt_{Co} \times R_{Co}) + (Wt_{Ti} \times R_{Ti})\}$$

$$= \frac{1}{2}\{(0.96 \times R_{Al}) + (0.99 \times R_P) + (0.04 \times R_{Co}) + (0.01 \times R_{Ti})\}$$

$$= \tfrac{1}{2}\{(0.96 \times 0.39) + (0.99 \times 0.17) + (0.04 \times 0.58) + (0.01 \times 0.42)\}$$

$$= \boldsymbol{0.28505\,\mathring{A}}$$

The a(=b) parameter is plotted against the calculated relative average ionic radii for all the mono- and multi- metal ion substituted AFI materials and shown in Figure 5.6. On comparison with the a(=b) unit cell parameter of the un-substituted analogue, AlPO-5, the results yield interesting information on the extent of metal ion substitution.

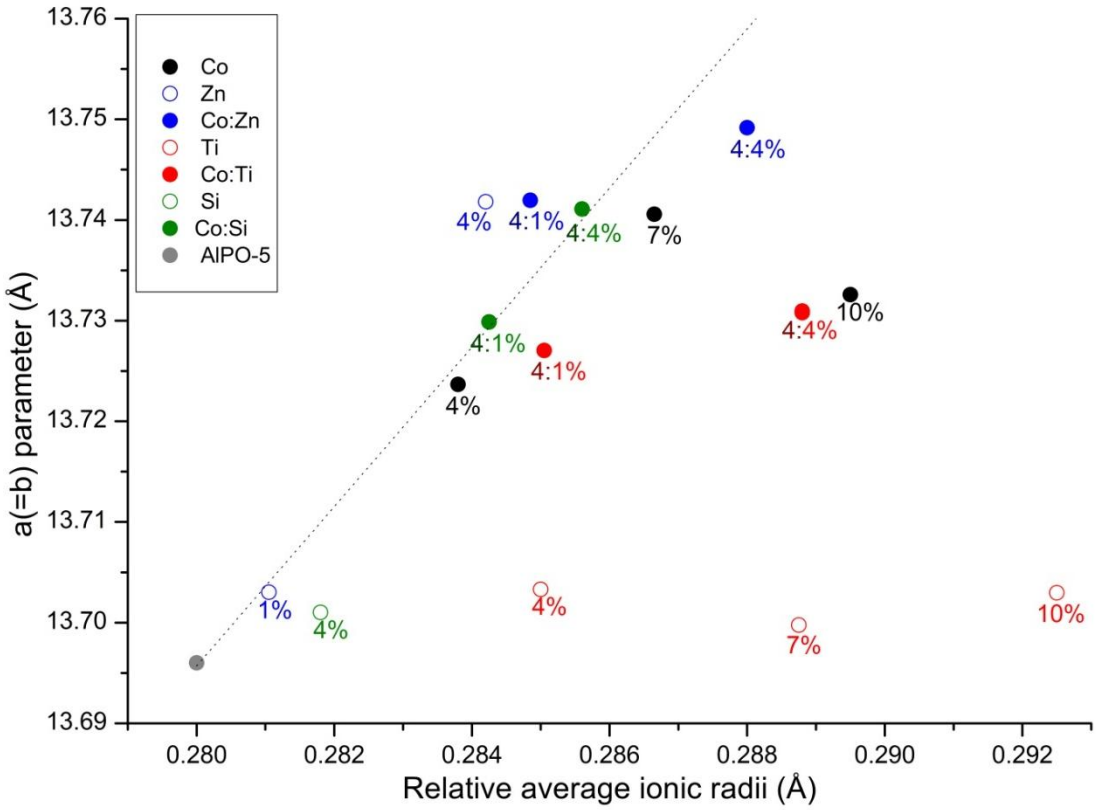

Figure 5.6. *A plot of the a(=b) unit cell parameter (Å) against the calculated relative ionic radii (Å), based on the gel composition for each mono- and multi- ion substituted AFI material. An estimated trend line is also shown but excludes the results from the Ti(IV) substituted AFI materials and CoAlPO-5 (10%). It is assumed that the divalent metal ions substitute for Al(III) and the tetravalent metal ions substitute for P(V).*

On analysis of both the mono- and multi-metal ion substituted AFI materials, it is clear that the a(=b) parameter increases with increasing metal loading, with the exception of the titanium containing samples and with a cobalt concentration above 7 wt. %. These exceptions are discussed in more detail later.

A linear trend line is plotted in Figure 5.6 which was calculated based on the a(=b) parameters for the mono- and multi- metal ion substituted AFI materials, excluding the data for CoAlPO-5 (10%) and the Ti containing samples (TAPO-5 and CoTAPO-5). It should be noted that this estimated trend line is used only as a tool for the *relative* comparison of the extent of metal ion substitution in the AFI materials. Unfortunately, this trend line is unreliable as it is based only the experimental data in this study and can therefore not be used to accurately measure the actual percent of metal ion substitution; for a more accurate trend, a theoretical study is required investigating a variety of metal ion substitutions with different compositions for the AFI structure.

Zinc(II). The a(=b) parameter for the Zn(II) containing AFI materials were found to fit the trend line reasonably well, with the ZnAlPO-5 (4%) and CoZnAlPO-5 (4:1%) structures having an a(=b) unit cell parameter which were slightly higher than that predicted by the trend line. This suggests that either, the trend line underestimates the level of metal incorporation, or there is a higher level of Zn(II) in the AFI frameworks compared to the gel composition which may be a result if the yield of the Zn-AFI materials was low. The a(=b) parameter for the CoZnAlPO-5 (4:4%) material was found to be lower than the predicted trend line indicating that the metal ions were not fully incorporated into the AFI framework; XRD cannot distinguish between the cobalt and zinc ions, therefore information such as how much of each metal is incorporated into the multi-ion frameworks is unattainable. However, it is reasonable to believe that there are both Co(II) and Zn(II) ions

incorporated into the AFI framework as the a(=b) parameter for CoZnAlPO-5 (4:4%) is larger than that of CoAlPO-5 (4%) and ZnAlPO-5 (4%).

Cobalt(II). Analysis of the a(=b) parameter for the CoAlPO-5 materials revealed that as the cobalt concentration increased the cell parameter diverged away from that predicted by the trend line. For example, the unit cell parameter of CoAlPO-5 (4%) was found to be comparable to that predicted by the trend line, however the a(=b) parameter for CoAlPO-5 (7%), although larger than the 4 % equivalent, was calculated to be slightly lower than the trend line indicating that not all of the cobalt (7 %) was incorporated into the AFI structure. This was even more apparent when 10% of cobalt was incorporated into the synthesis gel; the a(=b) parameter was found to be smaller in comparison to the trend line and that of the CoAlPO-5 (7%) material. However, here only Co(II) ions are considered to exclusively substitute for Al(III). In addition, clustering (Co-O-P-O-Co) has been proposed in many systems which may affect the trend. Here it is assumed that Co(II) ions are isolated. This suggests that as the divalent metal ion concentration increases it becomes more difficult to incorporate Co(II) into the AFI framework. The maximum cobalt loading was achieved when 7 wt. % of Co(II) was employed in the synthesis gel, this resulted in a unit cell parameter of a(=b) = 13.7406(3) Å. Assuming that the trend line *is* an accurate representation of the extent of cobalt substitution, this a(=b) parameter corresponds to an AFI framework with a cobalt incorporation of 5.97%, similarly, the CoAlPO-5 (4%) parameter corresponds to 3.72% of substituted Co(II) and the a(=b) parameter calculated for CoAlPO-5 (10%) relates to only 4.91 % of framework cobalt.

For the multi-ion substituted materials containing 4 weight % of cobalt in addition to either Zn(II), Si(IV) or Ti(IV); the a(=b) parameter was calculated to be larger than that of the mono-substituted CoAlPO-5 (4%). Assuming that the CoAlPO-5 (4%) material has a cobalt substitution between 3.7 and 4 %, the larger a(=b) parameter for the multi-substituted cobalt containing AFI materials suggests that an incorporation of two different heteroatoms has occurred. However, the extent to which each metal has been substituted into the framework is unknown. It should be noted that if the trend line is an under-estimation of the extent of metal substitution, the larger a(=b) parameters observed with the multi-ion substituted may not represent the incorporation of two heteroatoms and may instead indicate an improvement in the substitution of Co(II) into the framework when another heteroatom is present in the gel. This latter possibility is doubtful; although the introduction of another metal into the synthesis gel may encourage the substitution of cobalt into the AFI framework, it is reasonable to presume that there is some incorporation of the other metals (Zn / Si / Ti) along with Co(II) into the AlPO-5 structure as it is evident in many literature reports[1, 2, 11]. To fully support this statement, X-ray absorption spectroscopy (XAS) at the K-edge of each metal would be required.

Silicon(IV). The a(=b) unit cell parameter of the mono substituted Si(IV) containing AFI material, SAPO-5 (4%), was calculated to be larger than its un-substituted analogue, indicating the presence of framework Si(IV). However, if the trend line is assumed to be an accurate representation of the metal ion substitution and if Si(IV) substitutes solely for P(V), the a(=b) parameter of SAPO-5 (4%) corresponds to an AFI framework with only 1.49 % of framework silicon. It should

be noted that the pH of the synthesis gel can have an effect on the substitution of silicon for P(V): at low pH, silicon island (Si(IV) substitution for P(V) and Al(III)) formation is favoured. In this study, pH 7 was employed, therefore silicon island formation was not anticipated [30]. Upon addition of Co(II) to the synthesis gel, CoSAPO-5 (4:1%) and CoSAPO-5 (4:4%), the a(=b) parameter increases with increasing metal content and becomes comparable to that predicted by the trend line. This indicates an increase in framework metal ions and may suggest that the presence of a divalent metal ion promotes the substitution of Si(IV) for P(V).

Tetravalent metal ions are known to primarily substitute for P(V) ions in the AlPO framework, however, there are reports which suggest a substitution of both the P(V) and Al(III) sites together can occur forming silicon islands[31]. If this is the case, then the calculated relative average ionic radii and the resulting a(=b) parameter would decrease or remain constant with increasing Si(IV) substitution of the Al(III) site since the ionic radii for tetrahedral Si(IV) is only 0.26 Å compared to tetrahedral Al(III), 0.39 Å. If the trend line is assumed to be an accurate representation of the extent of metal ion incorporation into the AFI framework, then it is clear that the Si(IV) ions solely substitute for P(V) in the multi-ion substituted CoSAPO-5 materials using the preparation method described here. For the mono substituted SAPO-5 (4%) material; the a(=b) parameter is smaller than predicted, as stated before this could be due to a smaller percent of silicon atoms being incorporated into the AFI framework (substituting solely for P), however, a smaller a(=b) parameter may also be representative of some of the Si(IV) ions substituting for Al(III). The formation of silicon islands in SAPO-5 materials has been investigated through both

experimental and computational studies; the results suggest that silicon islands are unlikely to form unless a silicon content of more than 9% is reached[32]. Therefore, it is reasonable to presume that the smaller a(=b) parameter observed in the SAPO-5 (4%) material is due to a lower substitution of Si(IV) into the AFI framework.

Titanium (IV). The a(=b) parameter of the titanium containing AFI samples are also shown in Figure 5.6 and compared to the other mono- and multi- metal ion substituted AlPO-5 materials. Assuming that the Ti(IV) ion substitutes solely for P(V), the unit cell parameters were found to be much lower than expected when compared to the trend line. This indicates that a limited amount of titanium has been incorporated into the AFI framework. For example, assuming the trend line is an accurate representation of the extent of metal ion incorporation into the AlPO-5 structure, then the unit cell parameters calculated for TAPO-5 4wt.%, 7wt.% and 10wt.% are actually representative of only a 0.77%, 0.41% and 0.73% Ti(IV) AFI substitution, respectively. This difficulty to incorporate titanium into the framework of AlPOs and other zeolitic materials is well documented to be difficult unless there are Si(IV) species present, as hydrolysis of the Ti source and precipitation of the stable species, TiO_2, during the gel preparation can readily occur[11, 33, 34].

On analysis of the a(=b) parameter of the multi metal CoTAPO-5 materials; it is clear that the unit cell parameter is smaller than predicted. If it is assumed that all of the cobalt (it is well known in the literature that Co(II) incorporation into AlPO-5 is relatively easy) has been substituted into the AFI framework; the introduction of a different heteroatom to the synthesis gel results in less titanium being incorporated into the structure. For example, (based on the predicted trend line) the a(=b)

parameter of CoTAPO-5 (4:4%) is equivalent to a Ti(IV) substitution of only 0.52% if it is assumed that there is 4% of Co(II). A reduction of framework titanium in the AFI framework when another heteroatom is incorporated into the synthesis has been reported before in the literature for the case of VTAPO-5 (vanadium(V) and titanium(IV))[4], however the reduction in framework Co(II) species cannot be ruled out. On comparison of the increase in the a(=b) parameter of TAPO-5 (4%), CoAlPO-5 (4%) and CoTAPO-5 (4:4%) with the un-substituted analogue AlPO-5, it is clear that the total combined increases of TAPO-5 (*ca.* 0.007 Å) and CoAlPO-5 (*ca.* 0.027Å) is equivalent to that observed in CoTAPO-5 (*ca.* 0.035 Å) and suggests that the substitution of Co(II) and Ti(IV) is equivalent in the mono- and multi- metal substituted AFI materials.

In this analysis of the unit cell parameter of the titanium containing AFI materials it was assumed that the Ti(IV) species solely substituted for P(V). Although there are many reports in the literature which suggest that Ti(IV) ions can substitute for an Al(III) and P(V) couple forming framework linked Ti-O-Ti bridges in aluminophosphate materials such as TAPO-34, TAPO-11 and TAPO-36, there is no evidence to suggest that this double substitution occurs in the AFI structure[35, 36]. If this was the case, then the a(=b) parameters observed would be representative of TAPO-5 materials containing a larger proportion of framework titanium since the Ti(IV) ionic radii is 0.42 Å compared to Al(III), 0.39 Å, and P(V), 0.17 Å.

The c parameter of all the mono- and multi- metal substituted AFI materials is plotted against the calculated relative average ionic radii in Figure 5.7, with the assumption that divalent metal ions substitute for Al(III) and the tetravalent metal

ions substitute solely for P(V). It is clear from the plot that there is no trend in the c parameter of the AFI structure as metal ions become incorporated into the framework. There are few reports in the literature which investigate the change in the c parameter as the isomorphous substitution of metal ions into the framework increases; with mixed conclusions on whether the c parameter increases or decreases with an increase in the metal ion substitution. Studies on the change in the unit cell parameters of the transition metal ions, cobalt or vanadium, reported an increase in the a(=b) parameter but a decrease in the c parameter as the metal ion concentration increased[13, 16, 37]. On the other hand, investigations on the isomorphous substitution of alkali earth metals such as magnesium and calcium, reported an increase in both the a(=b) and c parameters[12, 14].

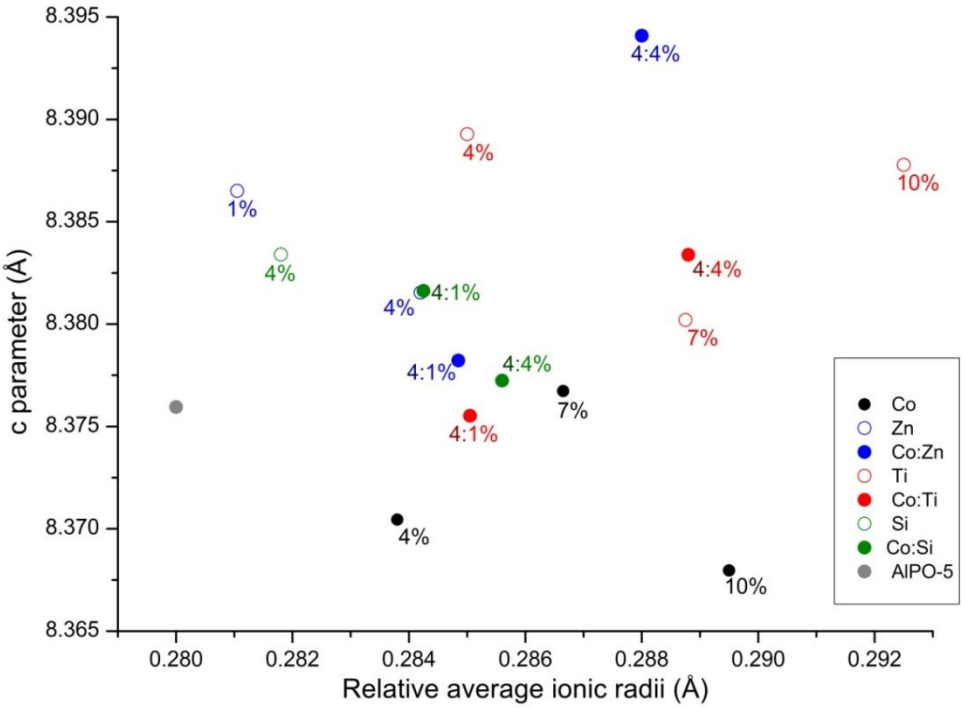

Figure 5.7. *A plot of the c parameter (Å) against the calculated relative ionic radii (Å), based on the gel composition for each mono- and multi- ion substituted AFI material. It is assumed that the divalent metal ions substitute for Al(III) and the tetravalent metal ions substitute for P(V)*

.

The results show that there is a large variation in the c parameter as metal ions are incorporated into the AFI framework. The previous *in situ* XRD investigation during the formation of AFI materials with Co(II) and Zn(II) metal ions, Chapter 3, found the c parameter to increase during crystal growth and was attributed to the uptake of water molecules in the channel system. The effect of water molecules on the c parameter of AlPO-5 was investigated through ex situ HRXRD; a diffraction pattern was collected on a powder which was exposed to the moisture in the atmosphere and a powder which was dried and sealed under vacuum in the capillary, the results

revealed a large decrease in the c parameter of *ca.* 0.11 Å. Therefore, in accordance with Concepción et al.[12], it can be concluded that the c parameter is difficult to determine with high precision.

The unit cell volume of all the mono- and multi- metal substituted AFI materials is plotted against the calculated relative average ionic radii in Figure 5.8, once again assuming divalent metal ions substitute for Al(III) and tetravalent metal ions substitute solely for P(V). As expected the unit cell volume increases with increasing metal ion substitution due to the increases in the T-O bond distances from Al-O (1.78 Å) to Co-O (1.94 Å) and Zn-O (1.94 Å), or from P-O (1.54 Å) to Si-O (1.61 Å) and Ti-O (1.81 Å) and has a similar trend to that observed with the a(=b) parameter. Of the small number of literature reports on the cell parameter change with increasing metal ion substitution into the AFI framework, the majority have used the unit cell volume to convey, indirectly, whether isomorphous substitution has occurred. Although this method does portray the general conclusion as to whether isomorphous substitution has taken place, it may not be with high precision as it takes into account the change in the c parameter which is affected by the uptake of water. Therefore, the a(=b) parameter change may be a more reliable method in determining the extent of metal ion substitution in the AFI structure.

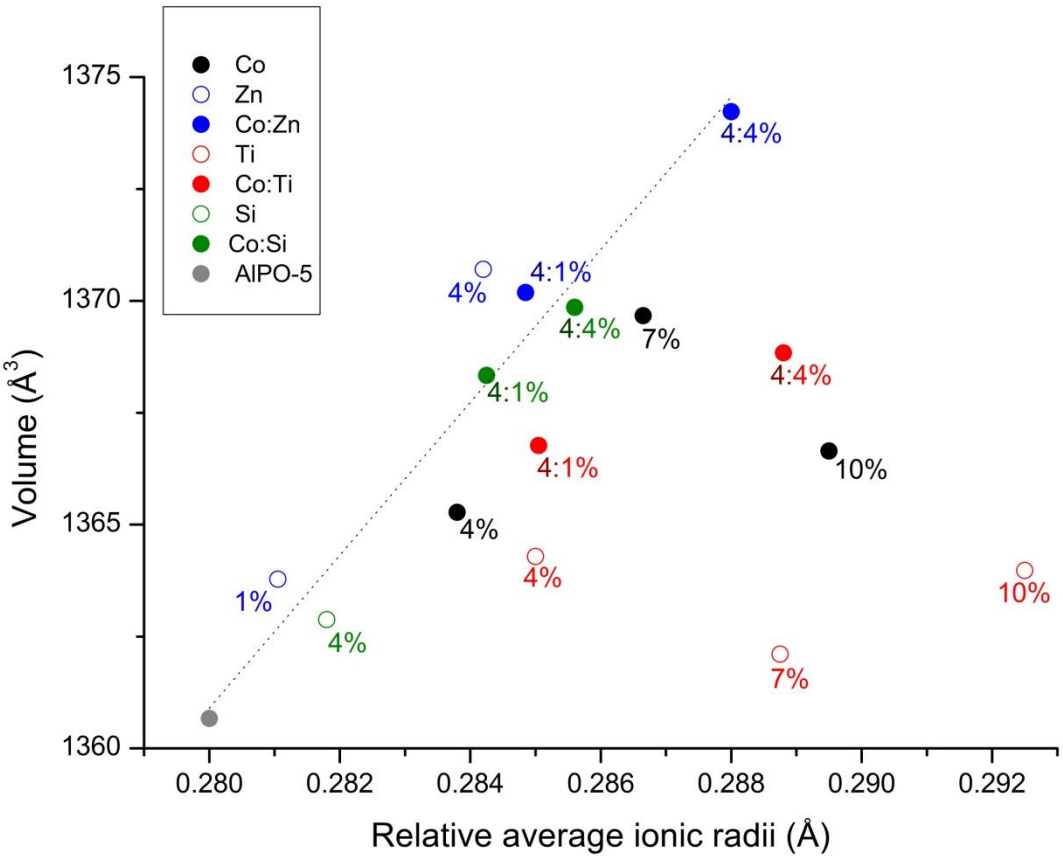

Figure 5.8. *A plot of the unit cell Volume (Å^3) against the calculated relative ionic radii (Å), based on the gel composition for each mono- and multi- ion substituted AFI material. An estimated trend line is also shown but excludes the results from the Ti(IV) substituted AFI materials and CoAlPO-5 (10%). It is assumed that the divalent metal ions substitute for Al(III) and the tetravalent metal ions substitute for P(V).*

5.4.2 XANES study of mono- and multi- metal substituted AFI materials containing titanium

Titanium containing zeolites and aluminophosphate materials have been extensively studied for a number of oxidation reactions, such as the epoxidation of alkenes and the oxidation of alkanes to their respective acids such as adipic acid[18-20]. The catalytic property of these titanium containing molecular sieves depends on the hydrophobicity and amount of active sites (Ti(IV) in a tetrahedral environment) present in the material, this has been found to be less than 2 wt. % in the titanosilicate TS-1[38]. Effectively increasing the titanium content in the frameworks of molecular sieves is still a huge challenge, with research moving towards substituting titanium into aluminophosphate materials. The advantage with the aluminophosphate type-5 structure is that a large variety of metals can be easily incorporated into its framework; substituting a heteroatom along with titanium into the AFI structure may have a positive effect on the extent of titanium incorporation.

The substitution, oxidation state and coordination environment of titanium in the framework of a variety of as-synthesised mono and multi-metal substituted AlPO-5 materials was investigated by X-ray absorption spectroscopy (XAS). Previous investigations on the amount of tetrahedral titanium sites present in different zeolite structures have found that it depends on the sample preparation and the dehydration level[39]. Therefore, to reliably obtain information on whether titanium is incorporated into the framework of the samples, *in situ* measurements during calcination in air at 530°C are required to remove any deviations in the coordination

environment from water or template molecules. *In situ* X-ray absorption near edge structure (XANES) data was collected during the calcination of as-synthesised TAPO-5 (4%), CoTAPO-5 (4:4%), FeTAPO-5 (4:4%) and TAPSO-5 (4:4%). In addition XANES spectra were collected during the calcination of TAPO-5 (4%) prepared by a different method ('method 2'), in which the titanium source was added after the organic template. The data were compared to the known titanosilicate, TS-1 (already calcined) and model compounds, $Ti(OSiPh_3)_4$ and anatase TiO_2.

5.4.2.1 Model titanium compounds

The normalized XANES data of the model compounds and their associated structures are shown in Figure 5.9. $Ti(OSiPh_3)_4$ is a monomeric compound that consists of Ti(IV) species in a tetrahedral coordination (TiO_4) surrounded by silicon atoms and bulky triphenyl groups[40]. The XANES spectra has a large pre-edge feature at 4969.87 eV which is attributed to transitions from Ti 1s to bound Ti 3d orbitals, this feature is large due to contributions from the oxygen 2p orbitals as a result of shorter bond distance in the non symmetric tetrahedral environment. Anatase (titanium dioxide, TiO_2) is a pyramidal crystal with tetragonal symmetry, Ti(IV) species are found in an octahedral coordination environment[41]. The pre-edge feature of the XANES spectra of anatase was found to not be so pronounced and consisted of a shoulder of four peaks with a maximum at 4971.39 eV. The assignment of this multiplet feature has been debated extensively in the literature with

reports suggesting that it is a result of transitions from 1s to mixed p-d orbitals, both from the oxygen 2p orbitals and the neighbouring titanium 3p and 3d orbitals, or from a mixture of quadrupolar and dipolar transitions to the t_{2g} and e_g orbitals which the five d orbitals of Ti split into (crystalline field effect)[42].

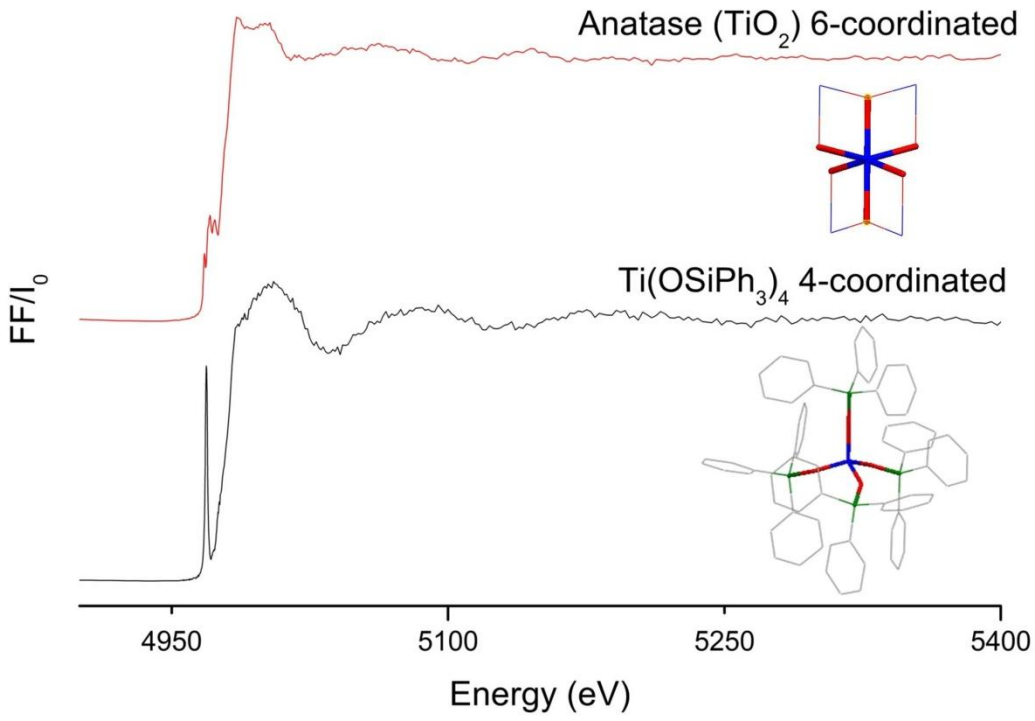

Figure 5.9. *Ti K-edge XAS plots and structures of the model compounds containing Ti in a tetrahedral or octahedral coordination. The respective colours of the atoms are: Ti (blue), O (red), Si (green) and C (grey).*

The intensity of the pre-edge feature, as shown in the model compounds, is related to the geometry of the Ti-O polyhedra, in particular the coordination number of titanium. For example, the pre-edge intensity increases with decreasing coordination

number (6-, 5- and 4- coordinated) due to the increase in contribution from the oxygen 2p orbitals as the Ti-O bond distance decreases. However, there are issues regarding the analysis of the pre-edge intensity; Sankar et al. reported that the intensity of the pre-edge feature for a number of tetrahedral Ti(IV) containing materials (TS-1, Ti-zeolite beta and Ti-MCM-41) were not the same and was attributed to differences in the static disorder around the Ti(IV) species[43]. The position of the pre-edge feature can also be used to reveal information on the coordination number of titanium with a shift to higher energy as the coordination number of titanium increases; this has been attributed to an increase in the Fermi energy. Once again, however, the exact energy position of the pre-edge position has been found to deviate slightly for given Ti(IV) coordination numbers[44].

The variation in the position and intensity of the pre-edge feature makes it difficult to use any one of these alone to derive a reliable coordination number for titanium when it is present in several coordination environments. In 1996, through both theory and experimental studies on a number of model compounds, Farges et al. were able to make a direct correlation between the pre-edge position and its intensity which could be use to derive reliable information on the Ti coordination, in particular they were able to distinguish between a fivefold coordination and a 50:50 mixture of six- and four-fold coordinated titanium[44].

5.4.2.2 *In situ* XANES studies of titanium containing AlPOs

The XANES plots of the as-synthesised Ti-containing AFI materials are shown in Figure 5.10 and compared to TS-1 (calcined) and the model compounds; $Ti(OSiPh_3)_4$ and anatase (TiO_2). From the position and intensity of the pre-edge (1s→3d transition) and the shape of the edge (1s→4p transition) features of the XANES plots, it is clear that the titanium species present in calcined TS-1 have a tetrahedral coordination environment since both features are very similar to the model compound $Ti(OSiPh_3)_4$. The edge position of all the mono- and multi- metal substituted AFI materials, including the TS-1 sample, were found to be identical and comparable to the model compounds, indicating that the titanium species present in all materials were in the +4 oxidation state.

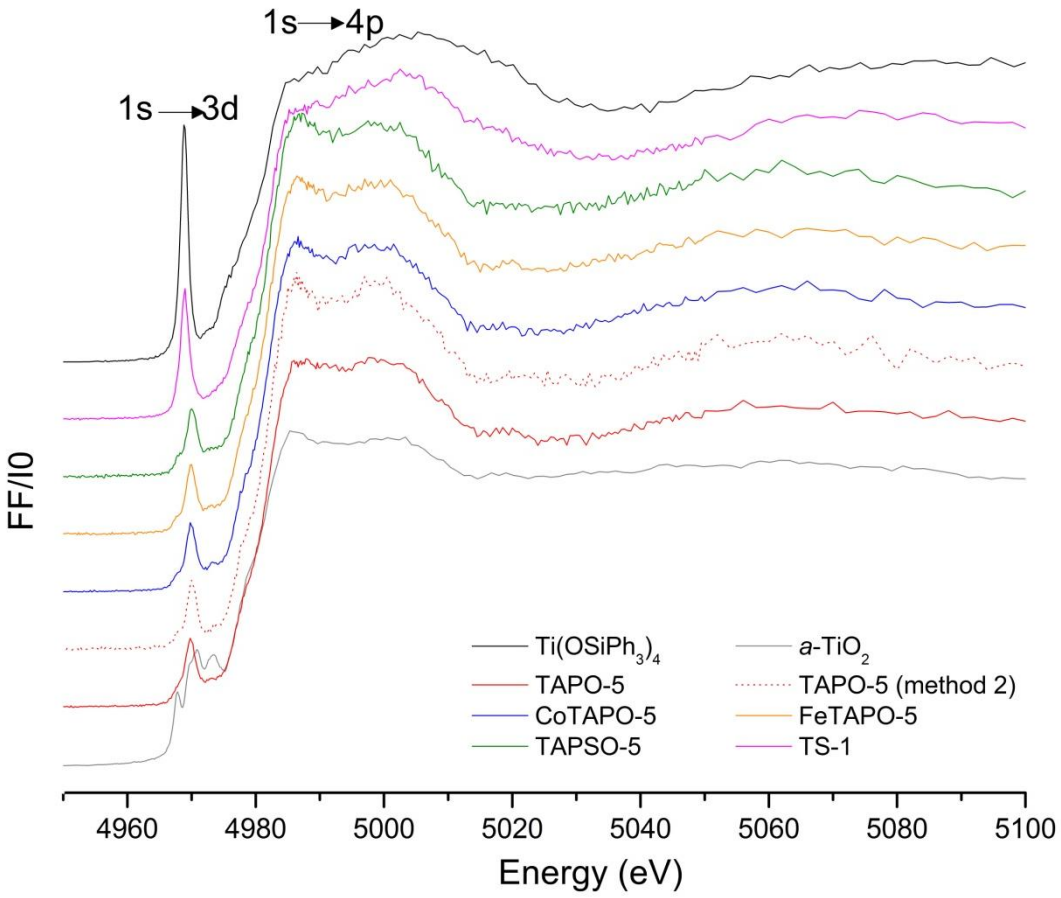

Figure 5.10. *XANES spectra of the **as-synthesised** titanium containing AFI materials are compared to that of the calcined TS-1 and the model compounds $Ti(OSiPh_3)_4$ and anatase (a-TiO_2).*

The XANES plots of the as-synthesised mono- and multi- metal substituted AFI materials were found to be very similar to each other; the pre-edge feature consisted of a well resolved peak at *ca.* 4970 eV with two very small features either side at *ca.* 4968 and 4973 eV. A multiplet in the pre-edge region was also observed in the XANES spectra of anatase, therefore this may suggest the presence of 6-coordinated titanium species or Ti-O-Ti linkages in the AFI materials. Upon calcination of the AFI materials at 550°C (removal of the template and loosely bound water molecules),

Figure 5.11, the multiplet observed in the pre-edge region of the Ti K-edge XANES spectra is found to vanish and the resolved peak at 4970 eV increases in intensity and shifts to lower energy towards that observed in the model compound $Ti(OSiPh_3)_4$ (Ti(IV) in tetrahedral environment).

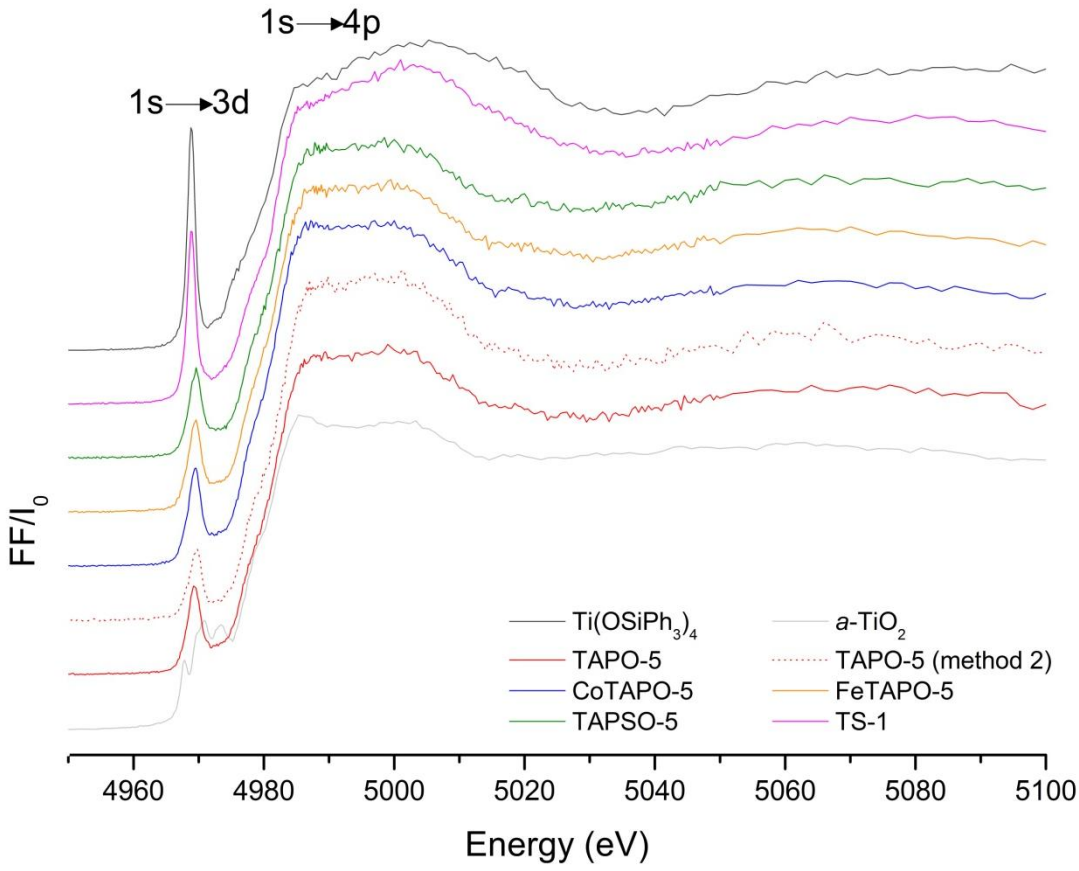

Figure 5.11. *XANES spectra of the titanium containing AFI materials recorded during calcination at* ***550 °C****, are compared to that of the calcined TS-1 and the model compounds* $Ti(OSiPh_3)_4$ *and anatase (a-*TiO_2*).*

The change in the pre-edge area of the Ti K-edge XANES spectra of the AFI materials upon calcination is exemplified in Figure 5.12 with the FeTAPO-5 framework. The small peaks of the triplet observed in the XANES spectra of the as-synthesised FeTAPO-5 material appear to vanish upon calcination suggesting that these pre-edge peaks are associated with 6-coordinated titanium species in which loosely bound water molecules may have been coordinated to framework Ti(IV). The pre-edge region of the XANES spectra collected at 550 °C during calcination in air, showed the dominance of what appeared to be a single peak which was more intense and shifted to lower energy. However, on further analysis through the fitting of Gaussian peaks, it became apparent that this pre-edge peak (4969.4 eV) had a shoulder peak at lower energy (4967.7 eV) which coincides with one of the multiplets observed in the as-synthesised FeTAPO-5 material. Therefore, this may suggest the presence of octahedral Ti(IV) species in the calcined materials. It should be noted that the pre-edge region of the XANES spectra of all the AFI materials consisted of peaks for the as-synthesised samples and 1 main peak with a shoulder for the calcined samples at 550 °C.

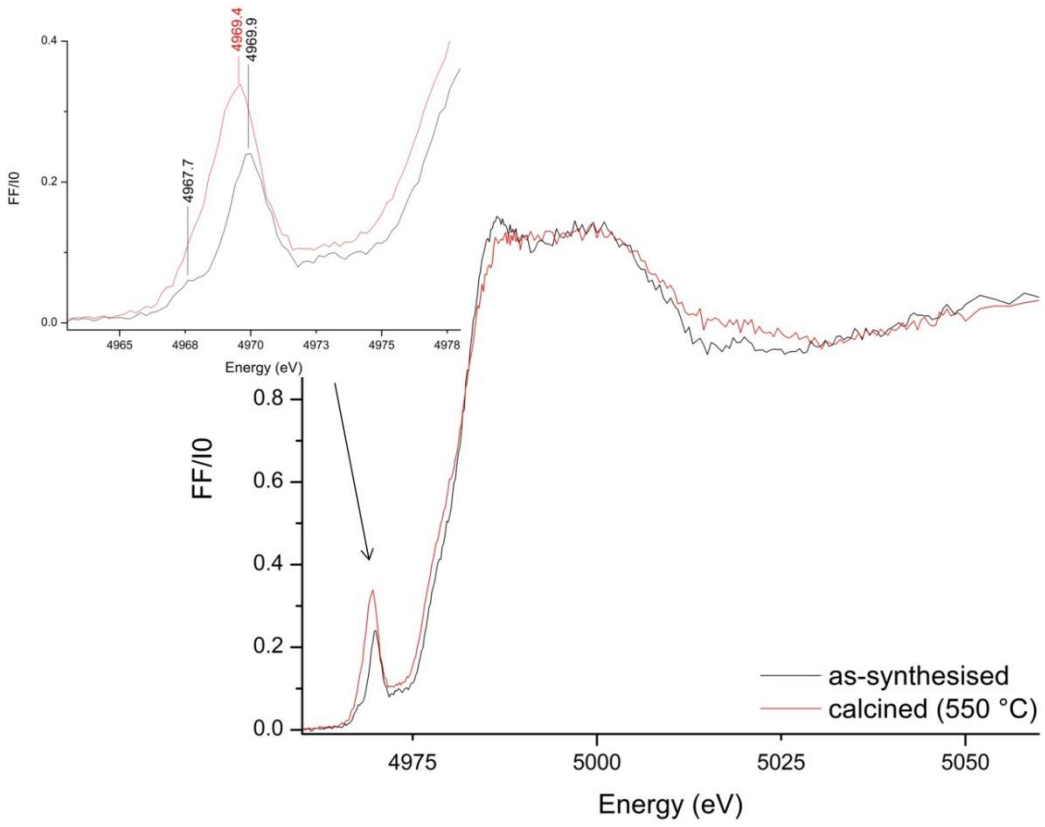

Figure 5.12. *Ti K-edge XANES spectra of FeTAPO-5, as-synthesised and collected at 550°C during calcination in air. The multiplet observed in the pre-edge region is highlighted.*

To derive reliable information on the Ti coordination in the mono- and multi- metal AFI materials, the intensity of the pre-edge feature was plotted against its position and compared to the model compounds. Figure 5.13 shows the change in the pre-edge feature during the calcinations at 550 °C of all the AFI materials including the TS-1 sample. It is clear that in all materials, the pre-edge feature increases in intensity and shifts to lower energy during calcination (removal of the organic template and loosely bound water molecules), this is illustrative of the materials containing hydrophilic Ti(IV) sites. TS-1 was found to differ from the AFI materials,

with a pre-edge feature which closely resembled that observed in the model compound $Ti(OSiPh_3)_4$. On comparison of the AFI materials, it is apparent that the pre-edge feature is comparable in the *as-synthesised* mono- and multi- metal substituted AlPO-5 materials, irrespective of the synthesis method employed. It is only upon calcination in air at 550 °C that the pre-edge feature of the AFI XANES spectrum differs.

On comparison of the TAPO-5 materials synthesised by the two different methods, it is clear that there is a smaller change in the pre-edge feature of the TAPO-5 material synthesised by method 2 compared to TAPO-5 synthesised by the standard method 1. The smaller increase in the pre-edge intensity and the smaller shift in its positions for TAPO-5 (method 2) indicates that removal of the template and loosely bound water molecules does not have a great effect on the coordination environment of the Ti(IV) species present in the AFI material. The pre-edge feature at 550 °C for TAPO-5 (method 1) is more intense and has a position more similar to that of the model compound $Ti(OSiPh_3)_4$ compared to TAPO-5 (method 2) and suggests the presence of more Ti(IV) species which have a lower coordination number close to 4 in TAPO-5 (method 1). The change in the pre-edge during calcination was found to be comparable for all the mono- and multi- metal substituted AFI materials synthesised by the standard method 1.

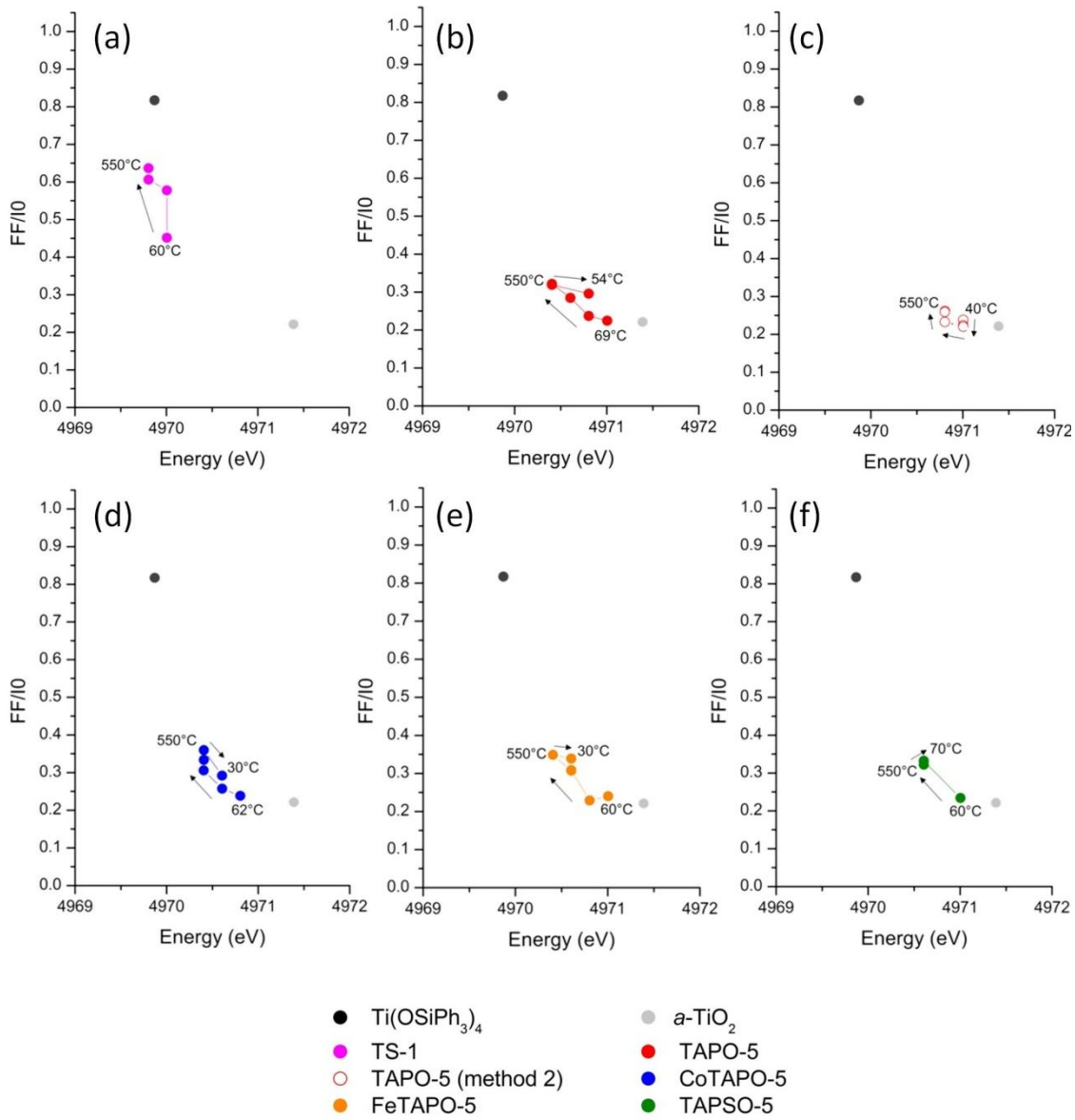

Figure 5.13. *Plots of the intensity of the pre-edge feature against its position during calcination at 550 °C of (a) TS-1, (b) TAPO-5, (c) TAPO-5 prepared by method 2, (d) CoTAPO-5, (e) FeTAPO-5, and (f) TAPSO-5. The results are compared to the model compounds* $Ti(OSiPh_3)_4$ *and anatase (a-*TiO_2*).*

To further evaluate the Ti coordination in the mono- and multi- metal substituted AFI materials, the intensity and position of the pre-edge feature of the XANES spectra collected at 550 °C during calcination was compared to that of TS-1, $Ti(OSiPh_3)_4$, anatase and results from Farges et al.'s experimental study on a number of 4-, 5- and 6- coordinated model titanium compounds[44]. The results are shown in Figure 5.14; the Ti(IV) species present in TS-1 is indicative of having a tetrahedral coordination environment, however the pre-edge feature observed in the Ti K-edge XANES spectra for the AFI materials are not comparable with any of the model compounds. This illustrates that there is a mixture of Ti coordinations in the AFI materials.

As previously discussed, Farges et al. also carried out a theoretical study on the intensity and position of the pre-edge feature for a number of different mixtures of 4-, 5- and 6- coordinated Ti materials, these results are summarised in Figure 5.15[44]. It should be noted that no theoretical study was carried out on Ti coordination mixtures which involved more than 2 different coordination environments.

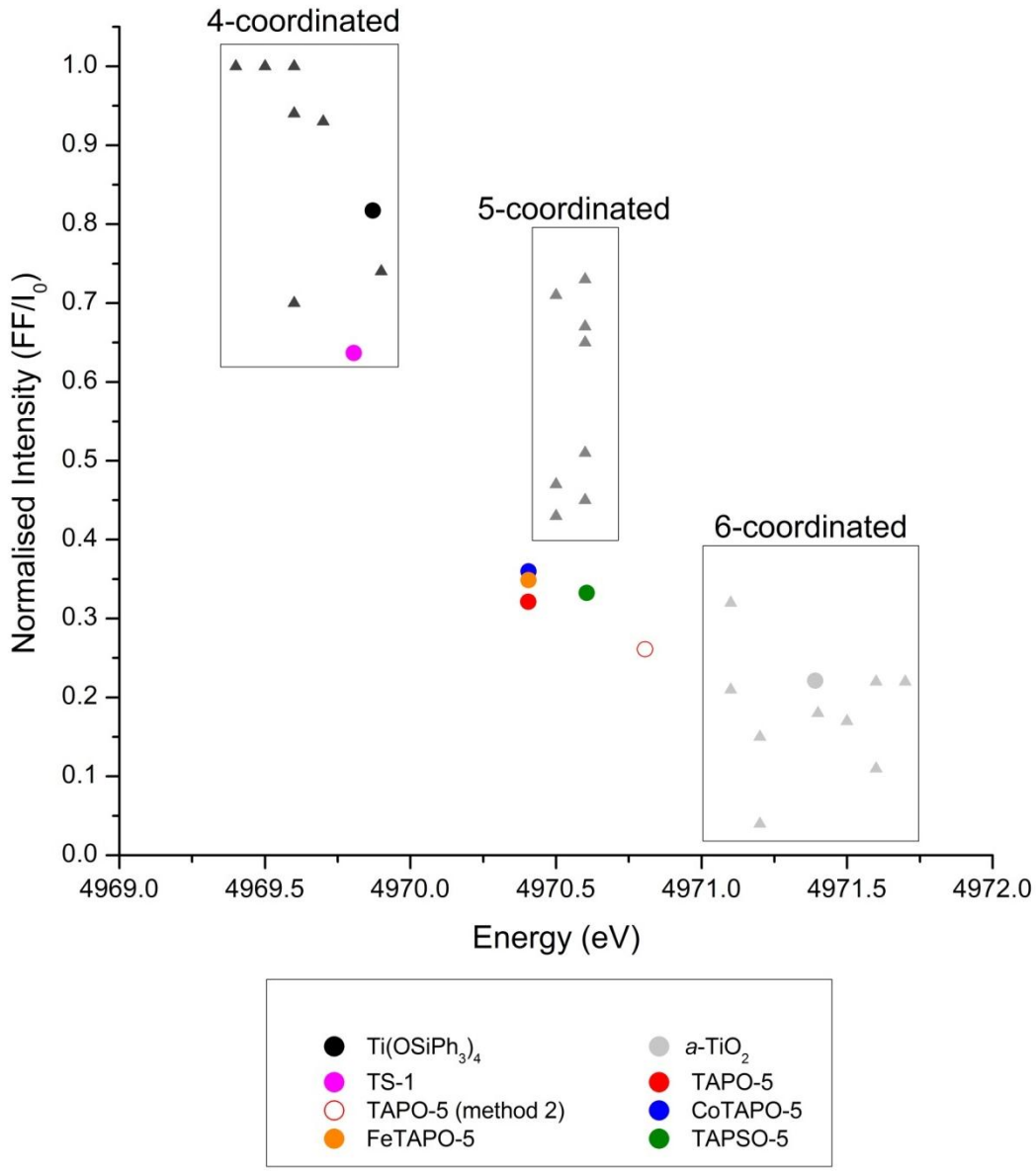

Figure 5.14. *The intensity of the pre-edge feature vs its position (energy) of the Ti K-edge XANES spectra collected at 550°C of the AFI materials, including TS-1 and the model compounds. Also shown are the results from Farges et al.'s study on a number of 4-, 5- and 6- coordinated model compounds (triangles)*[44].

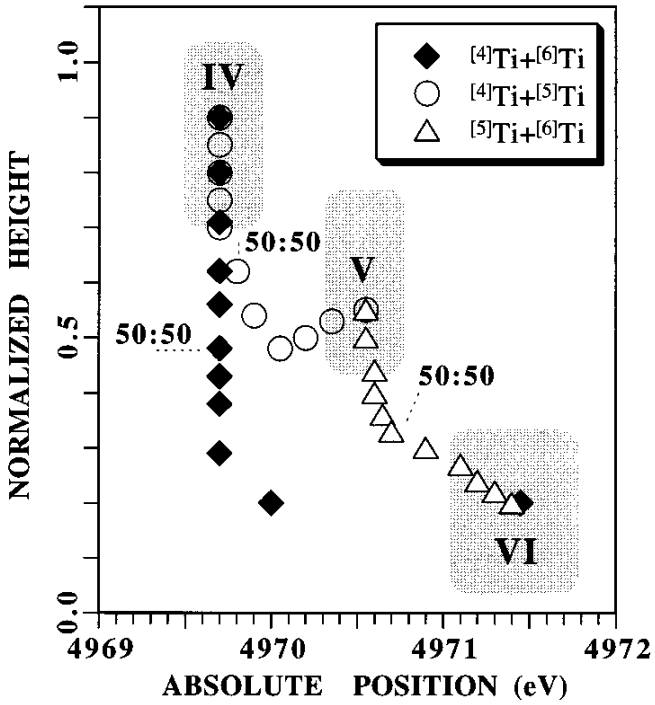

Figure 5.15. *Theoretical values of the normalised intensity and the position of the Ti pre-edge feature for a number of different mixtures of 4-, 5- and 6- coordinated titanium. Taken directly from Farges et al.'s work*[44].

Comparison of these experimental results with Farges et al.'s theoretical study, indicate the presence of both 5- and 6- coordinated Ti(IV) species (denoted Ti^{V} and Ti^{VI}) present in TAPO-5 (method 2) and TAPSO-5 with Ti^{V}:Ti^{VI} ratios of 40:60 and 60:40, respectively. The position of the pre-edge feature observed in TAPO-5, CoTAPO-5 and FeTAPO-5 were equivalent with small difference observed in the intensity. However, on comparison with Farges et al.'s theoretical study no matches were found which may indicate that there is more than two different Ti coordinations present in these AFI materials. The pre-edge feature of TAPO-5, CoTAPO-5 and FeTAPO-5 were found to have comparable intensities with a number of $Ti^{IV:VI}$ and

$Ti^{V:VI}$ mixed coordination environments but the position of the pre-edge was found to lay in-between these mixtures. This is suggestive of TAPO-5, CoTAPO-5 and FeTAPO-5 all containing 4-, 5- and 6- coordinated Ti(IV) species, unfortunately without a theoretical study on tri-mixes of Ti coordinations, the amounts of each coordination is unknown but is not unreasonably to believe that the Ti^{IV} coordinated species has the lowest concentration.

5.5 Summary and Conclusion

HRXRD data of a variety of mono- and multi- metal substituted AFI materials revealed that the crystallinity of the AlPO-5 product was limited by the heteroatom which had the slowest crystallisation rate or the longest induction period. For example, the diffraction patterns revealed identical crystallinities for ZnAlPO-5 (4%) and CoZnAlPO-5 (4:4%), but was much greater for CoAlPO-5 (4%). In addition, the weight percent of each metal ion present in the multi- metal substituted AFI materials were found to independently affect the crystallinity of the product, e.g. the crystallinity of TAPO-5 (4%) was equivalent to CoTAPO-5 (4:4%), although that of TAPO-5 (7%) was found to be less crystalline. These results are important in understanding the kinetics of formation which could lead to a more rational approach in the synthesis of new molecular sieves.

On evaluation of the structural parameters of the AFI materials with hexagonal symmetry, it was apparent that the a(=b) parameter expanded with an increase in

metal incorporation. The divalent metal ions, Zn(II) and Co(II), which replace Al(III) in the AlPO frameworks were found to readily substitute into the mono-metal substituted AFI materials at concentrations of 7 wt. % and below. Above this concentration, the incorporation was found to be more difficult as observed for CoAlPO-5 (10%). On analysis of the multi divalent metal ion substituted materials, CoZnAlPO-5 (4:1% and 4:4%), both metals were incorporated into the AFI framework (less so at higher concentration).However, the extent to which *each* divalent metal ion is substituted into the framework is difficult to determine through this indirect method.

Tetravalent metal ions, Si(IV) and Ti(IV), are known to substitute for P(V) in mono-substituted AFI materials unless the silicon concentration is above 9 wt. %, above which silicon island formation occurs[32]. With this assumption, HRXRD data revealed that Si(IV) ions readily substitute into the AFI framework upon the introduction of a divalent metal ion (silicon incorporation greater for CoSAPO-5 compared to SAPO-5). Titanium was found to be difficult to incorporate into the mono- substituted AFI framework, with only very small increases observed in the a(=b) parameter upon the introduction of Ti(IV) ions to the synthesis gel, with the largest a(=b) parameter observed for TAPO-5 (4%). This a(=b) parameter was small in comparison to that predicted by the ionic radii increase of P(V) to Ti(IV), and suggested that only 0.77 wt.% of titanium was incorporated into the AFI framework. Upon the addition of a divalent metal ion, CoTAPO-5 (4:1% and 4:4%), to the synthesis gel, the a(=b) parameter was found to increase. The extent to which each metal is substituting into the framework could not be accurately determined through

XRD, however it was apparent that the change in the a(=b) parameter from AlPO-5 to TAPO-5 (4%) and CoAlPO-5 (4%) totalled to an equivalent increase in the a(=b) parameter of CoTAPO-5 (4:4%) which suggests that the addition of another heteroatom to the synthesis gel does that have a significant effect on its incorporation into the AFI framework.

A Ti K-edge *in situ* XANES study during the calcination of a number of mono- and multi- metal substituted AFI materials agreed with the HRXRD study on the structure of CoTAPO-5 (4:4%) in which the introduction of a divalent metal ion, Co(II) or Fe(II), to the TAPO-5 synthesis gel did not have a significant effect on the incorporation of Ti(IV) into the AFI framework, with only a small increase observed in the pre-edge intensity compared to TAPO-5. On the other hand, the incorporation of a tetravalent metal ion, Si(IV), to the TAPO-5 synthesis gel decreased the amount of framework titanium. Both Si(IV) and Ti(IV) ions are known to substitute for P(V) in *mono*-substituted AFI materials unless the silicon concentration is above 9 wt. %, above which silicon island formation occurs[32]. For the *multi* substitution of Ti(IV) and Si(IV) in aluminophosphate materials, the incorporation of titanium into the framework is expected to be easier due to the formation of Ti-O-Si linkages, Ti(IV) and Si(IV) substituting for both P(V) and Al(III) [11, 33, 34]. However, the opposite trend for TAPSO-5 was observed. Titanium incorporation into the AFI framework was found to be more difficult compared to TAPO-5, which suggests that both Ti(IV) and Si(IV) ions are competing with each other to substitute solely into the P(V) site.

In addition, the Ti K-edge XANES study exposed the importance of the synthesis method in incorporating metals into the framework of AlPOs, a smaller amount of framework Ti(IV) species were found to be present in TAPO-5 synthesised by method 2 (titanium source added after the organic template) compared to the standard method 1.

Overall, this study has shown that XRD is a good indirect tool for verifying the substitution of heteroatoms into the framework of AFI and other AlPO frameworks (expansion of the unit cell has also been observed in other AlPO frameworks such as AlPO-31[45] and AlPO-20[46]). However, it is difficult to distinguish between incorporated metals when more than one heteroatom has been substituted into the AlPO framework, therefore more direct methods such as XAS is required to evaluate the extent of substitution of each type of metal. Further investigations with theoretical calculations and the combination of more direct and indirect methods, would result in a more reliable picture of the trend in the unit cell parameters which could then be used to predict the expansion of the cell of a large range of metal ions and concentrations in AlPO frameworks.

5.6 References

[1] Akolekar, D. B., *Applied Catalysis a-General*, (1998) **171**, 261.

[2] Fan, W. B.; Fan, B. B.; Song, M. G.; Chen, T. H.; Li, R. F.; Dou, T.; Tatsumi, T.; Weckhuysen, B. M., *Microporous and Mesoporous Materials*, (2006) **94**, 348.

[3] Hartmann, M.; Kevan, L., *Chemical Reviews*, (1999) **99**, 635.

[4] Kapoor, M. P.; Raj, A., *Chemical Communications*, (1999), 1409.

[5] Tuel, A., *Zeolites*, (1995) **15**, 228.

[6] Arends, I.; Sheldon, R. A.; Wallau, M.; Schuchardt, U., *Angewandt Chemie-International Edition in English*, (1997) **36**, 1144.

[7] Wilson, S. T.; Flanigen, E. M., *Acs Symposium Series*, (1989) **398**, 329.

[8] Concepcion, P.; Corma, A.; Nieto, J. M. L.; PerezPariente, J., *Applied Catalysis a-General*, (1996) **143**, 17.

[9] Blasco, T.; Fernandez, L.; Martinez-Arias, A.; Sanchez-Sanchez, M.; Concepcion, P.; Nieto, J. M. L., *Microporous and Mesoporous Materials*, (2000) **39**, 219.

[10] Weckhuysen, B. M.; Rao, R. R.; Martens, J. A.; Schoonheydt, R. A., *European Journal of Inorganic Chemistry*, (1999), 565.

[11] Hartmann, M.; Kevan, L., *Res. Chem. Intermed.*, (2002) **28**, 625.

[12] Concepcion, P.; Nieto, J. M. L.; Mifsud, A.; PerezPariente, J., *Zeolites*, (1996) **16**, 56.

[13] Montes, C.; Davis, M. E.; Murray, B.; Narayana, M., *Journal of Physical Chemistry*, (1990) **94**, 6425.

[14] Saha, S. K.; Waghmode, S. B.; Maekawa, H.; Komura, K.; Kubota, Y.; Sugi, Y.; Oumi, Y.; Sano, T., *Microporous and Mesoporous Materials*, (2005) **81**, 289.

[15] Sanchez-Sanchez, M.; van Grieken, R.; Serrano, D. P.; Melero, J. A., *Journal of Materials Chemistry*, (2009) **19**, 6833.

[16] Shiralkar, V. P.; Saldarriaga, C. H.; Perez, J. O.; Clearfield, A.; Chen, M.; Anthony, R. G.; Donohue, J. A., *Zeolites*, (1989) **9**, 474.

[17] Simmance, K.; Sankar, G.; Bell, R. G.; Prestipino, C.; van Beek, W., *Physical Chemistry Chemical Physics*, (2010) **12**, 559.

[18] Sankar, G.; Raja, R.; Thomas, J. M., *Catalysis Letters*, (1998) **55**, 15.

[19] Sheldon, R. A.; Wallau, M.; Arends, I.; Schuchardt, U., *Accounts of Chemical Research*, (1998) **31**, 485.

[20] Thomas, J. M.; Raja, R.; Sankar, G.; Bell, R. G., *Nature*, (1999) **398**, 227.

[21] Thompson, S. P.; Parker, J. E.; Potter, J.; Hill, T. P.; Birt, A.; Cobb, T. M.; Yuan, F.; Tang, C. C., *Review of Scientific Instruments*, (2009) **80**,

[22] Software, C., TOPAS-Academic Version 4.1, In Coelho, A. Ed. Brisbane, Australia, (2007).

[23] Klap, G. J.; van Koningsveld, H.; Graafsma, H.; Schreurs, A. M. M., *Microporous and Mesoporous Materials*, (2000) **38**, 403.

[24] OriginLab, OriginPro 8 SRO, In Northampton, USA, (1991-2007).

[25] Dent, A. J.; Cibin, G.; Ramos, S.; Smith, A. D.; Scott, S. M.; Varandas, L.; Pearson, M. R.; Krumpa, N. A.; Jones, C. P.; Robbins, P. E., B18: A core XAS spectroscopy beamline for Diamond, In *14th International Conference on X-Ray Absorption Fine Structure*, DiCicco, A.; Filipponi, A. Eds.; Iop Publishing Ltd: Bristol, (2009); Vol. 190.

[26] Ravel, B.; Newville, M., *Journal of Synchrotron Radiation*, (2005) **12**, 537.

[27] Baerlocher, C.; McCusker, L. B.; Olson, D. H., *"Atlas of Zeolite Framework Types", 6th edition*, Elsevier: Amsterdam, (2007).

[28] Sanchez-Sanchez, M.; Sankar, G.; Simperler, A.; Bell, R. G.; Catlow, C. R. A.; Thomas, J. M., *Catalysis Letters*, (2003) **88**, 163.

[29] Shannon, R. D., *Acta Crystallographica Section A-Foundations of Crystallography*, (1976) **A32**, 751.

[30] Roldan, R.; Sanchez-Sanchez, M.; Sankar, G.; Romero-Salguero, F. J.; Jimenez-Sanchidrian, C., *Microporous and Mesoporous Materials*, (2007) **99**, 288.

[31] Pastore, H. O.; Coluccia, S.; Marchese, L., *Annual Review of Materials Research*, (2005) **35**, 351.

[32] Sastre, G.; Lewis, D. W.; Catlow, C. R. A., *Journal of Molecular Catalysis a-Chemical*, (1997) **119**, 349.

[33] Jiao, X. L.; Chen, D. R.; Pang, W. Q.; Yue, Y., *Mater. Lett.*, (2001) **51**, 236.

[34] Ulagappan, N.; Krishnasamy, V., *Journal of the Chemical Society-Chemical Communications*, (1995), 373.

[35] Gianotti, E.; Frache, A.; Coluccia, S.; Thomas, J. M.; Maschmeyer, T.; Marchese, L., *Journal of Molecular Catalysis a-Chemical*, (2003) **204**, 483.

[36] Zahedi-Niaki, M. H.; Kapoor, M. P.; Kaliaguine, S., *Journal of Catalysis*, (1998) **177**, 231.

[37] Blasco, T.; Concepcion, P.; Nieto, J. M. L.; Perezpariente, J., *Journal of Catalysis*, (1995) **152**, 1.

[38] Fan, W. B.; Duan, R. G.; Yokoi, T.; Wu, P.; Kubota, Y.; Tatsumi, T., *Journal of the American Chemical Society*, (2008) **130**, 10150.

[39] On, D. T.; Bittar, A.; Sayari, A.; Kaliaguine, S.; Bonneviot, L., *Catalysis Letters*, (1992) **16**, 85.

[40] Johnson, B. F. G.; Klunduk, M. C.; Martin, C. M.; Sankar, G.; Teate, S. J.; Thomas, J. M., *J. Organomet. Chem.*, (2000) **596**, 221.

[41] Ballirano, P.; Caminiti, R., *Journal of Applied Crystallography*, (2001) **34**, 757.

[42] Yamamoto, T., *X-Ray Spectrom.*, (2008) **37**, 572.

[43] Sankar, G.; Thomas, J. M.; Catlow, C. R. A., *Topics in Catalysis*, (2000) **10**, 255.

[44] Farges, F.; Brown, G. E.; Rehr, J. J., *Phys. Rev. B*, (1997) **56**, 1809.

[45] Umamaheswari, V.; Kannan, C.; Arabindoo, B.; Palanichamy, M.; Murugesan, V., *Proc. Indian Acad. Sci.-Chem. Sci.*, (2000) **112**, 439.

[46] Rajic, N., *Journal of the Serbian Chemical Society*, (2005) **70**, 371.

Chapter 6. The influence of the degree of metal ion substitution in nanoporous catalysts for the conversion of methanol to light olefins

6.1 Chapter Overview

Cobalt substituted silicoaluminophosphate materials with CHA structure were prepared by two different methods and investigated for their activity and selectivity in the methanol to olefin (MTO) reaction and compared of that of unmodified CoAlPO-34 and SAPO-34. The nature and location of the heteroatoms present in the AlPO frameworks were investigated by X-ray diffraction, Infrared spectroscopy and X-ray absorption spectroscopy. These studies revealed the incorporation of both Si(IV) and Co(II) ions in the CHA framework, with little or no formation of silicon islands. For CoSAPO-34 prepared by one procedure (method 1), XAS showed the presence of extra-framework cobalt species which was attributed to the large amounts of methane produced after 30 minutes for the MTO reaction. CoSAPO-34 synthesised by a second procedure (method 2) did not reveal the presence of any extra-framework cobalt species, and had an extremely high selectivity towards ethylene after 30 minutes on stream.

6.2 Introduction

Natural gas is abundant in nature and has been acknowledged as the fuel for the 21st century with a projected consumption increase of nearly 70% between 2002 and 2025[1]. Through steam reforming, natural gas (mostly methane, CH_4) readily produces a mixture of carbon monoxide and hydrogen (synthesis gas) which can then be converted to a number of liquid products such as methanol, ammonia, dimethylether and Fisher-Tropsch products. In particular, methanol can then be catalytically converted to either gasoline (MTG) or olefins (MTO); this provides an indirect route of converting fossil fuels to industrially valuable products such as polymers and fine chemicals.

The conversion of methanol to light olefins (MTO) has significant industrial interest as it reduces the dependency on petroleum naphtha to produce the highly desired ethene and propene products. The MTO mechanism involves the formation of C-C bonds from C_1 fragments generated in the presence of acidic catalysts and reagents[2]. The zeolite ZSM-5 has been primarily used as the acid catalyst in the MTG and MTO process as it possesses shape selectivity and therefore enhances olefin yield through inhibiting the diffusion of large aromatic hydrocarbons. Improvement of the process has been researched through; modifying the reaction conditions (temperature, pressure etc), modifying the zeolite catalyst (reducing strength and number of acid sites etc) and through increasing the shape selectivity of the zeolite[1]. In recent years, it has been well established that the small pore

silicoaluminophosphates, SAPO-34, is an extremely efficient shape selective catalyst for the MTO process owing to its weaker acidity in comparison with ZSM-5[3].

6.2.1 Small pore CHA structure

The structure of SAPO-34 is analogous to the natural zeolite chabazite (CHA). CHA-type materials are small pore 3-dimensional frameworks, built from chabazite cages which connect through double 6-membered rings, see Figure 6.1[4]. They consist of 8-, 6- and 4- membered rings which results in a pore opening of 3.8 Å, therefore they can only sorb straight chain molecules, such as primary alcohols and linear olefins. However, the ability to prohibit the diffusion of branched isomers and aromatics also has the disadvantage of coke formation (condensing of the aromatics to polyaromatics) which causes catalyst deactivation.

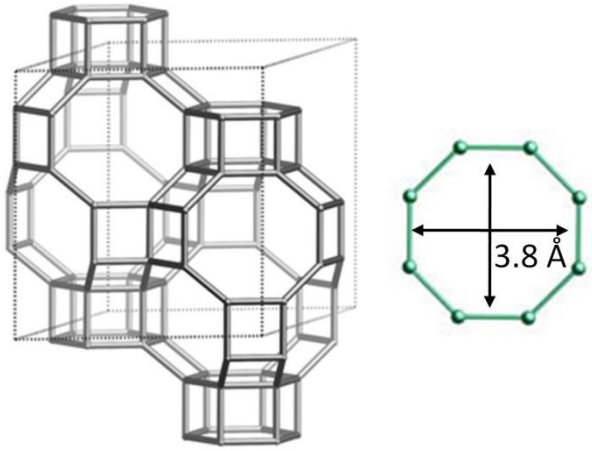

Figure 6.1. *Showing the 3- dimensional cage structure of the Chabazite (CHA) framework, with a pore opening of 7.3 Å.* [5]

Other small pore AlPO structures have also been reported to exhibit good selectivity towards ethene and propene, these include SAPO-18, SAPO-35 and SAPO-17[6-9]. The activity and selectivity towards the desired ethene and propene products is determined by a number of factors such as the structural and chemical properties of the molecular sieve catalyst; this includes the acidity, pore size and shape, particle size and the presence of heteroatoms, for example Ni(II), Co(II), Mg(II), Fe(III) etc, in the SAPO framework[10-12]. In particular, the isomorphous incorporation of Ni(II) into the SAPO-34 framework (NiSAPO-34) has been found to have a high selectivity towards ethene due to the reduction in the acid strength and framework distortions of the CHA type material[10].

6.2.2 The formation of acid and Redox sites in the framework of metal substituted SAPO-34

Isomorphous substitution of Al(III) and P(V) ions with heteroatoms is of importance as it allows the control of acidity and has a direct influence on the activity and selectivity of the AlPO catalyst. The substitution of Al(III) with a divalent metal ion, Co(II) (CoAlPO-34), or the substitution of P(V) with a tetravalent metal ion, Si(IV) (SAPO-34), renders the aluminophosphate framework negative and after removal of the organic template (calcination between 400-600 °C in air), generates Brønsted acid centres when a proton is used to charge balance. Furthermore, framework Co(II) ions can be readily oxidised to Co(III) by thermal treatment in air therefore framework ion substitution can also introduce redox centres[13].

The acidity of these AlPO catalysts depends on a number of factors including; bond angle, bond length and the electrostatic potential around the acid centres and within the cages[3]. The relative strength of Brønsted acid sites in metal substituted CHA-type AlPO materials has been found to differ depending on the type of metal incorporated into the framework; Elanany et al. found the Brønsted acid strength of MeAlPO-34 to follow the order: MnAlPO-34 > CoAlPO-34 > FeAlPO-34 > NiAlPO-34 > SAPO-34 > CrAlPO-34 > TAPO-34[14].

Multi-ion substitution with both a divalent metal ion, Co(II), and a tetravalent ion, Si(IV), has the advantage of introducing both redox and Brønsted acid centres, differing in acid strength, if silicon ions substitute primarily for P(V) (otherwise a

neutral framework would result with equal amounts of heteroatoms). An example of the formation of a Brønsted acid and a redox site in a MeSAPO-34 material is presented in Figure 6.2.

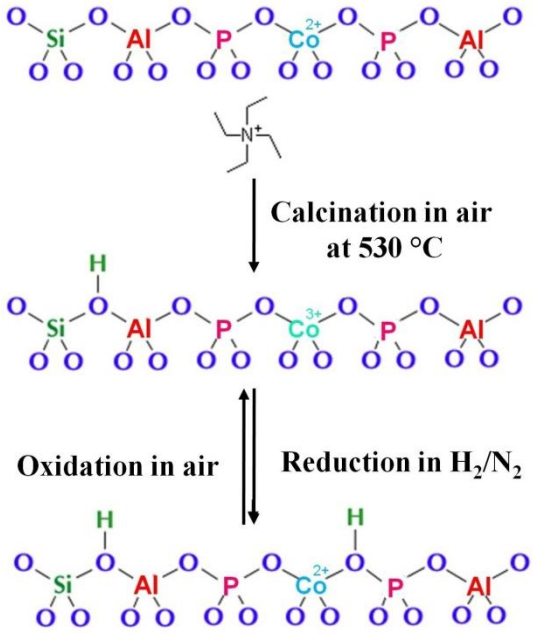

Figure 6.2. *Schematic illustration of the formation of Brønsted acid and redox sites in CoSAPO-34 catalysts.*

6.2.3 Aims and objectives

The aim of this work was to investigate the effect of the addition of a redox metal cation, Co(II), on the acid catalytic properties of SAPO-34 to transform methanol to light olefins. A recent study on the substitution of Ti(IV) into the P(V) sites of the

large pore AlPO-5 framework (Chapter 5) found that the addition of another tetravalent metal ion, Si(IV), to the synthesis gel decreased the incorporation of titanium into the AlPO-5 framework, whereas the incorporation of a divalent metal ion, Co(II), with Ti(IV) had no significant effect on the extent of titanium substitution. If this is true for the substitution of all tetravalent metal ions into the framework of AlPOs, then the extent of Si(IV) incorporation in SAPO-34 should be equivalent to CoSAPO-34. Upon calcination, these materials would therefore result in an equivalent number of Brønsted acid centres, assuming that all the Co(II) were oxidised to Co(III), with differences in the strength of the acid sites. In addition, the incorporation of divalent metal ions along with Si(IV), influences the formation of silicon islands in the CHA structure which in turn changes the acidity strength of the AlPO framework and may have a positive effect on its ability to acid catalyse the conversion of methanol to light olefins [14].

The synthetic strategy for the isomorphous substitution of metal ions into the AlPO framework has been found to have a significant effect on their incorporation into the tetrahedral framework sites (observed for TAPO-5 in Chapter 5 and by Dubois et al. for the incorporation of Ni(II) into the NiSAPO-34 framework[10]). Therefore, this work focussed on understanding the effect of order of addition of chemicals on the nature and extent of substitution of Co(II) and Si(IV) in CoSAPO-34. The nature and location of the transition metal ions, Co(II), in CoSAPO-34 prepared by two different methods were studied by X-ray diffraction, Fourier-transform Infrared Spectroscopy (FTIR) and Co K-edge X-ray absorption Spectroscopy (XAS). Results from these characterization studies give insights into the CoSAPO-34 acid catalytic properties

which were compared to CoAlPO-34 and SAPO-34 for the conversion of methanol to light olefins.

6.3 Experimental

6.3.1 Synthesis procedure

Hydrothermal treatment was employed to prepare each of the transition metal substituted chabazite aluminophosphate materials with tetraethyl ammonium hydroxide (TEAOH) as the organic template. For the synthesis of all materials, the following chemicals were used: phosphoric acid (H_3PO_4, 85 wt.%), aluminium hydroxide hydrate ($Al(OH)_3$), TEAOH ($N(C_2H_5)_4$, 35 wt.% in H_2O) and distilled water. For the cobalt substituted materials, the cobalt source was cobalt(II) acetate tetrahydrate ($(CH_3COO)_2Co$), and for SAPO-34 and CoSAPO-34, the silicon source was LUDOX AS-40 colloidal silica (SiO_2, 40 wt % in H_2O). All reagents were purchased from Aldrich.

CoSAPO-34 (Method 1): P – Al – Co – Si – TEAOH.

In a typical synthesis, phosphoric acid was first diluted with water, followed by the addition of aluminium hydroxide hydrate with vigorous stirring until homogeneous. Cobalt acetate solution (cobalt acetate tetrahydrate diluted separately in distilled water) was added to the gel and stirred for 30 minutes before the addition of the

silicon source. The mixture was stirred for 30 minutes followed by the dropwise addition of TEAOH. After 2 hours of stirring with a magnetic stirrer bar, the pH was recorded and adjusted to 7 by varying the ratio of template to phosphorus, e.g. the pH was decreased by adding phosphoric acid.

CoSAPO-34 (Method 2): P – Al – Co –TEAOH – Si.

A second sample of CoSAPO-34 was prepared, following a different synthesis route which involved a change in the order of addition of the silicon source. The key difference is that the organic template, TEAOH, was added after the cobalt source followed by 30 minutes stirring. To this solution the silicon source was added with subsequent stirring for 2 hours. Once again the pH was adjusted to 7.

It should be noted that for the synthesis of CoAlPO-34 and SAPO-34, method 1 was employed as it has been found previously that adding the metal source prior to the organic template increases its incorporation into the framework (see Chapter 5). The gel composition used throughout the synthesis procedures of the CHA-type materials was; (1-*x*) Al: (1-*y*) P: *x* Co: *y* Si: 25 H_2O: 1.0 TEAOH, where *x* and *y* were either 0 or 0.04. The AlPO-5 material, employed for comparison over the methanol to olefin catalytic reaction, was synthesised as described in Chapter 5. The resulting gels were placed in a Teflon-lined stainless steel autoclave and heated at 160 °C for 2.5 days. The products were centrifuged, washed with distilled water and dried overnight at 100 °C.

6.3.2 Characterization

6.3.2.1 High-resolution X-ray diffraction

Ex situ HRXRD data was collected at the I11 beamline of the Diamond Light Source in Oxford, England[15]. The set-up of this beamline is described elsewhere (Chapter 4: 4.3.2.2). The samples were loaded into 0.5mm capillaries and data collected at $\lambda = 0.82743$ Å employing the position-sensitive detector (PSD) available, with an acquisition time of 1 minute per scan (total of 2 scans per sample).

6.3.2.2 Fourier-Transform Infrared Spectroscopy

In situ Fourier-Transform infrared (FTIR) spectroscopy measurements were carried out to investigate the formation of Brønsted acid acids during the calcination and reduction of SAPO-34, CoAlPO-34 and the two CoSAPO-34 materials. IR analysis was achieved using a Perkin Elmer Spectrum One FT-IR spectrometer fitted with a specially designed *in situ* cell (Figure 6.3).

In a typical experiment, *ca.* 20 mg of sample was pressed into a 13 mm disc and placed into the custom built sample holder of the *in situ* cell. The sample was heated in an atmosphere of oxygen (air) at 5 °C/minute to 530 °C and held for 40 minutes. The sample was cooled back down to room temperature and flushed with nitrogen for

safety precautions; this was followed by heating in 2% H_2/N_2 at 5 °C/minute to 500 °C. 4 scans per analysis were employed at approximate intervals of 10 °C, with a resolution of 4 cm^{-1}.

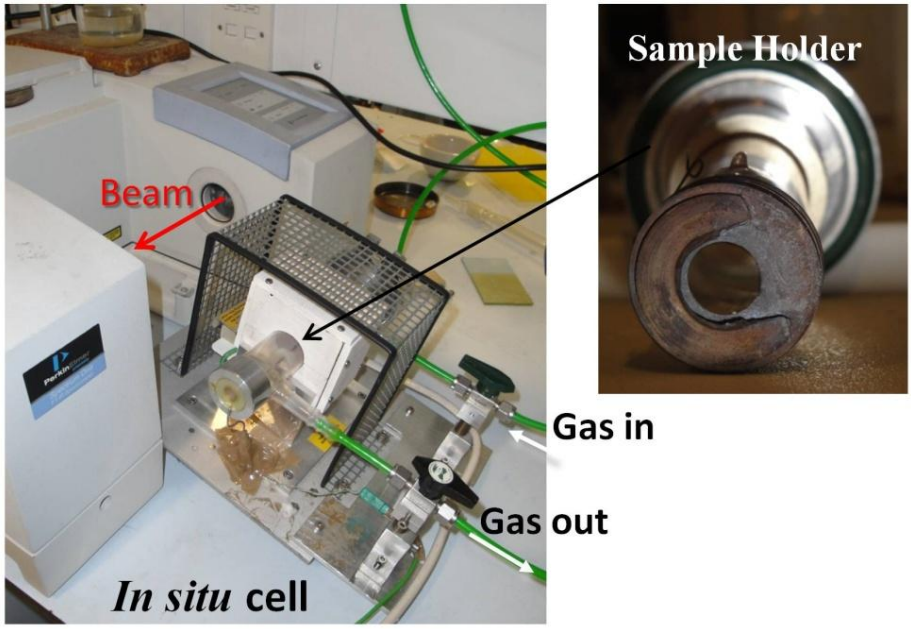

Figure 6.3. *Photographs showing the in situ FTIR cell and sample holder used. The cell has been slotted out of the beam for clarity.*

6.3.2.3 X-ray Absorption Spectroscopy

In situ X-ray Absorption Spectroscopy (XAS) measurements at the Co K-edge were carried out to determine the substitution, oxidation state and coordination environment of cobalt in both the CoSAPO-34 materials during calcination in air. XAS measurements were collected at the B18 (core EXAFS) beamline[16] of

Diamond Light Source, the set-up of this beamline is described elsewhere (Chapter 5.3.2.2).

In a typical experiment, *ca.* 80 mg of sample was pressed into a 13 mm disc and placed into a custom built *in situ* high temperature furnace (see Chapter 5.3.2.2) for heat treatment to 530 °C (5 °C/minute), which was dwelled for 40 minutes, in an atmosphere of oxygen (air). XAS measurements were recorded at the Co K edge in transmission mode; Extended X-ray Absorption Fine Structure (EXAFS) data was collected before calcination, at 530 °C and after cooling, and X-ray Absorption Near Edge Structure (XANES) data was collected during the heating and cooling stages. All XAS data was processed utilising the program Athena to background remove and normalize the data. Further analysis of the EXAFS data was carried out fitting the first cobalt shell using Artemis[17].

6.3.2.4 Catalytic analysis – Gas chromatography

Each methanol conversion reaction was carried out using a custom built continuous flow reactor shown in Figure 6.4. In a typical experiment, 200 mg of the as-prepared catalyst was crushed using a mortar and pestle, and pelletized using a 50 micron mesh sieve. The catalysts were activated by heating (calcination) the samples in air at 530 °C (ramp of 5 °C/minute, dwell for 2 hours) to remove the template occluded within the pores of the CHA-type materials. The samples were then cooled to a specific

temperature and loaded into a tubular quartz reactor (inside the furnace), held in place by a quartz frit.

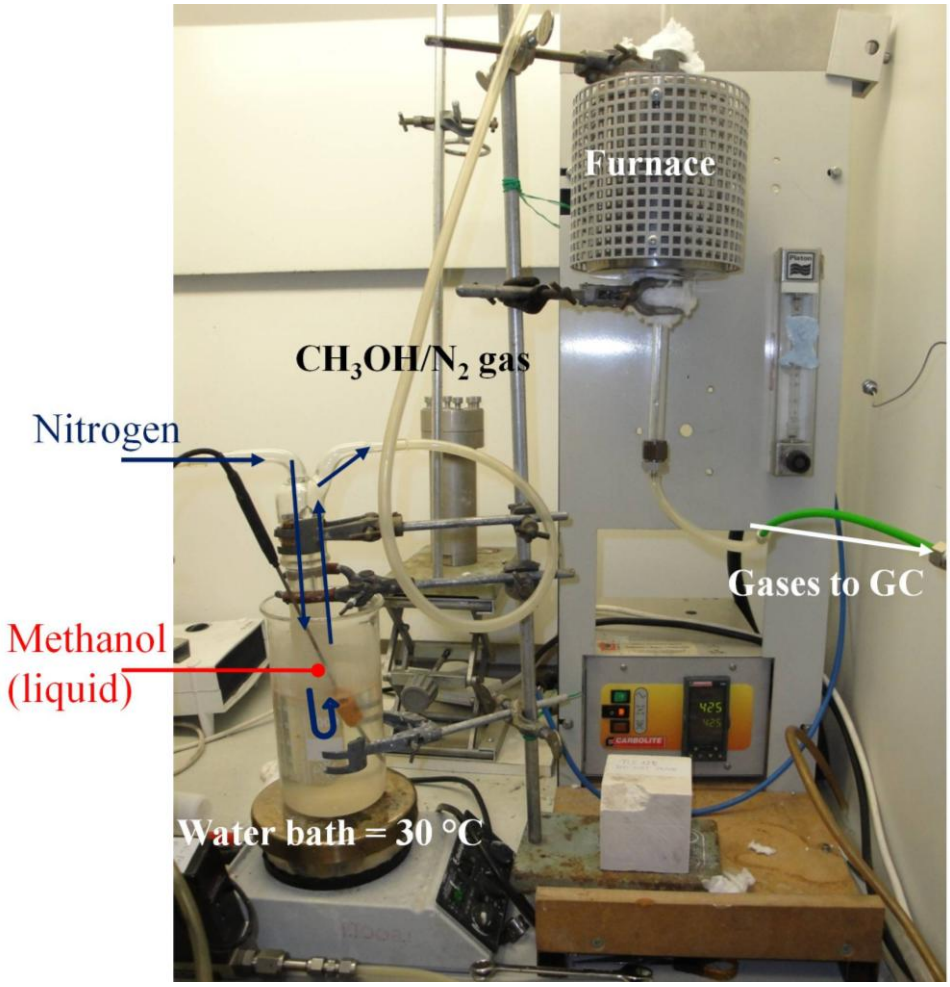

Figure 6.4. *Photograph of the MTO catalytic reaction set-up employed*

The calcined catalysts were heated to 425 °C (5 °C/min) in the furnace and subjected to nitrogen gas (20 ml/min) which had been bubbled through methanol (Aldrich). Gas Aliquots of the products were collected at 30 minutes and 1 hour, and

analysed using a Perkin Elmer Varian gas chromatograph equipped with a Porapak N column and both a Flame Ionisation Detector (FID) (for hydrocarbon detection) and a Thermal Conductivity Detector (TCD) (for nitrogen detection).

6.3.2.4.1 Data Analysis

Retention times for a number of olefins and paraffins were obtained through calibration of a known mixture of gases, consisting of methane, ethylene, ethane, propylene, propane, butane, butene, dimethyl ether and nitrogen. The degree to which a component produces a signal in a mixture of a known amount of substance can be very different for each component, and is known as the response factor. For example, the analysis would be weighted towards a component which produces a greater signal for the same amount (greater response factor). Therefore, it is necessary to calculate a relative response factor (RRF) in order to correct the area of the signal observed. The RRF of each component were calculated based on the molar mass of each product relative to methane (Equation 6-1). The area of each product peak was corrected depending on the relative response factor, and normalised with respect to nitrogen.

Equation 6-1. *Relative Response Factor*

$$\boldsymbol{Relative\ response\ factor\ (RRF)} = \frac{\boldsymbol{Molar\ mass(product)}}{\boldsymbol{Molar\ mass(methane)}} \times \frac{\boldsymbol{Area(methane)}}{\boldsymbol{Area(product)}}$$

The methanol conversion percent was calculated using Equation 6-2, where t_0 is the area under the peak corresponding to methanol prior to the reaction and t is the area under the methanol peak after the reaction at a set time.

Equation 6-2. *Methanol Conversion*

$$Methanol\ Conversion = \frac{Area(t_0)\ -\ Area(t)}{Area\ (t_0)} \times 100$$

Finally, the selectivities of the main products; methane, ethylene, propylene, dimethyl ether, butene and butane products detected were calculated relative to each other using Equation 6-3.

Equation 6-3. *Product Selectivity*

$$Product\ Selectivity\ (\%) = \frac{RRF(product)}{RRF(total\ products)} \times 100$$

6.4 Results and Discussion

The results from a high-resolution X-ray diffraction (HRXRD) study on the effect of mono and multi ion substitution into small pore aluminophosphate type-34 structures is first examined. Next, the effect of the order of addition of the cobalt and silicon precursors on the structure of the active sites in multi-ion substituted CHA materials is discussed. Results from an *in situ* Fourier-Transform (FT) infrared spectroscopy study and an *in situ* Co K-edge X-ray absorption spectroscopy (XAS) investigation are presented. Catalytic analysis of the small pore AlPO materials were subsequently carried out for the conversion of methanol to light olefins.

6.4.1 HRXRD of the as-synthesised materials

The HRXRD patterns acquired for the as-synthesised mono- and multi- heteroatom substituted CHA- type materials are shown in Figure 6.5. Comparison of the diffraction patterns with literature indicates, irrespective of the dopant ion, all materials were crystalline and phase pure (rhombohedral CHA structure with space group R-3m) [4].

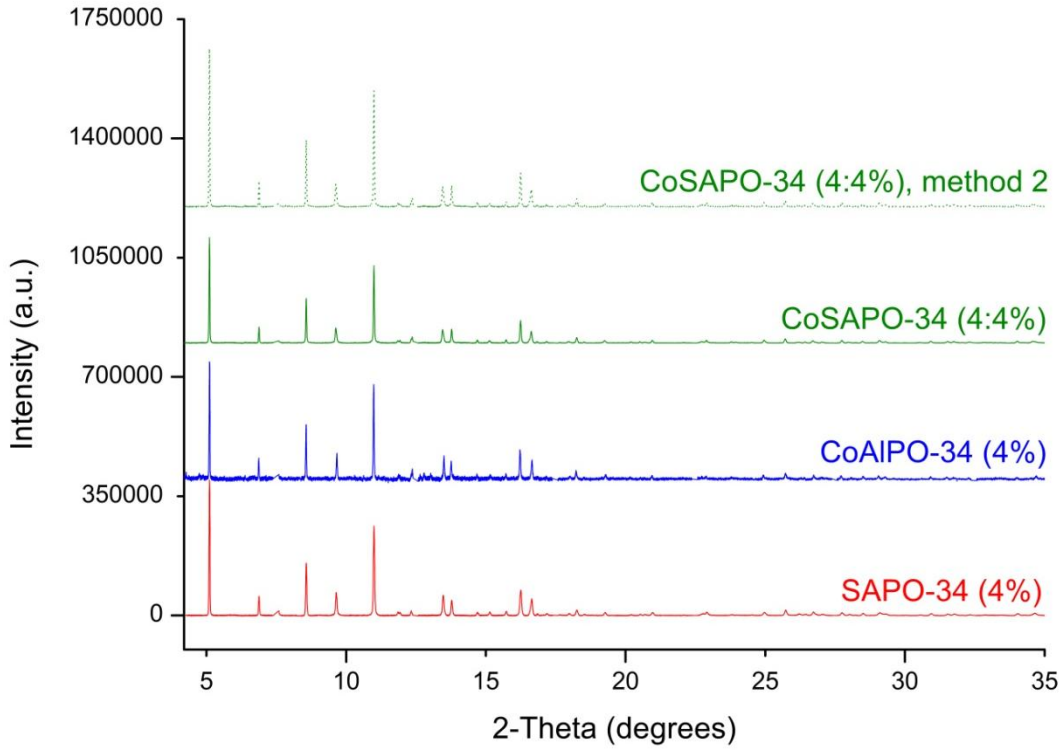

Figure 6.5. *Background subtracted HRXRD patterns of the as synthesized SAPO-34, CoAlPO-34, and CoSAPO-34 (prepared by both method 1 and 2) materials. All reflections could be indexed to the small pore CHA structure. Only data in the 2-theta range of 4 - 35° are shown for clarity.*

The unit cell parameters, determined with a Pawley fit utilised in Topas-Academic, are listed in Table 6-1 along with the average ionic radii determined from the initial gel composition (as calculated in Chapter 5: 5.4.1.2).

Table 6-1. *Gel composition and calculated unit cell parameters of the as-synthesized CHA type materials.*

Sample	Gel composition	Average Ionic Radius (Å)†	Unit cell parameters		
			a=b (Å)	c (Å)	Volume (Å^3)
SAPO-34	0.96P:1.0Al:0.04Si	0.2818 *(0.2796)*	13.8006(1)	14.7692(2)	2436.0(5)
CoAlPO-34	1.0P:0.96Al:0.04Co	0.2838	13.8216(3)	14.7413(8)	2438.8(2)
CoSAPO-34 (method 1)	0.96P:0.96Al:0.04Co:0.04Si	0.2856 *(0.2834)*	13.8045(1)	14.7919(3)	2441.2(6)
CoSAPO-34 (method 2)	0.96P:0.96Al:0.04Co:0.04Si	0.2856 *(0.2834)*	13.8240(1)	14.8000(3)	2449.3(5)

†Average ionic radius calculated assuming Co(II) substitutes for Al(III) and Si(IV) for P(V). The average ionic radii calculated based on Si(IV) substituting equally for both Al(III) and P(V) is given in brackets.

It is well known that Co(II) solely substitutes for Al(III) and Si(IV) *preferentially* substitutes for P(V) in the AlPO framework. On comparison of the cell parameters of CoSAPO-34 (4:4%) with SAPO-34 (4%), synthesised by method 1, an increase in the a(=b) and c parameters with the addition of Co(II) to the gel is observed. Assuming that the silicon incorporation into both frameworks is identical[18], this increase in the unit cell parameters is indicative of Co(II) ions substituting for Al(III) in the CoSAPO-34 framework. For analysis of the substitution of silicon into the framework, the unit cell parameters of CoSAPO-34 (4:4%) with CoAlPO-34 (4%) both synthesised with method 1, were compared. An increase in the c parameter (and

unit cell volume) but a small decrease in the a(=b) parameter upon the addition of Si(IV) was observed. Although all samples were dried above 100 °C, the uptake of water molecules from a moist atmosphere cannot be ruled out which may have a significant effect on the unit cell parameters, in addition the CHA framework is known to show negative thermal expansion[19]. It should be noted that un-substituted AlPO-34 cannot form under the reaction conditions employed in this work (HF is required)[20], therefore difficulties arise in comparing the unit cell parameters to that of the un-substituted analogue to assist in determining the extent of substitution.

On comparison of the unit cell parameters of CoSAPO-34 synthesised with method 1 and 2; it is clear that the unit cell is larger for CoSAPO-34 synthesised with method 2 (silicon source added after the template). A larger unit cell may be indicative of a larger incorporation of heteroatoms in the tetrahedral framework sites of CoSAPO-34. Results from a structural investigation on the incorporation of divalent or tetravalent metal ions with Ti(IV) in the AFI framework (Chapter 5) concluded that the addition of a divalent metal ion did not affect the extent of Ti(IV) substitution. If this can be extended for substitution of Si(IV) into the CHA framework, then the larger unit cell parameters observed in CoSAPO-34 (method 2), may be indicative of a larger incorporation of Co(II) ions. It should also be noted that although the number of silicon sites in the different CHA materials may be equivalent, their substitution mechanism may differ; if Si(IV), 0.26 Å, substitutes for P(V), 0.17 Å, then an expansion of the unit cell is expected due to the increase in ionic radii. However, if Si(IV), 0.26 Å, substitutes equally for both P(V), 0.17 Å, and Al(III), 0.39 Å, in the CHA framework, forming silicon islands, then a small decrease in the

unit cell would be expected. Therefore, the larger unit cell parameters observed for CoSAPO-34 (method 2) may also be indicative of a different Si(IV) substitution mechanism, in which the formation of silicon islands in CoSAPO-34 (method 1) is more dominant compared to CoSAPO-34 (method 2). For a more direct analysis, X-ray absorption spectroscopy at the Co K edge would be required to reliably determine the extent of Co(II) substitution in the small pore CHA framework of the CoSAPO-34 materials.

On comparison of the unit cell volume of SAPO-34, CoAlPO-34, CoSAPO-34, and CoSAPO-34 (method 2), in Figure 6.6, the following trend is observed; the volume increases as the calculated average ionic radii increases. Although analysis of the individual a(=b) and c parameters proved inconclusive, it is clear from the larger unit cell volumes that both cobalt and silicon ions are substituting into the CoSAPO-34 frameworks, irrespective of the method. The smaller unit cell volume of CoSAPO-34 synthesised with method 1, as stated previously, may be due to a lesser extent of heteroatom incorporation or due to the formation of silicon islands. Therefore, infrared spectroscopy and XAS was carried out to investigate the incorporation of Si(IV) and Co(II) in the CoSAPO-34 materials.

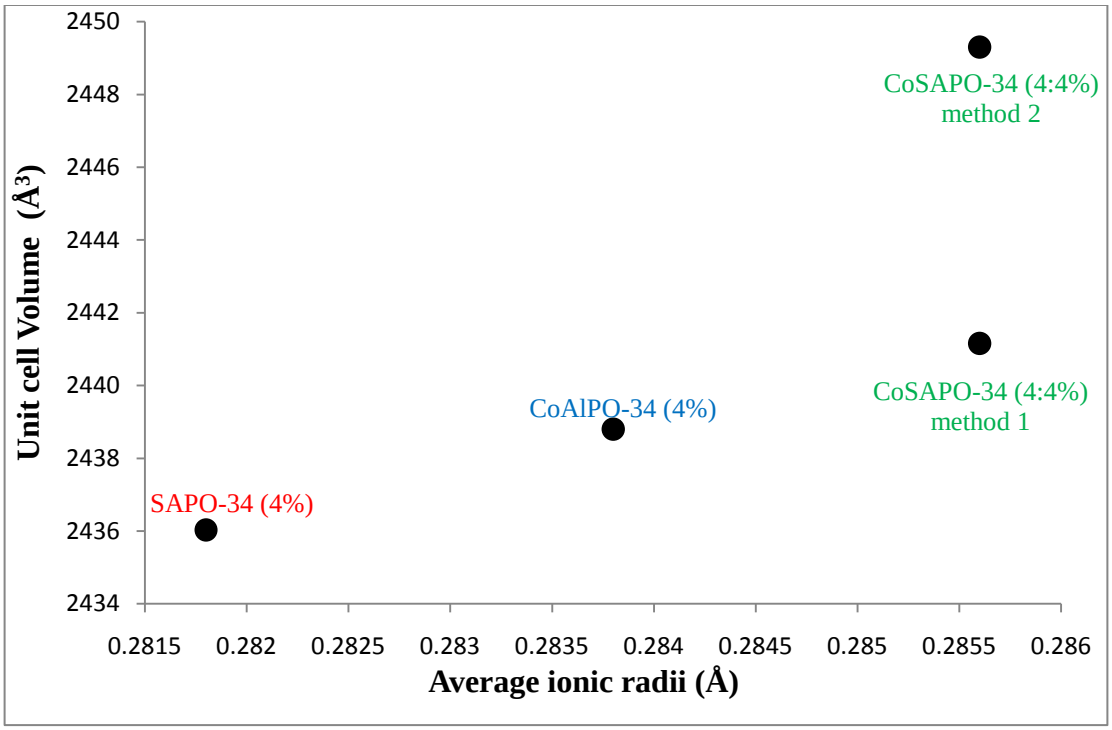

Figure 6.6. *A plot of the unit cell volume of the CHA-type materials as a function of the average ionic radius, assuming that Si(IV) substitutes solely for P(V).*

6.4.1.1 FT infrared study of the Brønsted acid sites

The substitution of Al(III) by divalent metal ions or the substitution of P(V) with tetravalent cations renders the aluminophosphate framework negative and after removal of the organic template (calcination between 400-600 °C in air), generates Brønsted acid centres when a proton is used to charge balance. Multi-ion substitution with both Co(II) and Si(IV) has the advantage of introducing both redox and Brönsted acid centres if silicon ions substitute primarily for P(V) (otherwise a neutral framework would result with equal amounts of heteroatoms). To confirm substitution

of P(V) with Si(IV) in the CoSAPO-34 frameworks, *in situ* Fourier-Transform infrared (FTIR) spectroscopy was carried out to investigate the formation of Brönsted acid sites during calcination in air (oxidation) followed by reduction ($2\%H_2/N_2$) and compared to that of SAPO-34 and CoAlPO-34.

FTIR spectra collected during the calcination and subsequent reduction of CoSAPO-34 synthesized by method 1, were found to be noisy, possibly due to large inhomogenities in the sample. For this reason, only FTIR data collected after calcination and after reduction were analyzed for comparison with CoSAPO-34 (method 2), these results are shown and compared later.

Figure 6.7 shows the transmittance FTIR spectra collected *in situ* during calcination in air (up to 530 °C) of CoSAPO-34 prepared via method 2. The C-H stretching (2850 – 3000 cm^{-1}) and bending (1350 – 1470 cm^{-1}) from the organic TEAOH template, could be assigned and were found to completely vanish after heating to *ca.* 420 °C. This introduced two broad bands at 3307 and 3102 cm^{-1} which could be assigned to N-H stretching due to the decomposition of the template, which eventually vanished at 530 °C[20].

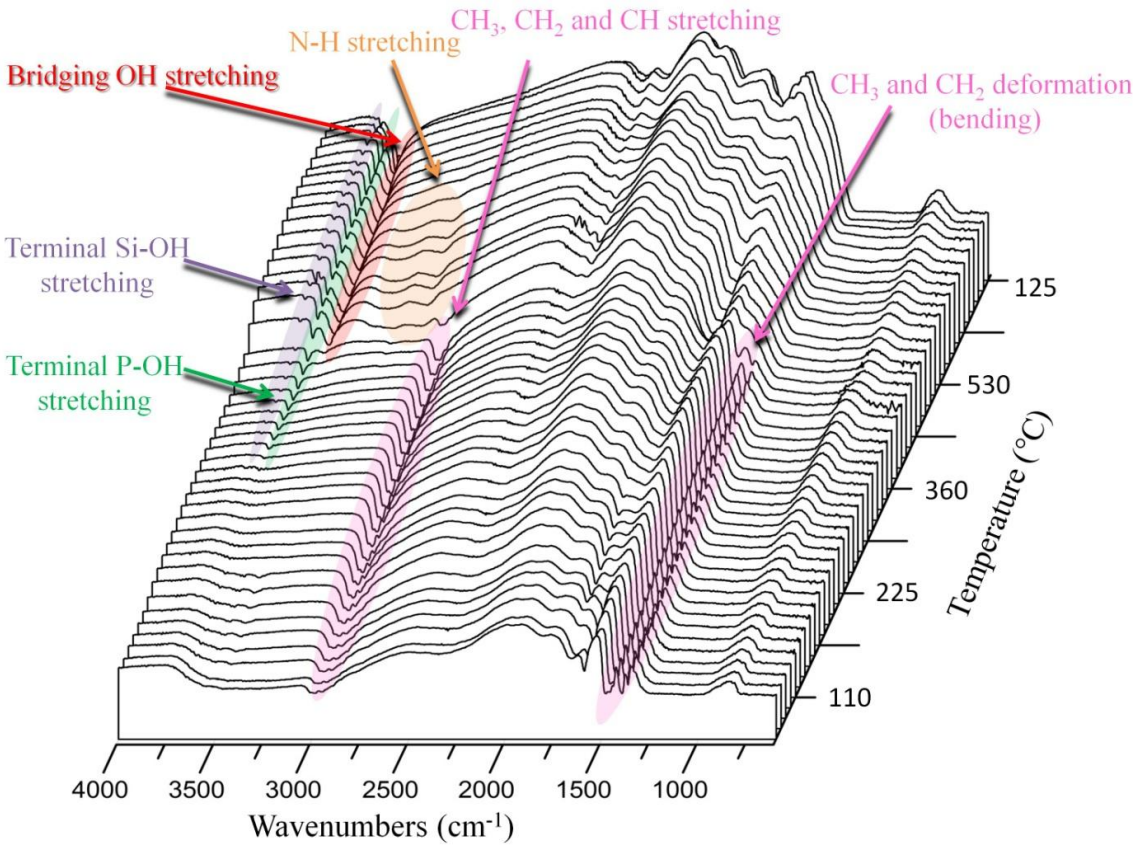

Figure 6.7. *FTIR spectra collected in situ during the calcination and oxidation of CoSAPO-34 synthesized with method 2. The band assignment is also indicated.*

As the organic template decomposes and leaves the voids of the small pore CoSAPO-34 material, charge compensating protons are required to charge balance. These protons first bond to phosphorus and silicon surface defects, and appear in the FTIR spectra, prior to the full decomposition and removal of the template, in the form of terminal P-OH and Si-OH stretching at *ca.* 3670 and 3733 cm^{-1}, respectively[21]. After the C-H stretching bands from the template vanish (*ca.* 420 °C), an additional broad band is observed in the FTIR spectra in the region of 3620 to 3561 cm^{-1}, which is attributed to bridging hydroxyl groups (Si-OH-Al and Co-OH-P)[22]. After being

held at 530 °C for *ca.* 40 minutes, the area of this Brønsted acid feature starts to decrease and becomes more resolved at higher wavenumbers. This can be attributed to the Co(II) species oxidizing to Co(III), which results in the loss of Co-OH-P species. The FTIR spectra of the calcined CoSAPO-34 (method 2) material after cooling at 120 °C is shown in Figure 6.8, and clearly shows two distinct bands in the bridging OH region. Assuming that the majority of the framework Co(II) ions were oxidized to Co(III), then these FTIR bands can be attributed to the Si-OH-Al hydroxyl groups. The higher wavenumber band at 3625 cm^{-1} is ascribed to un disturbed Si-OH-Al hydroxyl groups in the chabazite cage, whereas the band at 3600 cm^{-1} is from hydroxyl groups interacting with oxygen atoms in the framework and are located in the double 6-membered rings[23, 24]. This is analogous to what was observed in both the calcined and reduced FTIR spectra of the prepared SAPO-34 material.

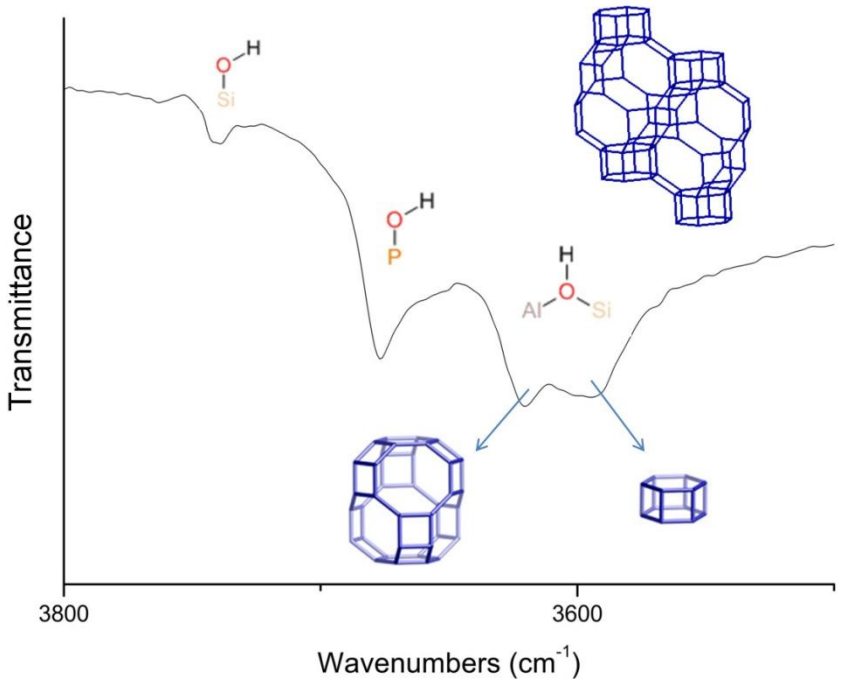

Figure 6.8. *The hydroxy region of the CoSAPO-34 (method 2) FTIR spectra collected at 120 °C after calcination. The terminal Si-OH and P-OH regions are indicated, including the bridging OH region with the different sites of the CHA structure.*

Futhermore, the CoSAPO-34 (method 2) material was reduced in an atmosphere of hydrogen and nitrogen (2% H_2/N_2) up to 420 °C. The resulting FTIR spectra of the reduced sample is shown in Figure 6.9 and compared to the calcined analogue (both recorded at 420 °C). It is clear that the reduced CoSAPO-34 material has a more intense band in the bridging hydroxy region (*ca.* 3600 cm^{-1}) which is due to the OH stretching from the additional Brønsted acid sites when Co(III) is reduced back to Co(II). A difference IR spectrum (the oxidized spectra minus the reduced spectra) is also shown in Figure 6.9, which reveals a maxima at 3554 cm^{-1}.

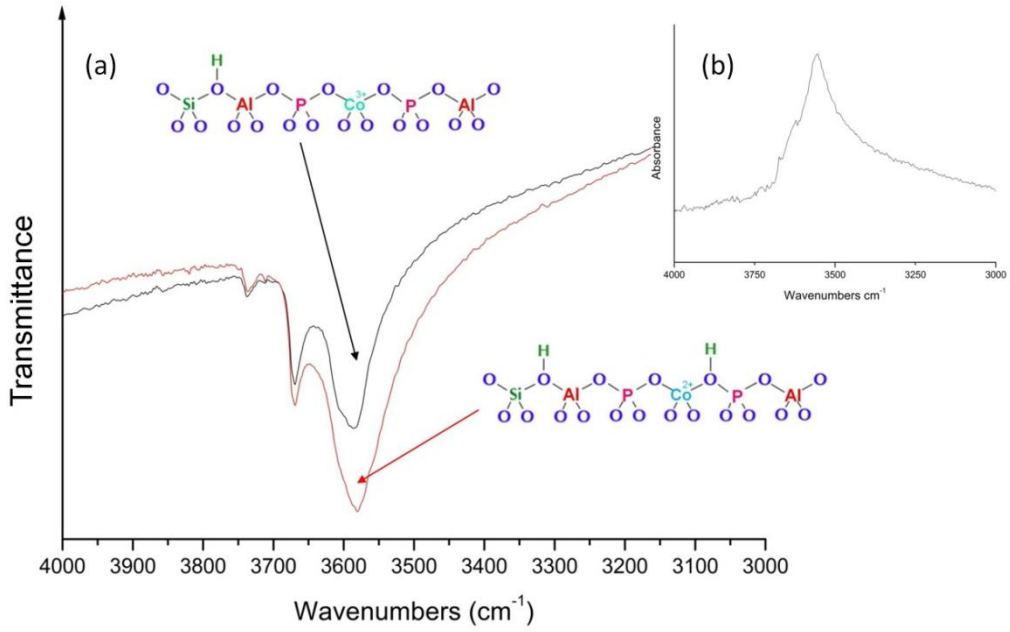

Figure 6.9. *Showing the hydroxy region of the FTIR spectra of CoSAPO-34 synthesised with method 2 (a); after calcination in air (black) and the reduced form (red). Also shown is the difference IR spectra (b) for the calcined and reduced data.*

The FTIR spectra of CoSAPO-34 (method 2) are compared to that of calcined and reduced CoAlPO-34 in Figure 6.10. It is clear that there is no indication of bridging hydroxyl groups in the calcined CoAlPO-34 data which is expected when the majority of Co(II) species are oxidized to Co(III). This is in contrast to CoSAPO-34 (method 2) in which the band representing the bridging hydroxyl groups is still apparent after calcination. Upon reduction, the band representing the bridging hydroxyl groups in CoSAPO-34 (method 2) increases in area, becoming more pronounced at lower wavenumbers. The formation of bridging hydroxyl groups becomes apparent in the FTIR spectra of CoAlPO-34 during reduction and has a broad feature at 3560 cm^{-1}. This band is comparable to the maxima observed in the

difference spectra (Figure 6.9), before and after reduction of CoSAPO-34 (method 2), revealing the contribution from the Co-OH-P hydroxyl groups.

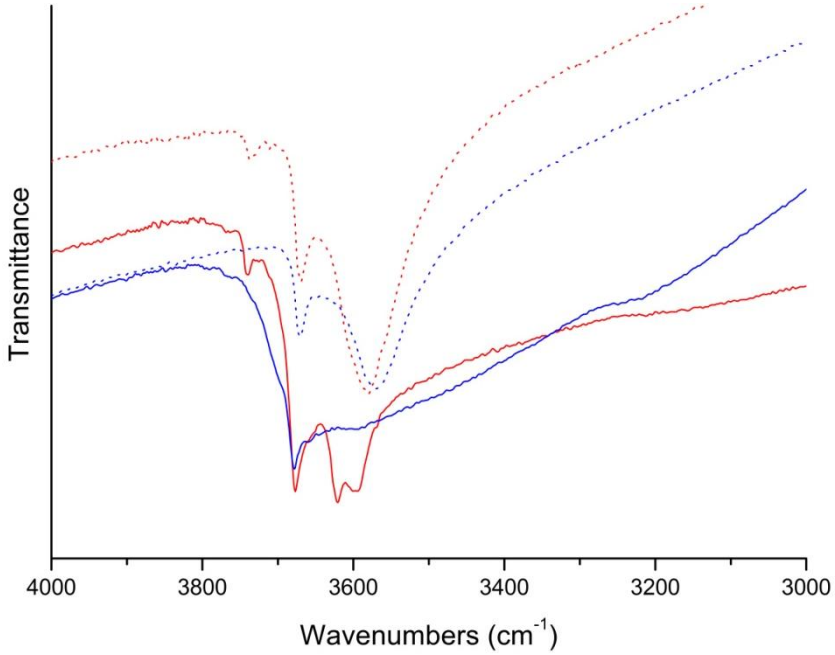

Figure 6.10. *Comparison of the hydroxy region of the calcined (solid line) and reduced (dotted line) FTIR spectra collected for CoSAPO-34 synthesized by method 2 (red) and CoAlPO-34 (blue).*

CoSAPO-34 prepared by method 2, has been found to show Brønsted acidity composing off both Co-OH-P and Si-OH-Al species, with the addition of both Si-OH and P-OH terminal defects at the surface and/or from amorphous impurities. The FTIR spectra of the calcined and reduced CoSAPO-34 materials synthesized from method 1 are shown in Figure 6.11. As stated before the data are noisy, however there is evidence of bridging hydroxyl groups in both the calcined (3625 and 3600 cm^{-1}) and reduced (3577 cm^{-1}) spectra, along with Si-OH (3738 cm^{-1}) and P-OH

(3670 cm^{-1}) terminal defects as seen also in CoSAPO-34 (method 2). Due to the difference in the quality of the data it is difficult to compare the CoSAPO-34 materials prepared by the two different methods.

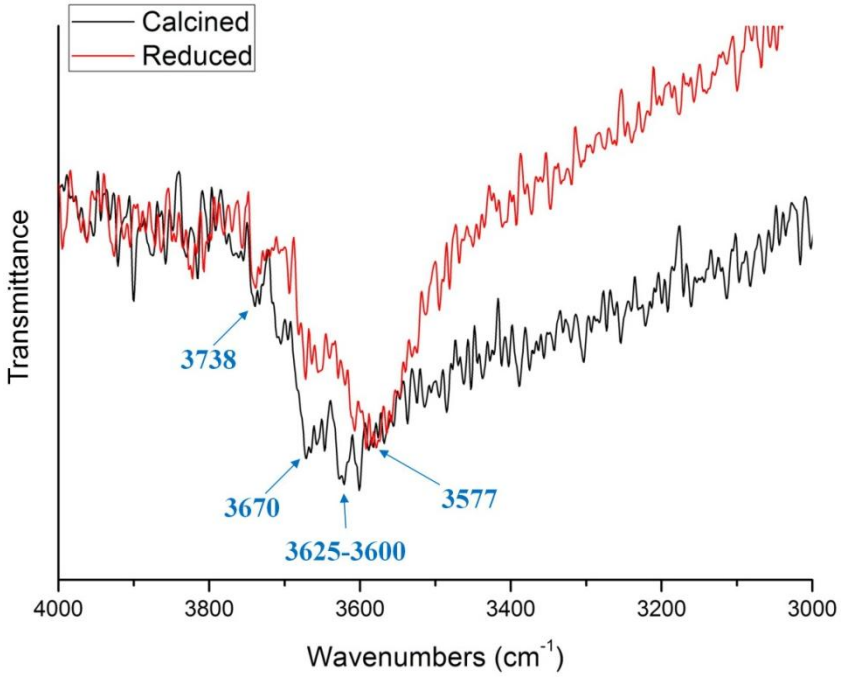

Figure 6.11. *The hydroxyl region of the FTIR spectra collected after calcination (black) and reduction (red) of CoSAPO-34 prepared by method 1.*

6.4.1.2 *In situ* XAS study during the calcination of CoSAPO-34

The substitution, oxidation state and coordination environment of cobalt in the framework of as-synthesised CoSAPO-34, prepared by the two different methods; method 1 (Silicon added before template) and method 2 (silicon added after template), was investigated by X-ray absorption spectroscopy (XAS) during calcination in air at 530°C. In both materials, the as-synthesised form was coloured blue, and after calcination the powders were green in colour suggesting cobalt transforming from Co(II) to Co(III) in a tetrahedral environment.

The normalized XAS spectra of the as-synthesised CoSAPO-34 materials, prepared by method 1 or method 2, are shown in Figure 6.12 along with the standards; cobalt aluminate $CoAl_2O_4$ (Co(II) surrounded by 4 oxygen atoms in a tetrahedral environment[25]) and cobalt acetate solution (Co(II) surrounded by 6 oxygen atoms in an octahedral environment[26]). On comparison of the X-ray absorption near edge structure (XANES) it is clear that irrespective of the synthesis method employed, both spectra were found to be closely similar to that of $CoAl_2O_4$. The XANES data for the CoSAPO-34 samples and $CoAl_2O_4$ all consist of a pre-edge (marked 1s→3d) feature and a smaller white line feature (marked 1s→4p) which indicates that the majority of the cobalt species are in a tetrahedral environment in the as-synthesised materials.

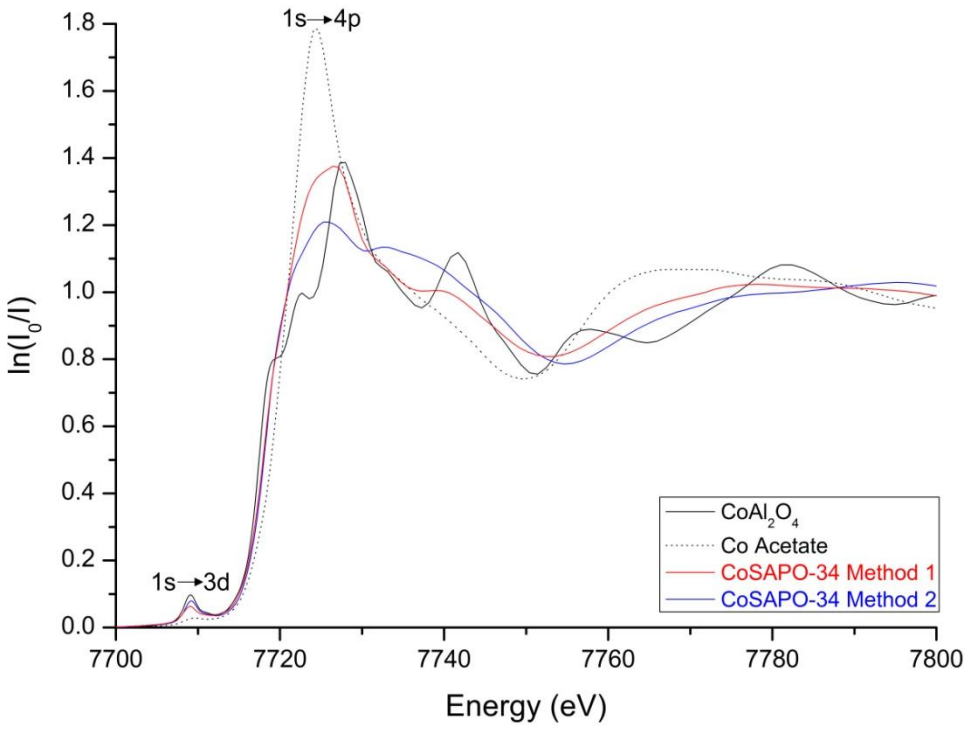

Figure 6.12. *Normalized XAS spectra of the as-synthesized CoSAPO-34 materials, prepared with method 1 (red) or method 2 (blue), are compared to $CoAl_2O_4$ (solid black line) and Co acetate solution (dotted black line).*

The Co K-edge Extended X-ray Absorption Fine Structure (EXAFS), together with the associated Fourier transforms (FT) of the experimental and calculated data of as-synthesized CoSAPO-34 (prepared by both methods) are presented in Figure 6.13. The calculated data is based on the best fit to the first shell (Co-O), in R space, since the primary aim of the study is to understand the oxidation state and local environment around the central cobalt atom. Typical Co-O bond distances resulted from the analysis of the $CoAl_2O_4$ (1.94 Å[25]) and cobalt acetate (2.08 Å[27]) solids, with a cobalt coordination number of 3.9 and 6.2 respectively, confirming the validity

of the analysis. It should be noted that the standard errors calculated through EXAFS for the coordination number is 10 % and for the bond distances is ~ 0.02 Å.

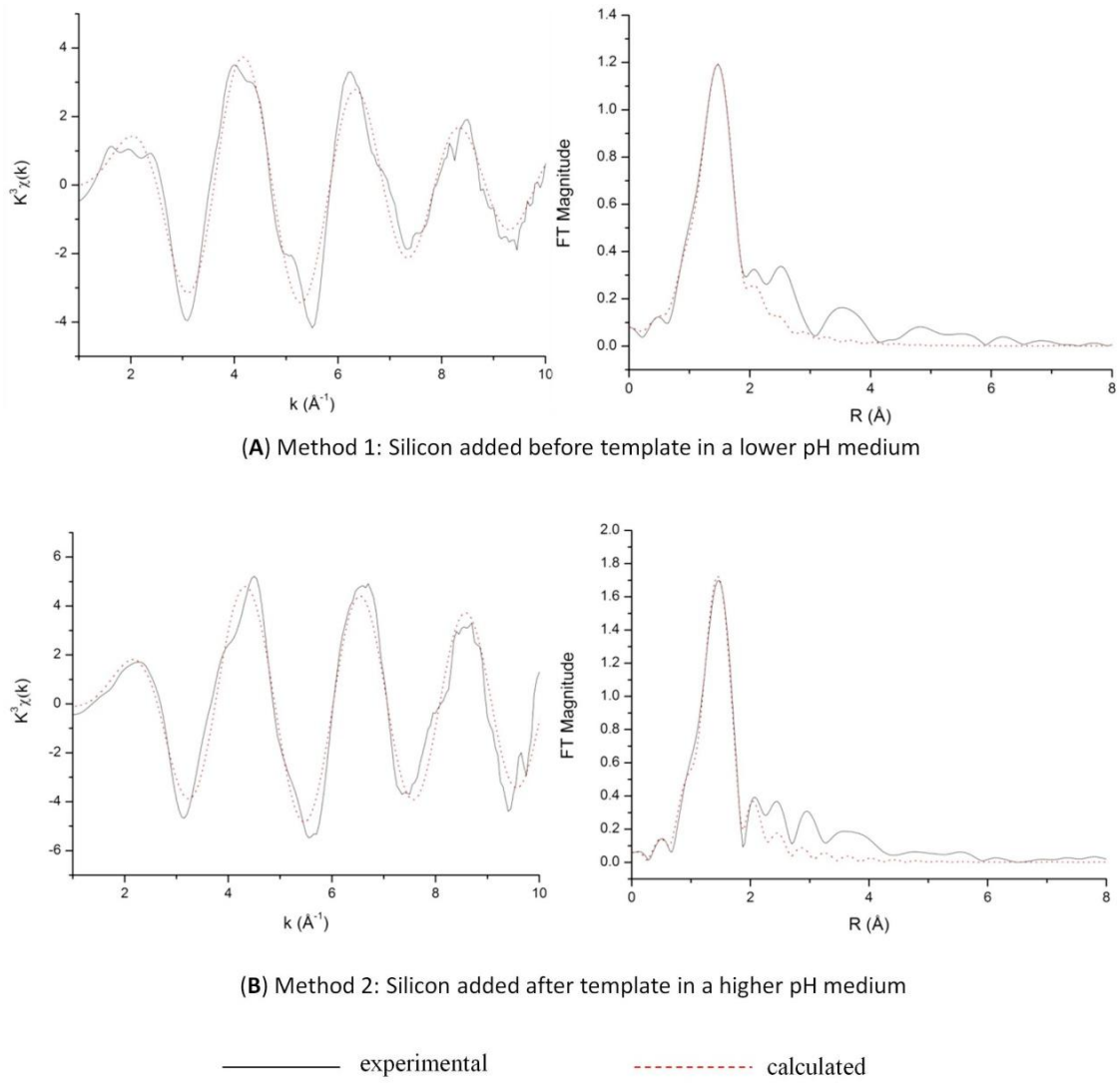

Figure 6.13. *Co K-edge EXAFS (left) and associated Fourier Transforms (right) of the experimental (black solid curve) and calculated (red dashed curve) data of as-synthesized CoSAPO-34, formed from method 1 (A) or method 2 (B).*

The cobalt species present in both materials were found to have approximately four oxygen neighbours, with an average Co-O bond distance of 1.97 Å and 1.93 Å for CoSAPO-34 synthesized with method 1 and 2, respectively. This suggests that the majority of high spin Co(II) species are present in the tetrahedral sites of the CoSAPO-34 structure. Typically, the spatially averaged Co(II)-O bond distance of cobalt in a tetrahedral environment is 1.94 Å ($CoAl_2O_4$[25]), however a slightly shorter Co(II)-O bond distance of 1.93 Å has been observed in other aluminophosphate structures[28, 29]. The higher Co-O bond distance (1.97 Å) in CoSAPO-34 synthesized with method 1, may indicate the presence of extra-framework Co(II) octahedral species. From these bond distances it is possible to calculate the percentage of Co(II) tetrahedral species using the Vegard relationship shown in Equation 6-4.

$$R = R_1x + R_2(1-x)$$

Equation 6-4. *The Vegard relationship*

For calculating the percentage of Co(II) tetrahedral species; R is the average bond distance obtained from EXAFS, R_1 is the Co(II)-O bond distance for a tetrahedral environment (as observed in other AlPOs, 1.93 Å[28, 29]), R_2 is the typical Co(II)-O distance in an octahedral environment (2.08 Å from the cobalt acetate standard[27]) and x is the fraction of Co(II) species with tetrahedral coordination. The resulting calculated percentages of Co(II) species in a tetrahedral environment are shown in Figure 6.14. The results reveal a lower percentage (73 %) of Co(II) tetrahedral

species in CoSAPO-34 when it is synthesized with method 1, compared to method 2 in which 100 % of the cobalt species were found to be in a tetrahedral environment.

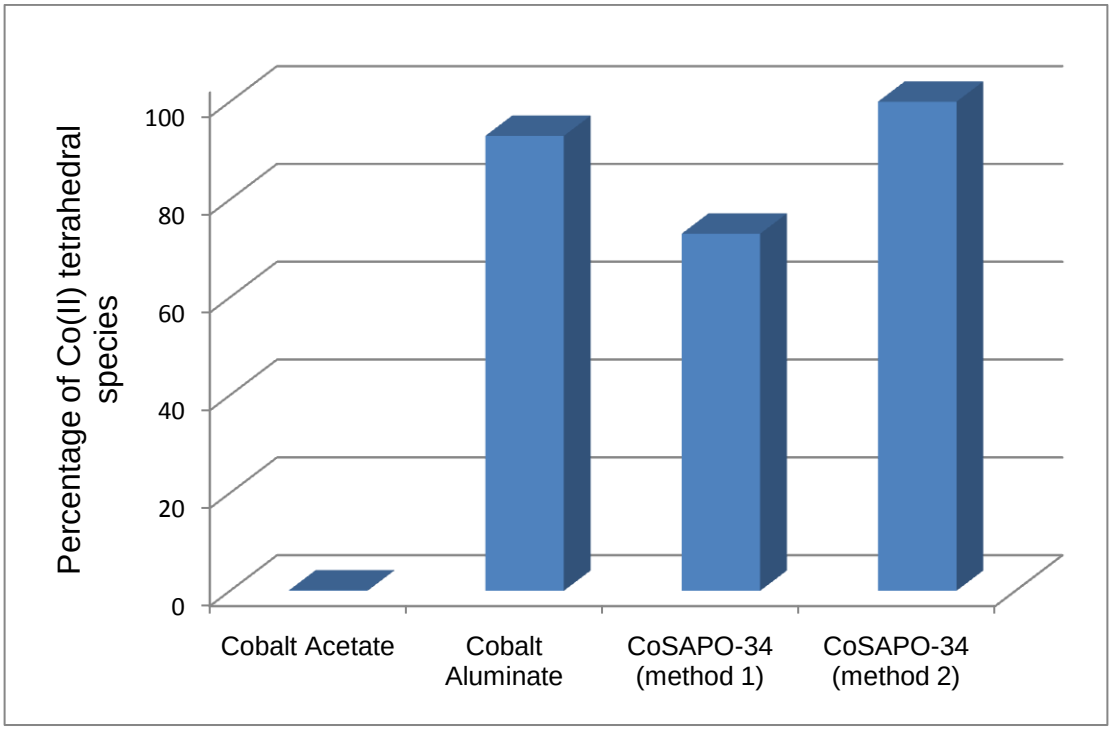

Figure 6.14. *The percentage of Co(II) tetrahedral species in the as-synthesized CoSAPO-34 samples and the standards, cobalt aluminate ($CoAl_2O_4$) and cobalt acetate. It should be noted that the typical Co(II)-O bond distances for a tetrahedral environment was taken to be 1.93 Å and for an octahedral environment 2.08 Å.*

The height of the first peak (1st shell) in the FT spectra (Figure 6.13) and the amplitude of the EXAFS data are highly correlated with the coordination number of cobalt. Therefore, it is apparent that there are also discrepancies in the coordination number between the two methods. CoSAPO-34 synthesized with method 2 was found to have a larger coordination number of CN = 4.5 compared to method 2, CN = 4.2. This once again confirms the presence of extra framework octahedral Co(II)

species in CoSAPO-34, method 1 (silicon added before the template in a lower pH medium).

The as-synthesized CoSAPO-34 materials, prepared by the two different methods, were calcined in air at 530 °C to remove the TEAOH template occluded within the pores and to study the redox behaviour of the cobalt species. The normalized XAS spectra of the two CoSAPO-34 samples at room temperature before calcination, at 530 °C and at room temperature after calcination are shown in Figure 6.15.

There are marked differences in both data sets before and after calcination; both the pre-edge feature (1s→3d transition) and the edge shifts to higher energies after removal of the template. Previous comparisons of the edge position in Co(II) and Co(III) containing oxides and cobaloximes suggests that a positive edge shift in the order of 1.5 – 3 eV indicates a change in the oxidation state from Co(II) to Co(III)[13, 30, 31]. CoSAPO-34 synthesized with method 1 showed an edge shift of the order of 0.92 eV, whereas CoSAPO-34 formed from method 2 revealed a larger shift in the edge position of the order of 2.28 eV. These observations indicate incomplete oxidation of the cobalt species in the CoSAPO-34 framework synthesized from method 1.

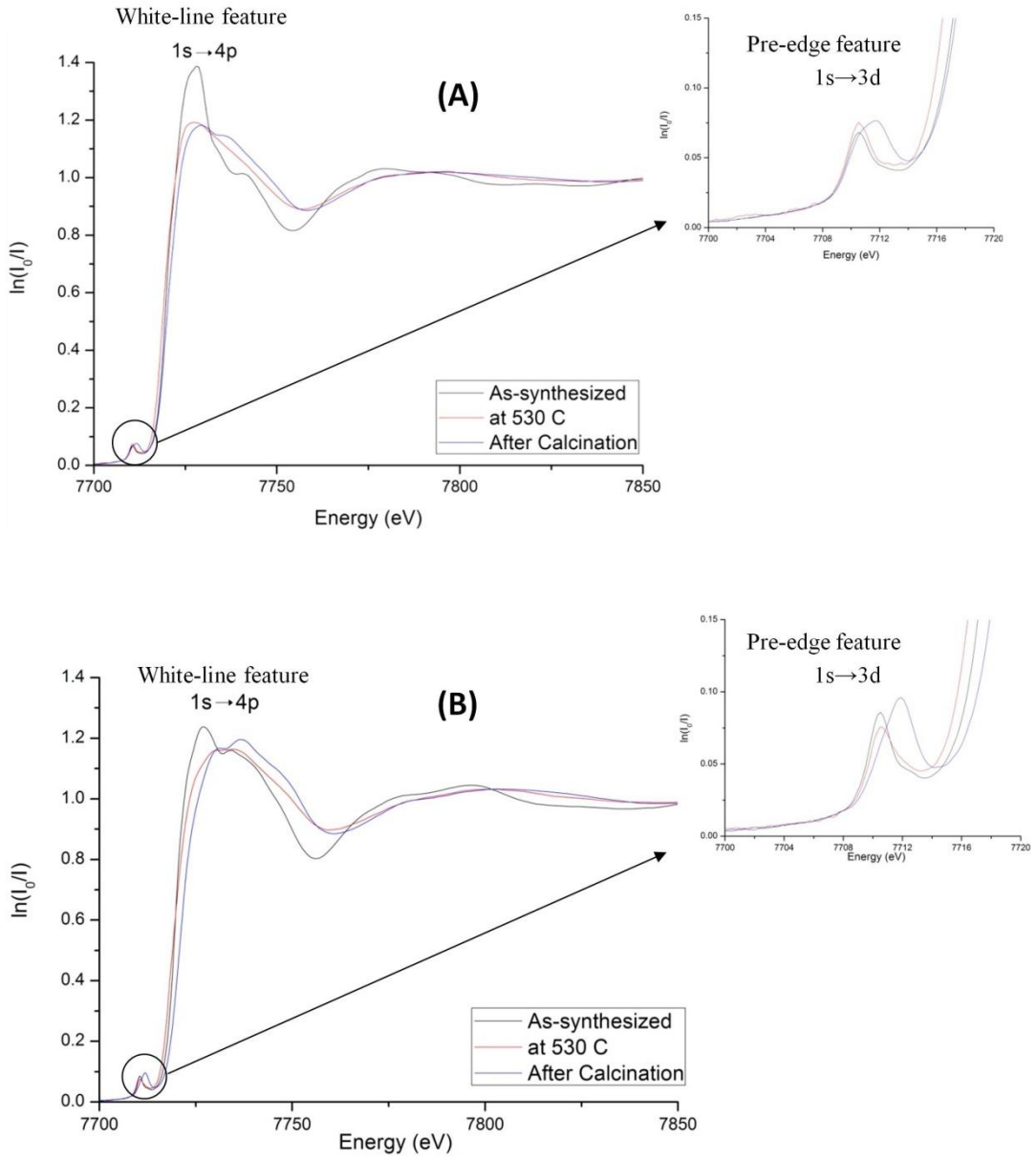

Figure 6.15. *Normalized XAS spectra of CoSAPO-34 synthesized with method 1 (A) or method 2 (B); as-synthesized (black), at 530 °C (red) and after calcination (blue). It should be noted that the scales are the same for comparison.*

The intensity of the white line feature is directly correlated with the coordination number of the cobalt species. This feature is found to be large in the as-synthesized CoSAPO-34 (method 1) material, and as discussed before is due to the presence of extra-framework Co(II) ions. During and after calcination, this white line feature in CoSAPO-34 (method 1) is found to decrease to an intensity comparable to that observed in CoSAPO-34 (method 2) which may suggest that the majority of the cobalt species are now in a tetrahedral environment. This is possible since the extra-framework octahedral Co(II) species may be surrounded by extra water molecules which are lost upon dehydration.

The Co K-edge EXAFS and the associated FT of the experimental and calculated data collected prior to, at 530 °C and after the calcinations of CoSAPO-34 prepared by method 1 and method 2 are given in Figure 6.16 and Figure 6.17, respectively. The best fit parameters of the first shell (Co-O) obtained from analyzing the EXAFS data are summarized in Table 6-2; given are the Co-O bond distances (R_{Co-O}), the Debye-Waller factor ($2\sigma^2$), and the cobalt coordination number (CN).

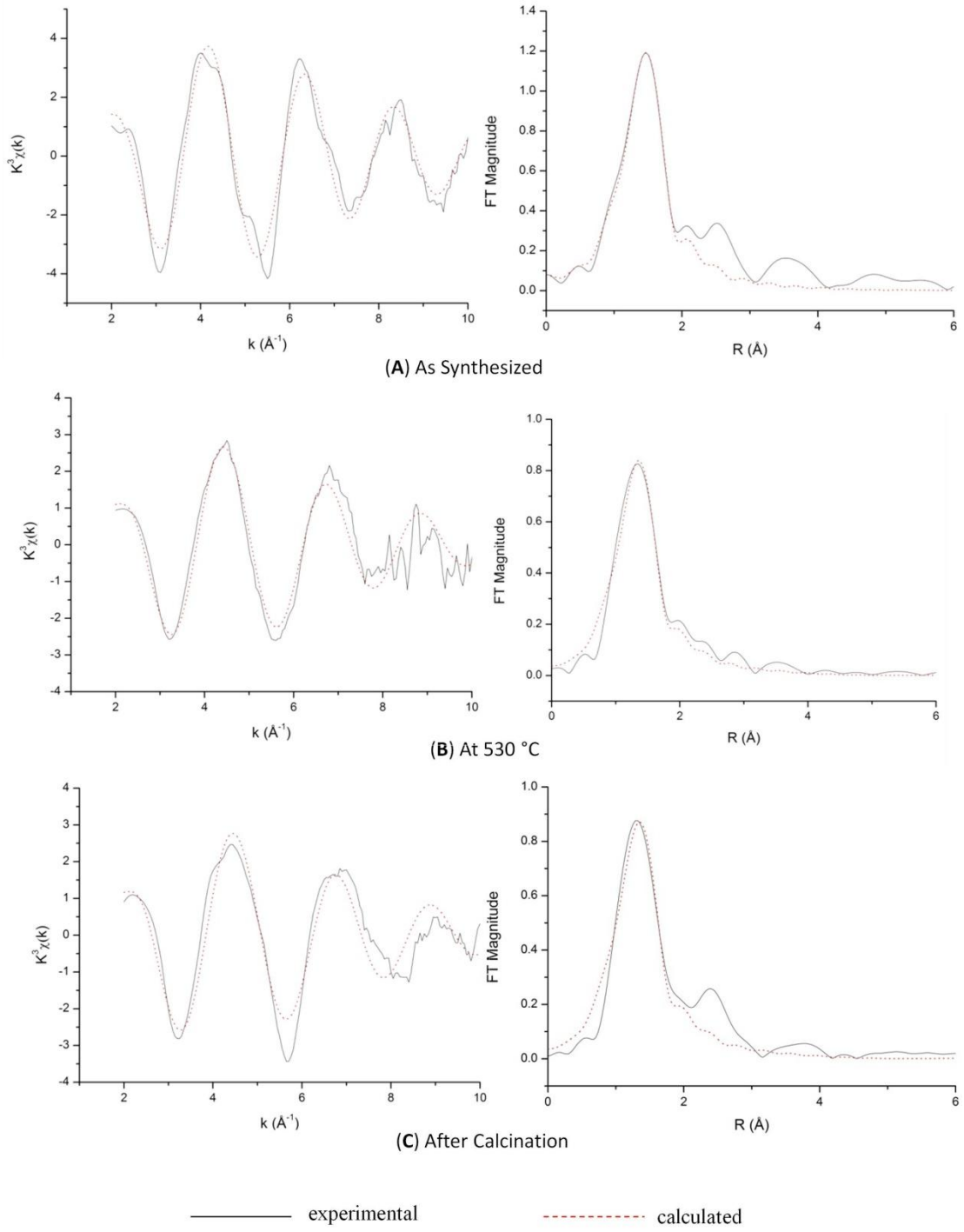

Figure 6.16. *Co K-edge EXAFS (left) and associated Fourier transforms (right) of the experimental (solid black line) and calculated (dashed red line) data of CoSAPO-34 synthesized with* ***method 1****, before (A), at 530 °C (B) and after (C) calcination.*

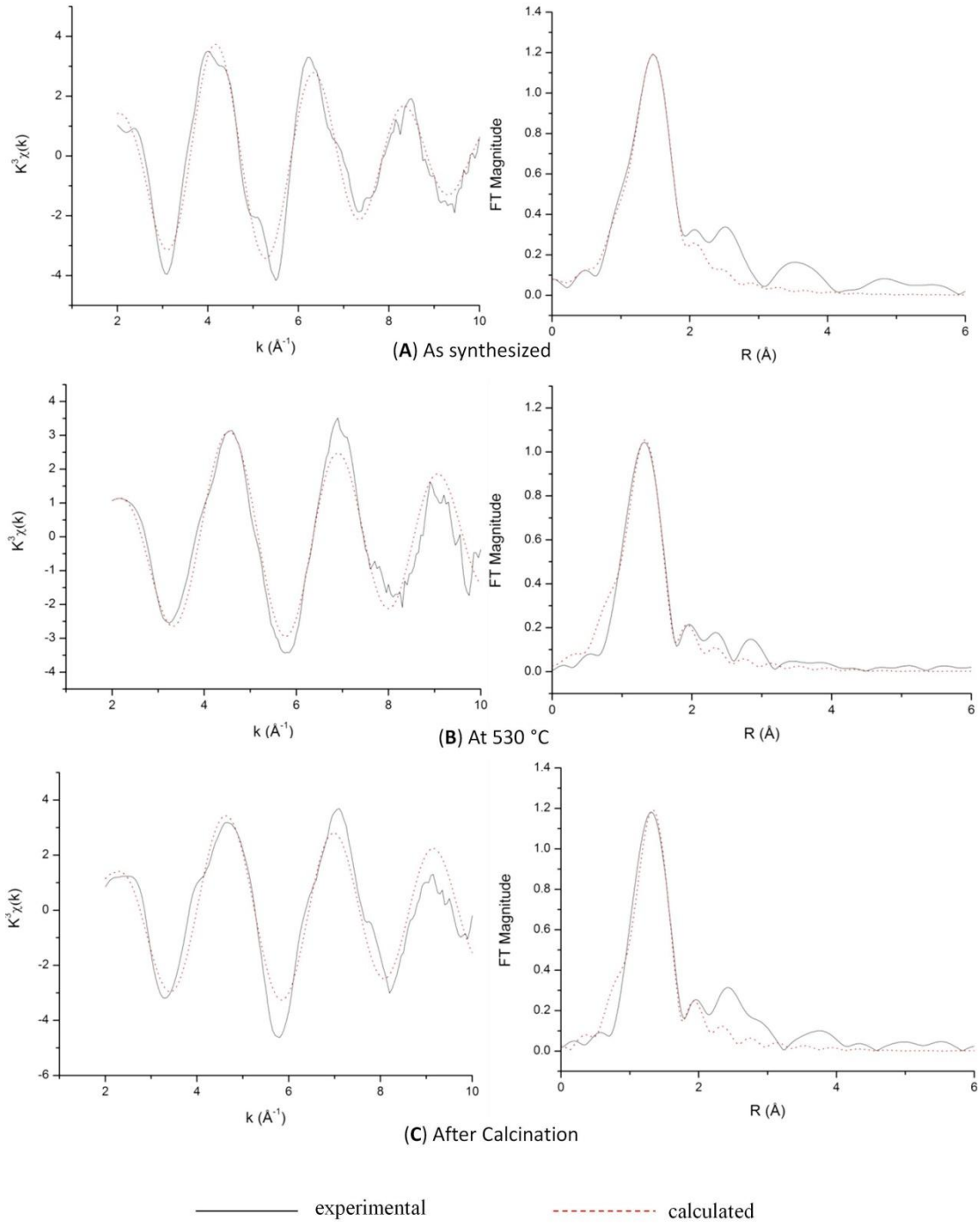

Figure 6.17. *Co K-edge EXAFS (left) and associated Fourier transforms (right) of the experimental (solid black line) and calculated (dashed red line) data of CoSAPO-34 synthesized with* ***method 2****, before (A), at 530 °C (B) and after (C) calcination.*

Table 6-2. *First shell best fit parameters obtained from Co K-edge EXAFS data of; the standards (cobalt acetate and $CoAl_2O_4$) and of CoSAPO-34 synthesized with method 1 (Si added before template) and method 2 (Si added after template) at room temperature as synthesized (AS), at 530 °C and at room temperature after calcination (AC).*

R_{Co-O}: Co-O bond distance, $2\sigma^2$: Debye-Waller factor, CN: number of neighbours.

	Cobalt Acetate	**$CoAl_2O_4$**	**CoSAPO-34 (method 1)**			**CoSAPO-34 (method 2)**		
Temperature (°C)	25	25	25 (AS)	530	25 (AC)	25 (AS)	530	25 (AC)
R_{Co-O} (Å) ±0.02	2.08	1.94	1.97	1.87	1.85	1.93	1.83	1.82
$2\sigma^2$	0.009	0.003	0.007	0.008	0.010	0.002	0.004	0.003
CN	6.2	3.9	4.5	3.3	3.5	4.2	2.9	3.0
Error in CN (± 10%)	0.6	0.4	0.5	0.3	0.4	0.4	0.3	0.3

Based on the bond distances between Co and the surrounding O atoms obtained from the EXAFS analysis, it is clear that the local environment undergoes dramatic changes upon calcination in the CoSAPO-34 materials. Irrespective of the method utilised to synthesise the CoSAPO-34 materials, the Co-O bond distance decreases by *ca.* 0.1 Å upon removal of the TEAOH template. The Co-O bond distances of 1.85 and 1.82 Å, obtained for the calcined CoSAPO-34 materials using methods 1 and 2,

respectively, are similar to that found in other calcined cobalt substituted aluminophosphates; the Co(III)-O bond distance in CoAlPO-18 is 1.83 Å[13] and in CoAlPO-34 is 1.82 Å[29]. Therefore, this decrease in the C-O bond distance is indicative of the oxidation of Co(II) to Co(III).

The larger observed Co-O distance in CoSAPO-34 (1.85 Å) prepared with method 1 is likely to be the result of incomplete oxidation of all the Co(II). Consequently, using the Vegard relationship (Equation 6-4), but in terms of the fraction of oxidised Co(III) species in the structure, e.g. R_1 is the typical Co(III)-O distance (1.82 Å[29]), R_2 is the Co(II)-O bond distance (1.93 Å[29]) and *x* is the fraction of oxidised Co(III) species, the percentage of Co(III) species in the CoSAPO-34 structures upon calcination were obtained. For the synthesis of CoSAPO-34 with method 1, the results indicated that only 73 % of the cobalt species were oxidised to Co(III) in a tetrahedral environment, this is lower compared to that of CoSAPO-34 synthesized from method 2 where the results indicated that 98 % of the Co(II) species were oxidised to Co(III). The reason for a larger number of un-oxidised cobalt species in CoSAPO-34 (method 1) could be due to the presence of extra framework octahedral cobalt species found in the as-synthesised form. Therefore, it's possible that almost all of the tetrahedral Co(II) species present in either of the CoSAPO-34 materials were oxidised to Co(III); as stated previously, 73 % of tetrahedral Co(II) was found to be present in the as-synthesized CoSAPO-34 (method 1) and 100 % of tetrahedral Co(II) in CoSAPO-34 (method 2).

It should be noted that there is evidence to suggest that the Co(III)-O bond distance for cobalt in a tetrahedral environment could be much shorter than that observed;

through an EXAFS and single crystal X-ray diffraction study, Muncaster et al.[28] found the Co(III)-O bond distance in the heteropolytungstate $K_5CoW_{12}O_{40}\cdot_{20}H_2O$ (Co(III) in a slightly distorted tetrahedral environment) to be ~1.79 Å. Although the extended environment of this material is different to that in aluminophosphates, it may still be possible to achieve a Co(III)-O bond distance of 1.79 Å in cobalt substituted AlPOs. Therefore, the estimated percentages of Co(III) species in the two CoSAPO-34 materials should be considered as the absolute maximum percentage.

Upon further analysis of the pre-edge feature, it is evident that the pre-edge of both calcined CoSAPO-34 materials which peaks at ~7712 eV has a shoulder feature at lower energy (~7710 eV) which coincides with the maxima observed in the as-synthesized materials, see Figure 6.18. This suggests that there are Co(II) species present in both calcined CoSAPO-34 materials. Furthermore, the pre-edge feature of the calcined materials was fitted with two Gaussian peaks using the fityk program[32], and a ratio of the area underneath each curve calculated. This revealed a Co(II):Co(III) ratio for CoSAPO-34 synthesized from method 1 of 50:50 and for CoSAPO-34 formed with method 2 of 40:60. It should be noted that the position of each fitted Gaussian peak was equivalent in each CoSAPO-34 material. This once again confirms that there is a larger number of oxidized Co(III) species when method 2 is employed to synthesize CoSAPO-34, but also shows that is a larger amount of un-oxidized cobalt species present in the calcined CoSAPO-34 compared to the percentage calculated from the bond distances.

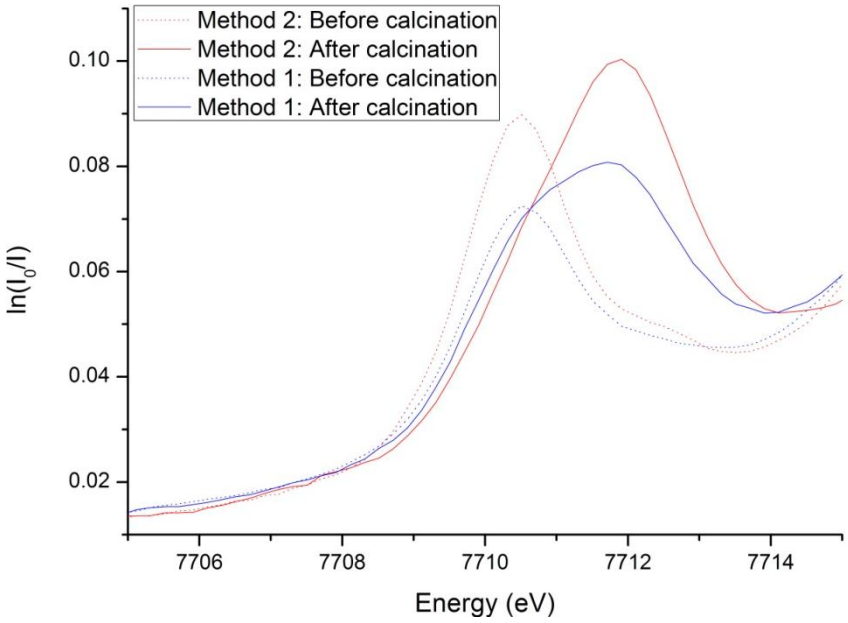

Figure 6.18. *Showing the shoulders observed in the pre-edge of the calcined CoSAPO-34 materials.*

On analysis of the coordination number, a decrease upon calcination is observed; from 4.5 to 3.5 for CoSAPO-34 (method 1) and a decrease from 4.2 to 3.0 for CoSAPO-34 (method 2). This decrease in coordination number observed in both CoSAPO-34 materials, irrespective of the method, can be attributed to distortions in the local cobalt environment; distortions instigate a decrease in the EXAFS amplitude which in turn decreases the calculated coordination number. The calculated coordination numbers (3.5 and 3.0) of the cobalt species in the calcined CoSAPO-34 materials are low and can be justified through comparison with a previous XAS investigation carried out during the calcination of CoAlPO-18[13]. This study revealed a coordination number for cobalt of 2.6 (R_{Co-O} = 1.82 Å) which was found to be due to the presence of 3 short Co-O bonds (1. 82 Å) and 1 long (2.04 Å) Co-O

bond as illustrated in Figure 6.19. The EXAFS amplitude which is directly related to the coordination number, has a $1/R^2$ dependency, therefore short distance dominate the data. Therefore, the low coordination number observed in the two CoSAPO-34 materials is possibly due to distortions around the Co(III) species with 3 shorter bonds and one long bond, the longer bond most probably being bonded to the Brönsted acid site.

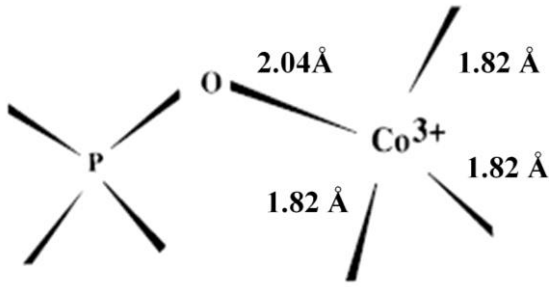

Figure 6.19. *Illustration of the distorted Co(III) environment observed in CoAlPO-18*[13].

Comparison of the EXAFS amplitude and FT magnitude for the CoSAPO-34 materials, before and after calcination, indicate the presence of larger distortions in the CoSAPO-34 structure synthesized with method 1 as a decrease in FT magnitude is observed upon calcination (for method 2 the FT magnitude stays relatively constant). In addition, the Debye-Waller factor is larger for CoSAPO-34 (method 1), 0.007 – 0.010, compared to CoSAPO-34 (method 2) which was found to be comparable to that of $CoAl_2O_4$ (0.003) throughout the calcination. Suggesting

significant static disorder in the structure when method 1 (silicon added prior to the template) is employed in the synthesis of CoSAPO-34.

This higher static disorder may be the result of either differing cobalt environments, e.g. Co(II) and Co(III), or due to the cobalt and silicon ordering in the framework. Divalent metal ions, such as Co(II), substitute for Al(III) in the framework, whereas Si(IV) ions preferentially substitute for P(V). Although Si(IV) has also been known, in some cases, to substitute for Al(III), however this is unlikely in the materials synthesised in this work since if it were true, it would result in a neutral framework with no Brønsted acid sites (both CoSAPO-34 were found to possess Brønsted acidity when a proton charge balanced, see section 6.4.1.1). Therefore it is assumed that all the silicon substitutes for the preferred phosphorus site. In method 1, the silicon source is added after the cobalt precursor, which may result in the presence of Co-O-Si units in the framework, Figure 6.20(A). Both cobalt (0.58 Å) and silicon (0.26 Å) atoms have larger ionic radii than their substituted analogues Al (0.39 Å) and P (0.17 Å), respectively, therefore substituting into neighbouring sites may result in larger distortions around the cobalt species. The organic template is added after the cobalt precursor in method 2 which may produce more P-O-Co-O-P units, as a consequence the addition of silicon after TEAOH may produce a Co-O-P-O-Al-O-Si ordering, Figure 6.20(B). The substitution of Si(IV) for a P(V) site at a further distance from the cobalt species could result in a smaller amount of distortions around Co(III).

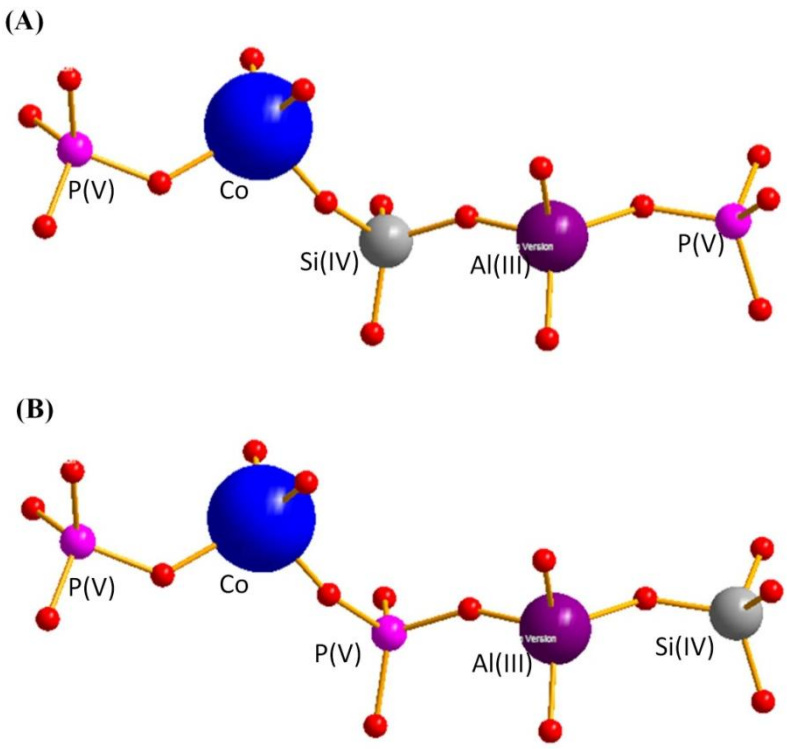

Figure 6.20. *An illustration of the possible different cobalt-silicon ordering in the aluminophosphate materials; assuming Co substitutes for Al and Si for P. Oxygen (red), phosphorus (pink), aluminium (purple) cobalt (blue) and silicon (grey) atoms are drawn with the relative ionic radii.*

To further evaluate the changes in the coordination number and oxidation state, additional XANES data was collected during the heating and subsequent cooling of the calcination process. Plots of the normalized intensity of the pre-edge and white line feature are shown in Figure 6.21 for CoSAPO-34 synthesized with method 1 or method 2.

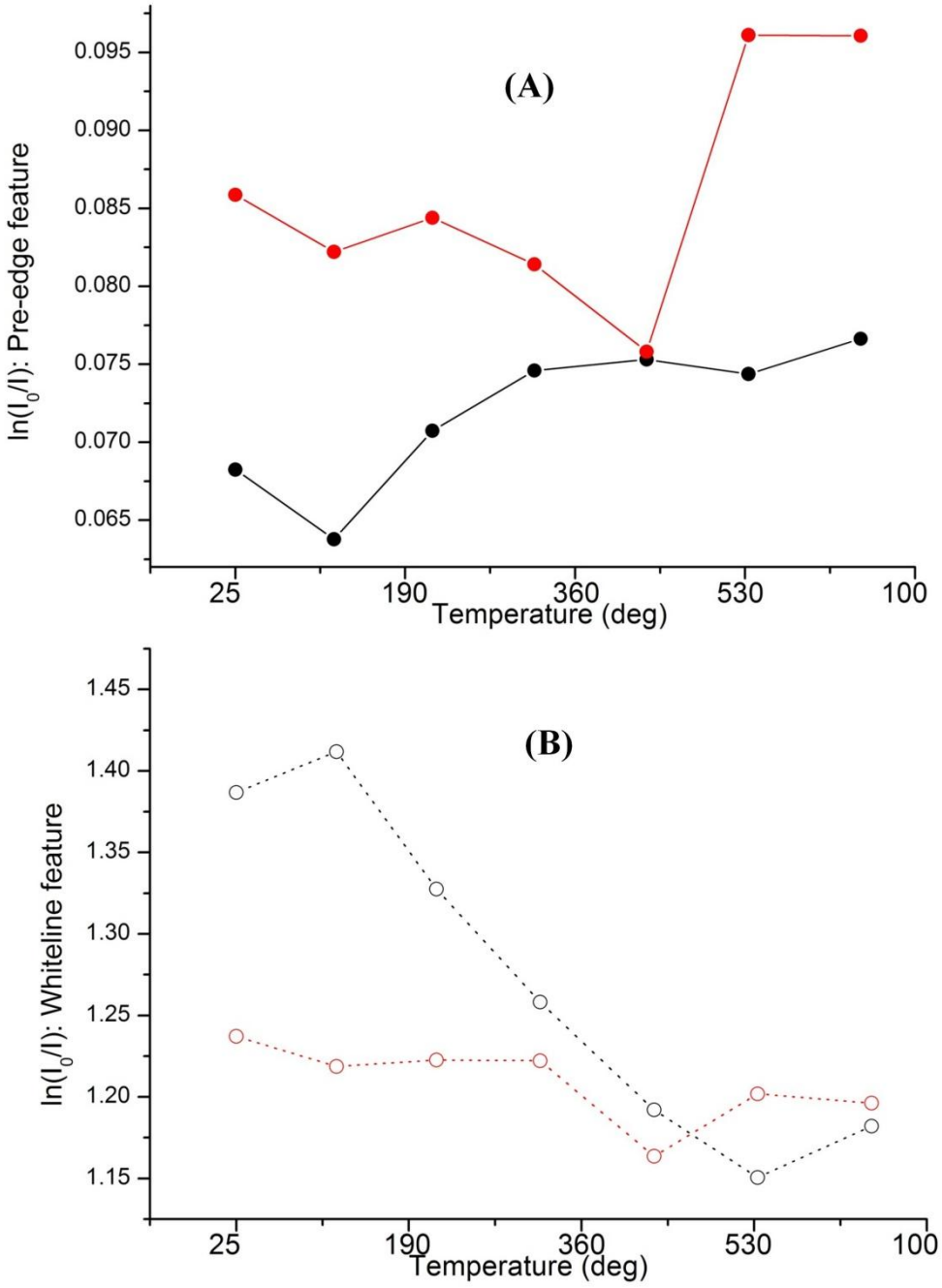

Figure 6.21. *The change in the normalized intensity of the pre-edge (A) and the white-line (B) feature observed in CoSAPO-34 prepared by method 1 (black) or method 2 (red).*

The normalised intensity of the pre-edge feature (1s→3d), which is directly related to the number of unoccupied d states (coinciding with the number of cobalt tetrahedral species) was found to be more intense for the as-synthesized CoSAPO-34 (method 2) material compared to CoSAPO-34 (method 1) confirming the presence of more extra-framework cobalt species when method 1 is employed. This is also evident on analysis of the normalised intensity of the white line feature (1s→4p), which is not only affected by electronic factors but also the coordination environment of the metal[33]. The white-line feature was found to be much larger for as-synthesised CoSAPO-34 (method 1) compared to CoSAPO-34 (method 2) and implies the presence of larger multiple scattering effects such as those in an octahedral environment when method 1 is used to synthesise the CoSAPO-34 material.

During calcination, the white-line feature of CoSAPO-34 (method 2) remained relatively constant indicating that the cobalt species remained in a tetrahedral environment. The pre-edge feature for CoSAPO-34 (method 2), remained relatively constant prior to reaching 530 °C and then rapidly increased to 0.096 coinciding with the shift in the edge position. This increase in the pre-edge is attributed to an increase in the density of unoccupied states as Co(II) oxidises to Co(III); $d^6 \rightarrow d^5$.

The trend in the pre-edge feature and white-line intensity is found to differ from that of CoSAPO-34 (method 2) when method 1 is employed in the synthesis of CoSAPO-34. When method 1 is utilised, the pre-edge feature gradually increases during the calcination and the white-line feature steadily decreases until a temperature of 530 °C is reached. This is indicative of a gradual change from an octahedral to a

tetrahedral environment around the cobalt species in CoSAPO-34 (method 1) and can be attributed to the loss of water molecules and other binding fragments from the template upon heat treatment. Above 530 °C, the pre-edge feature increases, but this increase is relatively small compared to that observed in CoSAPO-34 (method 2) and once again confirms that there is a smaller amount of oxidised Co(III) species present in CoSAPO-34 when method 1 is employed.

It is clear from the Co K-edge XAS study carried out during the calcination of CoSAPO-34, that the order of addition of the precursors in the synthesis route affects not only the amount of substitution into the AlPO framework but also the distortions around the divalent ion. These differences may be vital in the activity and reactivity of these catalysts for the conversion of methanol to light olefins.

6.4.2 Methanol-to-olefin catalytic investigation

The catalytic conversion of methanol over metal and multi-metal AlPO-34 materials is discussed in this section and compared to that of AlPO-5, a large pore aluminophosphate framework with no Brønsted acid sites. The evolution of methanol conversion as a function of time is given in Figure 6.22.

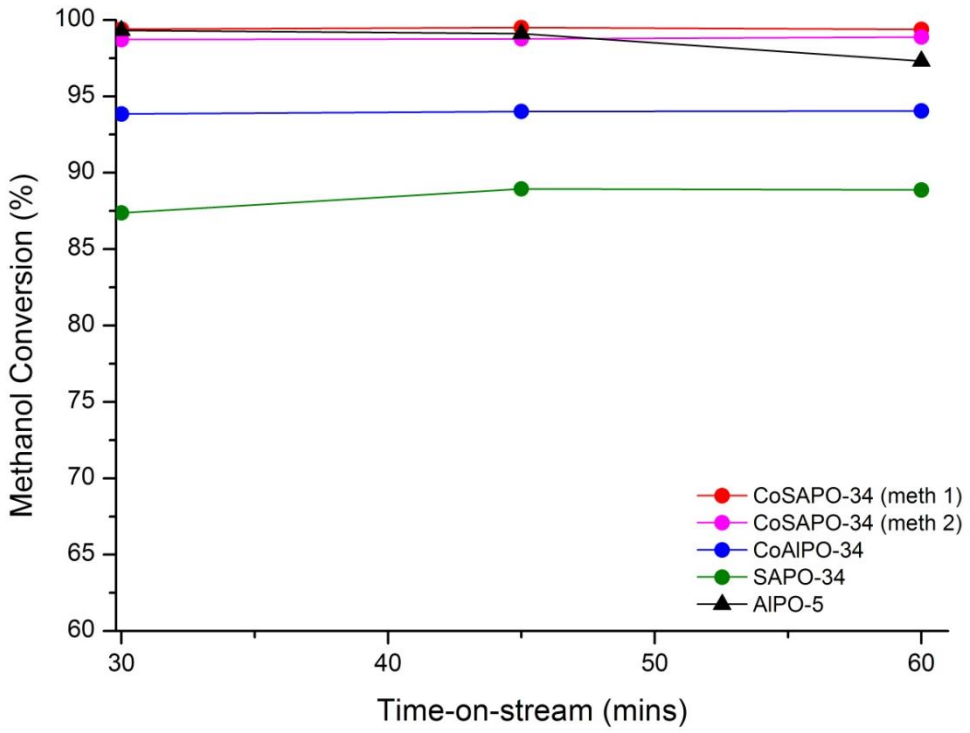

Figure 6.22. *Evolution of methanol conversion over time.*

At a time on stream (TOS) of 30 minutes, all the catalysts present high methanol to hydrocarbon conversion indicating their high initial activity. As their time on stream increases to one hour, the methanol conversion increases slightly for all the CHA-type materials and decreases by 2% for the AlPO-5 catalyst. In particular, after 1hr on stream, both the CoSAPO-34 materials were found to have the highest methanol conversion, *ca.* 99 %, and SAPO-34 the lowest conversion, *ca.* 89%.

Although the methanol conversion was found to be similar for all catalysts, the product selectivity was various. A bar chart showing the product selectivity from the transformation of methanol over the various catalysts at TOS = 30 minutes is given in Figure 6.23.

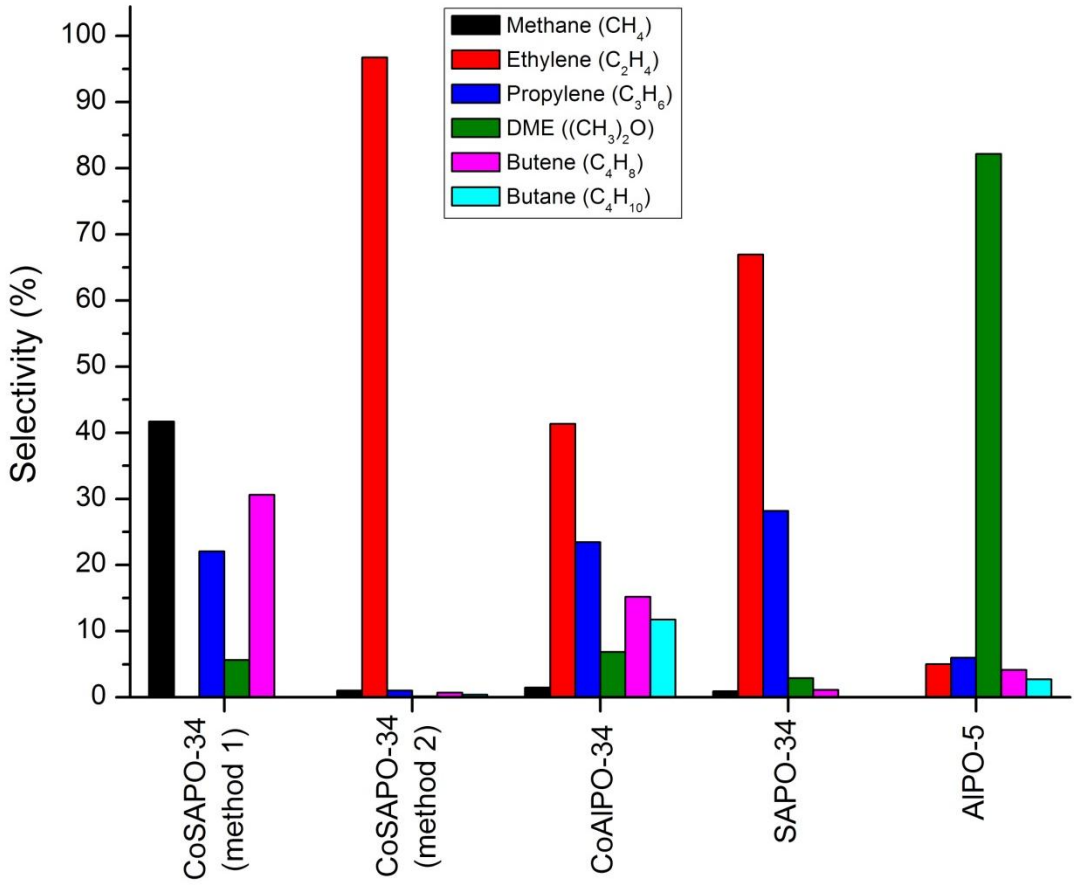

Figure 6.23. *Bar graph showing the product selectivity results from the catalytic conversion of methanol over the various catalysts, TOS =* ***30 minutes****, T = 425 °C.*

The results show that, at 425 °C and TOS = 30 minutes, the neutral large pore AlPO-5 framework transforms methanol to dimethyl ether (DME), 82.2 %. This catalytic conversion of methanol to the unwanted intermediate DME is due to its very low acidity. SAPO-34, on the other hand, was found to transform methanol to the highly desired olefins; ethylene (66.9%) and propylene (28.2%). This high selectivity towards light olefins is due to the shape selective nature of the small pore (3.8Å x 3.8 Å) material, as well as the increase in acid strength after the substitution of P(V) with

Si(IV). CoAlPO-34 was also found to transform methanol to the olefins ethylene (41.4 %) and propylene (23.5 %) but with a lower selectivity, with the addition of longer hydrocarbons in the form of butene (15.2 %) and the paraffin butane (11.7 %). These results are similar to what has been observed previously for the MTO reaction[34].

Incorporating both cobalt and silicon into the small pore framework results in the generation of new acid sites, thereby modifying the acidity of the material and subsequently its activity for the MTO reaction. CoSAPO-34, prepared by method 2, after 30 minutes, was found to convert methanol to ethylene with an astonishing 96.7 % selectivity. CoSAPO-34, synthesised by method 1 which was found to have a high percent of extra framework cobalt species, was found to differ considerably to that of CoSAPO-34, prepared by method 2, in the product selectivity of methanol transformation after 30 minutes on stream. CoSAPO-34 (method 1) converted methanol to a variety of hydrocarbons, in particular the paraffin, methane (41.7 %), was found to be the main product, along with the olefins butene (30.6 %) and propylene (22.1 %). This selectivity towards methane can be attributed to the extra-framework cobalt which is a well-known methanation catalyst[35, 36]. Similar observations have been observed for the highly selective NiSAPO-34 catalyst, in which the presence of extra framework nickel metal increases the selectivity of methane production which is thought to be through the decomposition of methanol on the extra-framework nickel to CO and H_2 which react to form methane[10, 37].

The product selectivity of the methanol transformation over the various catalysts after 1 hour on stream is shown in Figure 6.24.

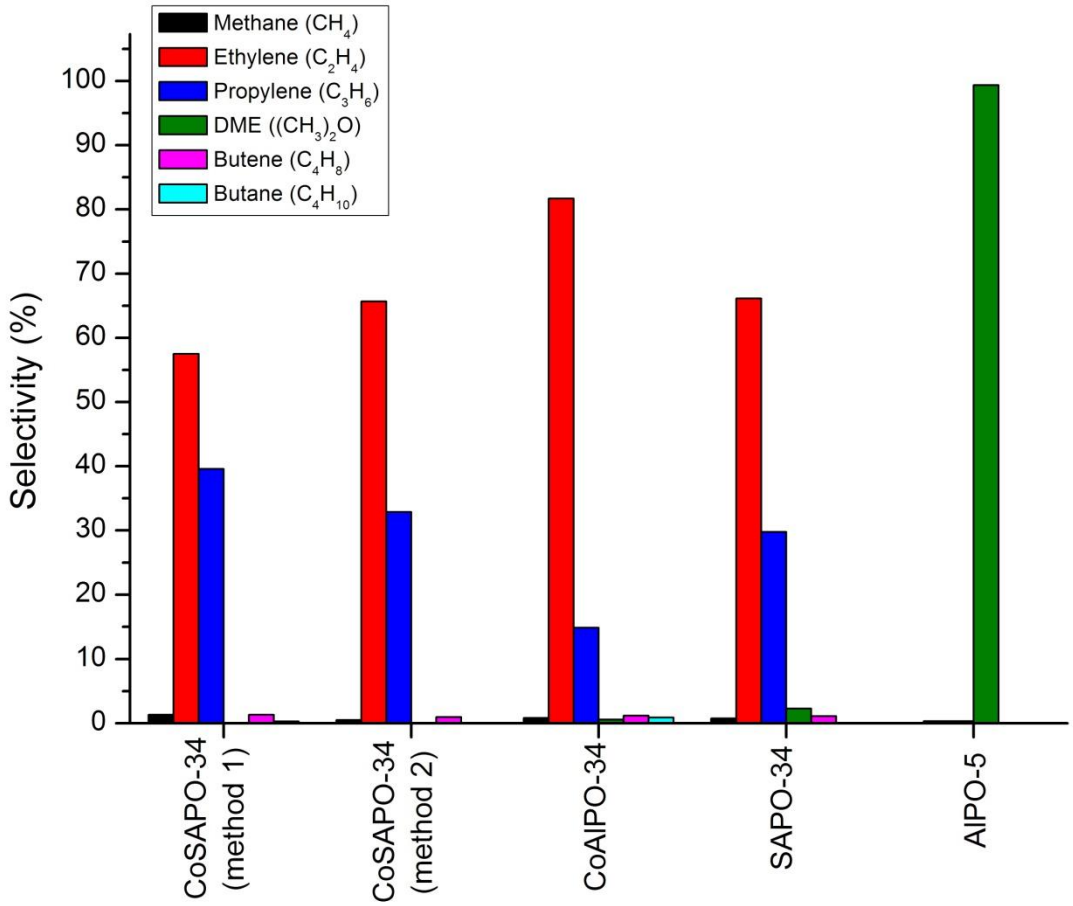

Figure 6.24. *Bar graph showing the product selectivity results from the catalytic conversion of methanol over the various catalysts, TOS =* ***60 minutes****, T = 425 °C.*

All four small pore CHA-type materials after 1 hour were found to convert methanol to the olefins, ethylene and propylene with a high selectivity. After a TOS = 1 hour with the utilization of CoAlPO-34 for the MTO reaction, the selectivity towards the desired ethylene (81.7 %) product increased substantially with subsequent decreases in the other hydrocarbon products, including propylene (14.9 %).

When CoSAPO-34 (method 1) was employed as the catalyst for the MTO reaction, the selectivity for methane and butene was found to reduce considerably with subsequent increases in the highly desired ethylene (57.5 %) and propylene (39.6 %) products. In contrast, CoSAPO-34 (method 2) showed a decrease in the high selectivity towards ethylene from 98.7 %, after 30 minutes, to 65.7 % after 1 hour, but also showed an increase in the selectivity towards propylene (32.9 %). This decrease in the selectivity towards ethylene may be due to inactive coke formation from olefins which may block or limit access to the active sites.

SAPO-34 was the only material which was found to have a moderately stable production of olefins, in which the selectivity towards ethylene (66.1 %) and propylene (28.8 %) stayed relatively constant over one hour, owing to its ability to not form deactivating coke over a long lifetime[10].

Overall, at 425 °C and TOS = 1 hour, the order in ethylene selectivity was followed as next; CoAlPO-34 > SAPO-34 > CoSAPO-34 (method 2) > CoSAPO-34 (method 1) with ethylene:propylene ratios of 5.48, 2.29, 1.99 and 1.45 respectively. The high selectivity towards ethylene for the catalytic conversion of methanol to olefins over CoAlPO-34 do not agree with previous studies and is unexplainable; in comparison to this study, at 425 °C, CoAlPO-34 has been found to transform methanol to olefins with an ethylene:propylene ratio of *ca.* 1.7 instead of the high ratio of 5.48 which was observed in this study[34, 38].

SAPO-34 and CoSAPO-34 (method 2) have been shown to be highly active catalysts for the MTO reaction with high selectivites for ethylene and propylene. In

particular, SAPO-34 was found to have a lower methanol conversion compared to CoSAPO-34 (method 2) however, there were signs of catalyst deactivation with the incorporation of cobalt.

On comparison of the two CoSAPO-34 materials which vary considerably in the amount of framework cobalt species, CoSAPO-34 prepared by method 2 was found to be the more active catalyst for the transformation of methanol to ethylene and propylene. The main differences were in the formation of methane, at TOS = 30 minutes, which was much higher for CoSAPO-34 (method 1), 41.7 %, compared to CoSAPO-34 (method 2), 1 %, which was attributed to the presence of extra framework cobalt cations. In addition, the selectivity towards propylene was slightly higher for CoSAPO-34 prepared by method 1, and the selectively towards ethylene higher for CoSAPO-34 (method 2).

This catalytic investigation has demonstrated that the nature and location of metal ions in small pore CHA-type materials can have a significant effect on catalyst selectivity as evidenced by the contrasting results observed on the two different CoSAPO-34 materials which vary in the amount of extra-framework cobalt species. Further studies are required into the lifetime of the active catalysts and the variation of inactive coke formation to fully understand how the synthesis route to the MeSAPO-34 material can affect the catalyst activation for the MTO reaction.

6.5 Summary and Conclusion

Multi-metal substituted CHA type materials were synthesised, characterized and studied for their performances in the MTO process and compared to their mono-substituted analogues, CoAlPO-34 and SAPO-34.

HRXRD revealed a larger unit cell volume for CoSAPO-34 compared to CoAlPO-34 and SAPO-34 suggesting the incorporation of both Co(II) and Si(IV) in the framework tetrahedral sites. The unit cell parameters of CoSAPO-34 prepared by the two different methods were compared revealing a larger volume for CoSAPO-34 (method 2) indicating a larger incorporation of heteroatoms in the framework or the formation of silicon islands in CoSAPO-34 (method 1). The formation of silicon islands was ruled out via FTIR, which revealed the presence of Brønsted acid sites in both the calcined and reduced CoSAPO-34 materials, irrespective of the synthetic route. In addition, XAS was employed to study the nature and location of the Co(II) ions in the multi-metal substituted CoSAPO-34 framework; a larger amount of extra-framework cobalt ions were observed in CoSAPO-34 (method 1) owing to the smaller unit cell volume. Upon calcination, XAS revealed that almost all of the framework Co(II) species were oxidised to Co(III), with larger distortions around the cobalt species in CoSAPO-34 (method 1).

Large differences were observed in the CoSAPO-34 catalysts for the C_2-C_4 selectivities at a time on stream of 30 minutes during the MTO process. As expected the SAPO-34 material was found to have high selectivities towards ethylene (66.9 %)

and propylene (28.2 %) with a high conversion of methane. Upon the addition of a divalent metal ion, the product selectivity altered, with additional differences depending on the synthesis route employed; CoSAPO-34, synthesised with method 1, produced a large amount of methane at a time of stream of 30 minutes. In contrast, CoSAPO-34 (method 2) produced a low amount of methane comparable to that observed in SAPO-3; this observation, together with the characterization studies, clearly suggests a difference in the location and nature of the cobalt species. CoSAPO-34 (method 2), which was characterized with 100 % framework cobalt, suggested a large improvement in the selectivity of ethylene (96.7 %), at a time on stream of 30 minutes, and a greater methane conversion compared to SAPO-34. However, after 1 hour on stream, the product selectivities for CoSAPO-34 (method 2) were found to be comparable to SAPO-34 suggesting a possible deactivation of the catalyst with no greater improvement.

6.6 References

[1] Mokrani, T.; Scurrell, M., *Catalysis Reviews-Science and Engineering*, (2009) **51**, 1.

[2] Haw, J. F.; Song, W. G.; Marcus, D. M.; Nicholas, J. B., *Accounts of Chemical Research*, (2003) **36**, 317.

[3] Pastore, H. O.; Coluccia, S.; Marchese, L., *Annual Review of Materials Research*, (2005) **35**, 351.

[4] Baerlocher, C.; McCusker, L. B.; Olson, D. H., *"Atlas of Zeolite Framework Types", 6th edition*, Elsevier: Amsterdam, (2007).

[5] Baerlocher, C.; McCusker, L. B., Database of Zeolite Structures. http://www.iza-structure.org/databases/, In.

[6] Aguayo, A. T.; Gayubo, A. G.; Vivanco, R.; Olazar, M.; Bilbao, J., *Applied Catalysis a-General*, (2005) **283**, 197.

[7] Chen, J. S.; Wright, P. A.; Thomas, J. M.; Natarajan, S.; Marchese, L.; Bradley, S. M.; Sankar, G.; Catlow, C. R. A.; Gaiboyes, P. L.; Townsend, R. P.; Lok, C. M., *Journal of Physical Chemistry*, (1994) **98**, 10216.

[8] Djieugoue, M. A.; Prakash, A. M.; Kevan, L., *Journal of Physical Chemistry B*, (2000) **104**, 6452.

[9] Franklin, I. L.; Beale, A. M.; Sankar, G., *Catalysis Today*, (2003) **81**, 623.

[10] Dubois, D. R.; Obrzut, D. L.; Liu, J.; Thundimadathil, J.; Adekkanattu, P. M.; Guin, J. A.; Punnoose, A.; Seehra, M. S., *Fuel Processing Technology*, (2003) **83**, 203.

[11] Kang, M., *Journal of Molecular Catalysis a-Chemical*, (2000) **160**, 437.

[12] Liang, J.; Li, H. Y.; Zhao, S.; Guo, W. G.; Wang, R. H.; Ying, M. L., *Applied Catalysis*, (1990) **64**, 31.

[13] Barrett, P. A.; Sankar, G.; Catlow, C. R. A.; Thomas, J. M., *Journal of Physical Chemistry*, (1996) **100**, 8977.

[14] Elanany, M.; Koyama, M.; Kubo, M.; Selvam, P.; Miyamoto, A., *Microporous and Mesoporous Materials*, (2004) **71**, 51.

[15] Thompson, S. P.; Parker, J. E.; Potter, J.; Hill, T. P.; Birt, A.; Cobb, T. M.; Yuan, F.; Tang, C. C., *Review of Scientific Instruments*, (2009) **80**,

[16] Dent, A. J.; Cibin, G.; Ramos, S.; Smith, A. D.; Scott, S. M.; Varandas, L.; Pearson, M. R.; Krumpa, N. A.; Jones, C. P.; Robbins, P. E., B18: A core XAS spectroscopy beamline for Diamond, In *14th International Conference on X-Ray Absorption Fine Structure*, DiCicco, A.; Filipponi, A. Eds.; Iop Publishing Ltd: Bristol, (2009); Vol. 190.

[17] Ravel, B.; Newville, M., *Journal of Synchrotron Radiation*, (2005) **12**, 537.

[18] Nguyen, K. D. H., University College London London, (2008).

[19] Amri, M.; Walton, R. I., *Chemistry of Materials*, (2009) **21**, 3380.

[20] Marchese, L.; Frache, A.; Gianotti, E.; Martra, G.; Causà, M.; Coluccia, S., *Microporous and Mesoporous Materials*, (1999) **30**, 145.

[21] Lourenco, J. P.; Ribeiro, M. F.; Borges, C.; Rocha, J.; Onida, B.; Garrone, E.; Gabelica, Z., *Microporous and Mesoporous Materials*, (2000) **38**, 267.

[22] Martucci, A.; Alberti, A.; Cruciani, G.; Frache, A.; Coluccia, S.; Marchese, L., *Journal of physical Chemistry B*, (2003) **107**, 9655.

[23] Zibrowius, B.; Löffler, E.; Hunger, M., *Zeolites*, (1992) **12**, 167.

[24] Zubkov, S. A.; Kustov, L. M.; Kazansky, V. B.; Girnus, I.; Fricke, R., *Journal of the Chemical Society-Faraday Transactions*, (1991) **87**, 897.

[25] Toriumi, K.; Ozima, M.; Akaogi, M.; Saito, Y., *Acta Crystallogr. Sect. B-Struct. Commun.*, (1978) **34**, 1093.

[26] Kaduk, J. A.; Partenheimer, W., *Powder Diffraction*, (1997) **12**, 27.

[27] Ghabbour, E. A.; Scheinost, A. C.; Davies, G., *Chemosphere*, (2007) **67**, 285.

[28] Muncaster, G.; Sankar, G.; Catlow, C. R. A.; Thomas, J. M.; Coles, S. J.; Hursthouse, M., *Chemistry of Materials*, (2000) **12**, 16.

[29] Sankar, G.; Wyles, J. K.; Catlow, C. R. A., *Topics in Catalysis*, (2003) **24**, 173.

[30] Renevier, H.; Hodeau, J. L.; Marezio, M.; Fontaine, A.; Michalowicz, A.; Tourillon, G., *Physics Review*, (1993) **B47**,

[31] Wirt, M. D.; Sagi, I.; Chen, E.; Frisbie, S. M.; Lee, R.; Chance, M. R., *Journal of the American Chemical Society*, (1991) **113**,

[32] Wojdyr, M., *Journal of Applied Crystallography*, (2010) **43**, 1126.

[33] Sankar, G.; Bras, W., *Catalysis Today*, (2009) **145**, 195.

[34] Stocker, M., *Microporous and Mesoporous Materials*, (1999) **29**, 3.

[35] Logdberg, S.; Lualdi, M.; Jaras, S.; Walmsley, J. C.; Blekkan, E. A.; Rytter, E.; Holmen, A., *Journal of Catalysis*, (2010) **274**, 84.

[36] Sachtler, J. W. A.; Kool, J. M.; Ponec, V., *Journal of Catalysis*, (1979) **56**, 284.

[37] Kang, M.; Inui, T., *Journal of Molecular Catalysis a-Chemical*, (1999) **144**, 329.

[38] Kaiser, S. W., 872 505, (1987).

Chapter 7. Discussion and Summary

An investigation into the crystallization, and substitution mechanisms of cobalt ions into the AFI framework was carried out to gain a greater understanding into the complex processes occurring during the formation of these catalytic materials, which could lead to a more rational approach in their synthesis. Over a decade ago, Sankar et al[1]. first combined XRD/XAS measurements sequentially and revealed a transformation in the cobalt coordination environment from octahedral to tetrahedral prior to crystallization. Later, utilizing advances in reactor and detector technologies, Grandjean et al[2]. re-examined this formation of CoAlPO-5 and obtained high quality XAS data combined with SAXS/WAXS, UV-Vis, and Raman spectroscopy to reveal Co-O-P species bound to the disordered Al-O-P network prior to a slow conversion to tetrahedral cobalt species. Through combining the different results, Grandjean et al[2]. were able to propose a crystallization model that involved the aggregation of a secondary amorphous phase, containing chains of -Co-O-P-O-Al- species, from a primary amorphous phase, which nucleates into the crystalline CoAlPO-5 material. This observation of chain-like species was of particular interest as it provided experimental evidence for the chain formation mechanism proposed by Oliver et al[3]. In particular, the XAS and UV-Vis results, in relation to the cobalt coordination environment, were interpreted as a mixture of octahedral and tetrahedral cobalt species in the secondary amorphous phase. This is in contrast to a previous *in situ*

UV-Vis study by Weckhuysen et al.[4] which indicated the presence of pseudo-octahedral cobalt species prior to the appearance of framework tetrahedral Co(II).

While these *in situ* measurements were conducted sequentially, the gap between measurements may have lost some vital information and hence we developed the simultaneous measurement method, bearing in mind all the issues of measuring XRD above the aborsption edge (fluorescence effects) and with a continuously changing wavelength. This resulted in the simultaneous measurement of XRD and XAS (at the Co K-edge) for the first time during a chemical reaction to follow changes in both the local and long-range order of CoAlPO-5.

The coordination environment of the substituting metal may play a vital role in the crystallization and substitution mechanism of cobalt substituted AFI materials. Therefore, the simultaneous XRD/XAS study presented in this thesis during the formation of CoAlPO-5, presented a more rapid and higher quality solution to the problem of low time resolution that can occur in combined measurements performed sequentially. In this simultaneous XRD/XAS study, an octahedral Co(II) species was found to transform to a tetrahedral environment in the framework via a two-stage conversion, in which a stable pseudo-octahedral Co(II) species partially bound to phosphorous exists. Although the differences observed between this study and the sequential XAS/WAXS investigation performed by Grandjean et al. could arise from the improved time resolution in the combination of the methods, an effect on the cobalt species in solution from the use of different organic templates could also play a vital role. The previous investigations discussed employed tetraethylammonium hydroxide as the organic template, which is well known to produce CHA phase as a

competing material under certain conditions. Although the CHA phase was not observed during the crystallization process, the use of this template may have a different effect on the Co(II) ions. This simultaneous XRD/XAS study was unique as it utilised methyldicyclohexylamine as the organic template and is known to form phase pure AFI over a wide range of pH and temperature. Since a number of templates can form the AFI structure and the same template can form not just AlPO-5 but a number of other structures, the role of the template is not thought to be specific to the AFI structure. However, the contrasting results from these studies reveal that the organic template may play a key role in the substitution mechanism of metal ions into the AFI framework.

In addition, when the results from the simultaneous XRD/XAS study were combined with an *in situ* HRXRD investigation, a possible solid-hydrogel transformation mechanism was proposed. CoAlPO-5 crystals were found to form under the same conditions in steam-assisted conversion experiments performed in our lab, and since Grandjean et al[2]. revealed the appearance of pre crystalline layered phases, this solid-hydrogel transformation mechanism appears rational.

Although these studies provide a wealth of information in regards to the substitution mechanism of cobalt into the AFI framework, the general crystallization mechanism of aluminophosphates is not fully probed with *in situ* XAS performed at the Co K edge. For example, our HRXRD, NMR, and TGA-MS studies revealed differences in the CoAlPO-5 and AlPO-5 materials in relation to the coordination environment of Al, the water content and possible defects in the structure. Recently, Beale et al.[5] also found differences in the amount of octahedral Al(III) species

present in AlPO-5 and CoAlPO-5 through an *in situ* XAS study at the Al K-edge which has the advantage of probing an element which constitutes the majority of the nanoporous framework, as oppose to Co(II) which makes up only a fraction of the final structure. In addition, the differences observed between the CoAlPO-5 and AlPO-5 frameworks demonstrate the significant effect which cobalt(II) ions have on the nanoporous material, indicating that these probe molecules can not necessarily be used as a spectroscopic probe as they clearly affect the overall process of formation[6]. However, XAS techniques which probe such light elements, such as Al, P and Si, are difficult to perform; any advancements in the methodologies concerned with the direct probing of such elements *in situ*, would therefore be essential for a greater and more complete understanding of the formation process as a whole.

Furthermore, combination of the simultaneous XRD/XAS method described in this thesis, along with other techniques such as UV-Vis and Raman spectroscopy would be beneficial in studying the formation of nanoporous materials. For a more complete understanding of the processes occurring during the formation of aluminophosphate materials, the current study should be extended to include other zeolitic framework types and the affect of template and water concentration investigated.

In addition to investigating the substitution mechanism of heteroatoms into the AFI framework, a kinetic study was carried out to investigate; the effect of the type and concentration of divalent metal cations, and the type of organic template on the crystallization of a number of AlPO-5 materials. Although an analysis of the crystallization curve alone does not present a complete or conclusive interpretation of

the nucleation and growth mechanisms, examination of this part of the growth process with *in situ* XRD can provide some useful indication. Results revealed that the introduction of cobalt ions to the AlPO-5 synthesis gel significantly increased the crystallization rate, with comparable nucleation. However, at cobalt concentrations above 6 wt. %, the crystallization rate was found to be similar to that of unsubstituted AlPO-5 with decreasing nucleation. This decrease in nucleation above 6wt. % Co was previously attributed to the presence of a CHA impurity phase, however, it is clear with the use of MCHA as the organic template which only forms phase pure AFI that this is not the reason for the change in kinetics[7]. Kinetic analysis was based on the Avrami-Erofe'ev model with results indicating that all the AFI materials crystallized with the same 1-D growth mechanism which was phase boundary controlled with differing nucleation. This interpretation of the dimensionality and growth mechanism was based on Hulbert's values for the Avrami constant, *n*, which may not be accurate for the interpretation of the growth mechanism of zeolites since these values were originally derived to described solid state reactions of ceramic mixes[6]. In addition, the agglomeration of the 1-D rod/needle shape crystals into 3-D spheres may have an effect on the calculated n value giving misleading results.

The Avrami-Erofe'ev model essentially describes solid-state reactions and not solution-mediated processes; our previous investigation suggested that AFI formation is via a solid-hydrogel transformation mechanism, therefore this model should present a reasonable analysis of the kinetics, especially since it provided a good fit of the kinetic curves. However, complexities may arise in this analysis method since both solid-solid and liquid mediated growth processes may operate together, with

their differentiation becoming a challenge. Pair distribution function (PDF) analysis method could provide valuable information, in particular characterising the amorphous component of the crystallising gel, but currently it is limited to *ex situ* methods since liquid components in the gel contribute more than the solid part[8]. In addition, time-resolution is also an issue; therefore, further work is needed to improve the methodology to use this technique as a characterising tool of the amorphous component of the growing system. This may offer additional information to provide a better understanding of the formation of nanoporous solids.

Understanding the incorporation of heteroatoms into the framework of aluminophosphate materials has been an important topic as the heteroatom imparts functional properties. In the majority of cases, the concentration of the heteroatom is low and is expected to substitute at random in the structure; therefore, the majority of previous studies discounted the use of XRD as a tool to determine the nature of substitution. X-ray absorption (XAS) and infrared (IR) spectroscopy have been the most widely used methods to infer the substitution of metal ions in the framework. While XAS has been successfully employed, use of this technique cannot provide unambiguous information of the substitution of the metal ions in the framework since it is an average technique and provides combined information about both framework and any extra framework species. Therefore, XRD may provide a better route into determining the extent of framework substitution where an expansion of the unit cell parameters maybe observed with an increase in heteroatom (with a larger ionic radius) incorporation. In the case of titanosilicate TS-1, XRD was used to demonstrate the substitution of Ti(IV) ions in place of Si(IV) in the framework,

however XAS was necessary to confirm Ti(IV) is in a tetrahedral coordination[9]. Similar such use of the XRD technique has been employed to examine framework substitution of heteroatoms in the AFI system, however no systematic studies have been carried out resulting in mixed opinions in the literature as to whether both the a(=b) and c parameter increase with an increase in heteroatom incorporation.

Here we showed for the first time, a systematic study on a number of mono- and multi- metal substituted AFI materials employing high-resolution XRD to determine the extent of framework substitution. This revealed that both the a(=b) and c unit cell parameters increase with an increase in heteroatom substitution. XRD analysis was performed on the as-synthesised AFI materials, although similar trends were observed with calcined samples, the extent to which the unit cell parameters expand may differ due to different interactions with the organic template and lead to an inaccurate picture of the degree of framework substitution. In addition, the previous *in situ* HRXRD study showed water present in the system affects the c parameter; therefore, the as-synthesised AFI samples may have different hydration levels. For these reasons, it appears that this XRD method would need to be developed based on calcined and dried samples so that any effects from the template or water interactions on the unit cell parameters would be eradicated. Although this XRD method proved to be a powerful technique in determining the extent of heteroatom substitution in mono-substituted AFI materials, it failed in providing an accurate measure of multi-metal framework incorporation, resulting in the need for other techniques, in particular XAS, which could probe one type of metal ion differing to another.

The results presented in this thesis may have some significance that may lead to future practical applications in the rational synthesis of new nanoporous materials; however, future work would be required to follow up preliminary studies and further results collected for a number of different structure types. In relation to the methods used within this thesis; these have been successfully employed to study industrially-used nanoporous materials, resulting in an improvement in the analysis turnaround time and the ability to directly correlate certain features of the nanoporous framework with stability and catalytic performance.

This thesis demonstrates how a number of methods, both *ex situ* and *in situ*, can be utilised to precisely determine the heteroatom substitution in nanoporous materials. Each technique probes different length-scales, time, spatial, elemental and concentration resolution, with their own advantage in providing specific information about the porous solid, however, at the same time all of the techniques have limitations. Hence, through a number of experimental examples described in this thesis, it is clear that the combination of different techniques is required to obtain a more complete understanding of the formation and framework substitution of metal incorporated aluminophosphate materials. In particular, synchrotron radiation is essential for advancements in the development of *in situ* and combination methodologies, however a better understanding of the complex formation and metal substitution processes still requires the inclusion of several independent techniques, including *ex situ* methods.

7.1 References

[1] Sankar, G.; Thomas, J. M.; Rey, F.; Greaves, G. N., *Journal of the Chemical Society-Chemical Communications*, (1995), 2549.

[2] Grandjean, D.; Beale, A. M.; Petukhov, A. V.; Weckhuysen, B. M., *Journal of the American Chemical Society*, (2005) **127**, 14454.

[3] Oliver, S.; Kuperman, A.; Lough, A.; Ozin, G. A.; Garces, J. M.; Olken, M. M.; Rudolf, P., New insights into the mode of formation of AlPO4-n moleculare sieves, In *Zeolites and Related Microporous Materials: State of the Art 1994*, Weitkamp, J.; Karge, H. G.; Pfeifer, H.; Holderich, W. Eds.; Elsevier Science Publ B V: Amsterdam, (1994); Vol. 84, pp 219.

[4] Weckhuysen, B. M.; Baetens, D.; Schoonheydt, R. A., *Angewandte Chemie-International Edition*, (2000) **39**, 3419.

[5] Beale, A. M.; van der Eerden, A. M. J.; Grandjean, D.; Petukhov, A. V.; Smith, A. D.; Weckhuysen, B. M., *Chemical Communications*, (2006), 4410.

[6] O'Brien, M. G.; Beale, A. M.; Weckhuysen, B. M., *Chem. Soc. Rev.*, (2010) **39**, 4767.

[7] Davies, A. T.; Sankar, G.; Catlow, C. R. A.; Clark, S. M., *Journal of Physical Chemistry B*, (1997) **101**, 10115.

[8] Wakihara, T.; Kohara, S.; Sankar, G.; Saito, S.; Sanchez-Sanchez, M.; Overweg, A. R.; Fan, W.; Ogura, M.; Okubo, T., *Physical Chemistry Chemical Physics*, (2006) **8**, 224.

[9] Millini, R.; Massara, E. P.; Perego, G.; Bellussi, G., *Journal of Catalysis*, (1992) **137**, 497.